

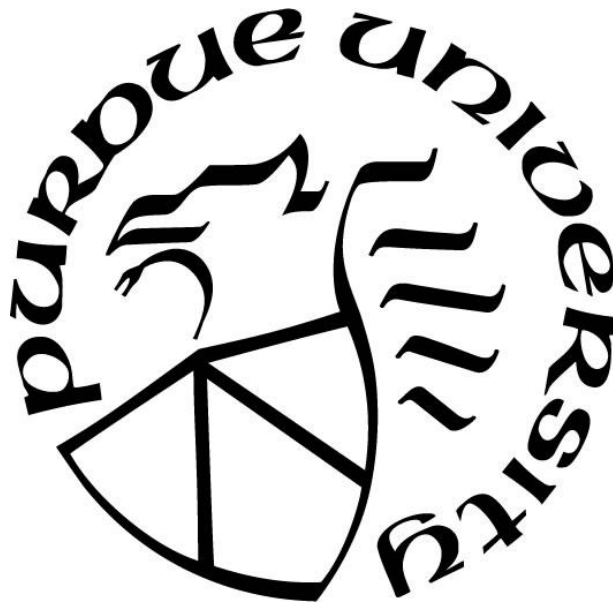
**NITRIDE-BASED NANOCOMPOSITE THIN FILMS TOWARDS  
TUNABLE NANOSTRUCTURES AND FUNCTIONALITIES**

by  
**Xuejing Wang**

**A Dissertation**

*Submitted to the Faculty of Purdue University  
In Partial Fulfillment of the Requirements for the degree of*

**Doctor of Philosophy**



School of Materials Engineering

West Lafayette, Indiana

August 2020

**THE PURDUE UNIVERSITY GRADUATE SCHOOL**  
**STATEMENT OF COMMITTEE APPROVAL**

**Dr. Haiyan Wang**

School of Materials Engineering

**Dr. Carol Handwerker**

School of Materials Engineering

**Dr. Rodney Trice**

School of Materials Engineering

**Dr. Peter Bermel**

School of Electrical and Computer Engineering

**Approved by:**

Dr. David Bahr

*To my parents and my husband.*

## ACKNOWLEDGMENTS

First and foremost, I would like to thank my advisor, Prof. Haiyan Wang, for her support and guidance throughout my doctoral studies. I always feel grateful joining her group at the time when she moved to Purdue University. We had great time setting up lab equipment and went through many difficulties together. She is always energetic and optimistic, and I was deeply impressed by her personality and her dedication to research. She is a great mentor and I feel lucky to conduct my PhD studies under her guidance.

I would like to thank all my committee members, Prof. Carol Handwerker, Prof. Rodney Trice, and Prof. Peter Bermel for their time and effort in assisting my thesis projects and providing valuable suggestions. I also thank Prof. John Blendell for attending my Preliminary exam.

I wish to thank Prof. Peter Bermel, Prof. Letian Dou, Prof. Oana Malis and Prof. Lia Stanciu from Purdue, Prof. Judith Driscoll from University of Cambridge, Prof. Xiaoshan Xu from University of Nebraska-Lincoln, Prof. Xiaoqin Li from UT Austin, Dr. Xuedan Ma from Argonne National Lab and Dr. Ping Lu from Sandia National Lab, and many not listed. We had great collaborations on many published and on-going works, I really appreciate those fruitful discussions and their experimental efforts and paper revisions.

I would like to thank all my group members at Purdue, especially those who offered help on my projects and collaborated on joint projects. Most notably, I appreciate Dr. Jie Jian for teaching me TEM and other hands-on skills, we had many collaborations and discussions. I also thank Dr. Jijie Huang for the collaborations when we started projects in nitride-metal nanocomposites. I also want to extend my gratitude to the college of engineering of Purdue University, for receiving the outstanding graduate researcher award in the 2019-2020 academic year.

Finally, I want to give my sincere thanks to my husband Zheng Zhang, and my parents, who have been continuously giving me love and support during the past few years, making me mentally strong and optimistic towards research and life.

## TABLE OF CONTENTS

LIST OF TABLES .....	7
LIST OF FIGURES .....	8
NOMENCLATURE .....	18
ABSTRACT.....	20
1. INTRODUCTION.....	22
1.1 Optical Metamaterial .....	22
1.1.1 Overview of Plasmonics .....	23
1.1.2 Plasmonic Nanostructures for Sensing and Light Harvesting .....	24
1.1.3 Overview of Metamaterial.....	27
1.1.4 Fabrication of Plasmonic Metamaterial.....	30
1.1.5 Applications of Metamaterials.....	35
1.2 Nanocomposites.....	41
1.2.1 Overview.....	41
1.2.2 Fabrication Methods of Nanocomposite Thin Films .....	42
1.2.3 Growth Mechanisms.....	45
1.2.4 Oxide-Oxide Nanocomposites.....	49
1.2.5 Metal-Oxide Nanocomposites .....	58
1.2.6 Alternative Plasmonic Candidates.....	67
1.2.7 Metal-Nitride Nanocomposites.....	71
2. EXPERIMENTAL TECHNIQUES.....	80
2.1 Pulsed Laser Deposition .....	80
2.2 X-Ray Diffraction.....	82
2.3 Transmission Electron Microscopy .....	83
2.4 Ellipsometry .....	87
2.5 UV-Vis Spectrophotometer .....	88
2.6 Physical Property Measurement .....	89
3. HYBRID PLASMONIC GOLD – TITANIUM NITRIDE VERTICALLY ALIGNED NANOCOMPOSITE: A NANOSCALE PLATFORM TOWARDS TUNABLE OPTICAL SENSING.....	91

3.1	Overview.....	91
3.2	Introduction.....	91
3.3	Results and Discussion .....	93
3.4	Conclusion .....	112
3.5	Additional Information .....	112
4.	SELF-ASSEMBLED SILVER – TITANIUM NITRIDE HYBRID PLASMONIC METAMATERIAL: TAILORABLE TILTED NANOPILLAR AND OPTICAL PROPERTIES.. .....	114
4.1	Overview.....	114
4.2	Introduction.....	114
4.3	Results and Discussion .....	116
4.4	Conclusion .....	130
4.5	Additional Information .....	131
5.	ALUMINUM NITRIDE-BASED HYBRID THIN FILMS WITH SELF-ASSEMBLED PLASMONIC GOLD AND SILVER NANOINCLUSIONS .....	133
5.1	Overview.....	133
5.2	Introduction.....	133
5.3	Results and Discussion .....	135
5.4	Conclusion .....	145
5.5	Additional Information .....	146
6.	THREE-DIMENSIONAL TRILAYER HYBRID METAMATERIALS WITH TUNABLE GOLD NANOSTRUCTURES AND OPTICAL PROPERTIES .....	147
6.1	Overview.....	147
6.2	Introduction.....	147
6.3	Results and Discussion .....	149
6.4	Conclusion .....	162
7.	SUMMARY AND OUTLOOK.....	163
7.1	Summary.....	163
7.2	Outlook .....	164
	REFERENCES .....	167

## LIST OF TABLES

Table 1.1 Crystal structure and physical parameters of common ceramic nitrides. <sup>[117]</sup> .....	74
Table 1.2 Crystal structure and physical parameters of common metals. <sup>[118]</sup> .....	75
Table 1.3 Crystal structure and lattice parameter of eight different phases of TaN. <sup>[119]</sup> .....	75
Table 3.1 Peak position of first-order acoustic modes from Raman measurements.....	110

## LIST OF FIGURES

Figure 1.1 (a) Surface plasmon polaritons (SPPs) and (b) localized surface plasmons (LSPs). ..	23
Figure 1.2 Ag nanostructures synthesized by polyol method, geometries include spheres, cubes, truncated cubes, right bipryamids, bars, spheroids, triangular plates, and wires. <sup>[13]</sup> .....	25
Figure 1.3 Effect of size and shape on localized surface plasmon resonance (LSPR) extinction spectra for Ag nanoprisms and nanodiscs fabricated by nanosphere lithography. <sup>[16]</sup> .....	26
Figure 1.4 Plasmonic light-trapping geometries in thin film solar cells. <sup>[18]</sup> .....	27
Figure 1.5 Left: unit cell or atom of natural materials. Right: meta-atom of metamaterial.....	27
Figure 1.6 The Lycurgus Cup viewed in (a) reflected light and (b) transmitted light, (c) TEM image of silver-gold alloy crystal embedded in the cup. <sup>[19]</sup> .....	28
Figure 1.7 Passage of rays of light through a plate of thickness $d$ made of a left-handed substance. <sup>[20]</sup> A: source of radiation; B: detector of radiation. (b) Resonance curve of a designed copper SRR with specified dimension. <sup>[22]</sup> .....	29
Figure 1.8 Metamaterial four-quadrant space built on $\epsilon$ and $\mu$ . 1 <sup>st</sup> : Double-positive (DPS), 2 <sup>nd</sup> : epsilon-negative (ENG), 3 <sup>rd</sup> : double-negative (DNG), 4 <sup>th</sup> : mu-negative (MNG).....	30
Figure 1.9 Fabrication processes using lithography. <sup>[26]</sup> .....	31
Figure 1.10 Metasurfaces fabricated by EBL method. (a) Gradient metasurface with V-shaped and bar-shaped antennas, <sup>[26]</sup> (b) nanofishnet, <sup>[27]</sup> (c) split-ring resonators. <sup>[28]</sup> .....	32
Figure 1.11 (a) Schematic illustration on polymer-solvent interactions creating gels and swelling. <sup>[24]</sup> (b) Fishnet patterns showing edges with residuals. <sup>[28]</sup> .....	32
Figure 1.12 SEM photographs of the porous nanohole (a) top projection and (b) cross-sectional view. <sup>[30]</sup> .....	34
Figure 1.13 Al <sub>2</sub> O <sub>3</sub> /Ag wire metamaterial with negative optical refraction. <sup>[31]</sup> .....	34
Figure 1.14 Cross-sectional and TEM images of Ag nanowire array embedded in Al <sub>2</sub> O <sub>3</sub> or SiO <sub>2</sub> matrix. <sup>[34]</sup> .....	35
Figure 1.15 Review of metasurfaces. (a) Nanodisks, <sup>[35]</sup> (b) rod antennas, <sup>[36]</sup> (c) V-shaped antennas, <sup>[26]</sup> (d) gammadions chiral metamaterial, <sup>[37]</sup> (e,f) split-ring resonators, <sup>[28, 38]</sup> (g) inverse asymmetric split-ring resonator, <sup>[39]</sup> (h) double-fishnet structure. <sup>[40]</sup> .....	36
Figure 1.16 Scanning electron microscope (SEM) image of V-shaped nanoantenna array composed of Au. Schematic illustration on experimental setup. <sup>[26]</sup> .....	37
Figure 1.17 Angle of incidence versus angle of (a) refraction and (b) reflection for ordinary and anomalous cases. <sup>[26]</sup> .....	38
Figure 1.18 Three-dimensional holography reconstructed by a gradient plasmonic metasurface. <sup>[46]</sup> .....	38

Figure 1.19 $k$ -space topologies for (a) isotropic dielectric, $\epsilon_x, \epsilon_y, \epsilon_z > 0$ , (b) type-I HMM ( $\epsilon_x, \epsilon_y > 0, \epsilon_z < 0$ ) and (c) type-II HMM ( $\epsilon_x, \epsilon_z < 0, \epsilon_y > 0$ ). .....	39
Figure 1.20 Schematics of (a) multilayer and (b) nanowire hyperbolic metamaterial. Red: metal, yellow: dielectric/semiconductor, blue: substrate crystal. ....	40
Figure 1.21 (a) Schematic of nanopatterned multilayer HMM. (b) STEM image showing the multilayer nanostructure. (c) Elemental mapping of constituent materials. Ag: green, Si: red. <sup>[49]</sup> .....	40
Figure 1.22 Schematic on two-phase nanocomposite geometries. ....	42
Figure 1.23 Pulsed laser deposition setup and description of deposition process. <sup>[63]</sup> .....	43
Figure 1.24 Film surface uniformity for point and surface sources, inset shows the illustration of evaporation from the source to substrate. <sup>[62]</sup> .....	44
Figure 1.25 Three growth modes of thin films. <sup>[62]</sup> .....	46
Figure 1.26 Schematic illustration of nucleation process of adatoms on substrate surface during vapor deposition. <sup>[62]</sup> .....	47
Figure 1.27 Free energy versus composition curve. ....	48
Figure 1.28 (a) Plan-view TEM image, (b) SAED patterns showing in-plane heteroepitaxy, (c) dark-field cross-section TEM. <sup>[74]</sup> .....	49
Figure 1.29 TEM plan-view image showing a quasi-hexagonal arrangement of CFO nanopillars, and corresponding (b) electron diffraction patterns. <sup>[53]</sup> .....	50
Figure 1.30 Geometrical tunability of the two-phase VANs. ....	50
Figure 1.31 Cross-sectional STEM images of MgO-LSMO VAN system. <sup>[75]</sup> .....	51
Figure 1.32 (a) STEM micrographs of cross-section and plan-view images of the BFO-SmO VAN system. <sup>[69]</sup> (b) TEM and STEM micrographs of the LSMO-ZnO VAN system. <sup>[76]</sup> .....	52
Figure 1.33 High-resolution plan-view TEM images showing the change of shape of the Fe nanowire with respect to deposition temperature. <sup>[74]</sup> .....	52
Figure 1.34 Cross-section TEM image of LSMO : ZnO VAN grown under (a) 1 Hz frequency and (b) 10 Hz. <sup>[63]</sup> .....	53
Figure 1.35 Summary of oxide-oxide nanocomposite functionalities. <sup>[60]</sup> .....	54
Figure 1.36 (a,b) Illustration of FM-I-FM tunneling junction as vertical or planar mode. (c) Temperature dependence of resistivity and MR% at different magnetic field. <sup>[63]</sup> .....	55
Figure 1.37 MR% versus temperature for LSMO-ZnO VANs deposited at different laser frequencies. <sup>[63]</sup> .....	56
Figure 1.38 (a) Microstructure of BZO nanoparticles embedded in YBCO matrix as effective flux pinning centers. (b) $J_c$ versus magnetic field curves, inset shows the anisotropic effect showing stronger enhancement along $H//c$ . <sup>[73]</sup> .....	57

Figure 1.39 3D microstructure of Au-BTO VAN thin film. (e) 3D schematic illustration of the nanostructure. (a-c) Plan-view images and (d,f,g,i) cross-sectional images and SAED patterns. (h) Diffraction patterns. (j) Atomic model at Au/BTO interface. <sup>[56]</sup> .....	59
Figure 1.40 (a) Cross-sectional STEM images of Au-BTO system with changes of film thickness. (b,c) Uniaxial real-part permittivity with stack of different films. Inset shows a $k$ -space isofrequency surface. <sup>[80]</sup> .....	60
Figure 1.41 (a,b) Top view SEM image of Ni nanowire grown in alumina matrix. (c) Kerr rotation measured as a function of photon energy. <sup>[83]</sup> .....	61
Figure 1.42 Microstructure of Co-BZO VAN deposited on STO, including plan-view and cross-sectional STEM images, EDX mapping and diffraction patterns. <sup>[57]</sup> .....	62
Figure 1.43 Au-ZnO VANs deposited under different laser frequency: 2 Hz, 5Hz and 10 Hz. <sup>[58]</sup> .....	63
Figure 1.44 Schematic illustration on the templated method of growing ordered CFO : BFO nanocomposite. <sup>[91]</sup> .....	64
Figure 1.45 Microstructure of Au shell - Ag core nanoplates. (a) TEM image, (b) HTREM image, inset shows diffraction patterns, (c) STEM image and (d) EDX elemental mapping. <sup>[100]</sup> .....	65
Figure 1.46 Interband transition of Au at visible wavelength range. <sup>[93]</sup> .....	66
Figure 1.47 (a) Schematic illustration of fabrication process of the graphene-based metamaterial. (b) SEM image of the grating. (c) Measured absorptivity spectra under TE and TM polarizations and unpolarized light. <sup>[104]</sup> .....	67
Figure 1.48 Rock salt crystal structure. <sup>[98]</sup> .....	68
Figure 1.49 Cross-sectional TEM images of epitaxial TaN/TiN grown on Si substrate. <sup>[111]</sup> .....	69
Figure 1.50 Real and imaginary part dielectric constant of TiN, Ag and Au. <sup>[115]</sup> .....	69
Figure 1.51 SEM images of TiN metamaterial (a) after annealing, (b,e) laser irradiation with different energies. (b) Absorption spectra before and after thermal treatment. SEM images of Au metamaterial (c) after 800 °C annealing and (f) laser irradiation. <sup>[116]</sup> .....	70
Figure 1.52 Second harmonic generation (SHG) measurement and modeling of TiN nanoantenna array. <sup>[118]</sup> .....	71
Figure 1.53 (a) Real part and (b) imaginary part dielectric constant of TiN, TaN, HfN and ZrN. <sup>[114]</sup> .....	73
Figure 1.54 Real and imaginary part dielectric constant of selected metals and nitrides at (a) 500 nm and (b) 1.5 $\mu$ m. (Data source: <a href="https://refractiveindex.info/">https://refractiveindex.info/</a> ) .....	77
Figure 1.55 3D microstructure of Au-TaN VAN system. (a) 3D STEM configuration rebuilt from 2D images. (b-e) Plan-view STEM micrographs, EDX mapping and IFFT image. (f-h) Cross-sectional STEM micrograph, EDX mapping and IFFT image. <sup>[59]</sup> .....	78

Figure 1.56 Raman scattering data of (a) TaN and Au-TaN thin films grown on MgO, (b) TiN and Au-TiN thin films grown on MgO. (c) P-pol output and (d) s-pol output SHG signals with inset showing the polar plots of TaN and Au-TaN nanocomposite thin films. <sup>[59]</sup> .....	79
Figure 2.1 (a) Experimental setup of the PLD chamber and laser. (b) Schematic illustration of chamber configuration, and a zoomed area showing the laser plume and substrate surface.....	81
Figure 2.2 Diffraction of X-ray onto the crystalline lattice plane.....	82
Figure 2.3 Panalytical X'Pert X-ray diffractometer, inner part of the goniometer, X-ray source and detector.....	83
Figure 2.4 Talos F200X TEM.....	84
Figure 2.5 A typical two-lens (C1, C2) column of TEM, C2 aperture can change the beam convergence angle.....	85
Figure 2.6 Two types of operations of TEM including (a) diffraction mode (projection of diffraction patterns) and (b) image mode (projection of image onto the screen). .....	86
Figure 2.7 RC2 ellipsometer with vertical configuration (J.A. Woollam co. inc).....	87
Figure 2.8 UV-Vis Spectrophotometer (PerkinElmer Lambda 1050).....	89
Figure 2.9 The PPMS system from Quantum Design.....	90
Figure 2.10 Four-wire setup for (a) typical resistance measurement, and (b) Hall measurement.	90
Figure 3.1 3D microstructure of Au-TiN nanocomposites grown on MgO substrates with tailored Au density. (a-c) Plan-view TEM images from top projections. (d-f) Cross-sectional TEM images and their diffraction patterns (insets) from $\langle 100 \rangle$ zone axis.....	94
Figure 3.2 Growth mechanism of Au-TiN VAN. Step1: Au nucleation as islanded seed layer. Step 2: TiN and Au co-growth, TiN forms the matrix layer and Au nucleates on top of the seeds. Step 3: Completed VAN film, with smooth surface and protruded Au nanopillars. ....	95
Figure 3.3 Quantification. (a-c) Plan-view TEM images and their calculated density expressed by number of nanopillars per centimeter square ( $\#/cm^2$ ). (d-f) Quantified Au dimension bar plots, which indicate nanopillar widening as Au density increases.....	96
Figure 3.4 Microstructure analysis of low-density Au-TiN VAN. (a) Plan-view STEM image and high resolution of Au nanopillar at top projection. (b) EDS mapping plan-view sample. (c) Cross-sectional STEM and EDS mapping. (d) Cross-sectional HRSTEM at Au/TiN interface and the atomic model.....	97
Figure 3.5 (a) $\theta$ - $2\theta$ scans of density tuned Au-TiN nanocomposites versus a pure TiN for reference. A general widening of (002) TiN peak and continuous increase of (002) d-spacing is observed with increase of Au density. (b) Phi scan of Au-TiN on MgO substrate, indicating a four-fold symmetry without in-plane rotations. (c) $\theta$ - $2\theta$ scans of the samples grown on (0001) sapphire substrates, the films are oriented as (111) for better lattice match. (d) Phi scan of films grown on sapphire, indicating a hexagonal (six-fold) symmetry of (111) Au and (111) TiN. ....	99

Figure 3.6 Optical spectra and numerical simulations. (a) Measurement and (b) Simulated transmittance spectra with of five samples, including a pure 80 nm Au for reference. (c) Reflectance spectra of five samples. (d) Plan-view TEM images (upper pane) and simulated electric field map at 440 nm of hybrid plasmonic metasurface (lower pane) with three different Au densities,  $d$  is the diameter of Au nanopillar. Scale bar of upper pane represents 5 nm. .... 100

Figure 3.7 Surface scattering spectra. The scattering intensity of the three samples are too low to contribute to any reflectance signals, indicating high specular reflectance from the smooth metasurfaces. (b) Dark-field optical imaging of three thin film samples: pure TiN, low density Au-TiN and high density Au-TiN. The bright spots are attributed to micron-scale surface defects or agglomerations. .... 101

Figure 3.8 EDS mapping of critical elements from a large scale for atomic percentage quantification of Au nanopillars in the TiN matrix. Atomic percentage of elements (Mg, O, C, Ti, Au) are shown at top corner. Insets are SEM images which confirm smooth surfaces of the Au-TiN/MgO samples, with quantified Au densities: (a) 11.1 at%, (b) 15.4 at%, (c) 16.7 at% and (d) 28.6 at%. Au density calculation is carried using:  $\rho_{Au} \text{ at\%} = \text{Au at\%} / (\text{Au at\%} + \text{Ti at\%})$ . .... 102

Figure 3.9 Angular dependent reflectance intensities for s- and p-polarized light excitations of (a-b) low density Au-TiN, and (c-d) high-density Au-TiN. (e)  $\Psi$  and (f)  $\Delta$  ellipsometric and fitted parameters of pure TiN and Au-TiN nanocomposites. (g)  $n$  and (h)  $k$  of Au nanorods (calculated), pure TiN film and four Au-TiN films with different Au densities. The extinction coefficient at higher wavelength range indicates lower losses of Au-TiN hybrids as compared to pure Au or TiN films. .... 104

Figure 3.10 (a) Real and (b) imaginary part permittivity of the listed samples: Au ( $r = 3$  nm) nanorods (calculated), pure TiN, Au-TiN films with different Au densities (11.1 at%, 15.4 at%, 16.7 at% and 28.6 at%). (c) Ordinary (in-plane) and (d) extra-ordinary (out-of-plane) real part dielectric constants. (e) Plasma frequency as a function of three Au densities: 11.1 at%, 16.7 at% and 28.6 at% and (f) their carrier densities from Hall measurements. Pure TiN (gray dashed line) carrier density is shown as reference, and the inset is the illustration of Hall experiment setup. .... 105

Figure 3.11 Anisotropic effective permittivity as a function of Au densities in Au-TiN hybrid thin films. (a) In plane (ordinary) real part dielectric constant, (b) out-of-plane (extra-ordinary) real part dielectric constant, (c) in plane imaginary part dielectric constant, and (d) out-of-plane imaginary part dielectric constant. Results are calculated from effective medium theory Maxwell-Garnett (MG) method. .... 106

Figure 3.12 (a-c) Proposed band diagram at Au-TiN junction, and the predicted electron density profile at nanocomposite cross-section. Bulk Au and TiN have a work function of 5.1 eV and 4.4 eV, respectively. At the metallic junction (boundaries) between Au and TiN, there could be electron density variances that electrons accumulated at the Au side while holes at the TiN side. Overall, the Au-TiN nanocomposites are showing enhanced charge carrier density with increased Au nanopillar densities. (d) Experimental setup of Hall measurements. .... 107

Figure 3.13 Chemical sensing demonstration. Total internal reflection spectra on set (a) low density Au-TiN film, set (b) high density Au-TiN film. Step 1: spectra after methanol treatment, signature dips located at 3000  $\text{cm}^{-1}$  correspond to the  $-\text{OH}$  stretch bonded with dangling Au at

metasurface; step 2: spectra after 24 hr functionalization with MPA solution. The signature dips are disappeared due to the thiol bond reaction with –OH stretch; step 3: spectra of samples after 20 minutes UV exposure which serves to break the thiol bonds. The speed of this recovering process has a dependency on Au densities. .... 109

Figure 3.14 Total internal reflection FTIR spectra from reference samples. Following the similar procedure, the samples were washed with methanol before collecting the spectra. (a) Spectra of pure TiN films from the first two steps, showing no interaction with –OH stretch. (b) Spectra of Au colloidal nanoparticles (NPs) and nanorods (NPs) with diameter of 10 nm. Both shows the –OH stretching at  $\sim 2965\text{ cm}^{-1}$ . .... 110

Figure 3.15 (a) Raman spectra of pure TiN, low and high density Au-TiN thin films. Enhancement on SERS signals shown as overall increase of spectrum intensity. First-order transverse acoustic (TA), longitudinal acoustic (LA), transverse optical (TO) and the second-order acoustic (2A) modes maintain comparable in Au-TiN nanocomposites and match with reported values of TiN, indicating a 1:1 ration of TiN while introducing Au phase. (b) Fluorescence (PL) images and (c,d) PL intensities and their normalized spectra excited at 365 nm for three samples: a reference glass, a pure TiN and an Au-TiN samples with spin-coated fluorescent conjugated polymer thin film ( $\sim 10\text{ nm}$ ). .... 111

Figure 4.1 Schematic illustration of Ag-nitride (TiN) hybrid plasmonic metamaterial thin film. Ag nanopillars with subwavelength scale are tailored in terms of their tilting angles (lower pane). The hybrid plasmonic configuration brings new functionalities such as optical anisotropy and angular selectivity. .... 116

Figure 4.2 Three-dimensional morphology of epitaxial Ag-TiN hybrid thin films with different nanopillar tilting geometries. (a-c) Plan-view TEM images of  $0^\circ$  tilted,  $25^\circ$  tilted and  $50^\circ$  tilted Ag. (d-f) Cross-sectional STEM images corresponding to each geometry. Insets are SAED patterns taken at  $\langle 100 \rangle$  zone axis, as well as EDS mapping of two extreme tilting angles. Ag: red, Ti: green. .... 117

Figure 4.3 (a) XRD  $\theta$ - $2\theta$  scan of pure TiN and three Ag-TiN hybrid films grown on MgO substrate. Ag nanopillar is grown as (00l). Satellite peaks of TiN indicate high film quality. (b) XRD phi scan at (220) plane. The four-fold geometry demonstrates desired in-plane matching of Ag, TiN and MgO substrate as (00l). (c) XRD  $\theta$ - $2\theta$  scan of Ag-TiN grown on c-cut sapphire substrate. (d) EDS mapping taken from  $\langle 1100 \rangle$  zone axis reveals tilted Ag nanopillars, which proves a repeatable tilting geometry by controlling the deposition rate. Note that films grown on sapphire is orientated as (111) with lowest surface energy, therefore, the tilting geometry would be stable under different growth rates. .... 119

Figure 4.4 3D STEM images of  $50^\circ$  Ag-TiN hybrid thin film. Schematic illustration is shown at top center showing three faces (100), (010) and (001). (a) Cross-sectional STEM and its (b) high magnification image taken at  $\langle 100 \rangle$  zone axis, (100) face. (c-d) IFFT filtered image both in-plane and out-of-plane with edge dislocations marked at Ag/TiN interface. (e) HRSTEM image of plan-view ((001) face) nanopillar. (f) Cross-sectional HRSTEM image taken from  $\langle 010 \rangle$  zone axis, showing projection of one tilted nanopillar from [010] direction. .... 120

Figure 4.5 Growth mechanism of Ag-TiN hybrid thin films on MgO substrate. Tilting of Ag nanopillar is controlled by tuning the deposition rate. Upper pane: fast rate deposition. Adatoms

diffusion is limited, Ag nucleates are small. High kinetic energy dominates the growth, Ag growth is suppressed (green arrow), leading to straight thin nanopillars. Lower pane: Low deposition rate. More adatoms diffusion (longer resting time) and broadened the Ag dimension (green arrow indicates smaller suppression), exposure of low-energy facets and tilted nanopillar growth. Tilted nanopillar growth is more thermodynamically favorable. .... 122

Figure 4.6 (a) Absorptance spectra of pure TiN, 0° tilted Ag-TiN and 50° tilted Ag-TiN hybrid thin films. Two peaks observed at 330 nm ~ 350 nm and 374 nm correspond to Ag SPR and TiN signals. (b) 2D electric electric field ( $E_y$ ) distribution on 0° tilted Ag-TiN and 50° tilted Ag-TiN hybrid films close to resonant frequencies (350 nm and 420 nm). (c) SHG of 50° tilted Ag-TiN hybrid film, collected from p- and s- output polarizations, inset is the polar plot of SH intensity. .... 124

Figure 4.7 Angular dependent specular reflectance. Two sets of data with 180° apart were measured for each sample, as illustrated in the inset images. (a,b) Specular reflectance from 50° Ag-TiN film. (c,d) Specular reflectance from 0° Ag-TiN film. (e) Electrical field maps at 420 nm of the 50° Ag-TiN film. .... 125

Figure 4.8 (a) Fitted  $n$  and (b)  $k$  of pure TiN and 50° tilted Ag-TiN hybrid film. (c-d) Fitted effective permittivity. (e)  $\Psi$  and (f)  $\Delta$  spectra of 50° tilted Ag-TiN hybrid film and fitted spectra from optical model. Results demonstrate a dielectric tuning of the hybrid film which is more pronounced in the near infrared region. The model is built using B-Spline function of film and MgO on substrate, with MSE of 1.529. .... 126

Figure 4.9 Electrical transport properties of pure TiN and 0° tilted Ag-TiN hybrid film. Both films show metallic behavior with increased electron concentrations at elevated temperatures. With addition of Ag phase, the hybrid Ag-TiN film exhibits enhanced conductivity..... 127

Figure 4.10 Room temperature specular reflectance of 50° tilted Ag-TiN hybrid film. FTIR reflectance spectra grouped by incident light propagating (a) along nanopillar tilting direction ([010]) and (b) backside of nanopillar ([010]), inset images show incident light direction from the cross-sectional view of unit cell. (c) Polar plot showing reflectance intensities versus incident angles at four wavelengths: 2  $\mu\text{m}$  (orange), 3  $\mu\text{m}$  (green), 5  $\mu\text{m}$  (blue) and 8  $\mu\text{m}$  (red)..... 128

Figure 4.11 Thermal stability tests. (a) Reflectance spectra and (b) XRD  $\theta$ -2 $\theta$  scans of Ag-TiN before and after 500 °C 1 hr vacuum annealing. (c) Emissivity spectra measured on a 50° Ag-TiN/sapphire hybrid at sample temperatures of 432 °C, 471°C and 519 °C. Spectra variations from room-temperature FTIR reflectance spectra may be caused by measurement angle mismatch or temperature effect. (d) Cross-sectional STEM images and diffraction patterns taken from two zones of sapphire substrate, <1100> and <1120>. The Ag/TiN interface remains clean without interdiffusion and the diffraction patterns remain sharp..... 129

Figure 4.12 Nano-indentation plots on thick TiN and Ag-TiN hybrid films on MgO. Results are retrieved from a set of loading-unloading cycles with dependence of indentation distance. The indent depth is controlled within 12% of film thickness to avoid substrate effect. Hardness data sets of (a) pure TiN bulk film and (b) Ag-TiN hybrid film. Elastic modulus of (c) pure TiN and (d) Ag-TiN hybrid film..... 130

Figure 5.1 XRD  $\theta$ -2 $\theta$  scans of vacuum grown films: (a) AlN (b) Au-AlN and (c) Ag-AlN on c-cut sapphire substrate. HAADF-STEM images (left) and corresponding SAED patterns of (d) AlN on

sapphire, (e) Au-AlN on sapphire and (f) Ag-AlN on sapphire. Samples were viewed from  $\langle 1100 \rangle$  zone axis..... 136

Figure 5.2 (a) SEM of Au-AlN (Vac) sample viewing from top, showing the saturation of Au particles at top surface. (b) EDX mapping of Au. (c) EDX spectrum of critical elements, including Al, O, N, and Au. (d) SEM of Ag-AlN (Vac) sample viewing from top, showing similarly the Ag saturation. (e) EDX mapping of Ag. (f) EDX spectrum of critical elements: O, Al, N, Ag. The quantified Au (Ag) atomic fraction is approximately 8.35 at% (4.65 at% for Ag), note that substrate ( $\text{Al}_2\text{O}_3$ ) signals could contribute to errors..... 138

Figure 5.3 (a) TEM image of Au-AlN nanocomposite grown in 50 mtorr  $\text{N}_2$ , insets are high resolution image of Au nanoparticle, and selected area electron diffraction (SAED) patterns of the film. (b) EDX mapping of Au-AlN ( $\text{N}_2$ ) sample, inset is corresponding STEM image with Au NPs marked out in yellow circles. Elements including Au and Al are mapped in red and green, respectively. (c) TEM image of Ag-AlN ( $\text{N}_2$ ) sample, inset is HRTEM image of Ag nanoparticle. (d) EDX mapping of Ag-AlN ( $\text{N}_2$ ). ..... 139

Figure 5.4 (a) Transmittance spectra of pure AlN, Au-AlN and Ag-AlN films grown in vacuum condition. (b) Tauc plot of the bandgap. (c) Absorptance spectra of the two nanocomposites, calculated from  $A = 1 - R - T$ . (d) Resistivity versus temperature curves of Au-AlN and Ag-AlN films, note that pure AlN resistivity is out of range..... 140

Figure 5.5 Optical parameters of  $\epsilon_1$  of Au-AlN and Ag-AlN films grown in vacuum. (a) Anisotropic  $\epsilon_1$  of Au-AlN, and (b) corresponding  $\epsilon_2$  values. (c) Anisotropic  $\epsilon_1$  of Ag-AlN, and (d) corresponding  $\epsilon_2$  values, inset images illustrate in-plane ( $//$ ) and out-of-plane ( $\perp$ ) direction with respect to the Au and Ag geometries..... 141

Figure 5.6 Ellipsometry fitted (a) real part dielectric constant and (b) imaginary part of Ag-AlN (Vac) and Au-AlN (Vac) films. (c, d) Raw and fitted ellipsometric parameters ( $\Psi, \Delta$ ) of the vacuum grown Ag-AlN (Vac) to show the accuracy of data fitting..... 142

Figure 5.7 Optical properties of Ag-AlN and Au-AlN films grown in  $\text{N}_2$ . (a) Transmittance spectra with inset STEM image showing the Au nanoparticles being embedded in nanocrystalline AlN matrix. (b-d) Fitted dielectric constant, effective refractive index of Ag-AlN ( $\text{N}_2$ ) and Au-AlN ( $\text{N}_2$ ) films. .... 143

Figure 5.8 (a) Mid-IR transmittance spectra of AlN/Si and Au-AlN/Si samples grown in vacuum, inset is the illustration of optical path through the sample. (b) Transmittance spectra in the near-IR range of Au-AlN/sapphire and Ag-AlN/sapphire, AlN spectrum is applied as baseline. Note that the transmittance is taken from ratio of p-pol intensity/s-pol intensity. .... 144

Figure 6.1 Illustrations of the trilayer film composed of metal-nitride nanocomposite claddings with a pure oxide spacer (left) and a metal-oxide nanocomposite spacer (right). Color represents different material, red: Au, yellow: TiN, blue:  $\text{BaTiO}_3$ , grey: MgO..... 149

Figure 6.2 Left: Au-TiN/BTO/Au-TiN film grown on MgO. (a-1) XRD  $\theta$ - $2\theta$  scan. (a-2) SAED patterns at  $\langle 001 \rangle$  zone axis, (a-3) cross-sectional STEM micrograph and (a-4) corresponding EDX mapping, Au: red, Ti: green, Mg: cyan. Plan-view (a-5) STEM and (a-6) EDX mapping of Au and Ti. Right: Au-TiN/Au-BTO/Au-TiN film grown on MgO. (b-1) XRD  $\theta$ - $2\theta$  scan. (b-2) SAED

patterns at  $\langle 001 \rangle$  zone axis. (b-3) Cross-sectional STEM micrograph and (b-4) EDX mapping. Plan-view (b-5) STEM image and (b-6) EDX mapping of Au and Ti. .... 150

Figure 6.3 (a,b) XRD  $\phi$  scan at (220) plane of Au-TiN/BTO/Au-TiN film grown on MgO substrate. XRD  $\theta$ - $2\theta$  scan of (c) Au-TiN/thick BTO/Au-TiN film grown on Si substrate, and (d) Au-TiN/thick Au-BTO/Au-TiN film grown on Si substrate..... 151

Figure 6.4 Cross-sectional STEM micrographs of (a) four-layer stack and (b) five-layer stack. (c,d) Corresponding cross-sectional EDX mapping. The Au nanopillar array in the hybrid Au-TiN cladding shows a gradual increase from 5 nm (1st layer) to approximately 20 nm (5<sup>th</sup> layer), as marked by the yellow arrows..... 152

Figure 6.5 Plan-view high resolution microstructure of trilayer with Au-BTO spacer. (a,b) STEM micrographs at Au interface. Scale bar represents 5 nm. (c) High-resolution plan-view STEM image. IFFT filtered images along (d) [100] and (e) [010] directions. (f) Atomic model built at Au/BTO interface corresponding to the yellow box of (c)..... 153

Figure 6.6 (a,b) EDX mapping of Au,  $d$  is the diameter of nanopillars,  $d = 5$  nm. (c,d) 2D illustrations of the two trilayer films. 3D illustration of the Au nucleation on (e) MgO substrate, on (f) strained BTO layer and on (g) strained Au-BTO layer. Colors represent different adatoms. TiN: yellow, Au: red, BTO: blue, MgO: grey. .... 155

Figure 6.7 Simulated transmittance spectrum of Au-TiN/BTO/Au-TiN film. (a-1) 2D electric-field maps at 400 nm, 600 nm and 800 nm. (b) Simulated transmittance spectrum of Au-TiN/Au-BTO/Au-TiN film and (b-1) corresponding 2D E-field maps. (c,d) Measured transmittance spectrum of two trilayer films..... 156

Figure 6.8 (a,d) Schematic illustrations on the real samples and models applied for data fitting of two trilayer films. (b) S-polarized and (c) p-polarized angular dependent reflectance, measured (solid lines) and fitted spectra (dashed lines) for trilayer film with BTO spacer. (b) S-polarized and (c) p-polarized angular dependent reflectance, measured (solid lines) and fitted spectra (dashed lines) for the trilayer film with Au-BTO spacer. .... 158

Figure 6.9 (a) Model of Au-TiN/BTO/Au-TiN trilayer. Measured and fitted (b) Psi and (c) Delta spectra at three incident angles from 55° to 75°. (a) Model of Au-TiN/Au-BTO/Au-TiN trilayer. Measured and fitted (dashed lines) (e) Psi and (f) Delta spectra collected at three incident angles from 55° to 75°. The model shows desired matching with measurement, the mean square error (MSE) is below 3. .... 159

Figure 6.10 (a) Real-part and (b) imaginary-part dielectric functions of Au-TiN/BTO/Au-TiN trilayer, (c) real-part and (d) imaginary-part dielectric constant of Au-TiN/Au-BTO/Au-TiN film. .... 159

Figure 6.11 (a) Cross-sectional STEM micrograph of Au-TiN/BTO/Au-TiN film grown on Si (001), (b) HRTEM image of the top cladding. (c) SAED patterns corresponding to a large sample area. (d) Cross-sectional STEM micrograph and (e) HRTEM image at BTO/Au interface. (f,g) EDX mapping. .... 160

Figure 6.12 (a,b) P- and s-polarized reflectance spectra of Au-TiN/thick BTO/Au-TiN film measured at four (45° to 75° with 10° interval) incident angles. (c,d) P- and s-polarized reflectance of the Au-TiN/thick Au-BTO/Au-TiN film. (e) Multipath depolarized IR transmittance comparing

trilayers with thick spacers. The depolarized transmission intensity was derived from their polarized counterparts with incident beam propagating at  $45^\circ$  and bouncing multiple times inside the film. .... 161

Figure 7.1 Schematic of three-dimensional strain coupling of VAN.<sup>[90]</sup> ..... 165

## NOMENCLATURE

SPP	Surface Plasmon Polariton
LSP	Localized Surface Plasmon
SERS	Surface Enhanced Raman Scattering
MTM	Metamaterial
HMM	Hyperbolic Metamaterial
SRR	Split Ring Resonator
VAN	Vertically Aligned Nanocomposite
EBL	Electron Beam Lithography
FIB	Focused Ion Beam
AAO	Anodized Aluminum Oxide
PVD	Physical Vapor Deposition
PLD	Pulsed Laser Deposition
ALD	Atomic Layer Deposition
MBE	Molecular Beam Epitaxy
CVD	Chemical Vapor Deposition
SPS	Spark Plasma Sintering
SEM	Scanning Electron Microscopy
TEM	Transmission Electron Microscopy
HR	High Resolution
HAAD	High Angle Annular Dark Field
SAED	Selected Area Electron Diffraction
IFFT	Inversed Fast Fourier Transformation
EDS/EDX	Energy Dispersive X-ray Spectroscopy
SHG	Second Harmonic Generation
XRD	X-ray Diffraction
RSM	Reciprocal Space Mapping
PPMS	Physical Property Measurement System
MPMS	Magnetic Property Measurement System
FTIR	Fourier Transform Infrared Spectroscopy

RHEED	Reflection High-Energy Electron Diffraction
PL	Photoluminescence
MSE	Mean Square Error
UV	Ultra-violet
IR	Infrared
Vis	Visible
3D	Three-dimensional
2D	Two-dimensional
CMR	Colossal Magnetoresistance
LSMO	$\text{La}_{0.7}\text{Sr}_{0.3}\text{MnO}_3$
GB	Grain Boundary
YBCO	$\text{YBa}_2\text{Cu}_3\text{O}_{7-x}$
BZO	$\text{BaZrO}_3$
BTO	$\text{BaTiO}_3$
CFO	$\text{CoFe}_2\text{O}_4$
BFO	$\text{BiFeO}_3$

## ABSTRACT

Optical metamaterials have triggered extensive studies driven by their fascinating electromagnetic properties that are not observed in natural materials. Aside from the extraordinary progress, challenges remain in scalable processing and material performance which limit the adoption of metamaterial towards practical applications. The goal of this dissertation is to design and fabricate nanocomposite thin films by combining nitrides with a tunable secondary phase to realize controllable multi-functionalities towards potential device applications. Transition metal nitrides are selected for this study due to the inherent material durability and low-loss plasmonic properties that offer stable two-phase hybridization for potential high temperature optical applications. Using a pulsed laser deposition technique, the nitride-metal nanocomposites are self-assembled into various geometries including pillar-in-matrix, embedded nanoinclusions or complex multilayers, that possess large surface coverage, high epitaxial quality, and sharp phase boundary. The nanostructures can be further engineered upon precise control of growth parameters.

This dissertation is composed of a general review of related background and experimental approaches, followed by four chapters of detailed research chapters. The first two research chapters involve hybrid metal (Au, Ag) - titanium nitride (TiN) nanocomposite thin films where the metal phase is self-assembled into sub-20 nm nanopillars and further tailored in terms of packing density and tilting angles. The tuning of plasmonic resonance and dielectric constant have been achieved by changing the concentration of Au nanopillars, or the tuning of optical anisotropy and angular selectivity by changing the tilting angle of Ag nanopillars. Towards applications, the protruded Au nanopillars are demonstrated to be highly functional for chemical bonding detection or surface enhanced sensing, whereas the embedded Ag nanopillars exhibit enhanced thermal and mechanical stabilities that are promising for high temperature plasmonic applications. In the last two chapters, dissimilar materials candidates beyond plasmonics have been incorporated to extend the electromagnetic properties, include coupling metal nanoinclusions into a wide bandgap semiconducting aluminum nitride matrix, as well as inserting a dielectric spacer between the hybrid plasmonic claddings for geometrical tuning and electric field enhancement. As a summary, these studies present approaches in addressing material and fabrication challenges in the field of plasmonic metamaterials from fundamental materials perspective. As demonstrated in the following chapters, these hybrid plasmonic nanocomposites provide multiple advantages towards

tunable optical or biomedical sensing, high temperature plasmonics, controllable metadevices or nanophotonic chips.

# 1. INTRODUCTION

Metamaterials are artificial materials that are not observed in natural materials. Optical metamaterials have triggered extensive studies driven by their fascinating electromagnetic properties including negative refraction, enhanced spontaneous emission, Raman enhanced sensing. The introduction is divided into two sections. In the first section, the concepts of plasmonics and metamaterials, gradient metasurfaces and hyperbolic metamaterials are introduced. Various processing techniques including the top down approaches, including lithographic patterning and focus ion beam milling, and the bottom up approaches, such as anodize templated growth and thin film deposition techniques have been demonstrated and summarized in section 1.1. Novel properties including sensing and light harvesting, holography and negative refraction have been demonstrated. Aside from the extraordinary progress, challenges remain in scalable processing and material performance which limit the adoption of metamaterial towards practical applications. In Section 1.2, the concepts of vertically aligned nanocomposites (VANs), pulsed laser deposition (PLD) technique, thin film nucleation and growth mechanisms will be introduced in the first part, followed by the concepts of oxide-oxide, metal-oxide, metal-nitride nanocomposites and their related properties. These hybrid plasmonic nanocomposites provide multiple advantages towards tunable optical or biomedical sensing, high temperature plasmonics, controllable metadevices and/or nanophotonic chips.

## 1.1 Optical Metamaterial

Optical or plasmonic metamaterial is an emerging field of study fundamentally understood as manipulation of light or electromagnetic wave interactions of subwavelength scaled nanostructures using engineering method. It involves multidisciplinary studies, for example, new physics phenomena or unprecedented properties when material shrinks to nanoscale, material thermodynamics and crystal structures, chemical or physical processing methods, quantum sciences, and more beyond. Compared to metamaterials which is a relatively new concept, the field of plasmonics has been known for a long time. In the following sections, a detailed review on both divisions will be covered, followed by few selected topics in each category, including extreme light confinement using plasmonic nanostructures for enhanced sensing and photovoltaics,

patterned metasurface for effective manipulation of the wavefront, hyperbolic metamaterial with extreme anisotropy using the hybrid of metal and dielectrics. There are indeed many interesting topics, for example, negative index metamaterials, split-ring resonators or nonlinear optical metamaterials, these will not be discussed in detail here but can be found in many existed books and journal articles.

### 1.1.1 Overview of Plasmonics

The field of plasmonics mainly involves the exploration of electromagnetic (EM) wave interactions in subwavelength scaled structures or at metal-dielectric surface, mostly free electrons of metals. The concept of surface wave can be traced back to 1899<sup>[1]</sup> when Sommerfeld reported the wave propagation of a conductive wire. This has been followed up with some well-known studies including Wood’s anomaly (1902)<sup>[2]</sup>, Mie theory (1908)<sup>[3]</sup>, the anomalous diffraction gratings by Fano (1941)<sup>[4]</sup>, as well as the pioneer work from Kretschmann (1968)<sup>[5]</sup>. Fundamentally, plasmon describes the quantization of plasma oscillations, which means collective oscillations of the free electron gas. Luckily, the field of plasmonics falls within the regime of the classical theory such that most of the cases can be described by Maxwell’s equations, there are seldom occasions when we need to bother with quantum plasmonics (e.g. quantum confinement, quantum tunneling) to explain some specific physics phenomena.<sup>[6-8]</sup>

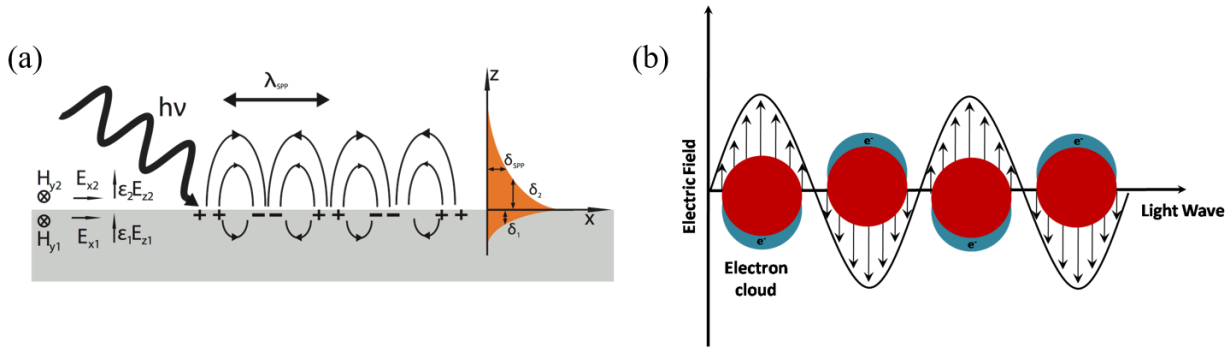


Figure 1.1 (a) Surface plasmon polaritons (SPPs) and (b) localized surface plasmons (LSPs).

Two subdivisions, surface plasmon polaritons (SPPs) and localized surface plasmons (LSPs) represent two major effects of plasmonics. Specifically, SPP (Figure 1.1a) describes the long-range propagation of EM wave at the interface between metal/air or metal/dielectric, while

along the perpendicular direction the field is evanescently confined. Such highly directional EM field confinement can be utilized in multilayer structures, for example, the metal-insulator-metal (MIM) sandwich which realizes two-dimensional (2D) confinement of EM field energy for waveguide design.<sup>[9]</sup> It is noted that for the multilayer systems, coupled SPP modes would be generated when the separation between adjacent single interfaces is at subwavelength scale. Direct excitation of SPP at a planar interface of MIM is not possible since the propagation factor is greater than wave vector in the dielectric, intentional phase matching should be considered such as applying prism or grating coupling geometry.<sup>[10]</sup> On the other hand, LSP (Figure 1.1b) describes a non-propagating excitation between metallic nanostructures and the EM wave, which results in electric field concentration locally at particle surfaces, and optical absorption at the plasmon resonant frequency. Different from SPP, the LSP resonance can be directly excited by light due to the curved nanoscale surfaces. The resonance of different metal nanoparticles could vary, for example, Au and Ag at visible frequency while some others fall into the ultraviolet. Also, the LSP can be strongly affected by the size and shape of the nanoparticles, which make the plasmonic property tunable at a large wavelength regime.<sup>[11]</sup> Most of the plasmonic particle interactions can be described by the quasi-static approximation ( $10 < d < 100$  nm), or the Mie theory ( $d > 100$  nm). It is important to note that for particle dimension smaller than 10 nm, additional factors such as chemical interfacial damping and quantum effect need to be considered. Taking advantage of SPP and LSP, extensive research studies have been explored in tunable plasmonics for bio-sensing applications.<sup>[12]</sup> However, there are still challenges or underexplored research topics which will be covered in next few sections.

### **1.1.2 Plasmonic Nanostructures for Sensing and Light Harvesting**

Plasmonic nanostructures are capable to convert EM radiation into intensively confined and localized fields that can be further redirected or coupled depending on specific applications. Reported studies on chemical synthesized plasmonic nanoparticles being freely dispersed in solution,<sup>[11, 13]</sup> patterned nanoantennas in a periodic fashion supported by solid state substrates,<sup>[14]</sup> have been reported for bio-medical sensing, light harvesting and many others. For example, chemical synthesis has been proved as an effective method in producing plasmonic nanostructures with controllable geometries (Figure 1.2), which is also more flexible in massive productions compare to ion-beam patterning. But achieving perfect periodicity is challenging and the

dispersion of particles requires additional processing efforts. The available spectroscopic detection is capable to approach single-particle surface or molecules to investigate the sensitivity of the surface enhanced Raman scattering (SERS) signals.<sup>[15]</sup>

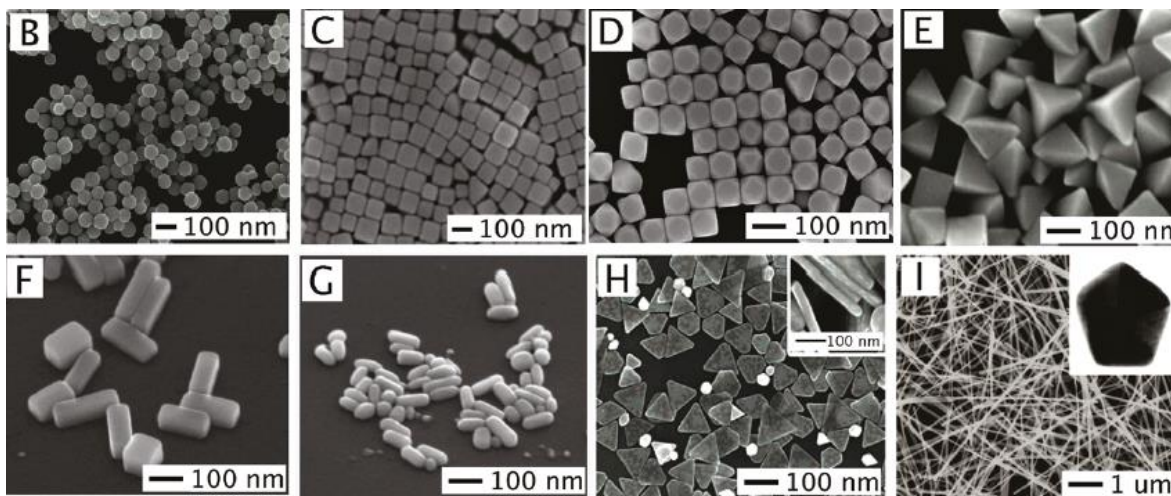


Figure 1.2 Ag nanostructures synthesized by polyol method, geometries include spheres, cubes, truncated cubes, right bipyramids, bars, spheroids, triangular plates, and wires.<sup>[13]</sup>

Among all plasmonic candidates, Au and Ag are well-studied due to their overall high SERS signals over a wide spectrum range, non-toxicity, as well as reasonable stability as noble candidates. Here, surface-enhanced Raman spectroscopy or SERS is understood as an enhanced Raman scattering signal when molecules being adsorbed on metallic nanostructured surfaces that are highly sensitive. Applying SERS to biomedical sensing or chemical detection is very effective and has been widely reported. As an example, Au nanoparticles have been demonstrated to be stable in different solutions (e.g. salts, strong acid and bases, and organic solvents), and biocompatible as effective nanotags for *in vivo* targeting of cancer cells or xenograft tumors.<sup>[12]</sup> Aside from SERS, biosensing using plasmonic nanostructures is attractive in terms of its tunable LSP effect. The tunability can be reached via different ways. It can be tuned by switching between different plasmonic materials (e.g. Au, Ag, Cu, Al) or nanoscale geometries, which are both achievable through multiple available fabrication methods (Figure 1.3).<sup>[16]</sup>

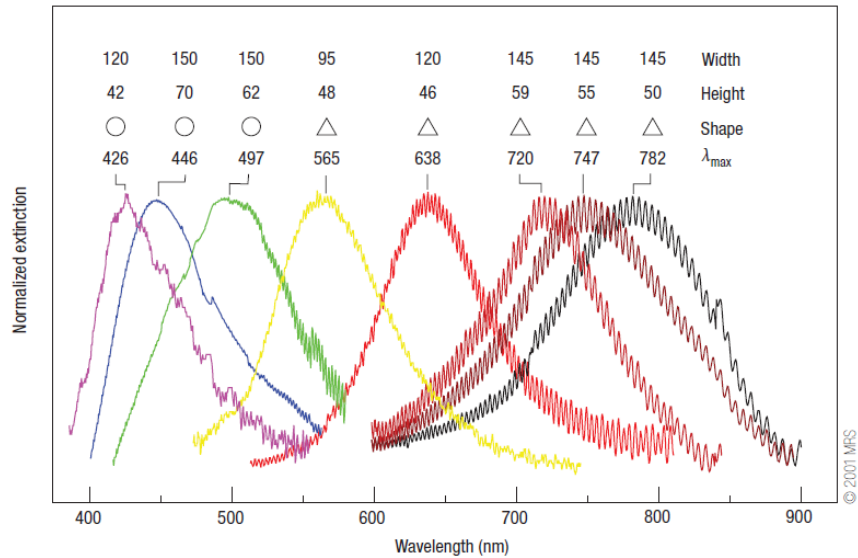


Figure 1.3 Effect of size and shape on localized surface plasmon resonance (LSPR) extinction spectra for Ag nanoprisms and nanodiscs fabricated by nanosphere lithography.<sup>[16]</sup>

In conventional Si solar cells, light trapping is realized by scattering of light at textured surface, mostly limited to bulky designs. However, benefit by plasmonics, the radiation energy trapped or localized at surfaces of nanostructures can be further effectively redirected and collected, or even enhanced using careful designs, meanwhile, the thickness is reduced significantly. Applying plasmonic nanostructures to enhance solar absorption was first demonstrated by Stuart et al in 1996.<sup>[17]</sup> Naturally, the granular formation of ultrathin metallic layers would be an intuitive nanostructured surface with LSPs due to the islanded (granular) nucleation of most metals. These granular shapes can form more rounded particles via annealing. Atwater et al. proposed three design schemes (Figure 1.4) for thin film plasmonic solar cells,<sup>[18]</sup> including (a) scattering and trapping of light into the semiconductor layer using metallic nanoparticles floating on top surface, with the metallic back surface further prevents radiation from escaping; (b) light trapping via LSPs of metal nanoparticles being embedded in the semiconductor layer, generating electron-hole pairs in the semiconductor; and (c) excitation of SPP at the metal/semiconductor interface with corrugated metallic back surface for effective coupling. These plasmonic coupling schemes offer opportunities in designing thin film solar cells to realize effective light trapping by “squeezing” light into nanoscale and effective manipulation of light energy through designable features. Aside from optical losses in the metals, noble metals including Au and Ag become the most favorable

candidates for plasmonics and metamaterial designs. Coupling metallic nanostructures with Si solar cells would bring additional engineering flexibility with potentials to replicate the entire solar spectrum.

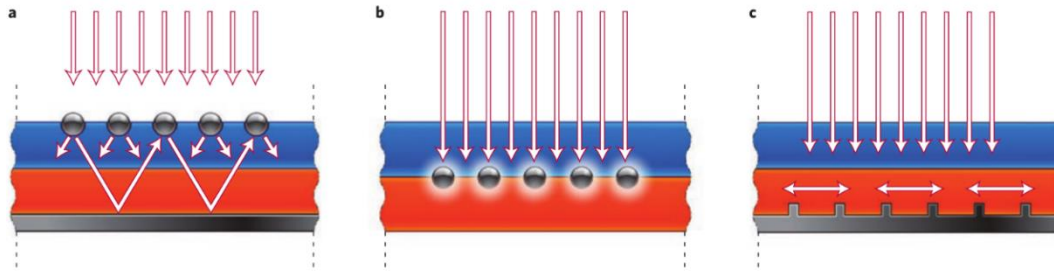


Figure 1.4 Plasmonic light-trapping geometries in thin film solar cells.<sup>[18]</sup>

### 1.1.3 Overview of Metamaterial

The prefix “meta” in Greek means “beyond”, therefore, metamaterial is artificially designed materials with properties unprecedented compare to natural materials. While conventional materials derive their properties from atoms or molecules, the unit of metamaterial is called “meta-atom” or “building block” that are of subwavelength scale being patterned at a periodic fashion (Figure 1.5). These building blocks are retrieved from natural materials but are engineered into certain geometries, the resulted metamaterial as a whole unit exhibit properties completely different from their constituents, making it especially attractive in terms of light-matter interactions.

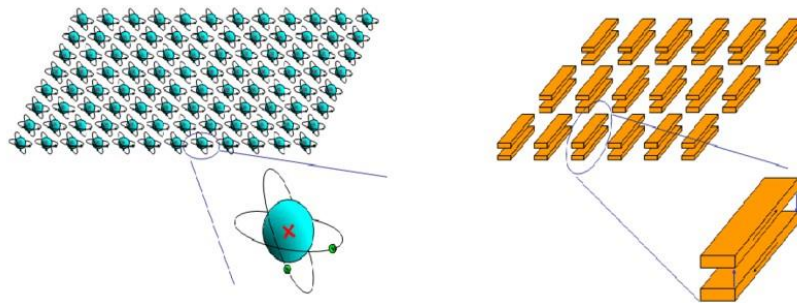


Figure 1.5 Left: unit cell or atom of natural materials. Right: meta-atom of metamaterial.

Date back to 4<sup>th</sup> century A.D., the Lycurgus Cup (Figure 1.6) is known to be the first metamaterial composed of ruby glass with embedded metal nanoparticles.<sup>[19]</sup> The cup shows unique optical effects. Under transmitted light the glass appears as deep wine-red and appears as opaque pea-green reflecting into the eyes. In fact, many artificial materials have been designed long before the term “metamaterial” became widely accepted in the field.

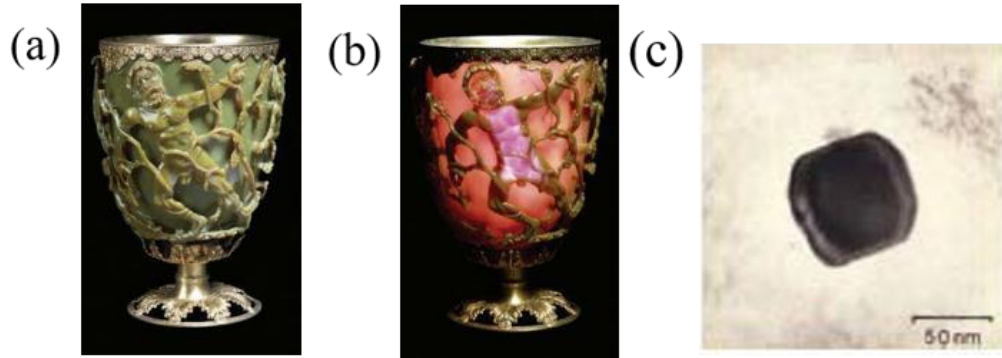


Figure 1.6 The Lycurgus Cup viewed in (a) reflected light and (b) transmitted light, (c) TEM image of silver-gold alloy crystal embedded in the cup.<sup>[19]</sup>

Modern development of metamaterials is represented by three seminal works, which have triggered extensive interests and explorations in the past few decades. V. G. Veselago (1968)<sup>[20]</sup> came up with the idea of “left-handed material” that when substances have simultaneous negative permittivity ( $\epsilon < 0$ ) and permeability ( $\mu < 0$ ), the passage of radiation through such media will be refracted oppositely ( $n < 0$ ) compare to conventional right-handed media (Figure 1.7a). Taking advantage of such negative index materials, J. B. Pendry (2000)<sup>[21]</sup> extended this idea towards the design of “superlenses” which can surpass the diffraction limit of conventional electron microscopy. The first experimental result on left-handed material was provided by D. R. Smith (2000)<sup>[22]</sup>, demonstrating a split ring resonator (SRR) (Figure 1.7b) that exhibits dual negative effective  $\mu$  as well as negative  $\epsilon$  at GHz range. Such designed nanostructure was then termed as “metamaterial”.

Fundamental EM parameters involved in metamaterials are electrical permittivity ( $\epsilon$ , dielectric constant) and magnetic permeability ( $\mu$ ), which respectively describes the electric and magnetic field responses upon EM radiation. Accordingly, four quadrants based on the two parameters have been built to categorize material properties, as shown in Figure 1.8. Specifically, common dielectric materials lie in the 1<sup>st</sup> quadrant, where both  $\epsilon > 0$  and  $\mu > 0$ . Noble metals at

optical frequencies are normally seen in the 2<sup>nd</sup> quadrant ( $\mu < 0$ ), while negative  $\mu$  is supported by polariton resonance of permeability, for example, in certain antiferromagnets (e.g. MnF<sub>2</sub>, FeF<sub>2</sub>) or insulating ferromagnets.<sup>[23]</sup> However, no natural material belongs to the 3<sup>rd</sup> quadrant satisfying both  $\epsilon < 0$  and  $\mu < 0$ , but metamaterials with artificially engineered optical parameters can realize such double-negative (DNG) property at specific frequency range. Theoretical predictions of isotropic media suggest that if  $\epsilon = \epsilon' + i\epsilon''$  and  $\mu = \mu' + i\mu''$  obey  $\epsilon'|\mu| + \mu'|\epsilon| < 0$ , the real part refractive index  $n = n' + in'' = \sqrt{\epsilon\mu}$  will be negative, which is called negative index metamaterial. Such requirement would be changed in anisotropic media such that it is no longer necessary to have both  $\epsilon$  and  $\mu$  negative to achieve negative refraction. However, the material anisotropy would also bring challenges not only to fabrications, but also to calculations and modeling.

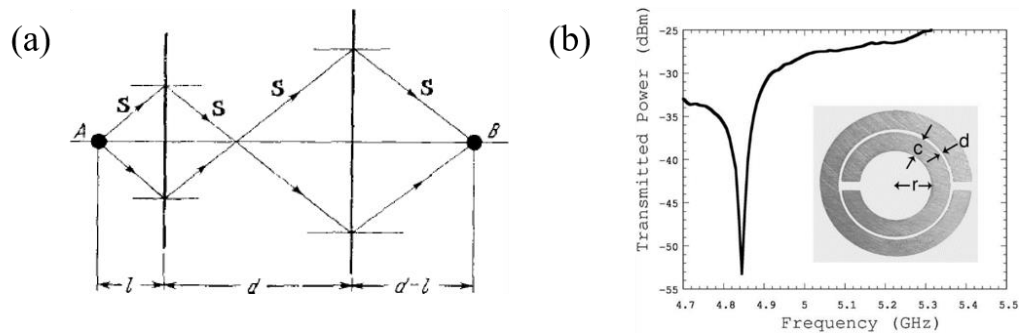


Figure 1.7 Passage of rays of light through a plate of thickness  $d$  made of a left-handed substance.<sup>[20]</sup> A: source of radiation; B: detector of radiation. (b) Resonance curve of a designed copper SRR with specified dimension.<sup>[22]</sup>

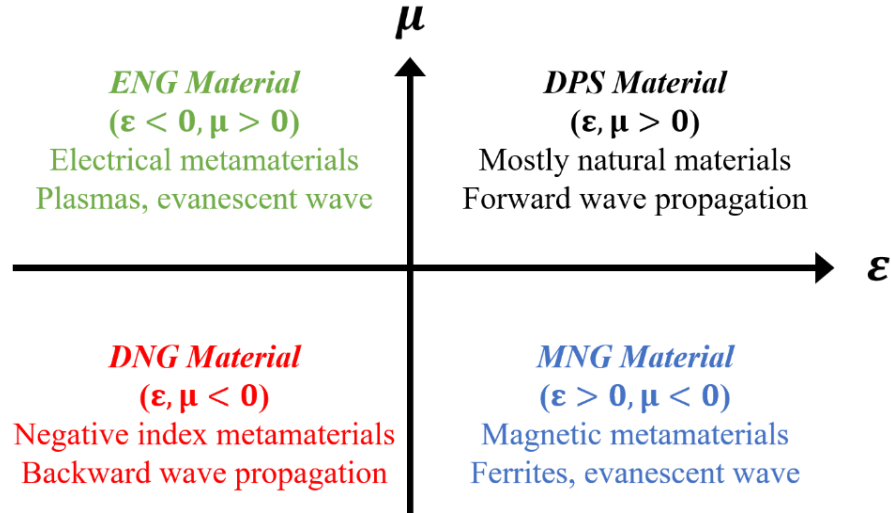


Figure 1.8 Metamaterial four-quadrant space built on  $\epsilon$  and  $\mu$ . 1<sup>st</sup>: Double-positive (DPS), 2<sup>nd</sup>: epsilon-negative (ENG), 3<sup>rd</sup>: double-negative (DNG), 4<sup>th</sup>: mu-negative (MNG).

#### 1.1.4 Fabrication of Plasmonic Metamaterial

Fabrication of plasmonic metamaterials can be realized by chemical and physical methods, here, physical methods including top-down approaches and bottom-up approaches will be discussed. Specifically, lithographic patterning, focused ion beam milling will be reviewed for top-down methods, templated growth and physical vapor deposition (PVD) will be discussed for bottom-up methods.

##### 1.1.4.1 Lithographic Patterning

The most well-known method of fabricating plasmonic metamaterial is the lithographic patterning which involves multiple subsidiary categories. The major category is called microlithography, namely photolithography which is capable of patterning nanostructures at scale of  $< 10 \mu\text{m}$ ; another one is called nanolithography or electron-beam lithography (EBL) with the capability of writing features smaller than 100 nm. The general fabrication process is shown in Figure 1.9. A resist layer is deposited first, and the patterns are “written” using focused high-energy electron probe. Next, either etching and resist removal, or metal deposition and lift-off processes are involved, depending on the type of the resist layer, producing the final output of the nanopatterns. Resist is the key element which determines the quality of the resulted structure, it can be either positive or negative that functions oppositely. The positive resist dissolves the part

being exposed, on the contrary, the negative resist dissolves the part not being irradiated. Poly methyl methacrylate (PMMA) is one of widely used positive resists for EBL due to its good property and reliability. The overall quality of the EBL fabrication is determined by the electron optics, the choice of resist, substrate and developer, and processing conditions such as beam energy and dose, development time and temperature.<sup>[24]</sup> More details on resist and technical descriptions of EBL can be found elsewhere.<sup>[25]</sup> EBL has been extensively applied for fabricating 2D metasurfaces, reaching patterning scale down to sub-20 nm with geometrical versatility. Selected examples are coupled in Figure 1.10, where metasurfaces with complex patterns can be fabricated with reasonably high quality. More importantly, it allows controls over designs such that specific geometrical parameters (e.g. dimension, packing distance, etc.) can be tailored. However, it is challenging if aggressively targeting at few tens of nm features. A typical problem would be the residuals or gel formation at the edge of the nanopatterns, which is shown as illustrations and real microstructures in Figure 1.11.

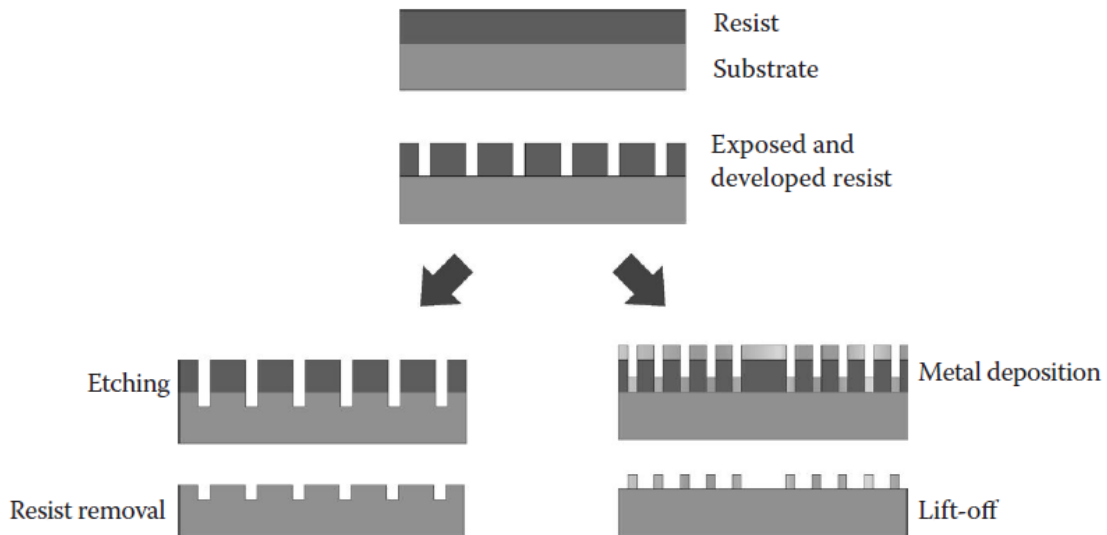


Figure 1.9 Fabrication processes using lithography.<sup>[26]</sup>

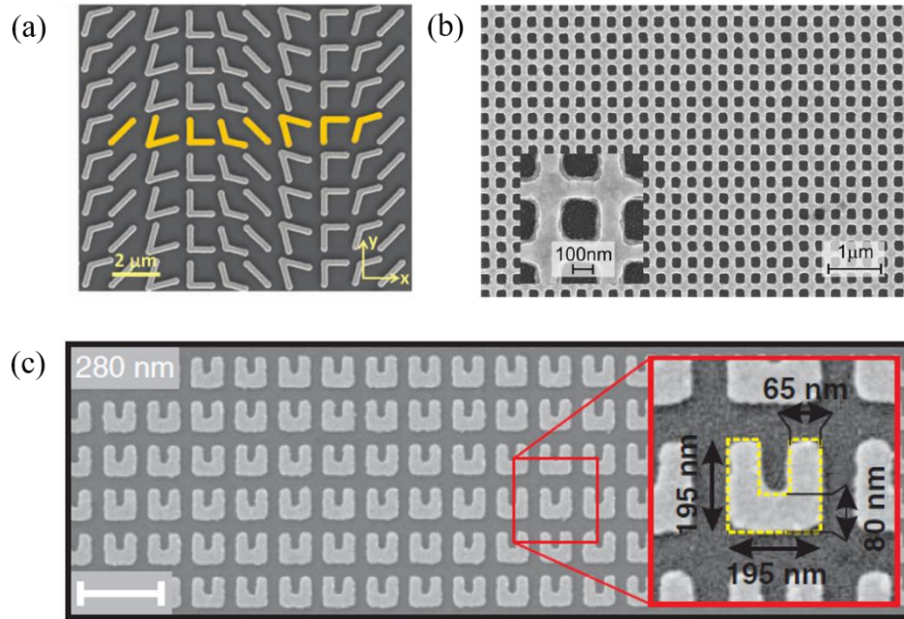


Figure 1.10 Metasurfaces fabricated by EBL method. (a) Gradient metasurface with V-shaped and bar-shaped antennas,<sup>[26]</sup> (b) nanofishnet,<sup>[27]</sup> (c) split-ring resonators.<sup>[28]</sup>

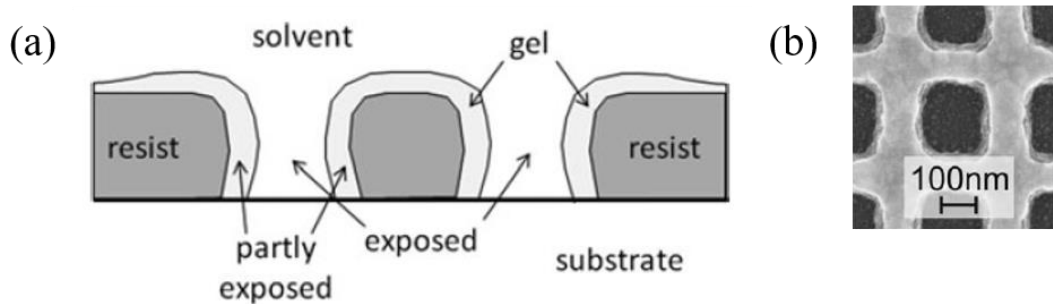


Figure 1.11 (a) Schematic illustration on polymer-solvent interactions creating gels and swelling.<sup>[24]</sup> (b) Fishnet patterns showing edges with residuals.<sup>[28]</sup>

EBL is relatively time-consuming with limited throughput for fabricating scalable structures towards three dimensions. Alternatively, interference lithography (IL) or nanoimprint lithography (NIL) are capable to produce relatively large-scale patterns with low processing time. On the other hand, focused ion-beam (FIB) milling is one comparable technique to EBL, but FIB is still slightly faster in terms of processing time, it has been considered with higher priority when fabricating nonlinear patterns such as split ring resonators (SRRs).

#### 1.1.4.2 Porous Templated Growth

Porous templated growth method is more specified in growing wire metamaterials. The method generally involves two steps: fabrication of the porous template, and nanowire growth using thin film deposition techniques such as e-beam evaporation or physical vapor deposition (PVD). In most occasions, the templates are commercially available, making it easier for fabricating wire metamaterials with massive production. The reason why such templates are applied is because of its unique hexagonal ordering. It provides an easy method to fabricate highly ordered nanowires as vertically aligned geometry, which is challenging in conventional growth methods. One additional advantage offered by this method lies in its flexibility of the constituent nanowire material that can be extended to semiconductors beyond metals.<sup>[29]</sup> In the field of optics, this method is advantageous in coupling metal and dielectrics for hyperbolic MTM design, with much higher scalability into three dimensions and cost-effectiveness compare to most of lithographic patterning methods.

The first demonstration of fabricating anodized aluminum oxide (AAO) template dates back to 1995,<sup>[30]</sup> when Masuda and Fukuda reported a two-step anodization of aluminum in producing highly ordered alumina nanohole template as shown in Figure 1.12. The degree of periodicity can be controlled by the anodization process. Benefit from the high-quality oxide template, metallic nanowires are easily integrated with high degree of ordering, enabling extreme anisotropy of dielectric dispersion in-plane and out-of-plane while generating negative refractive index in some cases.<sup>[31-32]</sup> Figure 1.13 show Ag nanowires grown in AAO template as a natural high-quality hyperbolic metamaterial. One critical disadvantage as revealed by most reported studies, lies in the limited material selection for the porous oxide template, which means it is technical challenging to fabricate anodized template aside from  $\text{Al}_2\text{O}_3$  which limits additional tunability.

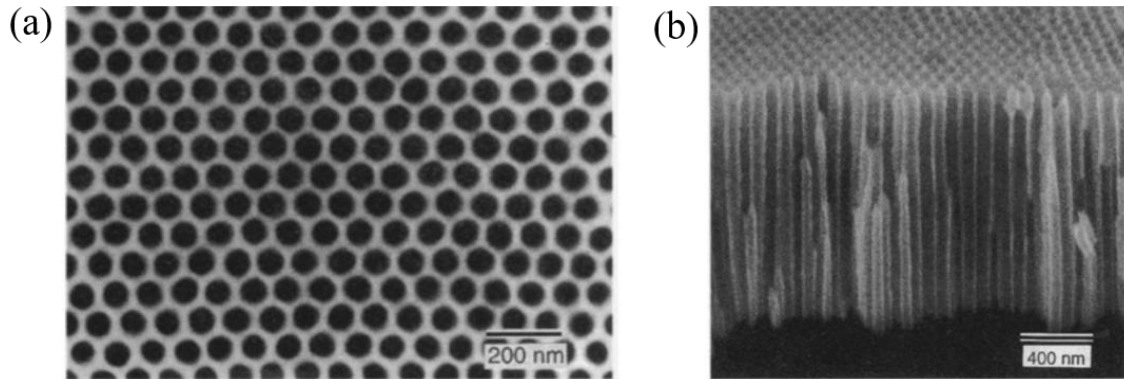


Figure 1.12 SEM photographs of the porous nanohole (a) top projection and (b) cross-sectional view.<sup>[30]</sup>

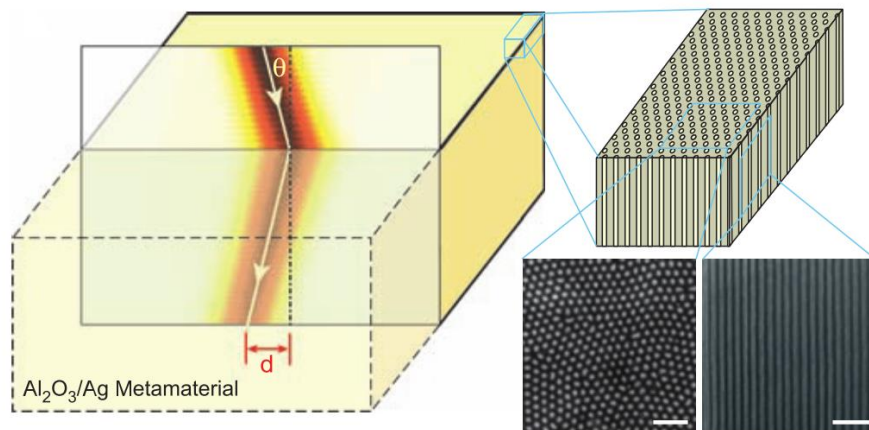


Figure 1.13  $\text{Al}_2\text{O}_3/\text{Ag}$  wire metamaterial with negative optical refraction.<sup>[31]</sup>

Thin film deposition as briefly mentioned, provides an alternative way in stacking metamaterials into three dimensions. Explorations of two-phase nanostructures using bottom-up fabrication is challenging but have shown promising prospects from recent demonstrations. As an example, Gao et al. (2017) demonstrated growing Ag nanowires in  $\text{Al}_2\text{O}_3$  or  $\text{SiO}_2$  matrix using sputtering instead of AAO templated method, the growth was achieved via involving a RF bias that affect the growth kinetics in the seeding layer (Figure 1.14).<sup>[33]</sup> More details will be discussed in the Nanocomposite section. Towards complex metamaterial design, a combination between different processing methods is necessary and desirable in manufacturing low-cost and scalable metamaterials for practical device applications.

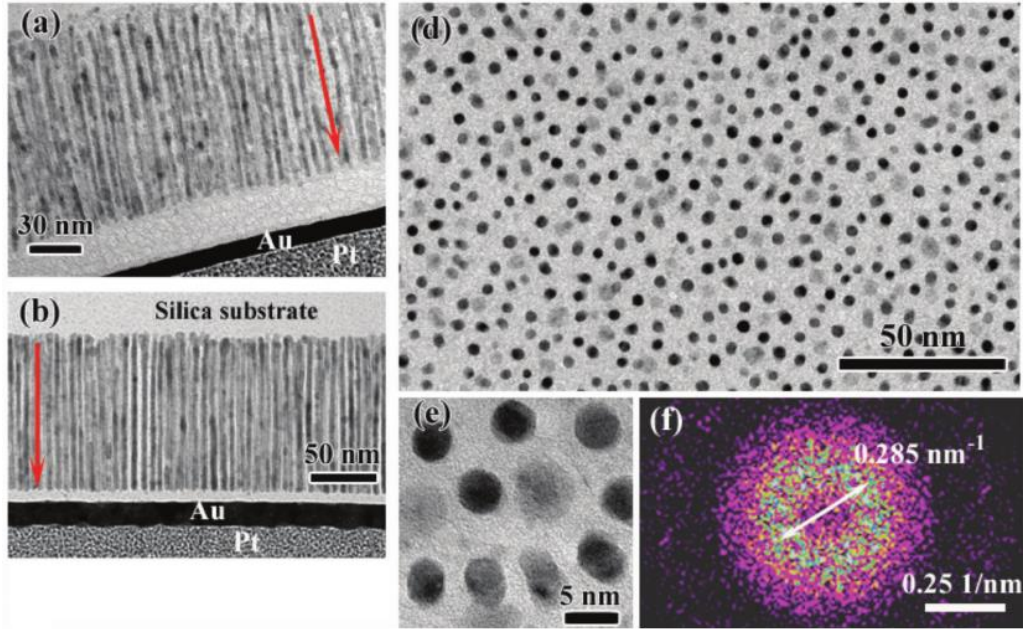


Figure 1.14 Cross-sectional and TEM images of Ag nanowire array embedded in  $\text{Al}_2\text{O}_3$  or  $\text{SiO}_2$  matrix.<sup>[34]</sup>

### 1.1.5 Applications of Metamaterials

Metamaterials enable many novel physical properties or unusual phenomena and can thus be applied for practical devices. Examples shown here include patterned metasurfaces (i.e., gradient metasurface) for applications such as wavefront manipulation and holography, hyperbolic metamaterial is introduced for achieving negative refraction and superlens designs.

### 1.1.5.1 Metasurface for Wavefront Manipulation

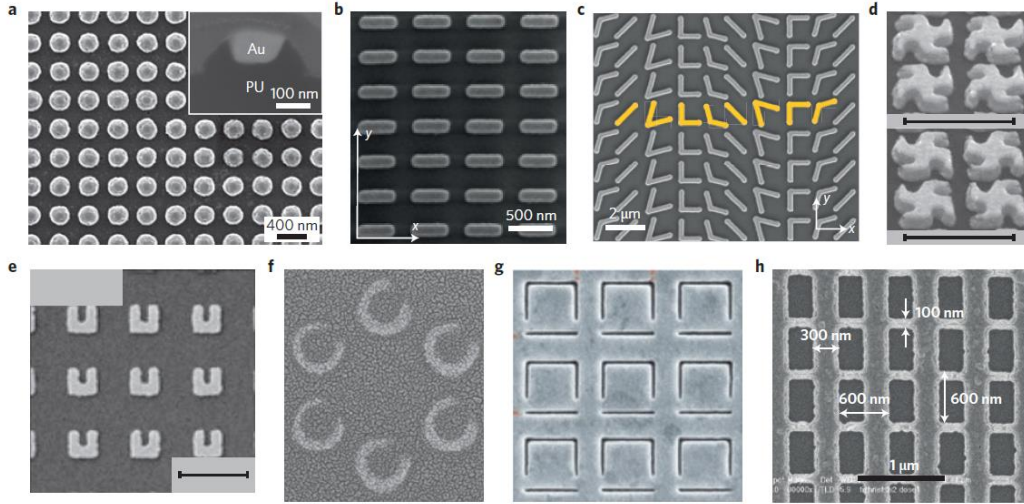


Figure 1.15 Review of metasurfaces. (a) Nanodisks,<sup>[35]</sup> (b) rod antennas,<sup>[36]</sup> (c) V-shaped antennas,<sup>[26]</sup> (d) gammadions chiral metamaterial,<sup>[37]</sup> (e,f) split-ring resonators,<sup>[28, 38]</sup> (g) inverse asymmetric split-ring resonator,<sup>[39]</sup> (h) double-fishnet structure.<sup>[40]</sup>

Metasurface is artificially patterned two-dimensional (2D) nanostructured surface which is composed of meta-atoms being arranged in a periodic or designable fashion.<sup>[41-44]</sup> Different from plasmonic nanostructures, metasurfaces are commonly solid-state 2D layers fabricated by techniques such as EBL. Instead of randomly dispersed, the spacing and geometry are controlled in a specific way in realizing manipulation of EM wavefront, for example, phase and amplitude, reflection and refraction, as well as polarization. Figure 1.15 shows a collection regarding a collection of metasurfaces with different geometries.<sup>[44]</sup> Instead of coherent patterned metasurfaces where the meta-atoms are geometrically and spatially identical, gradient metasurfaces attract more interest in terms of new physics phenomena such as generalized Snell's law.<sup>[45]</sup>

A representative study reported by Yu (2011) et al.<sup>[26]</sup> demonstrated anomalous light propagation with phase discontinuities observed from thin metallic nanostructures as shown in Figure 1.16. The modified Snell's law is expressed as

$$\sin(\theta_t) n_t - \sin(\theta_i) n_i = \frac{\lambda_0}{2\pi} \frac{d\Phi}{dx}$$

, where  $\theta_i$  and  $\theta_t$  represent angle of incidence and refraction, respectively,  $n_i$  and  $n_t$  are refractive indices of the two media,  $\lambda_0$  is the vacuum wavelength. This equation indicates a nonzero phase gradient. Reflection and refraction at wavefront are modified accordingly (Figure 1.17). The

specially designed V-shaped nanoantennas support symmetric and antisymmetric modes, which realize a wide tuning range of phase shift and amplitude (0 to  $2\pi$ ). Additionally, the structure enables a “negative” refraction and reflection for the cross-polarized light.

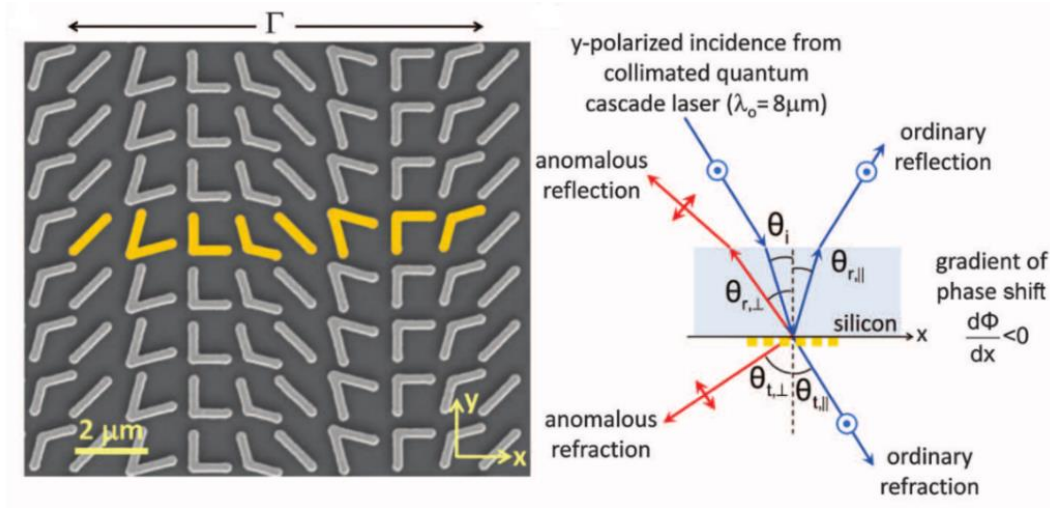


Figure 1.16 Scanning electron microscope (SEM) image of V-shaped nanoantenna array composed of Au. Schematic illustration on experimental setup.<sup>[26]</sup>

Using gradient metasurfaces, Huang et al.<sup>[46]</sup> reported a three-dimensional optical holography using a nanorod metasurface with spatially varied orientations. Each specific oriented nanorod serves as a “pixel”, its phase information is calculated and reconstructed to the resulted 3D holography (Figure 1.18). This method can be applied for high-quality holography imaging, storage and processing.

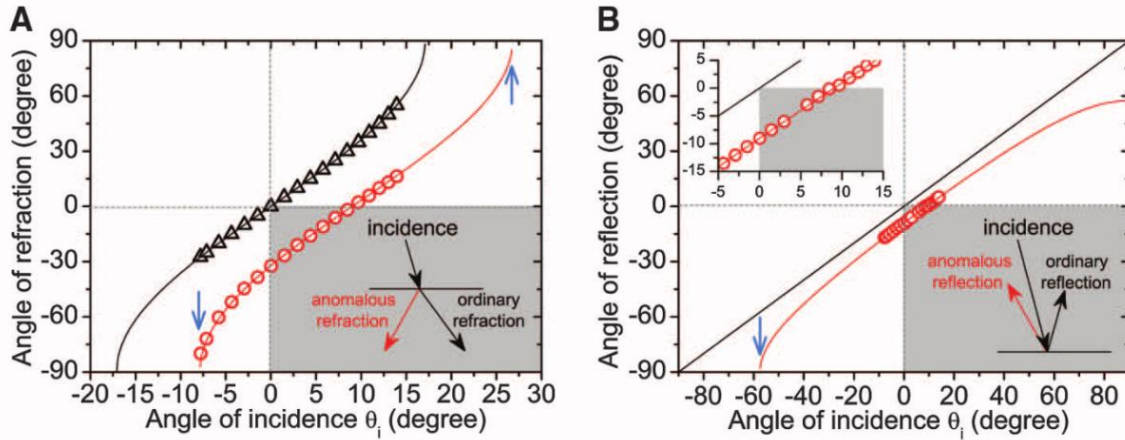


Figure 1.17 Angle of incidence versus angle of (a) refraction and (b) reflection for ordinary and anomalous cases.<sup>[26]</sup>

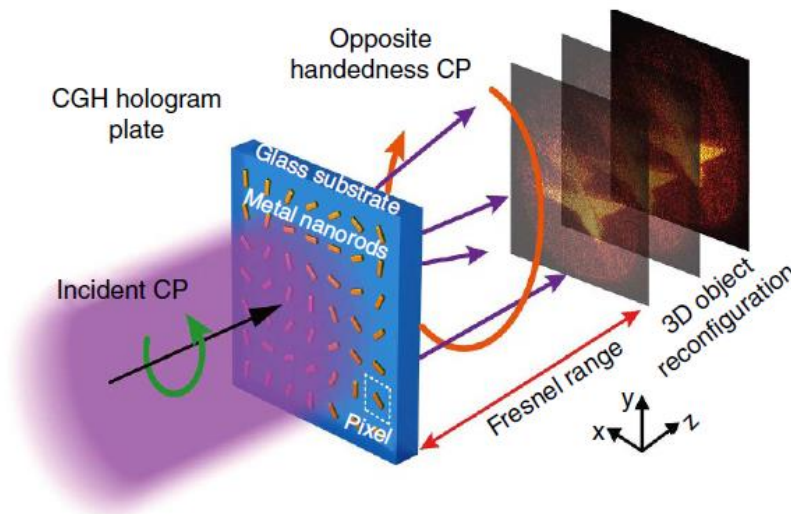


Figure 1.18 Three-dimensional holography reconstructed by a gradient plasmonic metasurface.<sup>[46]</sup>

### 1.1.5.2 Hyperbolic Metamaterial

Hyperbolic metamaterial (HMM) can be described as extreme anisotropic media with one direction being metallic and the other direction being dielectric. Different from isotropic media where the isofrequency contour or the  $k$ -space topology is mostly a sphere, hyperboloid with either one-fold or two-fold is generated in hyperbolic metamaterial due to the extreme anisotropy of the dielectric tensors along in-plane and out-of-plane directions (Figure 1.19).<sup>[47]</sup>

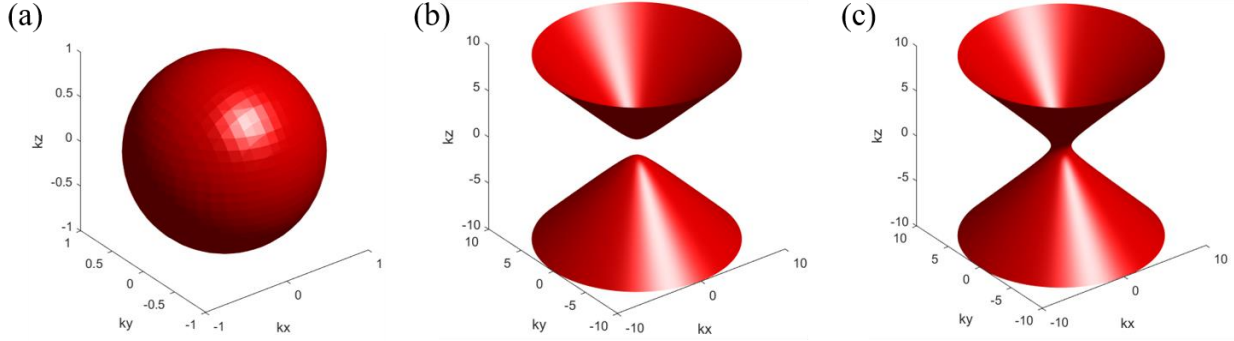


Figure 1.19  $k$ -space topologies for (a) isotropic dielectric,  $\epsilon_x, \epsilon_y, \epsilon_z > 0$ , (b) type-I HMM ( $\epsilon_x, \epsilon_y > 0, \epsilon_y < 0$ ) and (c) type-II HMM ( $\epsilon_x, \epsilon_y < 0, \epsilon_y > 0$ ).

Such extreme anisotropy originates from the permittivity ( $\hat{\epsilon}$ ) and permeability ( $\hat{\mu}$ ) tensors, in most cases of hyperbolic metamaterials, we only consider nonmagnetic media and therefore  $\hat{\mu}$  is treated as unit tensor. Then,  $\hat{\epsilon}$  is described as

$$\hat{\epsilon} = \begin{bmatrix} \epsilon_x & 0 & 0 \\ 0 & \epsilon_y & 0 \\ 0 & 0 & \epsilon_z \end{bmatrix}$$

, for uniaxial models  $\epsilon_x = \epsilon_y \neq \epsilon_z$ . The isofrequency surface is described by

$$\frac{k_x^2 + k_y^2}{\epsilon_z} + \frac{k_z^2}{\epsilon_x} = \left(\frac{\omega}{c}\right)^2$$

, where  $\omega$  is the wave frequency and  $c$  is the speed of light.

Naturally, hyperbolic metamaterial is composed of metals and dielectrics at subwavelength scale. Metals possess negative dielectric function below the plasma frequency due to the free electrons being polarized opposite to the electric field. For dielectrics, such polarization is reversed. The hyperbolic metamaterial simply generates extreme anisotropy of the dielectric tensor by restricting free-electron motion in one or two spatial directions. According to the equation,  $\epsilon_x, \epsilon_y > 0, \epsilon_y < 0$  generates a two-fold geometry which is called Type-I HMM, whereas  $\epsilon_x, \epsilon_y < 0, \epsilon_y > 0$  produces one-fold geometry which is called Type-II HMM. At nanoscale, such extreme anisotropy can be realized by two types of geometries (Figure 1.20), the nanowire-in-matrix and layered nanostructures composed of very dissimilar phases, for example, metals with dielectrics or semiconductors.

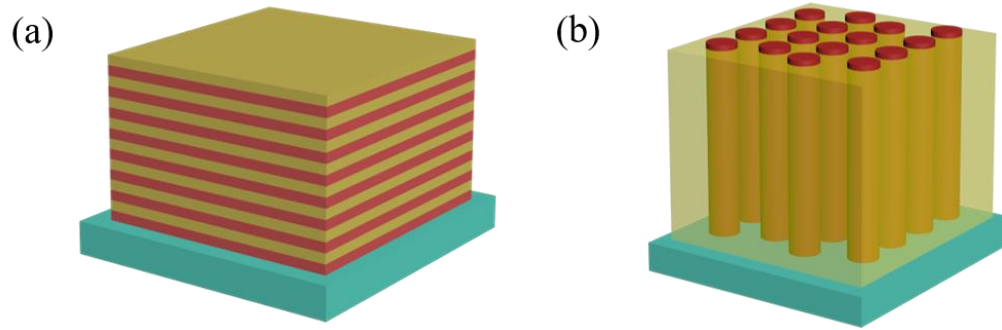


Figure 1.20 Schematics of (a) multilayer and (b) nanowire hyperbolic metamaterial. Red: metal, yellow: dielectric/semiconductor, blue: substrate crystal.

The layered nanostructure is composed of alternative stack of metals and dielectrics where the layer thickness is limited to subwavelength scale. More interestingly, the structure can be further engineered by creating “fishnet-like” patterns, which generate unique functionalities such as negative refractions or enhanced spontaneous emission in the visible wavelength regime.<sup>[48-49]</sup> An example shown in Figure 1.21 is a patterned Ag/Si multilayer stack with an average layer thickness of 10 nm fabricated by magnetron sputtering technique, the Ag-Si stacks is further engineered by FIB milling to create grating patterns.<sup>[49]</sup> From technical perspective, the nanowire HMM is easier to realize using AAO templates to grow metallic nanowires.<sup>[31, 50]</sup> Using different fabrication methods, systems with highly anisotropic dielectric tensors can be achieved in many proposed materials systems. Applications of HMMs include negative refraction, lensing and focusing, waveguides, as well as enhanced spontaneous emission.<sup>[51-52]</sup>

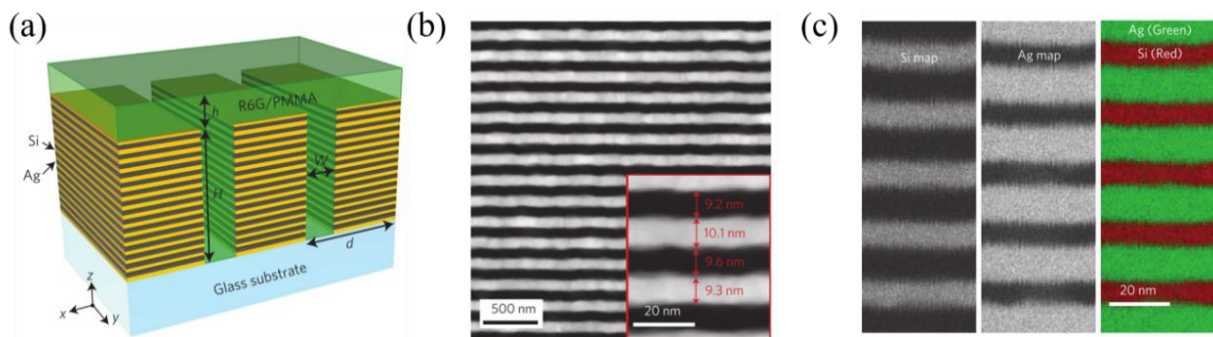


Figure 1.21 (a) Schematic of nanopatterned multilayer HMM. (b) STEM image showing the multilayer nanostructure. (c) Elemental mapping of constituent materials. Ag: green, Si: red.<sup>[49]</sup>

## 1.2 Nanocomposites

### 1.2.1 Overview

Comparable to metamaterials processed by the above mentioned top-down approaches, self-assembled nanocomposite thin film using bottom-up fabrication is a rising field of study. It involves multidisciplinary studies including thin film sciences, materials kinetics and thermodynamics, novel physical properties and nanodevice applications. The first reported study is the BaTiO<sub>3</sub>-CoFe<sub>2</sub>O<sub>4</sub> system,<sup>[53]</sup> forming a unique vertically aligned nanocomposite (VANs) geometry with one of the phases grown as nanopillars and another phase distributed as the supporting matrix, realized by a self-assembling single-step growth process. This study successfully extended the functional thin films from conventional single phase to two phases hybrids which plays significant role in terms of realizing multi-functionalities via a combination of two functional materials together. Since the first demonstration, extensive studies have been explored within the oxide-oxide combinations, and the geometries have been extended to different types including pillar-in-matrix, particle-in-matrix, superlattices or multilayered structures.<sup>[54-55]</sup> Recently, the material candidates and geometries have been extended to additional categories for more optical-based studies, for example, metal-ceramic oxide and metal-ceramic nitride systems that are highly promising for alternative metamaterial designs and plasmonic based sensing applications.<sup>[56-59]</sup>

One advantage of the two-phase nanocomposites lies in the geometrical tunability via careful control of material density and deposition conditions. Specifically, the ratio between two phases can be calculated when mixing the powders for target sintering, though the final output ratio of the nanocomposite is not guaranteed as the deposition could involve more complex mechanisms. In most cases, the secondary phase can be up to 50% filling factor within two-phase nanocomposites. In terms of VANs, the geometry, the aspect ratio, as well as the distribution of the second phase can be tuned.<sup>[60-63]</sup> In addition, deposition parameters play an important role in controlling the output geometries of the nanocomposites, including laser parameter tuning (e.g. energy, frequency, number of pulses), background pressure (e.g. vacuum, nitrogen, oxygen), substrate heating, as well as the distance between the target and the substrate. It is worth to mention that the vertically aligned geometry provides unique anisotropy along in-plane and out-of-plane directions, which is fundamentally crucial to many of the functionalities. A detailed schematic

overview of two-phase heterostructures is shown in Figure 1.22. So far, most of the reported systems are grown using pulsed laser deposition (PLD) or in some reported cases using magnetron sputtering.<sup>[33]</sup> The integration of multiphases as a solid thin-film form is dominated by a self-assembly process, the growth mechanisms will be discussed in the following sections. There are currently multiple good review articles covering the exploration of oxide-oxide nanocomposites, their growth mechanisms, tunabilities and functionalities achieved so far.<sup>[60, 64-66]</sup> Besides the extensive explorations, there are still challenges and unresolved puzzles, or underexplored materials systems and physics phenomena potentially driving the field of nanocomposite more attractive and promising.

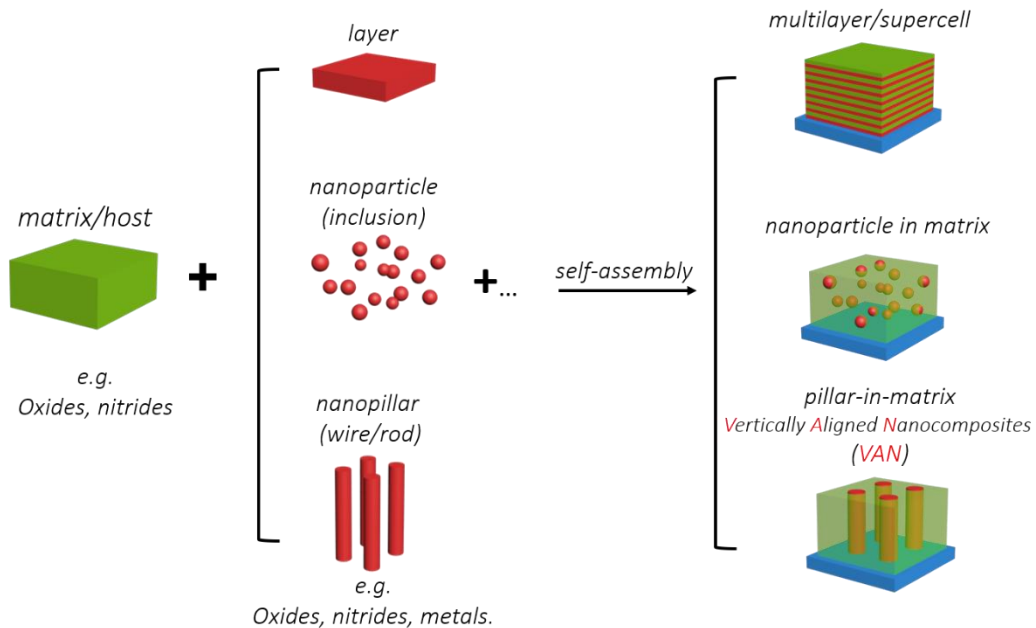


Figure 1.22 Schematic on two-phase nanocomposite geometries.

### 1.2.2 Fabrication Methods of Nanocomposite Thin Films

Conventional thin film fabrication relies mostly on bottom-up methods, for example, pulsed laser deposition (PLD), magnetron sputtering, e-beam evaporation, chemical vapor deposition (CVD), atomic layer deposition (ALD), and molecular beam epitaxy (MBE). These techniques have been developed since 19<sup>th</sup> century and are well-known in yielding thin films with epitaxial crystalline quality.<sup>[67]</sup> Note that CVD belongs to a rather different category, it is

dominated by the chemical evaporation process that molten sources are applied as precursors and chemical reactions controls the composition of the deposited films. On the contrary, physical vapor deposition (PVD) such as PLD is dominated by both evaporation and plasma-assisted sputtering.<sup>[68]</sup> A general setup of a PLD chamber is shown in Figure 1.23, a pulsed laser with high energy density is focused onto the target ejected a plasma plume containing the targeted material, then the plume is forward-directed towards the substrate surface as adatoms diffusing and resting on the surface forming thin films. The prerequisites of such process include sufficiently high vacuum, ultraviolet laser and nanosecond pulses to ensure the formation of high-energy plume. Depending on different materials, parameters such as temperature, laser energy, background gas pressure can be controlled to realize an optimal crystalline quality.

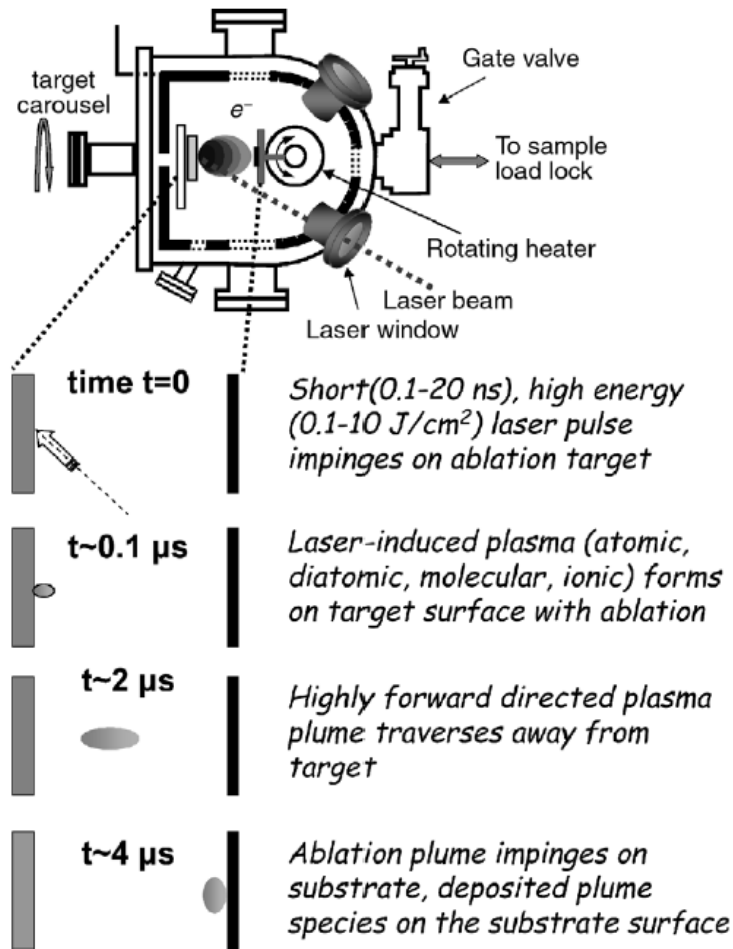


Figure 1.23 Pulsed laser deposition setup and description of deposition process.<sup>[63]</sup>

The advantages brought by PLD technique includes (1) desirable epitaxial quality, (2) scalability in terms of film thickness, (3) relative fast and simple process, (4) wide choice of material candidates including metals, semiconductors (e.g. III-V nitrides, SiC) and insulators (e.g. oxides), (5) capable of integrating complex heterostructures, such as nanocomposites. For most of the fundamental research studies, PLD can be a good choice to achieve fast and reproducible thin film growth of most material candidates (e.g. metals and ceramics). However, there are still limitations. One of the limitations lies in the output scale of the film if considering mass-productions for devices or on-chip fabrications for practical uses. This is the reason why the CVD fabrication is still dominated in semiconductor industries. Because the surface coverage is determined by the laser plume generated from the target, the output scale of PLD deposited films is limited by the size of the plume (cm to inch range). Commonly, the film thickness at the edges of the substrate is smaller reduced as compared to that at the center (Figure 1.24).

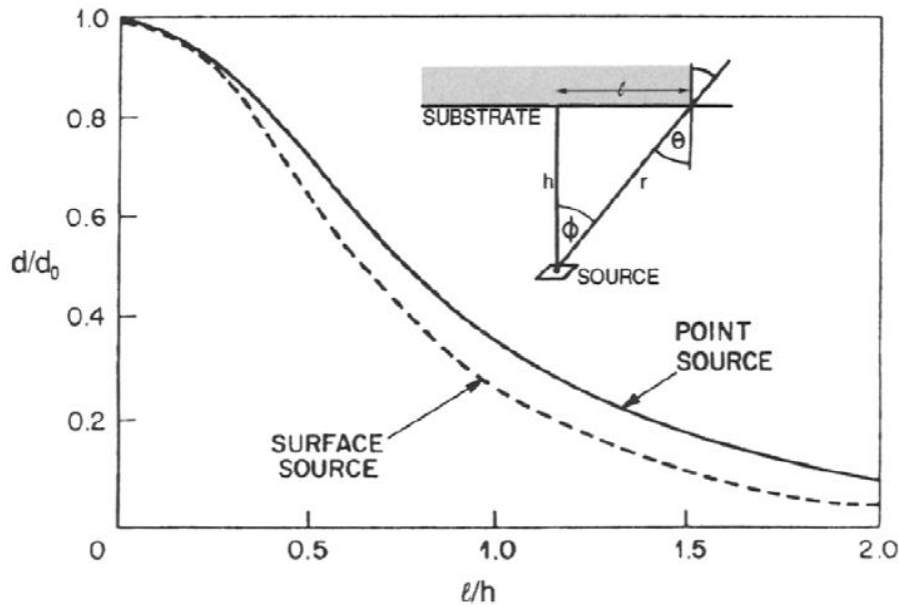


Figure 1.24 Film surface uniformity for point and surface sources, inset shows the illustration of evaporation from the source to substrate.<sup>[62]</sup>

Compare to single-phase thin films, growth of two-phase nanocomposites is more complicated. Such complexity starts from target preparation, when a careful calculation of concentration between the two phases is the prerequisite in determining the geometry of the as-grown nanocomposite films. Moreover, it could be challenging in mixing chemicals that are easily

interacted or diffused. Currently, the phase diagrams are limited thus a theoretical prediction is not available in many complex oxide-oxide or metal-oxide systems. Luckily, some simple predictions can be made based on the thermal, mechanical, and structural properties of materials. However, for most of the unexplored systems, extensive experimental effort needs to be devoted before making reliable conclusions or predictions.

### **1.2.3 Growth Mechanisms**

Most reported studies of two-phase nanocomposites originate from two growth mechanisms: (1) nucleation and growth, and (2) (pseudo-) spinodal decomposition. Depending on the miscibility between the constituent chemical elements or compounds, for instance,  $AO\alpha$ ,  $BO\alpha$ , A, B and O, Judith (2010) summarized each of the growth mechanism in detail supported by experimental results of many reported systems. <sup>[66]</sup>

#### **1.3.2.1 Nucleation and Growth**

The predominant growth mechanism of thin films is nucleation and growth. For two-phase self-assembly, the resulted geometry may vary from layered nanostructure, nanopillar-in-matrix, and nanoparticle-in-matrix, depending on factors such as thermodynamics, growth kinetics, and the concentration of the constituent components. Within the category of nanopillar-in-matrix, the shape and distribution of the nanopillars are also controlled by the above-mentioned factors, for instance, nano-checkerboard structure,<sup>[69]</sup> nanomaze structure,<sup>[70-71]</sup> and faceted nanopillars.<sup>[72]</sup> In general, there are three thin film nucleation and growth modes, (1) islanded (or Volmer – Weber) mode, (2) layered (or Frank – Van der Merwe) mode and (3) mixed (Stranski – Krastanov) mode,<sup>[68]</sup> which are illustrated in Figure 1.25.

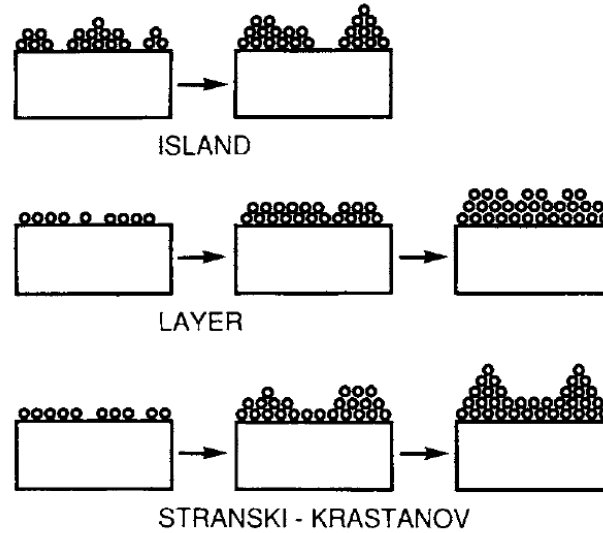


Figure 1.25 Three growth modes of thin films.<sup>[62]</sup>

Next, we want to apply these growth modes to explain the two-phase nanocomposite growth. First, the pillar-in-matrix geometry can be traced to a combination of islanded mode with either layered mode or the mixed mode, where the secondary phase is more favorable to nucleate as small islands while the dominating matrix phase is preferable to grow as layers. From thermodynamic perspective, the different mode of nucleation depends on the interfacial energy or wetting property of the nucleating material with respect to the substrate surface. As shown from Figure 1.26,  $\gamma_{fv}$ ,  $\gamma_{fs}$ , and  $\gamma_{sv}$  represents surface tension at film/vapor, film/substrate and substrate/vapor interface, respectively. If  $\gamma_{sv} < \gamma_{fs} + \gamma_{fv}$ , the wetting angle  $\theta > 0$  and the growth is preferred for island mode. When  $\gamma_{sv} \geq \gamma_{fs} + \gamma_{fv}$ , the layered growth is more favorable and when  $\theta \approx 0$ , the  $\gamma_{fs}$  almost vanishes to support the alternative layered stacking between A and B species. The mixed growth mode (or Stranski – Krastanov mode) is more complicated, requiring  $\gamma_{sv} > \gamma_{fs} + \gamma_{fv}$  and typically represented by a layered growth (2D) for the first few monolayers, followed by the island growth (3D) mode.

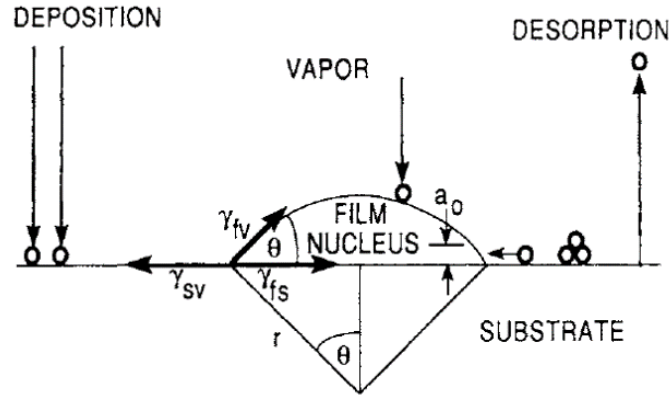


Figure 1.26 Schematic illustration of nucleation process of adatoms on substrate surface during vapor deposition.<sup>[62]</sup>

Surface energy is one subdivision of material thermodynamics. There are other factors that contribute to the formation of different geometries such as quantum dots (QDs), nanoparticles, and irregular shaped nano-inclusions. These factors include lattice strain and crystal structure, thermal expansion and adatom diffusion, relative concentration between the two phases, as well as the kinetic energy from the pulsed laser. It is interesting that thin film growth is dominated by an interplay of multiple factors. For example, small concentration, high kinetic energy and limited adatom diffusion would lead to nanoparticles instead of nanopillars, which has been reported in the  $\text{YBa}_2\text{Cu}_3\text{O}_{7-x}$  (YBCO)- $\text{BaZrO}_3$  (BZO) system where BZO is self-assembled as nanoparticles being embedded in the superconducting YBCO matrix.<sup>[73]</sup>

### 1.3.2.2 Spinodal Decomposition

Spinodal decomposition requires the Gibbs free energy per mole of a solution (denoted as  $G_m$ ) versus composition curve to be concave downward, which is

$$\frac{\partial^2 G_m}{\partial^2 X_2} < 0$$

, such that the solution tends to be decomposed into a mixture of  $\alpha$  and  $\beta$  phases to lower the overall free energy of the system. In addition, the spinodal decomposition requires the enthalpy of mixing (denoted as  $H_m^M$ ) to be positive, which serves as the segregation energy,  $G_m^M = H_m^M - TS_m^M$ . A typical spinodal curve can be referred to Figure 1.27.

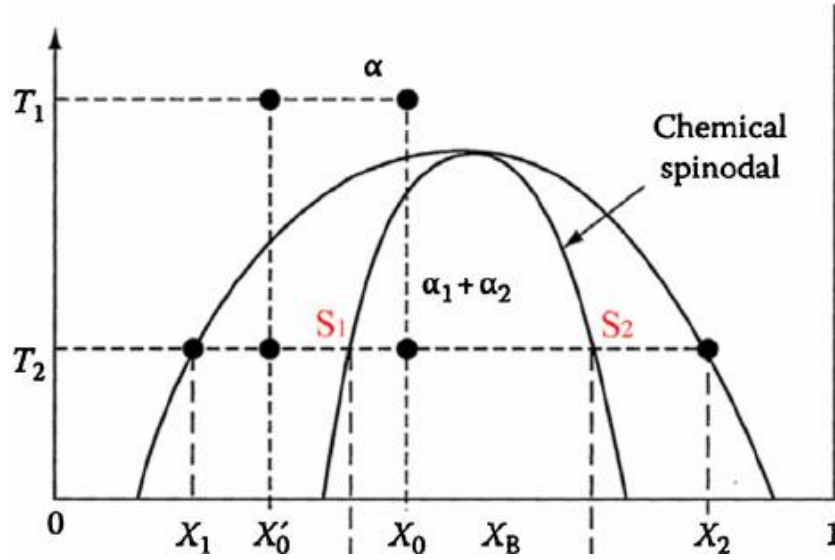
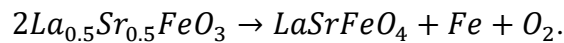


Figure 1.27 Free energy versus composition curve.

At high temperature, the  $-TS_m^M$  becomes more dominant and the solution is more stable. Once the temperature is reduced,  $H_m^M$  becomes more dominant and an instability region is developed which is sensitive to composition. The inner regime represented by Figure 1.27 is called the spinodal dome where the spontaneous phase separation would occur under small change of composition. Compare to the nucleation and growth, VANs by spinodal decomposition are still underexplored. As a representative example, Ramesh group (2004)<sup>[74]</sup> reported a nanocomposite system with self-assembled Fe nanowires embedded in a LaSrFeO<sub>4</sub> matrix. The microstructure is shown in Figure 1.28 where crystalline-sharp Fe nanopillars are well-aligned and distinguished as a single-phase. The chemical compositions of matrix and pillar phases were confirmed using conversion electron Mossbauer spectroscopy (CEMS), as a result, the chemical reaction was identified as



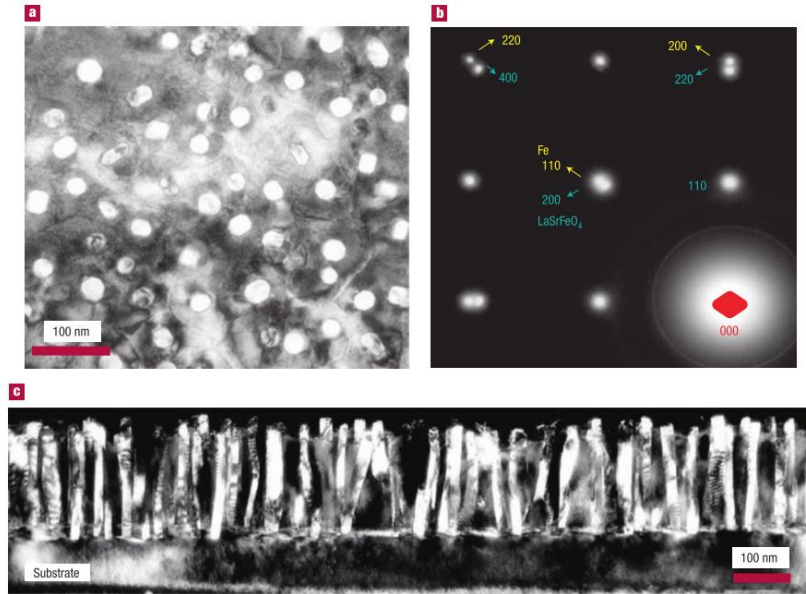


Figure 1.28 (a) Plan-view TEM image, (b) SAED patterns showing in-plane heteroepitaxy, (c) dark-field cross-section TEM.<sup>[74]</sup>

## 1.2.4 Oxide-Oxide Nanocomposites

### 1.2.4.1 Overview

As mentioned, the first reported study (Figure 1.29) on two-phase nanocomposite BFO-CFO demonstrated self-assembly of heteroepitaxial CFO nanopillars with dimension of 20 nm ~ 30 nm, embedded in the BTO matrix. The goal was to couple ferroelectric and magnetic phases together in realizing multiferroic property.<sup>[53]</sup> Since then, significant explorations have been dedicated to coupling of different functional oxide candidates. Zhang et al.<sup>[60]</sup> summarized recent studies on oxide-oxide nanocomposite thin films, for example, the 0-3 type denoted as nanoinclusions or nanoparticles within matrix, 1-3 type denoted as pillar-in-matrix, and 2-2 type denoted as multilayered structure. Such geometry variations are correlated to the factors including strain or lattice mismatch, ratio between two component, and growth parameters such as temperature, laser frequency, etc. For example, the strain involved in two-phase nanocomposites specifically for VANs is three-dimensional, which means both the film/substrate interface as well as the vertical strain coupling between the two competing oxides are involved. Therefore, strain analysis combining different methods such as XRD and STEM are necessary to understand the coupling mechanism.

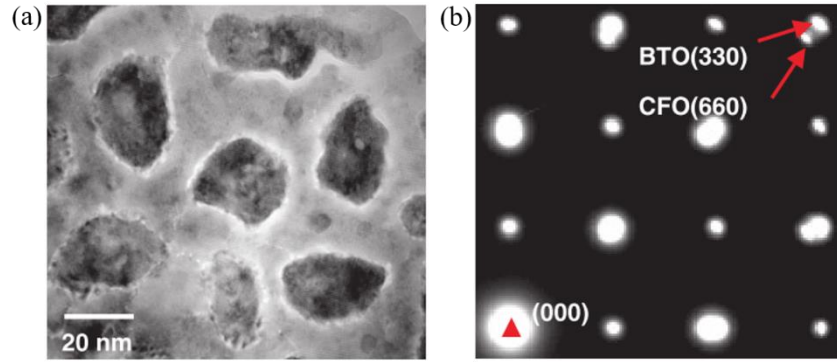


Figure 1.29 TEM plan-view image showing a quasi-hexagonal arrangement of CFO nanopillars, and corresponding (b) electron diffraction patterns.<sup>[53]</sup>

### 1.2.4.2 Geometrical Tunability

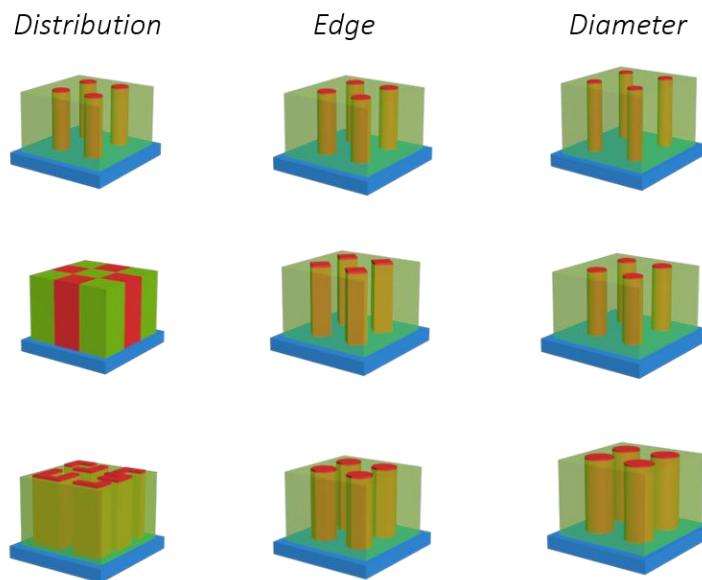


Figure 1.30 Geometrical tunability of the two-phase VANs.

From a large scale, the realization of multilayer, particle-in-matrix and pillar-in-matrix (VAN) belongs to one type of geometrical tuning. Within each category, more detailed tuning can be realized at nanoscale. As shown in Figure 1.30, general distribution of secondary phase, edges or facets of nanopillars, as well as the diameter or aspect ratios have been reported in oxide-oxide systems. Geometrical tuning in oxide-oxide VANs plays paramount role in controlling functionalities and device performance. The great advantages brought by two-phase

nanocomposite is not limited to a combination of materials with varied functionalities, controllable multi-functionalities via geometrical control is of great importance.

The typically reported secondary phase distribution include nanopillar, nano-checkerboard, and nano-maze structure. Majority of the oxide-oxide VANs lies in the first type, where one oxide grown as nanopillars being randomly or a preferred fashion aligned in another oxide matrix. We want to clarify that the term nanopillar would be the comparable to nanowire or nanorod, the terminology is depended on the aspect ratio reported by different synthesis methods, for instance, nanowires normally represent features with ultrahigh length or high aspect ratio (length/diameter). Figure 1.31 shows an example on oxide-oxide VAN. The MgO nanopillars with diameter of 4 nm are randomly aligned in  $\text{La}_{0.7}\text{Sr}_{0.3}\text{MnO}_3$  (LSMO) matrix.<sup>[75]</sup> On the other hand, a nano-checkerboard structure (Figure 1.32a) resulted from spontaneous phase ordering is reported in  $\text{BiFeO}_3$  (BFO)- $\text{Sm}_2\text{O}_3$  (SmO) VAN system,<sup>[69]</sup> while a self-organized nanomaze structure with rectangular nanodomains is revealed by the LSMO-ZnO system(Figure 1.32 b).<sup>[76]</sup> In both cases the underlying growth mechanisms are sophisticated. While not fully explained, it is highly possible that minimization of interfacial strain energy and/or surface energy are contributing factors.

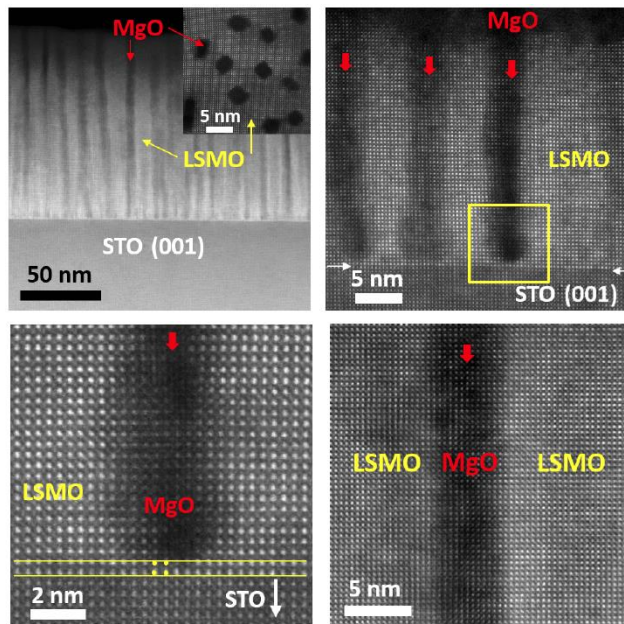


Figure 1.31 Cross-sectional STEM images of MgO-LSMO VAN system.<sup>[75]</sup>

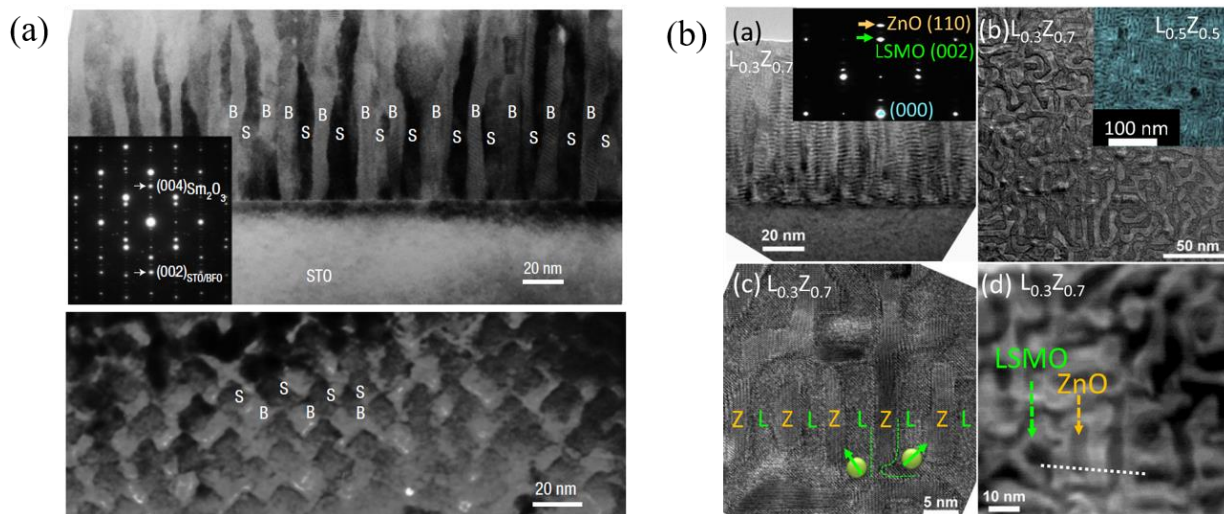


Figure 1.32 (a) STEM micrographs of cross-section and plan-view images of the BFO-SmO VAN system.<sup>[69]</sup> (b) TEM and STEM micrographs of the LSMO-ZnO VAN system.<sup>[76]</sup>

At a finer scale, the edge of the nanopillar can be tuned. An example shown here is the spinodal decomposition of  $\text{LaSrFeO}_4$  into metallic Fe nanowires. As shown from Figure 1.33, by tuning the growth temperature, the edge of the nanowire can be changed from squared shape with dimension of 40-50 nm (840 °C), to octagon with dimension of 15-20 nm (740 °C) and circular with 4-6 nm diameter (560 °C). Such changes are driven by thermodynamic factors including reduction of surface energy by exposing of low-energy facets, or adatom diffusion to control the nuclei sizes or lateral dimension of nanowire.

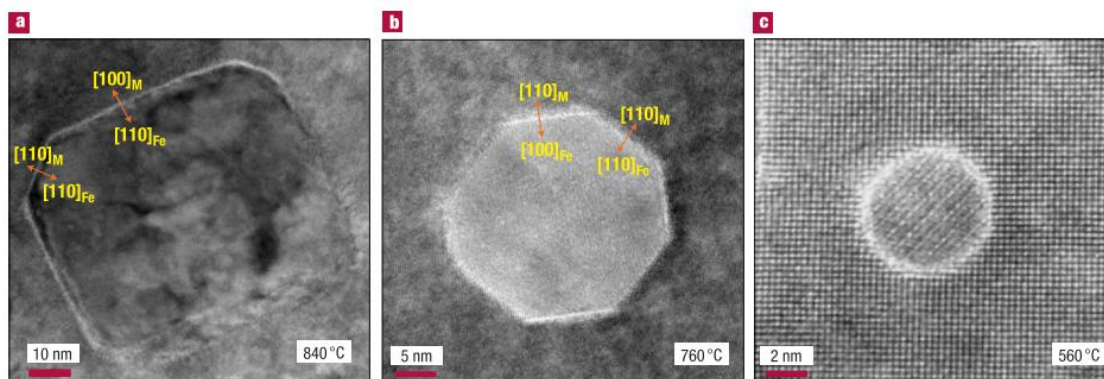


Figure 1.33 High-resolution plan-view TEM images showing the change of shape of the Fe nanowire with respect to deposition temperature.<sup>[74]</sup>

Lastly, the aspect ratio (length/diameter) of the secondary oxide phase can be controlled via deposition parameters. Since the length of the nanopillars is affected by the overall film thickness, an intuitive method is to control the deposition time. However, the width of the nanopillar can be affected by multiple factors including laser frequency, laser energy and temperature, assuming the concentration of the secondary phase is maintained. These factors will change the nucleation dimension and the adatom diffusion at the most beginning of the deposition. In common situations, high laser frequency, low temperature and high laser energy would suppress the adatom diffusion and size of the nuclei, which result in thinner or narrower pillars or columns. An example based on the LSMO-ZnO reported by Chen et al.<sup>[71]</sup> demonstrates a tunable nanocolumn width of ZnO by changing the laser frequency from 1 Hz to 10 Hz (Figure 1.34).

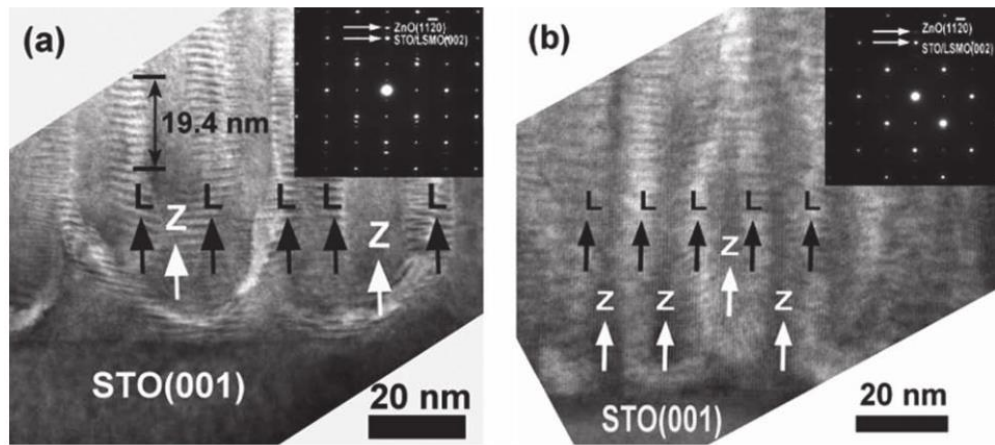


Figure 1.34 Cross-section TEM image of LSMO : ZnO VAN grown under (a) 1 Hz frequency and (b) 10 Hz.<sup>[63]</sup>

The tunable geometries achieved in oxide-oxide systems can be extended to metal-oxide and metal-nitride systems, although some of the controls are easier to realize in specific material group consider the difference in material thermodynamics and crystal structures. There are additional tunable geometries, for example, tuning the ratio between two phases results in a change of packing distance of nanopillars, tuning growth rate and materials to realize oblique or tilted nanopillars. These will be discussed in the following chapters when we introduce the metal-nitride nanocomposite systems.

### 1.2.4.3 Multifunctionalities

As demonstrated in the BFO-CFO nanocomposite, multiferroics exhibits more than one of primary ferroic orders mainly includes ferromagnetism and ferroelectricity. What makes multiferroic attractive not only because of its novel property that is not obtainable in natural materials, but also the electric force control in manipulating the magnetic spin, thus realizing more efficient data storage devices. Multifunctionality is not limited to multiferroics, Zhang’s review provides a more detailed summary on the reported self-assembled oxide-oxide systems with various properties, as shown in Figure 1.35. Novel functionalities include at least one of the following categories: electrical, magnetic, dielectric, optical and superconducting. The two-phase nanocomposite serves to (1) couple functionalities of more than one category, for instance, multiferroic, magneto-optical, electro-optical, etc., and (2) realize a tunable control and optimize one single property. We will now introduce these two key aspects in details by giving examples on magnetoresistance and superconductivity achieved in oxide-oxide systems.

**Table 1. Epitaxial nanocomposite heterostructures grouped by crystal structure and functionality.**

Vertically Aligned Nanocomposite Characteristics	Defect Engineering	Vertical Strain Control	Strong Coupling Effects	Vertical Heterointerface	Vertical Strain Control and Coupling
Nanocomposite family	Superconductivity	Ferroelectricity	Multiferroicity	Electronic and ionic transport	Dielectric and optical effects
Perovskite-related	BaZrO <sub>3</sub> - YBa <sub>2</sub> Cu <sub>3</sub> O <sub>7-δ</sub> (YBCO); BaSnO <sub>3</sub> -YBCO; BaHfO <sub>3</sub> -YBCO; Ba <sub>2</sub> YTaO <sub>6</sub> -YBCO; Ba <sub>2</sub> YNbO <sub>6</sub> -YBCO	BaTiO <sub>3</sub> -Sm <sub>2</sub> O <sub>3</sub> ; BaTiO <sub>3</sub> -CeO <sub>2</sub> ; BiFeO <sub>3</sub> -Sm <sub>2</sub> O <sub>3</sub>	BiFeO <sub>3</sub> -CoFe <sub>2</sub> O <sub>4</sub> ; BaTiO <sub>3</sub> -CoFe <sub>2</sub> O <sub>4</sub> ; BiFeO <sub>3</sub> -NiFe <sub>2</sub> O <sub>4</sub> ; La <sub>2</sub> CoMnO <sub>6</sub> -ZnO	La <sub>0.7</sub> Sr <sub>0.3</sub> MnO <sub>3</sub> (LSMO)-ZnO; LSMO-CeO <sub>2</sub> ; LSMO-Mn <sub>2</sub> O <sub>4</sub> ; LSMO-NiO; La <sub>1-x</sub> Ca <sub>x</sub> MnO <sub>3</sub> - MgO, SrTiO <sub>3</sub> -Sm <sub>2</sub> O <sub>3</sub> , SrRuO <sub>3</sub> -ZnO	Ba <sub>0.6</sub> Sr <sub>0.4</sub> TiO <sub>3</sub> - Sm <sub>2</sub> O <sub>3</sub> SrRuO <sub>3</sub> -CoFe <sub>2</sub> O <sub>4</sub>
Layered oxides			Bi <sub>5</sub> Ti <sub>3</sub> FeO <sub>15</sub> - CoFe <sub>2</sub> O <sub>4</sub>		

Figure 1.35 Summary of oxide-oxide nanocomposite functionalities.<sup>[60]</sup>

**Colossal magnetoresistance (CMR).** CMR belongs to a special physics phenomenon in materials such as La<sub>0.7</sub>Sr<sub>0.3</sub>MnO<sub>3</sub> (LSMO) with a dramatic change of electrical resistance under an applied magnetic field. Interestingly, the CMR can be controlled via introducing a secondary insulating phase which separates the uniform ferromagnetic domains at nanoscale. This has been achieved in oxide-oxide systems such as the LSMO-ZnO VANs reported by Chen et al.<sup>[63]</sup> As shown in Figure 1.36, the ferromagnetic-insulating-ferromagnetic (FM-I-FM) nanodomains form

a special tunneling junction that benefits from two sides, tune the transition temperature ( $T_C$ ) due to the suppressed double exchange (DE) interactions between the adjacent LSMO domains, and enhance the low-field MR significantly through the artificial grain boundary (GBs) effect. As mentioned in the previous section, the domain wall thickness or the width of the nanocolumns in the VAN can be tuned via control of laser frequency. Here, the structures grown under 1 Hz, 2 Hz, 5 Hz and 10 Hz exhibit a gradual shift of  $T_C$  as well as MR percentage (Figure 1.37). Such dramatic changes are owing to a tunable DE and GB effects affected by the insulating ZnO nanocolumns.

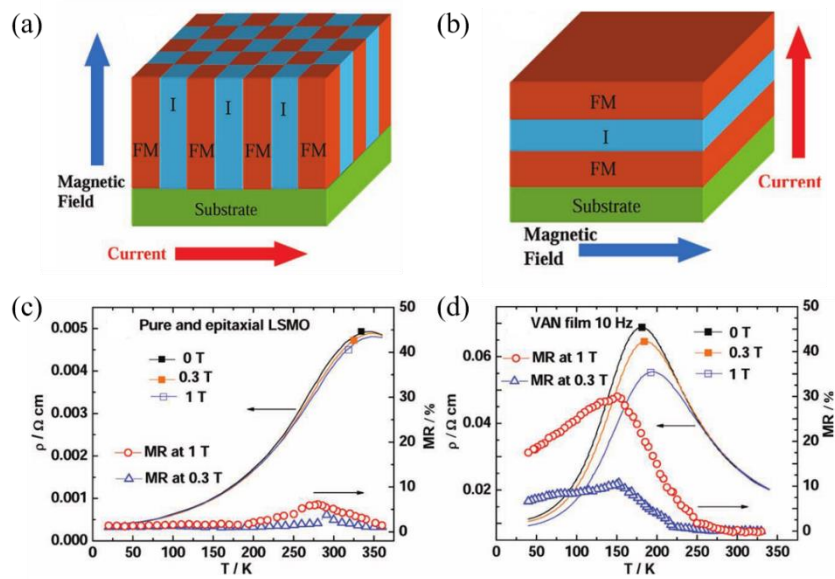


Figure 1.36 (a,b) Illustration of FM-I-FM tunneling junction as vertical or planar mode. (c) Temperature dependence of resistivity and MR% at different magnetic field.<sup>[63]</sup>

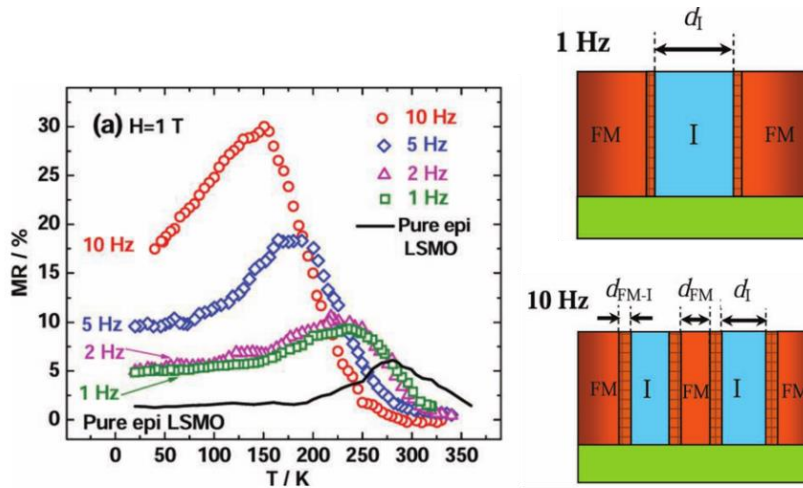


Figure 1.37 MR% versus temperature for LSMO-ZnO VANs deposited at different laser frequencies.<sup>[63]</sup>

**Enhanced superconductivity flux-pinning.** Materials such as  $\text{YBa}_2\text{Cu}_3\text{O}_{7-x}$  (YBCO) or  $\text{FeSe}_{0.5}\text{Te}_{0.5}$  exhibit superconductivity property denoted as an abrupt vanish of electrical resistance at their critical temperature ( $T_c$ ).<sup>[77-78]</sup> For YBCO thin film, the reported  $T_c$  lies in the range of 92 K which is much higher than many existed superconductors. Current density ( $J_c$ ) is another key factor limiting the performance of superconductor for practical applications. Driscoll et al.<sup>[73]</sup> explored the superconducting two-phase nanocomposites by involving a secondary phase in YBCO matrix,  $\text{BaZrO}_3$  (BZO) was picked because of its chemical inertness and low growth kinetics that help to form nanoparticles. Meanwhile, the large strain between BZO and YBCO has been demonstrated as an effective way in enhancing the magnetic flux pinning as well as the current density. The hybridization of BZO and YBCO nanocomposite thin film shows an increment factor of 1.5-2 of  $J_c$  values over a wide field range as compared to pure YBCO film. Figure 1.38 shows nanostructure of the BZO-YBCO film grown on STO substrate and the corresponding  $J_c$  versus magnetic field curve.

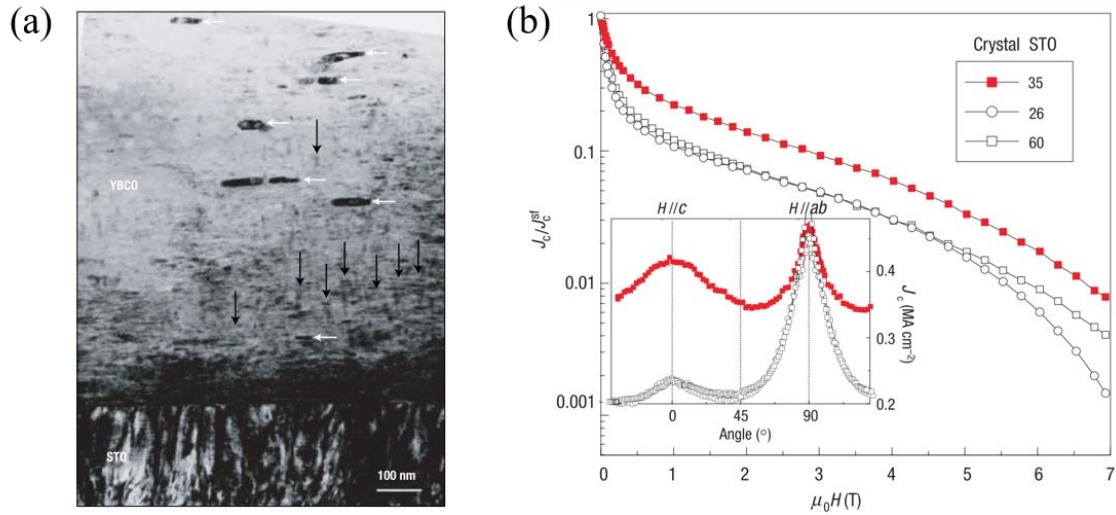


Figure 1.38 (a) Microstructure of BZO nanoparticles embedded in YBCO matrix as effective flux pinning centers. (b)  $J_c$  versus magnetic field curves, inset shows the anisotropic effect showing stronger enhancement along H//c.<sup>[73]</sup>

### 1.2.4.3 Challenges

Occasionally one would find it difficult in growing successful two-phase nanocomposites when the two phases are neither chemically stable nor discernable to visualize under the microscope. Even if the heterostructure appears to show two separate phases, the actual chemical composition or stoichiometry would be inaccurate in some cases, especially when the cations of the oxides are thermally intermixed with each other. Due to the fact of limited phase diagram explored so far in the oxide-oxide ceramics, some of the nanostructures turn to be deviated geometrically or chemically from expectations. This challenges the material scientists in terms of exploring the best material candidates as well as optimum conditions in coupling two oxides together, which requires extensive experimental effort on growth and characterizations before defining those as deposited films as two-phase nanocomposites. Under such conditions, some prerequisites for successful two-phase oxide-oxides nanocomposite growth have been proposed as guidelines, including: (1) close lattice match and comparable crystal symmetries between two film phases, (2) close lattice match with the substrate to ensure a smooth nucleation of adatoms at initial stage, (3) low solubility and thermal stability between the two phases, (4) ionic radii of cations should be sufficiently different to minimize possibility of intermixing, (5) a general comparable material property, such as elastic constants, thermal expansion.

### 1.2.5 Metal-Oxide Nanocomposites

Along with the wide range of functionalities being explored in the oxide-oxide nanocomposites, there are few areas such as electromagnetic (EM) properties that are underexplored. Consider the inherent insulating nature of many oxide candidates, the EM parameters lying in the similar range are considered not ideal for many interesting optical phenomena such as hyperbolic dispersion, negative refraction, nonlinearity, etc. This facilitates the demand in replacing one of the oxides into a dissimilar material, like metal. Indeed, extensive demonstrations of oxide-oxide combinations paved the way for metal-oxide nanocomposite growth, to some extent, it is very promising since the nucleation of metals is relatively easier. Recent explorations of metal-oxide nanocomposites have demonstrated the emerging importance in fabricating plasmonic metamaterial using bottom-up deposition techniques, as they provide advantages such as large surface coverage and a broad range of material candidates. Consider applications, we categorize common metals into two groups though each of the metals possesses its own optical constants (e.g.,  $n$  and  $k$ ).<sup>[79]</sup> The first group is behaving good plasmonic or optical properties, represented by Au, Ag, Cu, Al, etc., and the second group is ferromagnetic metals, represented by Co, Ni, Fe. However, there are few concerns in terms of growth of metals, typically because of their high reactive nature at elevated temperature or ambient atmosphere. Moreover, potential interactions between metal and oxide would be a big concern. Therefore, the metal-oxide nanocomposite growth was explored starting from Au-oxides since noble metals are much more stable.

#### 1.2.5.1 Tunable and Anisotropic Optical Properties

Coupling plasmonic metal with oxide as pillar-in-matrix geometry provides highly anisotropic dielectric dispersions along in-plane and out-of-plane directions. Via control of geometrical parameters such the aspect ratio or density of metal phase such dispersion property can be tuned in a wide UV to near-infrared (NIR) regime. The first demonstration on metal-oxide NAN was successfully achieved in Au-BaTiO<sub>3</sub> (BTO) system using the bottom-up, one-step PLD technique.<sup>[56]</sup> Its 3D nanostructure is presented in Figure 1.39. The Au nanopillars exhibit high crystalline quality and distinct vertical phase boundaries without intermixing with the oxide matrix. The effective permittivity calculated by effective medium theory was correlated with the polarized

reflectance data full-wave simulation, demonstrating the LSP resonance of Au at 550 nm and an anisotropic effective permittivity. The structure potentially possesses a hyperbolic transition approaching near-infrared. The success of metal-oxide hybridization brings dramatic possibilities in growing other metal-oxide nanocomposites using PLD. Direct follow-up studies from Zhang and Kalaswad<sup>[80-81]</sup> demonstrate the capabilities of tuning geometries or substrates (Si integration) of Au-BTO VAN films. As shown in Figure 1.40, by changing the film thickness from 70 nm to 3 nm, the aspect ratio of Au nanopillars can be tuned effectively. Such geometrical variation has a direct impact on dielectric properties, here, the hyperbolic transition frequency is tuned systematically close to 600-800 nm.

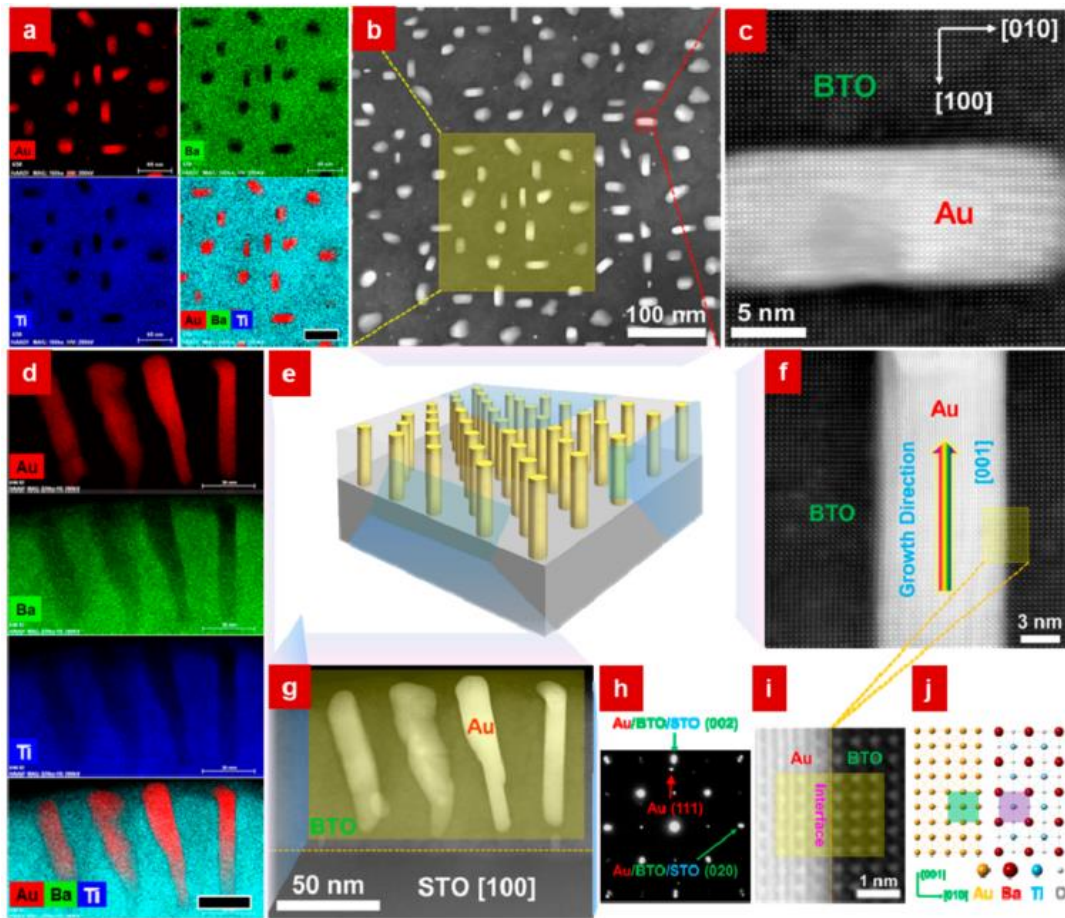


Figure 1.39 3D microstructure of Au-BTO VAN thin film. (e) 3D schematic illustration of the nanostructure. (a-c) Plan-view images and (d,f,g,i) cross-sectional images and SAED patterns. (h) Diffraction patterns. (j) Atomic model at Au/BTO interface.<sup>[56]</sup>

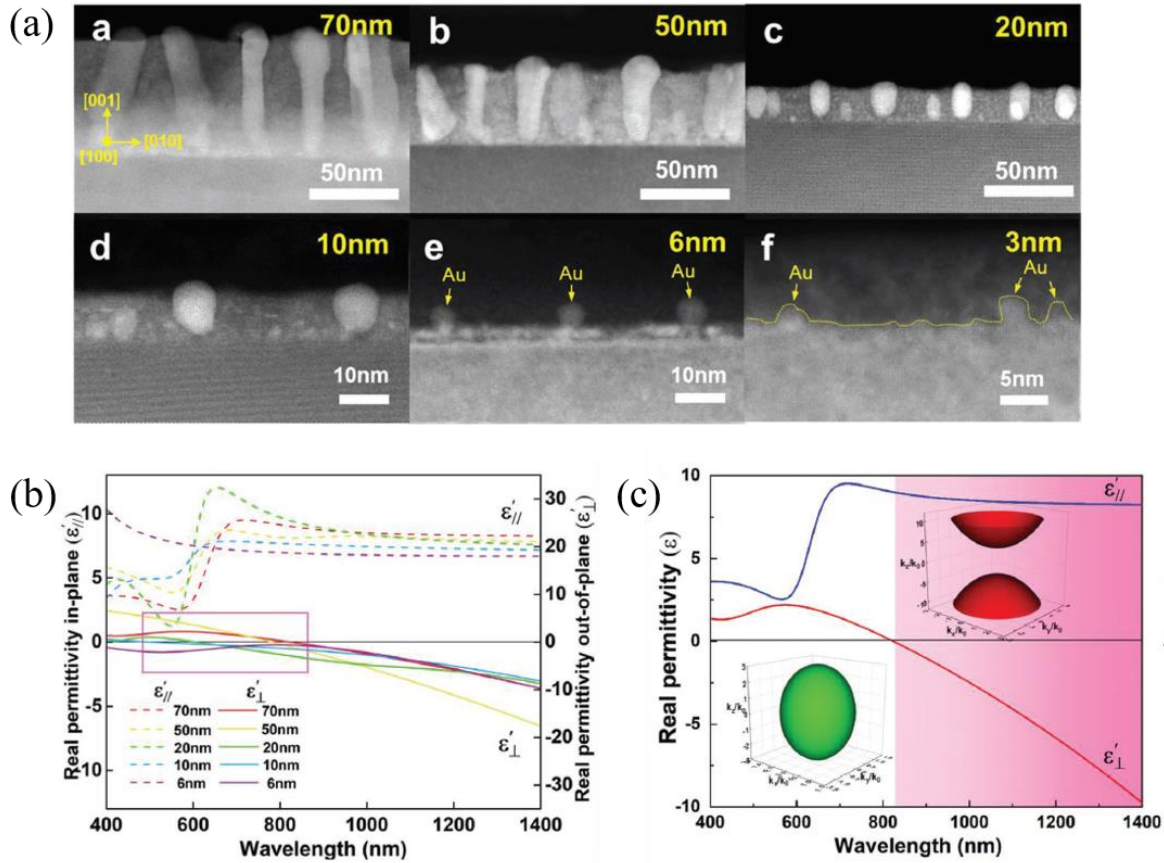


Figure 1.40 (a) Cross-sectional STEM images of Au-BTO system with changes of film thickness. (b,c) Uniaxial real-part permittivity with stack of different films. Inset shows a  $k$ -space isofrequency surface.<sup>[80]</sup>

### 1.2.5.2 Tunable and Anisotropic Magnetic Property

Fabrication of ferromagnetic nanostructures brings two important prospects, generating strong magnetic anisotropy, and magneto-optical (MO) effect as predicted when magnetic metals shrink to nanoscale.<sup>[82]</sup> Compare to noble plasmonic metals, ferromagnetic metals including Fe, Co and Ni are more reactive and easier to diffuse, thus, the growth of such metal-oxide heterostructure is challenging. Successful demonstrations using AAO templated method to grow Ni nanowires have been reported (Figure 1.41), which shows both strong ferromagnetic response and magneto-optical (MO) activity.<sup>[83]</sup> The ferromagnetic metal-oxide systems achieved by PLD growth techniques are the Co-BaZrO<sub>3</sub> (BZO) system and Ni-CeO<sub>2</sub>,<sup>[57, 84-85]</sup> potentially due to the fact that BZO or CeO<sub>2</sub> are relatively stable oxides (e.g. Zr<sup>4+</sup>, Ce<sup>4+</sup>) thus any intermixing of metal

phase was prohibited during the high-temperature growth. Figure 1.42 shows the nanostructure of Co-BZO VAN grown on SrTiO<sub>3</sub> (STO) substrate.

One major advantage brought by the PLD bottom-up fabrication technique, as mentioned few times, lies in the ability to extend growth to many additional materials systems. For metal-oxide VAN combinations, the oxide phase have already be extended to candidates such as ZnO, LSMO, CeO<sub>2</sub>, BaZrO<sub>3</sub> while the metallic phase such as Ag, Cu, Al and ferromagnetic metals such as Fe, Cu, Ni are desirable alternatives that bring additional properties beyond magnetic or optical.<sup>[57-58, 84-85]</sup> The reason why noble Au is the most favorable candidate is because of its ease of nucleation, thermal stability and chemical inertness compare to most of the metals, as it has been demonstrated as effective catalysis in growing semiconductor nanowires.<sup>[86]</sup>

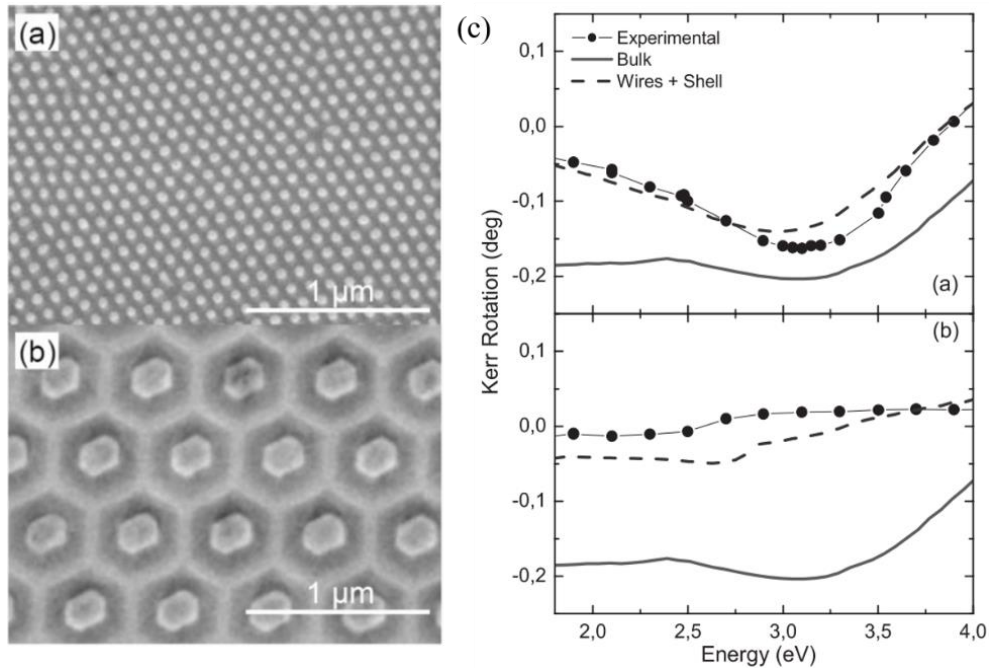


Figure 1.41 (a,b) Top view SEM image of Ni nanowire grown in alumina matrix. (c) Kerr rotation measured as a function of photon energy.<sup>[83]</sup>

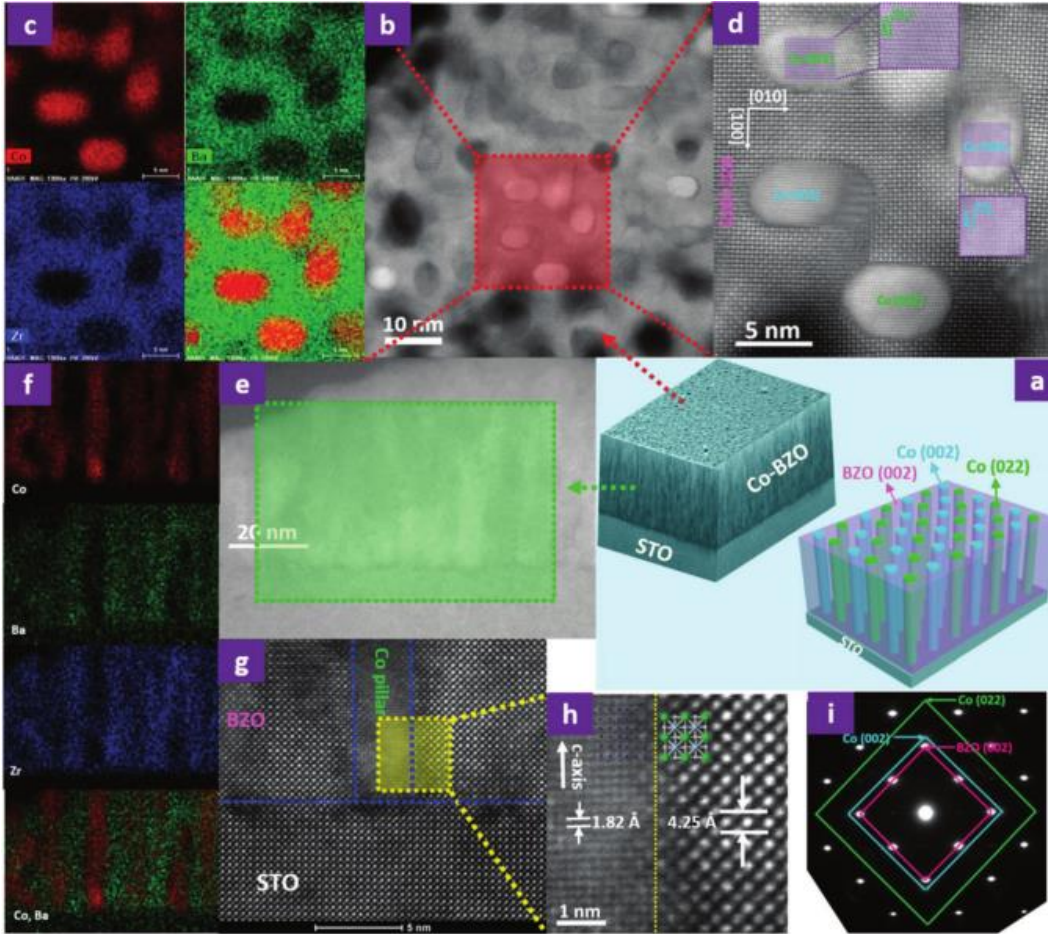


Figure 1.42 Microstructure of Co-BZO VAN deposited on STO, including plan-view and cross-sectional STEM images, EDX mapping and diffraction patterns.<sup>[57]</sup>

### 1.2.5.3 Challenges

**Periodicity.** The major difference between nanocomposites and metamaterial is the periodicity or coherency of the nanoscale “building blocks”. Metamaterials fabricated by EBL possess high degree of periodicity because the features are artificially written by controlled designs. Even for hyperbolic wire metamaterials fabricated by AAO assisted growth, the templates possess high degree of hexagonal ordering. However, bottom-up fabrication of metal-oxides or any two-phase nanocomposites is dominated by a self-assembling process, either by nucleation and growth or spinodal decomposition. Therefore, the coherency and periodicity could not be controlled or predicted which becomes a major obstacle to overcome. Such imperfection normally includes geometrical variations as well as the packing distance or the ordering of the secondary phase distribution, for example, some nanopillars are wider and some of them are thinner, being aligned as rather “random” fashion. An example as shown in Figure 1.43, the Au-ZnO system

exhibit high crystalline quality with large surface coverage and hyperbolic dispersion property, meanwhile the periodicity and the uniformity are out of control. Especially for plasmonic metamaterials or metasurfaces, the periodicity of metaatoms is crucial in accurate control of the wavefront, the spontaneous emission rate, quality factor of plasmon resonances, whereas the spacing in between would have an impact on the near-field interactions.<sup>[87-89]</sup>

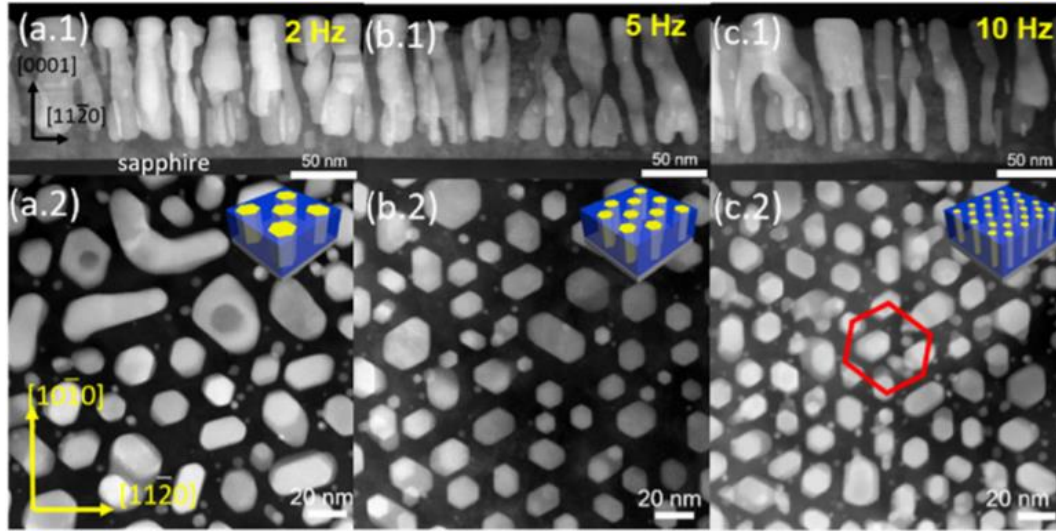


Figure 1.43 Au-ZnO VANs deposited under different laser frequency: 2 Hz, 5Hz and 10 Hz.<sup>[58]</sup>

To this end, few solutions have been proposed and explored in order to enhance the periodicity and control over geometry, including strain engineering, substrate treatment and template assisted growth method,<sup>[59, 64, 90-91]</sup> where the latter is believed as the most effective way in improving the ordering of two-phase nanocomposites so far. The method is described in Figure 1.44 for the growth of  $\text{CoFe}_2\text{O}_4$  (CFO) -  $\text{BiFeO}_3$  (BFO) VAN. In this specific study, focused ion beam (FIB) was applied to create periodic patterns. These patterns serve as “defective sites” that are then being etched and cleaned for growing an ultrathin layer (few nm) of pillar phase (CFO) was preferably grown at those defective sites filling the etched “pits”. Next, the matrix phase (BFO) was grown at a very low step to ensure the stable nucleation thus the template of ordered two-phase is formed. A final step is the two-phase co-deposition on top of the template to achieve a desirable thickness. One limitation lies in the fact that the e-beam or ion-beam writing is still a small-scale processing which is time consuming, but it provides a good starting point in achieving

high-degree periodicity using a combination of top-down and bottom-up methods to fabricate ordered two-phase VANs.

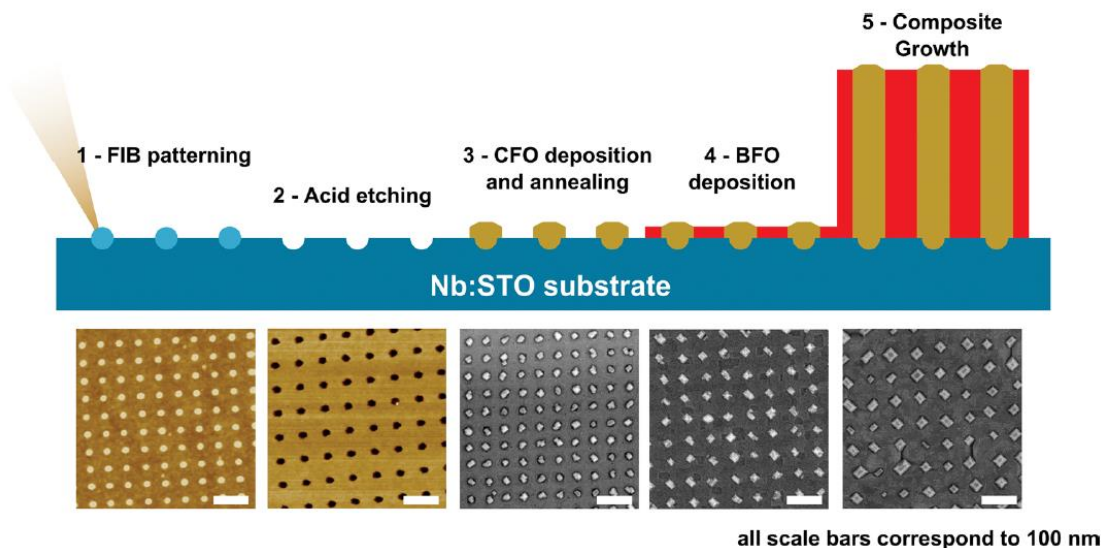


Figure 1.44 Schematic illustration on the templated method of growing ordered CFO : BFO nanocomposite.<sup>[91]</sup>

**Instability.** From material perspective, metals are thermally unstable mechanically soft. Among the functional metallic candidates, perhaps only Au and Pt possess relatively higher stability, the rest of the metals are either easily being diffused or chemically reactive with another medium. For example, metals such as Ag, Al and Cu own strong LSPR and SERS effect, but are unstable even at room temperature by forming a thin oxide layer at the top surface.<sup>[13, 92-95]</sup> Even though some of the reported studies take advantage of such natural oxidation as protective layer against further contamination,<sup>[96]</sup> the surface degradation is still a great concern for practical applications since most of the devices need to be operated at ambient atmosphere or at high temperature. On the other hand, as most of the metals are malleable and ductile, any mechanical stress would easily cause deformation of metals.

To address the instability issue, some solutions have been made along the path. Intuitively, it would be effective to fabricate a two-phase hybrid to cover the less stable metal with a more stable material. Core-shell nanostructure is one representative design. Ag as an example, multiple protective shell materials such as Au, silica (SiO<sub>2</sub>), Ag<sub>2</sub>S, graphene have been demonstrated to

enhance the chemical stability of Ag.<sup>[97-100]</sup> Figure 1.45 shows a hybrid Au shell - Ag core nanoplates formed by solution synthesis.

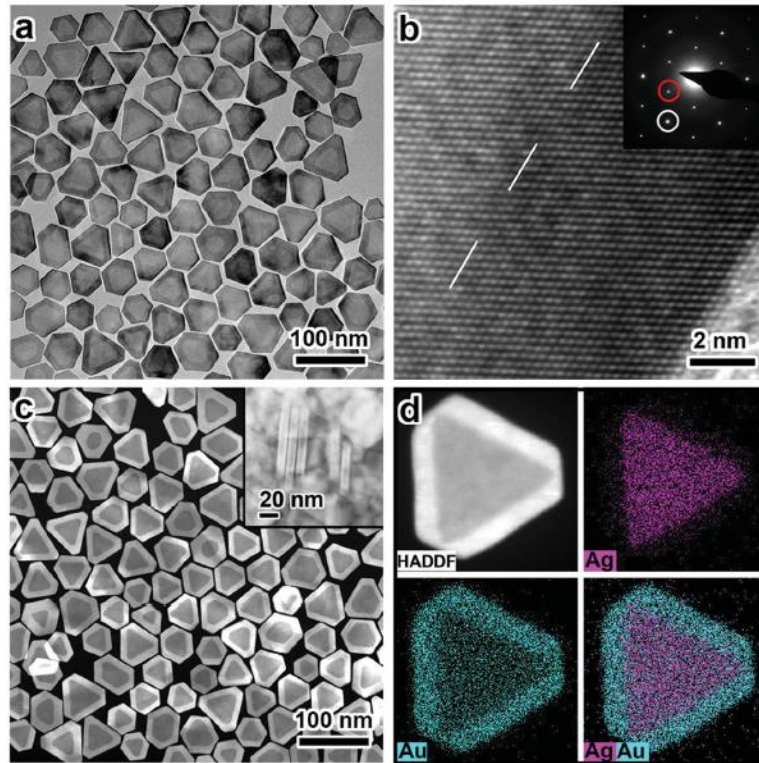


Figure 1.45 Microstructure of Au shell - Ag core nanoplates. (a) TEM image, (b) HTREM image, inset shows diffraction patterns, (c) STEM image and (d) EDX elemental mapping.<sup>[100]</sup>

In terms of metal-oxide nanocomposites, aside from oxidation from the metal phase, potential interdiffusion of metal with oxides would lead to significant challenges for hybridizing metals such as Ag, Cu, Co or Fe with oxides. The resulted nanostructures would face problems including (1) complete mixing between metal and oxides without phase segregation, (2) the metal phase is very blurry and partially mixed with oxide at the metal/oxide interface, (3) complete degradation of metals by forming oxides during high temperature growth or by reacting with the background pressure.

**Optical losses.** To bring operation of metamaterial into optical frequencies, a major concern is the inherit loss or absorption of metals even for highly conductive noble metals such as Au and Ag.<sup>[101]</sup> In general, absorption (or imaginary part of dielectric constant  $\epsilon_2$  or extinction coefficient  $k$ ) originates from the intraband transition induced by the free electrons within s-p band,

and interband transition induced by direct transition between the bands, for example, transition from the 5d state to the 6sp state of Au at 1.74 eV, as depicted by Figure 1. 46.

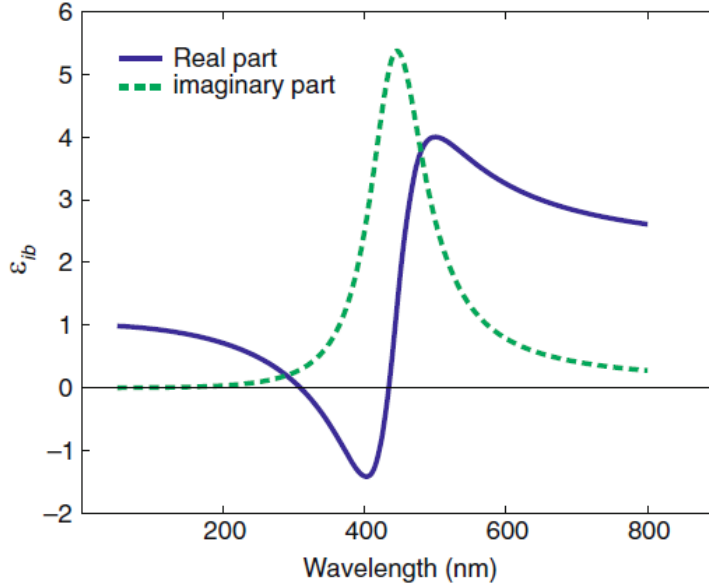


Figure 1.46 Interband transition of Au at visible wavelength range.<sup>[93]</sup>

The interband transition at lower frequencies causes strong absorption. Normally, one would avoid this frequency of operation and shift to the regime lower than  $\omega_p$ . Here,  $\omega_p$  is the plasma frequency at the interband absorption edge where the electron gas oscillates, which is expressed as:

$$\omega_p = \sqrt{\frac{ne^2}{\epsilon_0 m}}$$

,  $\epsilon_0$  is the vacuum permittivity ( $\epsilon_0 = 8.85 \times 10^{-12} F/m$ ),  $m$  and  $e$  represent effective mass and charge of electron, respectively. Taking interband transition into account, the modified Drude equation describing the dielectric constant of metals is written as:

$$\epsilon(\omega) = \epsilon'(\omega) + i\omega''(\omega) = \epsilon_\infty - \frac{\omega_p^2}{\omega^2 + \Gamma^2} + i \frac{\omega_p^2 \Gamma}{\omega(\omega^2 + \Gamma^2)}$$

, where  $\Gamma$  is the damping constant,  $\epsilon_\infty$  is the empirical value (typically 9 for Au and 5 for Ag).

### 1.2.6 Alternative Plasmonic Candidates

Given the above-mentioned facts, few approaches in addressing optical losses have been proposed<sup>[101]</sup>, including: (1) engineering plasmonic nanostructures in a way to reduce the energy confinement inside metals, (2) introducing optical gain media to compensate the losses, (3) searching for alternative plasmonic candidates with lower losses to partially or completely replace metals. Progress in terms of new plasmonic materials such as conductive oxides, graphene and transition metal nitrides has already shown astonishing advantages beyond achieving smaller losses.<sup>[102-103]</sup> For example, heavily doped oxides or III-V nitrides offer a wide range of tunable carrier concentration and operation frequencies, while transition metal nitrides or graphene provides as durable barrier that offers extraordinary thermal and mechanical stability. Graphene is attractive as a unique two-dimensional ultrathin absorber, it can be applied as either “metallic” component for graphene/dielectric hyperbolic metamaterial, or as protective shutter to prevent oxidation of unstable metals (e.g. Ag, Cu).<sup>[97, 104-105]</sup> An example shown in Figure 1.47 demonstrates a hyperbolic/polymer hyperbolic nanogratings which generate 85% absorption at the entire solar spectrum (300-2500 nm).

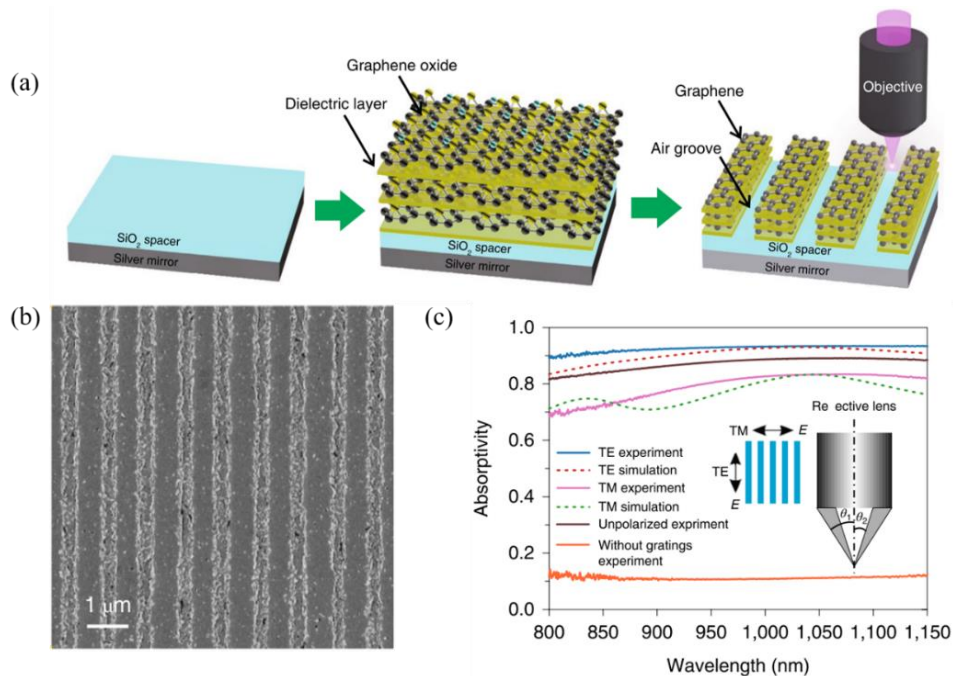


Figure 1.47 (a) Schematic illustration of fabrication process of the graphene-based metamaterial. (b) SEM image of the grating. (c) Measured absorptivity spectra under TE and TM polarizations and unpolarized light.<sup>[104]</sup>

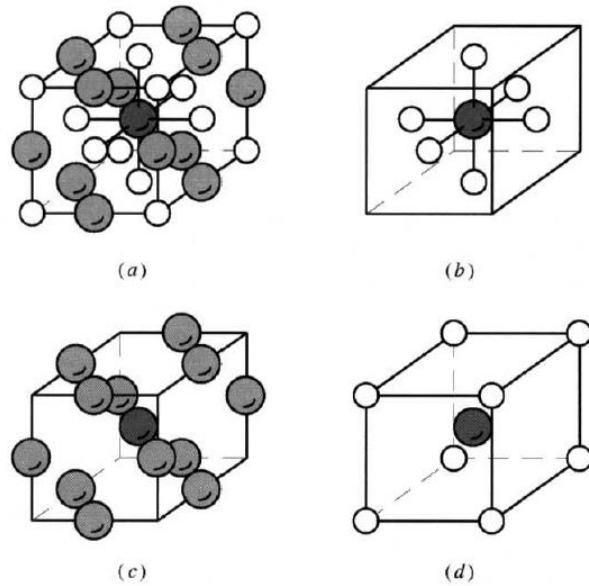


Figure 1.48 Rock salt crystal structure.<sup>[98]</sup>

Titanium nitride (TiN) as a representative material candidate in the transition metal-nitride family, owns unique chemical, mechanical, electrical and optical properties. Specifically, TiN has a NaCl rock salt crystal structure where the central cation is attracted to 6 anions as shown from Figure 1.48. It belongs to the space group of  $Fm\bar{3}m$ , and owns a lattice constant of 4.241 Å. Due to its high corrosion resistance, thermal stability and high hardness, as well as its shiny golden appearance, TiN is conventionally known as a desirable superhard coating or diffusion barrier candidate for machining and jewelry.<sup>[106-107]</sup> More recently, it has been applied as gate electrodes to prevent oxidation or diffusions for CMOS (complementary metal oxide semiconductor) technology.<sup>[108]</sup> Thin film growth of TiN with 1:1 stoichiometry ratio is achievable via PVD techniques,<sup>[109-110]</sup> mostly on MgO substrates because of the small lattice mismatch between TiN ( $a_{TiN} = 4.241 \text{ \AA}$ ) and MgO ( $a_{MgO} = 4.211 \text{ nm}$ ). Interestingly, the integration of TiN on Si shows epitaxial growth with a unique domain matching epitaxy as shown in Figure 1.49, here, the TiN works as a buffer layer grown on Si, which serves as a desired transition layer to deposit TaN layer on top.<sup>[111]</sup> Not limited to TaN, a wide range of materials can be integrated on Si through depositing a thin TiN buffer, which serves not only as epitaxial basis, but also as corrosion of diffusion barrier that plays fundamental role in many Si-based device applications.<sup>[112-113]</sup>

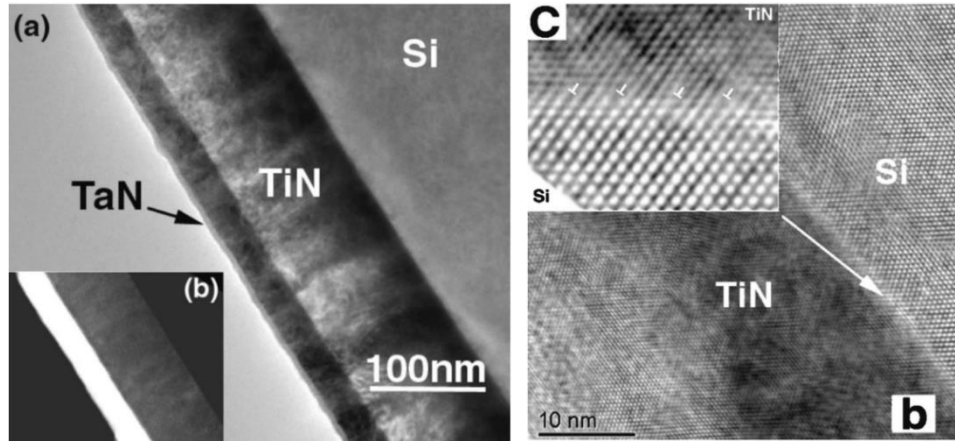


Figure 1.49 Cross-sectional TEM images of epitaxial TaN/TiN grown on Si substrate.<sup>[111]</sup>

On the other hand, plasmonic metamaterial-based research (e.g. studies from Shalaev and Boltasseva group) proposed that TiN can be an alternative plasmonic candidate that exhibits comparable properties with Au but shows smaller losses at higher wavelength regime.<sup>[102, 114-115]</sup> From conventional material perspective, TiN is treated as a ceramic nitride. But in the field of optics, TiN behaves as metallic with high charge carrier concentration and negative real part permittivity, which is similar with Au. Naik et al. performed a thorough study on optical properties of TiN and its comparison with conventional noble metals,<sup>[115]</sup> Figure 1.50 shows the dielectric function derived from ellipsometry measurements, comparing TiN, Au and Ag.

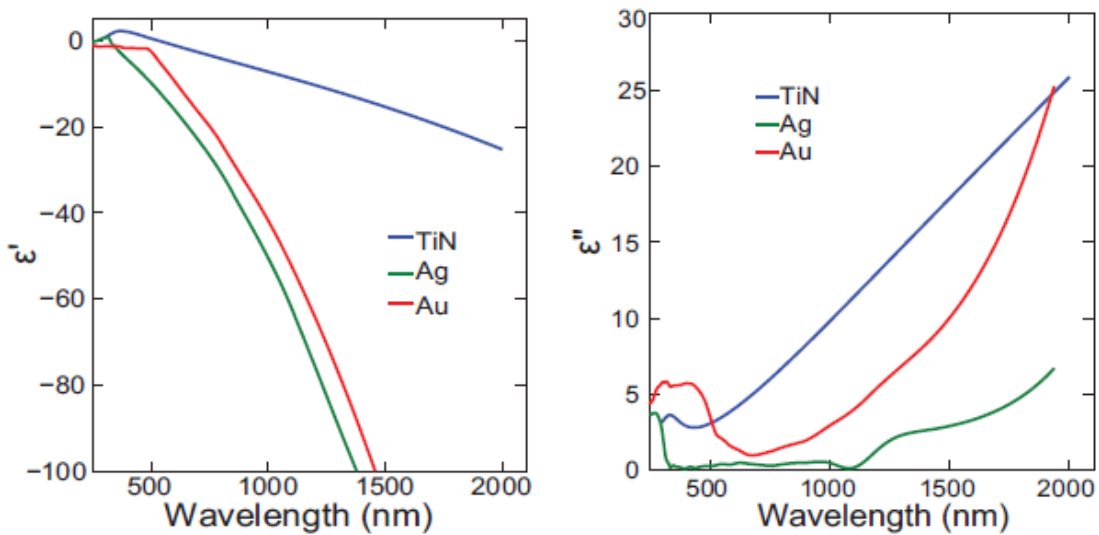


Figure 1.50 Real and imaginary part dielectric constant of TiN, Ag and Au.<sup>[115]</sup>

Applying TiN to plasmonics is not limited to its attractive optical performance, as described, TiN films integrated on single crystals, Si or glass exhibit much higher epitaxial quality and adhesion compared to Au. Nanostructured TiN shows flexibility in terms of its tunable surface plasmon polaritons (SPPs) or LSPs. In addition, the inherent thermal and mechanical stabilities applied for protective coatings are extremely beneficial for high temperature plasmonic applications, as the future of plasmonics would require high endurance of materials under extreme conditions. Refractory plasmonics based on TiN metamaterial have demonstrated its high absorption and stability. Figure 1.51 shows a study by comparing nanostructured Au and TiN metamaterial. TiN maintains almost intact upon thermal annealing and laser irradiation, while Au becomes either deformed or damaged.<sup>[116]</sup>

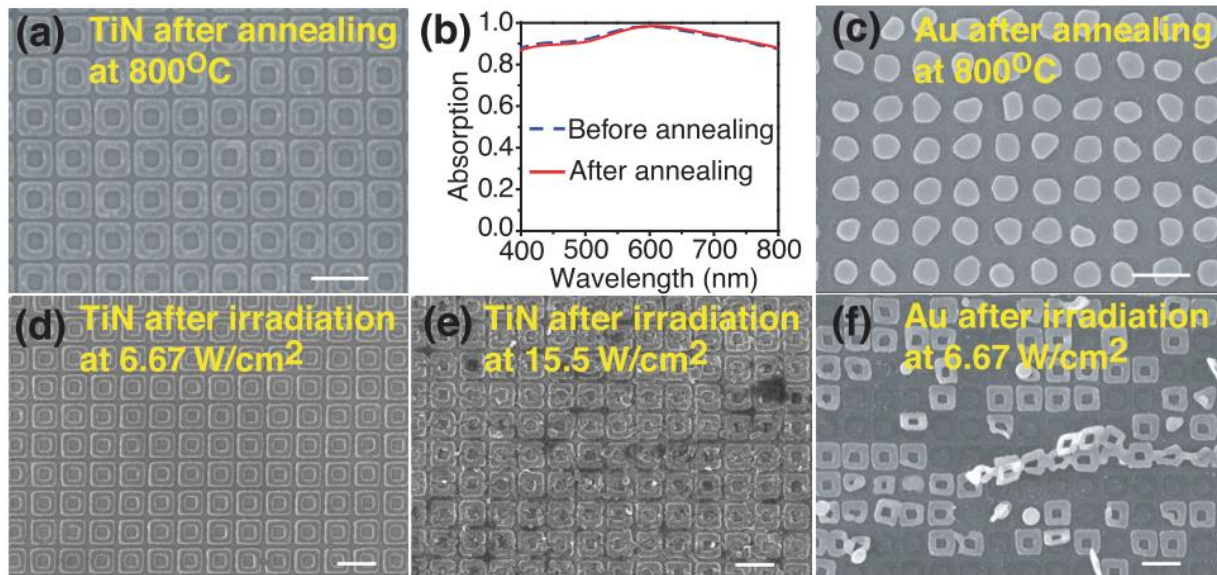


Figure 1.51 SEM images of TiN metamaterial (a) after annealing, (b,e) laser irradiation with different energies. (b) Absorption spectra before and after thermal treatment. SEM images of Au metamaterial (c) after 800 °C annealing and (f) laser irradiation.<sup>[116]</sup>

Interestingly, TiN exhibits certain degree of nonlinearity into 2<sup>nd</sup> and even 3<sup>rd</sup> orders.<sup>[117-119]</sup> As reported by Gui et al., TiN nanoantenna arrays exhibit comparable second harmonic generation (SHG) signals with Au. Again, much higher endurance under laser irradiation measurements has been effectively proved, demonstrating the unique advantage of TiN as compared to metals. These properties have made the material very attractive in future plasmonic explorations as proposed by Atwater (2007)<sup>[120]</sup>. In the next few sections, we take advantage of

TiN and couple it with different material components at nanoscale as two-phase nanocomposites for multiple novel structural design and applications.

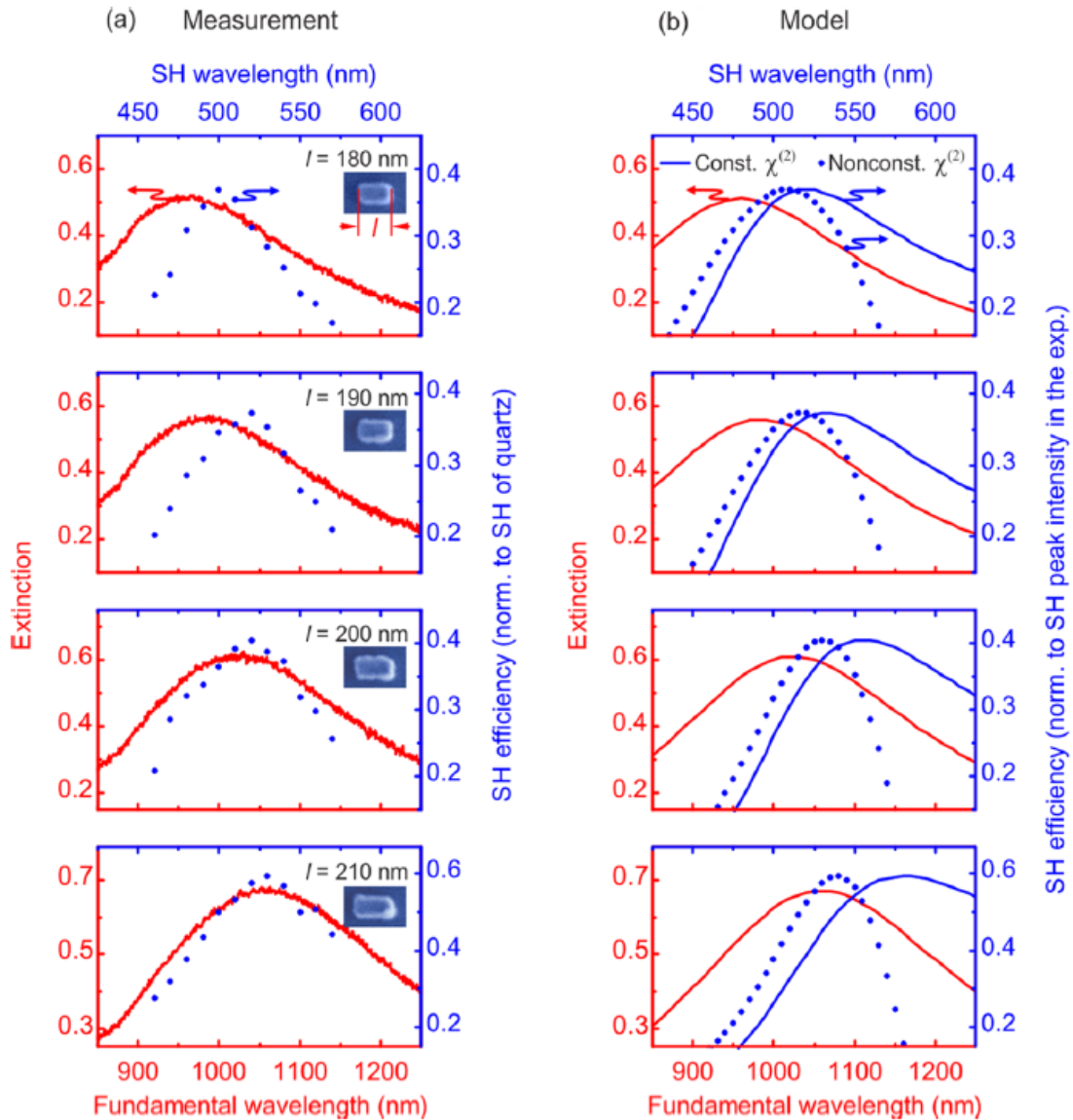


Figure 1.52 Second harmonic generation (SHG) measurement and modeling of TiN nanoantenna array.<sup>[118]</sup>

### 1.2.7 Metal-Nitride Nanocomposites

Research in oxide-oxide nanocomposites have shown us the possibility in coupling many existing material candidates together to design different nanostructures and properties. Indeed, the ceramic family is not limited to oxides, and as demonstrated by pioneer works, epitaxial thin films

non-oxides such as nitrides or carbides can also be realized by the bottom-up deposition technique.<sup>[121-123]</sup> We started to look into the nitride family that covers a range of interesting properties, for example, transition metal-nitrides as metallic and plasmonic candidates as introduced in previous sections, while the III-V nitrides with wide-bandgap can be applied semiconductor or light emitting diodes (LEDs). However, coupling of nitrides with oxides would be challenging in terms of potential intermixing of the anions (N and O), instead, metal becomes an alternative option to start with since the growth kinetics and thermodynamics would be very different between metal and nitrides, which offers possible phase segregations. To this end, the tables (Table 1.1 and 1.2) are presented in the next two pages which summarize the common ceramic nitrides and metals in order to compare their crystal structure and key physical properties in parallel. It is noted here that all the values are retrieved from bulk materials, solid-state thin films depending on growth methods and conditions would affect the lattice constants due to strain or defects, the degree of crystallinity would vary from amorphous to epitaxial films. These differences would result in variations of the physical properties especially for thin films.

In general, ceramic nitrides exhibiting high hardness and melting temperature would be desirable thermal or diffusion barrier candidates. The most obvious difference in nitrides can be revealed from their electrical resistivity (Table 1.1). The transition metal-nitrides are mostly conductive with high electron concentration, while the III-V nitrides are mostly semiconducting with wide bandgap. As TiN has been already introduced in Section 1.2.6, here, we briefly introduce TaN and AlN as they are more representative for the research projects covered in the next few chapters. Compare to TiN, tantalum nitride (TaN) exists both stable and metastable phases that possess different types of crystal structures, as summarized in Table 1.3. A general comparison of the optical constant between TaN and other transition metal nitrides (e.g. TiN, ZrN and HfN) reveals a less metallic nature seen from its more positive values of real-part dielectric constant (Figure 1.53) as reported by Naik et al.,<sup>[114]</sup> and it is also confirmed by a higher electrical resistivity of TaN according to Table 1.1. It is noted that most transition metal nitrides are possessing comparable lattice parameters and crystal symmetries with substrate crystals such as MgO ( $a = 4.21 \text{ \AA}$ ), STO ( $a = 3.91 \text{ \AA}$ ). Also, growth on Si (001) and *c*-cut sapphire substrates are also achievable via domain matching epitaxy.

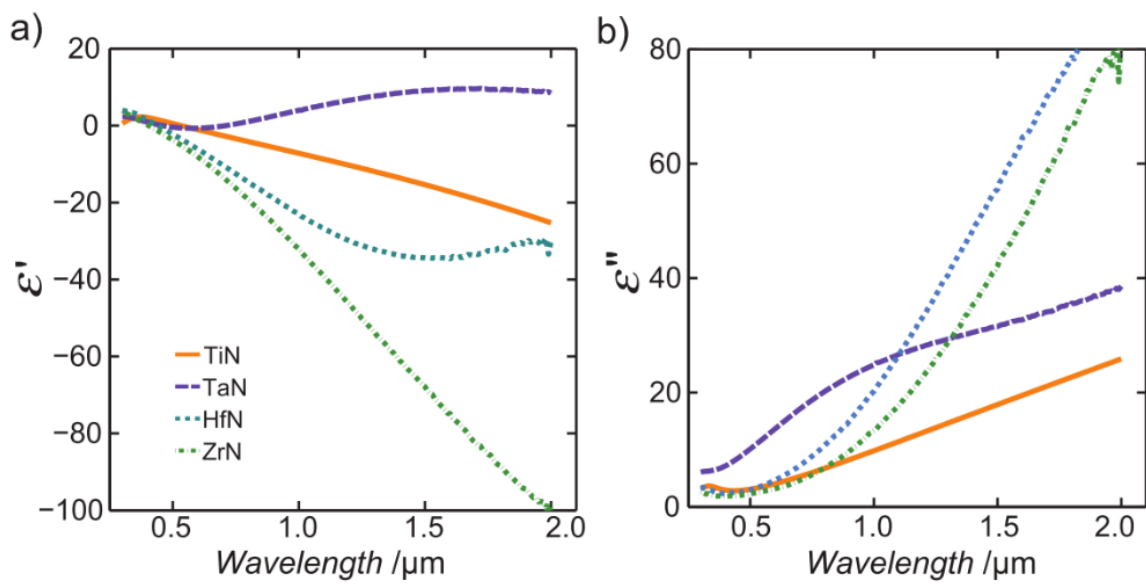


Figure 1.53 (a) Real part and (b) imaginary part dielectric constant of TiN, TaN, HfN and ZrN.<sup>[114]</sup>

Table 1.1 Crystal structure and physical parameters of common ceramic nitrides.<sup>[117]</sup>

Chemical Formula	Crystal Structure	Lattice Parameter (Å)			Appearance (solid)	Melting Point (K)	Young's Modulus E (GPa)	Electrical Resistivity $\rho \times 10^8$ ( $\Omega \cdot m$ )
		a	b	c				
<b>TiN</b>	Cubic (rocksalt)	4.241	-	-	Gold (yellow)	3220	390	40
<b>TaN</b>	Cubic (rocksalt)	4.34	-	-	Grey/blue	3360	576	180
<b>ZrN</b>	Cubic (rocksalt)	4.578	-	-	Light yellow	3250	328	18
<b>HfN</b>	Cubic (rocksalt)	4.392	-	-	Light brown	3580	480	32
<b>CrN</b>	Cubic (rocksalt)	4.149	-	-	Black		320	640
<b>VN</b>	Cubic (rocksalt)	4.136	-	-	Light brown	2320	350	60
<b>AlN</b>	Hexagonal (Wurtzite)	3.112	-	4.982	White to pale-yellow	2500	320	$> 10^{19}$
<b>GaN</b>	Hexagonal (Wurtzite)	3.189	-	5.185	Yellow	4532	181	$> 10^{20}$
<b>h-BN</b>	Hexagonal (Wurtzite)	2.502	-	6.617	Colorless	3270	60	$1.7 \times 10^{19}$
<b><math>\beta</math>-Si<sub>3</sub>N<sub>4</sub></b>	Hexagonal	7.602	-	2.907	Grey	2170	315	$> 10^{19}$

Table 1.2 Crystal structure and physical parameters of common metals.<sup>[118]</sup>

Chemical Formula	Crystal Structure	Lattice Parameter (Å)			Appearance (solid)	Melting Point (K)	Young's Modulus E (GPa)	Electrical Resistivity $\rho \times 10^8$ ( $\Omega \cdot m$ )
		a	b	c				
<b>Au</b>	FCC	4.072	-	-	Metallic yellow	1337.33	78	$2.2 \times 10^{-8}$
<b>Ag</b>	FCC	4.086	-	-	Lustrous white	1234.93	83	$1.63 \times 10^{-8}$
<b>Pt</b>	FCC	3.924	-	-	Silvery white	2041.4	168	$10.6 \times 10^{-8}$
<b>Cu</b>	FCC	3.615	-	-	Red to orange	1357.77	130	$1.72 \times 10^{-8}$
<b>Al</b>	FCC	4.050	-	-	Silvery gray	933.47	70	$2.7 \times 10^{-8}$
<b>Ni</b>	FCC	3.524	-	-	Lustrous silver-with gold tinge	1728	200	$7.2 \times 10^{-8}$
<b>Co</b>	HCP	2.507	-	4.070	Lustrous bluish gray	1768	209	$6 \times 10^{-8}$
<b>Fe</b>	BCC	2.867	-	-	Lustrous gray	1811	211	$10 \times 10^{-8}$

Table 1.3 Crystal structure and lattice parameter of eight different phases of TaN.<sup>[119]</sup>

Phase	TaN <sub>0.05</sub>	Ta <sub>2</sub> N	TaN	$\delta$ -TaN	$\epsilon$ -TaN	Ta <sub>5</sub> N <sub>6</sub>	Ta <sub>4</sub> N <sub>5</sub>	Ta <sub>3</sub> N <sub>5</sub>	
Structure	BCC	HCP	FCC	Hexagonal	Hexagonal	Hexagonal	Tetragonal	Tetragonal	
Lattice Parameter (nm)	a	0.337	0.305	0.433	0.293	0.518	0.293	0.683	1.022
	b	-	-	-	-	-	-	-	-
	c	-	0.492	-	0.286	0.290	0.286	0.427	0.387

On the other hand, III-V nitrides such as AlN, GaN, InN possess wurtzite structure with weaker ionic bonding. This gives them better sintering property while moderate hardness as compared to TiN. Recent developments of III-V nitrides have demonstrated great potential for applications in optoelectronic devices such as blue-ultraviolet LEDs or high-power transistors in the RF frequencies, benefit from its high thermal conductivity and piezoelectric coefficients.<sup>[124]</sup> Pure AlN owns a wide bandgap of around 6.1 eV, this energy gap can be further engineered by doping at controlled level depending on device application. Fabrication of III-V typically require high epitaxial quality represented by ultra-smooth and sharp atomic layers. Growth of such thin films have been achieved via CVD, MBE, ALD and PLD techniques. Epitaxial III-V nitride thin films can be realized on Si (111), *c*-cut sapphire and SiC crystals, or by applying buffer layer to compensate the large lattice mismatch between the film and substrate.

Towards successful hybridization of metal and nitrides for nanocomposite growth, we summarized the real and imaginary part dielectric constant at 500 nm and 1.5  $\mu\text{m}$ , separately, for potential candidates in the metal and nitride families, presenting as 2D plots in Figure 1.54. These data mainly come from the online database and for bulk materials. We know from theory that the dielectric constant of nanostructures at subwavelength scale would be different from their bulk counterparts, though the difference is not significant. Here, we use these values as general guidelines in order to predict the properties of metal-nitride nanocomposites.

Based on Figure 1.54, we conclude few important points: 1) Au and Ag are the well-known choices among all metallic candidates owing to their good plasmonic performance and lower losses, 2) TiN shows reasonable plasmonic property among metallic transition metal nitrides and potentially the plasmonic property can be enhanced by improving its crystallinity, 3) TaN, Si<sub>3</sub>N<sub>4</sub> and all III-V nitrides are behaving more dielectric without much difference from 500 nm to 1.5  $\mu\text{m}$ .

Accordingly, we proposed two coupling mechanisms of the metal-nitride nanocomposites, the first type is hybrid plasmonic design to couple metallic nitrides with a metal mainly to enhance the overall stability and optimize the plasmonic performance. The second type is to combine metal with a dielectric nitride to tune the dispersion function and potentially extreme anisotropy such as hyperbolic property. Comparable to the oxide-based nanocomposites, there are several key factors to consider before achieving successful growth, including (1) comparable crystal symmetry and lattice parameters, (2) different nucleation energy or wetting properties of “pillar” and “matrix” phases, for example, islanded mode would potentially form nanopillars. (3) Two phases are

chemically stable, which means no intermixing, chemical reaction or diffusion are allowed. Without general guidance or resources such as phase diagrams or reported studies, growing nitride-metal under high temperature could be challenging. Therefore, selection of film components within nitride and metal families, precise growth conditions and selection of substrate materials need to be explored thoroughly to minimize potential solubilities, chemical interactions and irregular geometries.

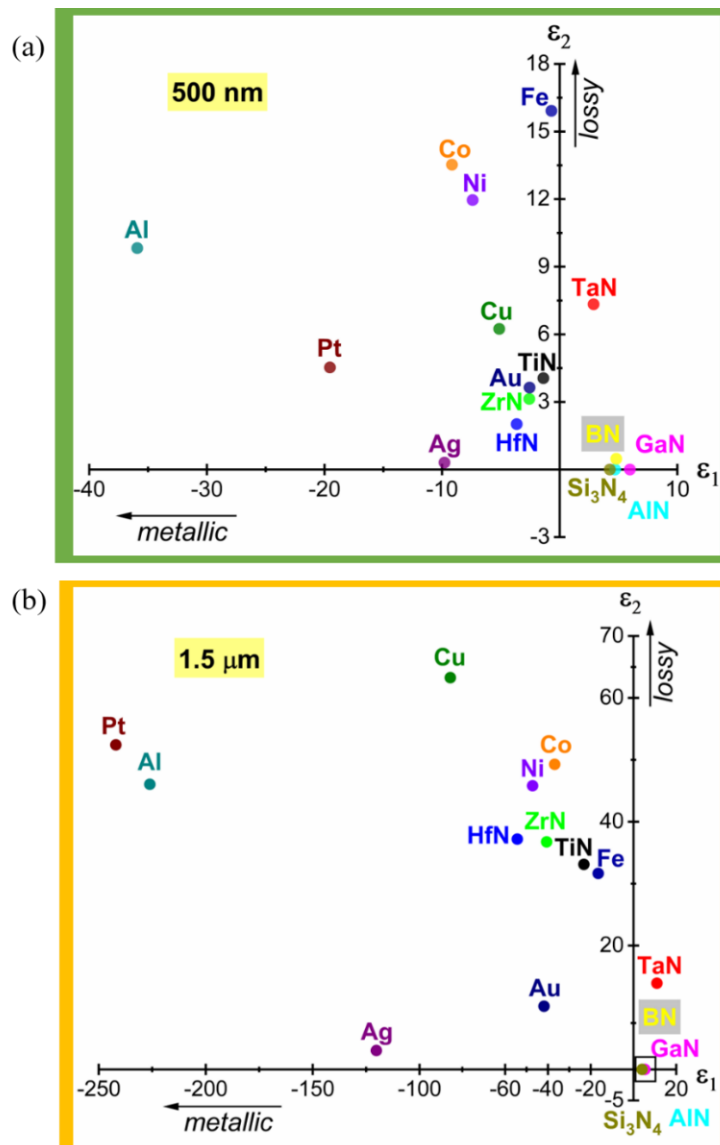


Figure 1.54 Real and imaginary part dielectric constant of selected metals and nitrides at (a) 500 nm and (b) 1.5  $\mu\text{m}$ . (Data source: <https://refractiveindex.info/>)

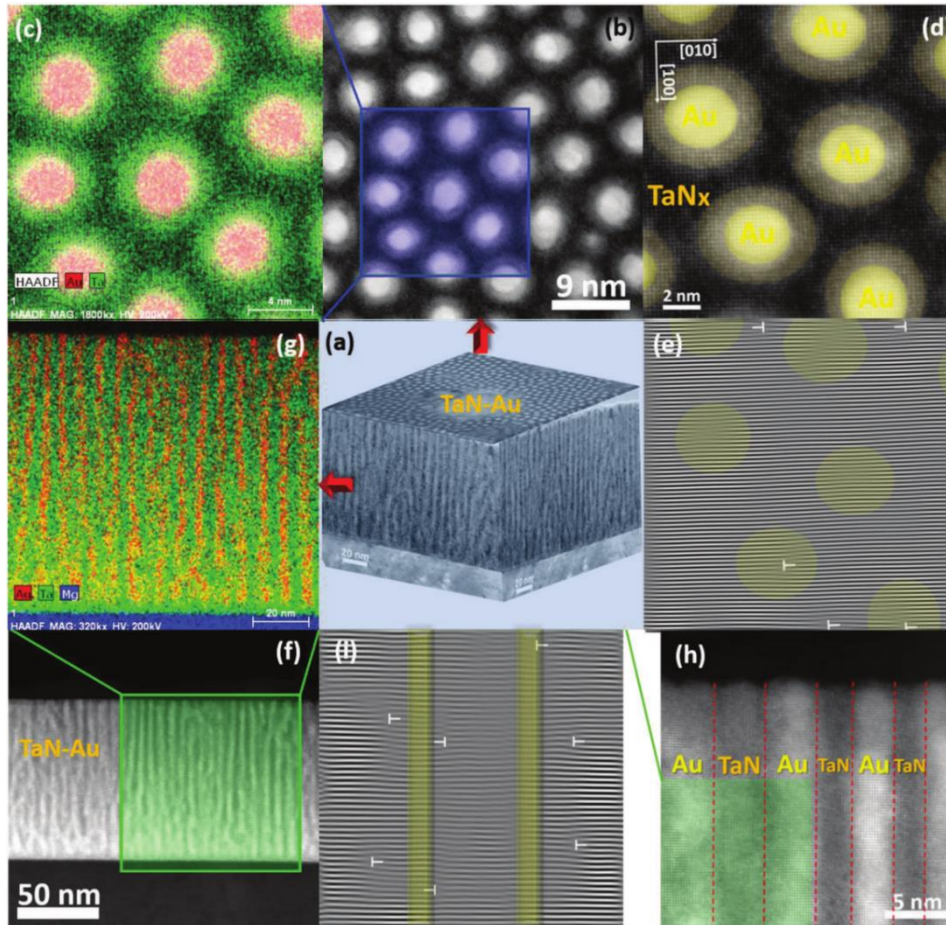


Figure 1.55 3D microstructure of Au-TaN VAN system. (a) 3D STEM configuration rebuilt from 2D images. (b-e) Plan-view STEM micrographs, EDX mapping and IFFT image. (f-h) Cross-sectional STEM micrograph, EDX mapping and IFFT image.<sup>[59]</sup>

The first study on metal-nitride nanocomposite was reported in 2018 by Huang and Wang et al.,<sup>[59]</sup> specifically on Au-TaN and Au-TiN VAN systems. Au is always the first candidate to explore due to its good plasmonic property and durability in general. Here, the small lattice mismatch between Au with either TaN or TiN ensures the VAN growth to a large extent. As shown in Figure 1.55, Au adatoms are self-organized into sub-10 nm nanopillars aligned vertically and followed certain hexagonal ordering inside the transition metal nitride matrix, the entire heterostructure exhibits sharp crystalline quality and interface boundaries without significant defects or distortions. The systems demonstrate significant progress towards hybridization of metal-nitride VAN nanocomposite, surprisingly forming the vertically aligned geometry comparable to the wire metamaterials for many possible optical applications. As shown from Figure 1.56, the combination of Au and transition metal nitride generates enhanced SERS effect

and SHG signal. In addition, the overall mechanical integrity has been improved significantly, which is comparable to single-phase transition metal nitrides while much greater than pure Au. This work presents a starting point for many possible metal-nitride combinations and tunabilities. In the following chapters, we will discuss each of the projects individually, from the motivation, nanostructure exploration, unique multi-properties, towards the device-driven functionality demonstrations. Before that, an overview of all the experimental results will be covered in the next chapter.

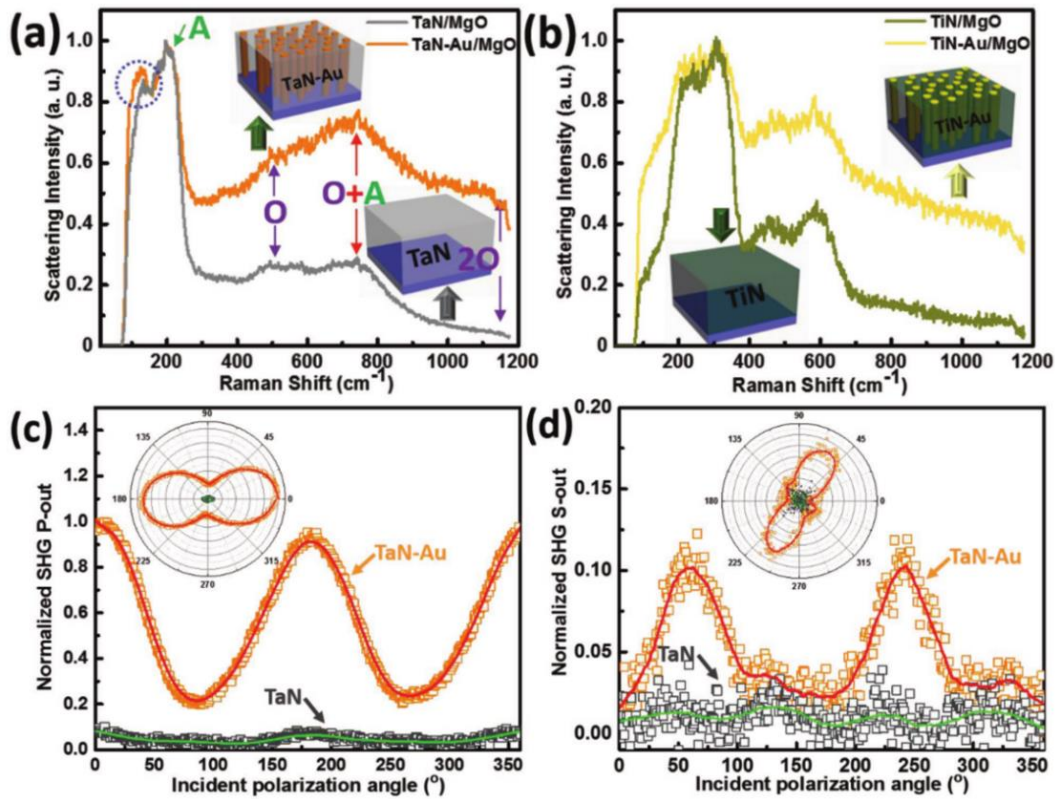


Figure 1.56 Raman scattering data of (a) TaN and Au-TaN thin films grown on MgO, (b) TiN and Au-TiN thin films grown on MgO. (c) P-pol output and (d) s-pol output SHG signals with inset showing the polar plots of TaN and Au-TaN nanocomposite thin films.<sup>[59]</sup>

## 2. EXPERIMENTAL TECHNIQUES

This chapter provides the technical details involved in experimental processes, including (1) fabrication: pulsed laser deposition (PLD), (2) structure characterizations: X-ray diffraction (XRD) and transmission electron microscopy (TEM), (3) property characterizations: ellipsometry, UV-Vis spectrophotometer, and physical property measurement system (PPMS). There are indeed other measurements involved such as photoluminescence, Fourier transform infrared spectroscopy (FTIR), Raman scattering. These will not be emphasized here but will be briefly introduced in the next few chapters.

### 2.1 Pulsed Laser Deposition

PLD technique has already been discussed in the previous sections when we introduce method of growing nanocomposite thin films, and potentially this technique can be applied as an alternative way for fabricating optical metamaterials. Specifically, the equipment being used is a Neocera deposition chamber with a krypton fluoride (KrF) laser (Lambda Physik Compex Pro) at wavelength of 248 nm. Here, the ultraviolet laser source necessitates the high energy beam being focused and bombard target elements with high kinetic energy. Figure 2.1 shows the chamber setup as well as a rough illustration of the inner part. The heating stage and target surface are aligned along vertical axis, which means the substrate is facing downward and laser plume is bombarded upward for deposition, as zoomed in on the right side of the figure. The system can be upgraded as shown in Figure 2.1 (b), external *in-situ* monitoring accessories such as reflection high-energy electron diffraction (RHEED) can be installed to monitor the surface crystallinity during the deposition. As introduced previously, the laser beam is focused at an angle of  $45^\circ$  on the target surface with energy density that can be controlled (normally around  $3 \text{ J} \cdot \text{cm}^{-2}$ ). The chamber can be pumped to less than  $1.0 \times 10^{-6}$  mbar and gases such as  $\text{O}_2$  or  $\text{N}_2$  can be flown with controlled pressure. Compare to conventional PLD chamber, this Neocera chamber allows additional automated or programmable functions such as cooling sequence, the laser bombardment mode, as well as substrate rotation. Depending on specific growth recipes, parameters such as laser energy, frequency, and substrate-target distance can be tuned.

Conventional target preparation uses mechanical sintering and annealing. Specifically, we need to calculate specific concentration between A and B chemical compounds, based on their molar mass and density. Next, the powder containing A and B are mixed together and pressed using mechanical die pressing and annealed under high temperature. The hardness, density and purity are difficult to control and could be varied depending on different recipes. A relative tricky way is to directly stick a piece of metal foil onto the target surface which is extremely beneficial for growing unstable metals with ceramic oxide or nitride phase. But it has some limitations as well. Additionally, a more advanced method of sintering is called spark plasma sintering (SPS) which is an electric field assisted sintering method with controlled sequence and gas flow.

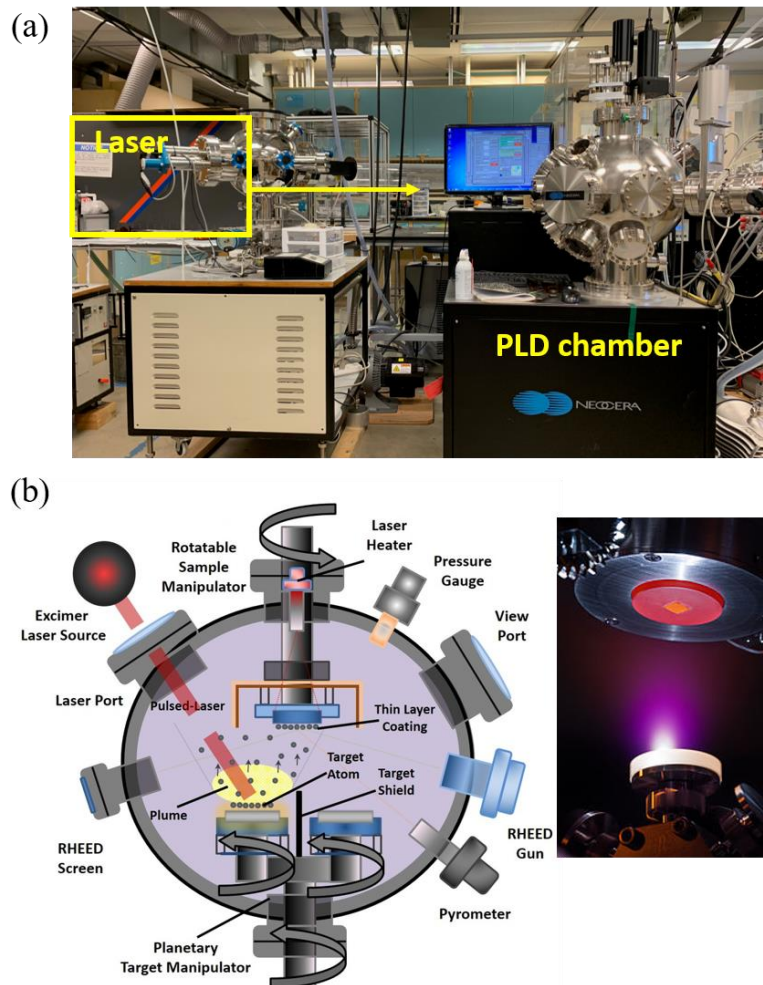


Figure 2.1 (a) Experimental setup of the PLD chamber and laser. (b) Schematic illustration of chamber configuration, and a zoomed area showing the laser plume and substrate surface.

## 2.2 X-Ray Diffraction

XRD is one of the most popular tools in material sciences whenever information of crystallinity needs to be collected. This technique can be applied to a broad range of materials such as thin films, bulk crystals and powders. X-ray is considered as electromagnetic radiation with high energy, when an incoming beam shining on the sample, it causes elastic scattering of the electrons, either as constructive interference or destructive interference. When the Bragg's condition is satisfied, we see constructive interference and reflection occurs. The Bragg's law is described as:

$$2d\sin\theta = n\lambda$$

. As shown from Figure 2.2,  $d$  is the interplanar spacing,  $\theta$  is angle of incidence,  $n$  is an integer and  $\lambda$  is the wavelength of the X-ray beam. The specific system being used is the Panalytical X'Pert X-ray diffractometer (Figure 2.3) with Cu  $K_\alpha$  radiation at 1.5406 Å. The sample is mounted on a goniometer which can change z-height, chi and phi angles for alignment of the specific crystalline orientation. This system allows multiple measurement types, including the basic  $\theta$ - $2\theta$  scans to determine crystallinity of the film, phi scan for studying in-plane symmetries and texture, as well as reciprocal space mapping (RSM) for determining the three-dimensional strain property.

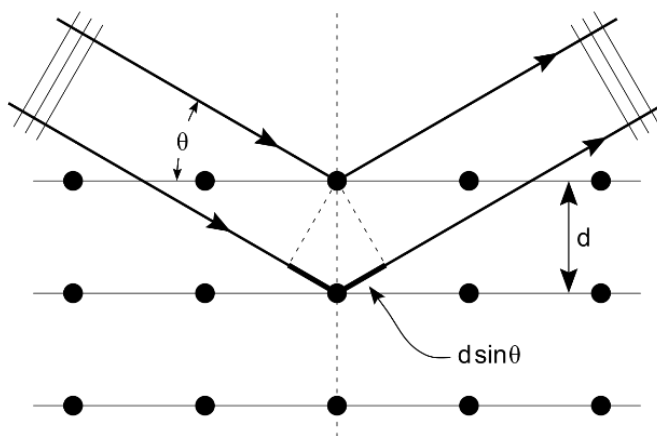


Figure 2.2 Diffraction of X-ray onto the crystalline lattice plane.



Figure 2.3 Panalytical X'Pert X-ray diffractometer, inner part of the goniometer, X-ray source and detector.

### 2.3 Transmission Electron Microscopy

TEM is the most crucial part for the nanocomposite thin films since morphology is critical and atomic scale analysis helps to understand the growth mechanism. The TEM we use is the FEI Talos F200X which is capable to perform HRTEM, STEM, energy dispersive X-ray spectroscopy (EDS) and additional capabilities such as *in-situ* heating, tomography and crystalline orientation mapping (ASTAR). These functions are extremely beneficial for nanomaterial structure characterizations. The Talos F200X system offers isolated operation which means the complete operation can be done separately where the sample can be visualized on the computer instead of the fluorescence screen in the conventional TEM system. It is beneficial if the column is installed at a cool and isolated room, noises or electromagnetic oscillations can be minimized to reduce the drifting and to improve the image acquisition.

In general, the TEM consists of three key components: the illumination system, the objective lens/stage and the imaging system. An electron beam with high acceleration energy being transmitted through the ultra-high vacuum column as either convergent or parallel mode onto the specimen surface which is electron transparent. Next, the information from the sample is collected by the detector or camera, for example, charge-coupled device (CCD) detectors. The column above and below the specimen are shown in Figure 2.5 and 2.6, respectively, details can be found in the book written by Williams and Carter. The Talos F200X module offers smooth switching between

TEM and STEM mode, which helps to analyze different samples as desired. For advanced STEM systems, additional spherical and chromatic aberration correctors are installed to enhance the resolution of the imaging.



Figure 2.4 Talos F200X TEM.

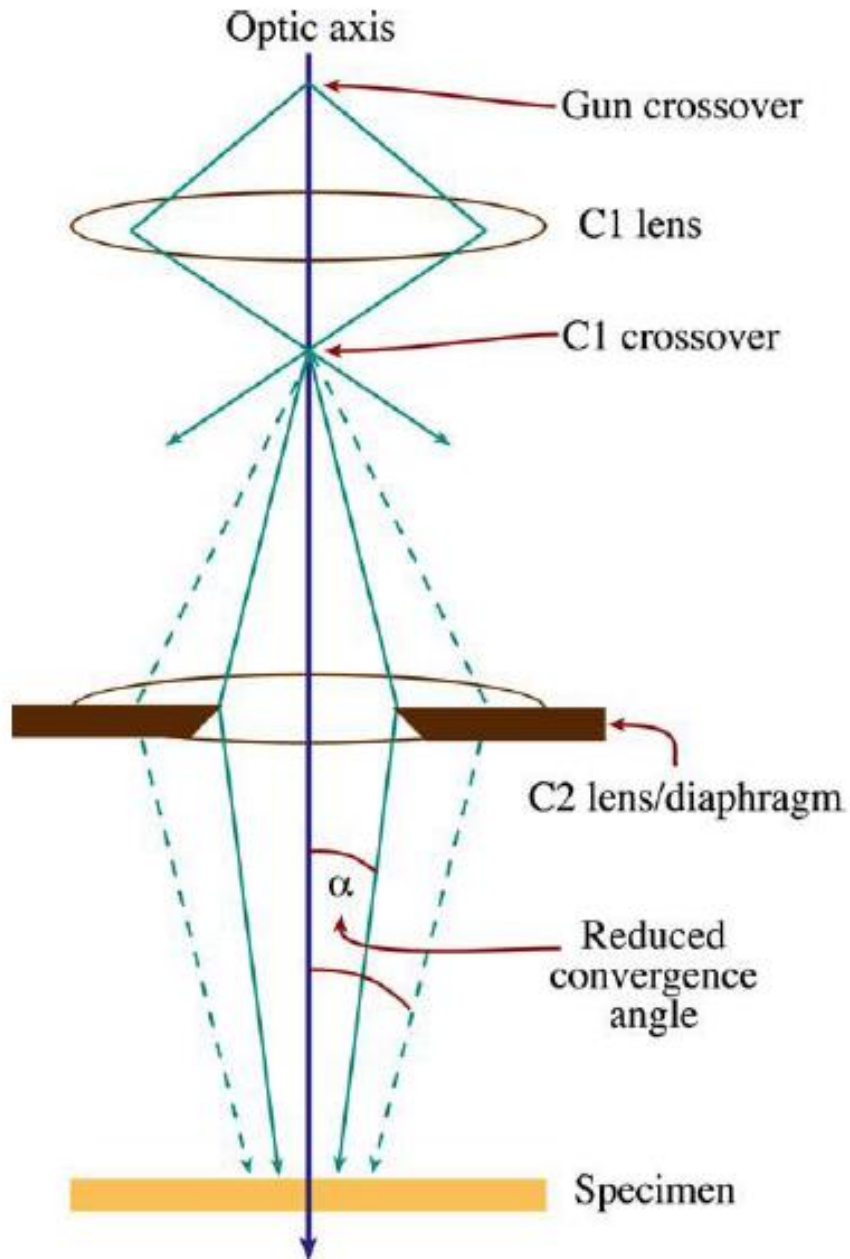


Figure 2.5 A typical two-lens (C1, C2) column of TEM, C2 aperture can change the beam convergence angle.

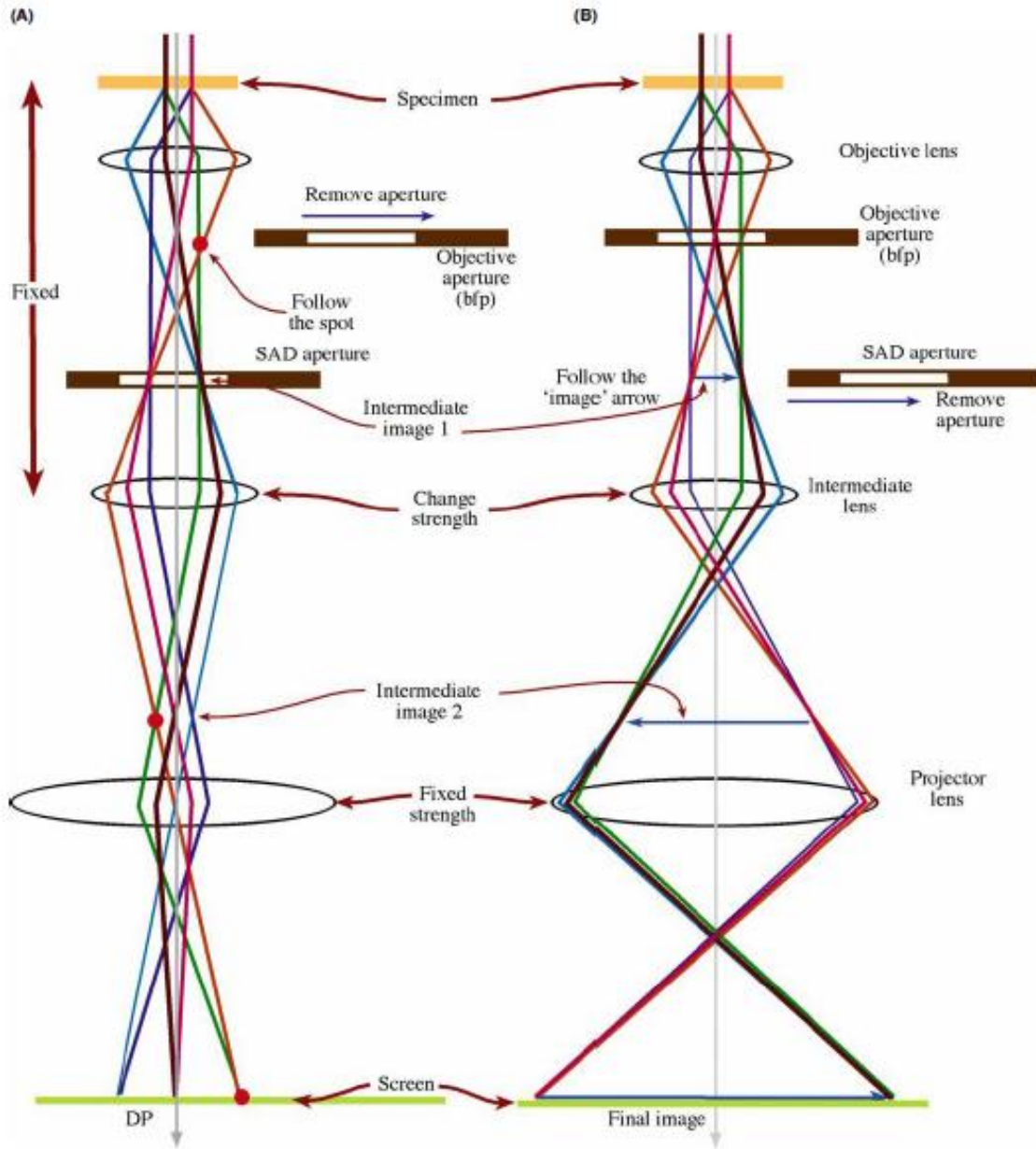


Figure 2.6 Two types of operations of TEM including (a) diffraction mode (projection of diffraction patterns) and (b) image mode (projection of image onto the screen).

One prerequisite for good TEM imaging is the sample preparation. Thin specimen can be prepared via conventional mechanical polishing method, or focused ion-beam method. Though mechanical polishing seems tedious and challenging, it provides some advantages such as less beam damage. However, when treating with soft samples or sensitive samples, FIB can be a preferable method for fast output. For most of ceramic nanocomposite thin films, the conventional method was applied most of the time, which involves grinding, dimpling and ion milling (PIPS

691 precision ion polishing system, 4.0 keV) until a hole is formed, the electron transparent areas can always be found close to the holes.

## 2.4 Ellipsometry

Spectroscopic ellipsometry is a fundamental optical characterization tool. However, direct measurement of electromagnetic parameters is not available. Instead, ellipsometry collects amplitude ratio  $\Psi$  and phase difference  $\Delta$  as function of wavelength and incident angles. The incident light impinges onto the sample, and its original polarization is modified and changed to “elliptical” after reflection from the surface. Next, a model is built to fit the measured parameters, under a desired fitting mean square error (MSE), the results are reliable to retrieve the dielectric functions or optical constants such as  $n$  and  $k$  values based on the model.

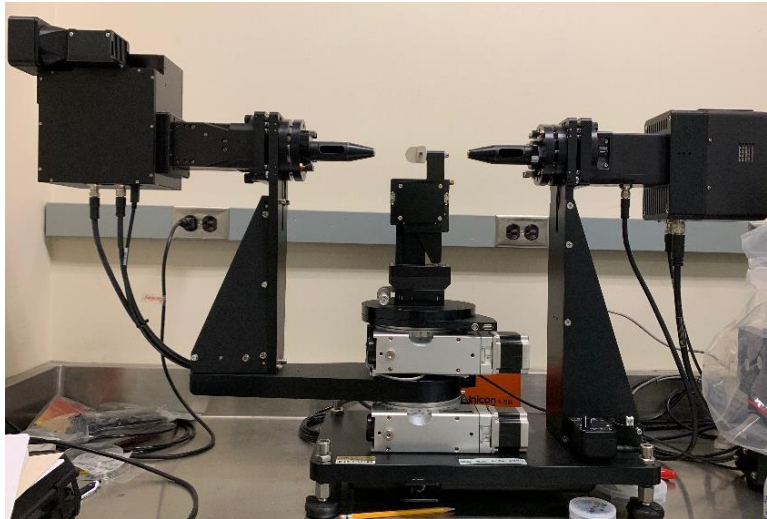


Figure 2.7 RC2 ellipsometer with vertical configuration (J.A. Woollam co. inc).

RC2 (J.A. Woollam co. inc) ellipsometer (Figure 2.7) with a vertical measurement setup is capable to integrate all wavelengths from 210 nm ~ 2500 nm at one time which means one measurement can be done within few seconds. It has focusing probes installed at the incoming and receiving sections such that the beam size will be reduced sufficiently for measuring small samples. Besides, it can perform intensity measurements such as angular dependent transmittance and reflectance, auxiliary functions such as heating / cooling stage are available as well. The tool brings huge advantages to optical-based nanocomposite thin film studies. For most of the measurements,

signals at incident angle between  $55^\circ \sim 75^\circ$  are maximized since the ellipsometry is performed in reflection mode.

Data fitting is the trickiest part, the measurement can be done within few minutes while retrieving reliable optical constants takes more than few hours. Depending on the dielectric property, three models can be considered including Cauchy, Gen-Osc or B-spline. Cauchy applies to dielectric or insulating materials, but in most of the nanocomposite thin films, the latter two models are more favored. Gen-Osc contains a set of oscillators with built-in functions such as Lorentz, Harmonic, Gaussian, Drude, or the Tauc-Lorentz and Cody-Lorentz. Each of these oscillators has its own functions in calculating the dielectric functions and follows the Kramers-Kronig (K-K) consistency. Essentially, by combining different Gen-Osc functions a desirable fitting can be obtained. B-spline is a relatively simple and newly developed method, it is defined as a series of nodes with each of the nodes described by a polynomial B-spline function. This method applies to most of the absorbing layers, for example, when metallic material is involved. It provides a much easier way as compared to Gen-Osc and K-K consistency can be applied to improve the accuracy of the data fitting. Detailed theoretical description can be found elsewhere (Cheney and Kincaid, "Numerical Mathematics and Computing," Third Edition, Brooks/Cole Publishing Company 1994). The RC2 ellipsometry has its own software package CompleteEASE which contains huge materials library and different fitting options. For example, information such as surface roughness, gradient film, automatic model optimization can be applied to acquire optimized results. The MSE value and errors represent the accuracy of the data fitting, in general,  $1 < \text{MSE} < 5$  indicates a desired match.

## 2.5 UV-Vis Spectrophotometer

The ultraviolet-visible (UV-Vis) spectrophotometer measures the light transmittance, reflectance or absorption of a wide range of materials including thin films, bulk and chemical solutions. It has been widely applied for analytical chemistry analytes or to determine the bandgap of semiconductors. The Lambda 1050 UV-Vis Spectrophotometer (Figure 2.8) can capture a wavelength range from 175 nm to 3300 nm with resolutions of  $\leq 0.05$  nm (UV-Vis) and  $\leq 0.2$  nm (NIR). The whole system consists of a light source (tungsten-halogen and deuterium), monochromator (chopper), beam splitter, and multiple detectors that include photomultiplier R6872 for UV-Vis regime, InGaAs for 860 nm to 1800 nm and a PbS detector for NIR range. The

module can be further upgraded with integrated spheres for measuring total reflectance or diffuse reflectance.

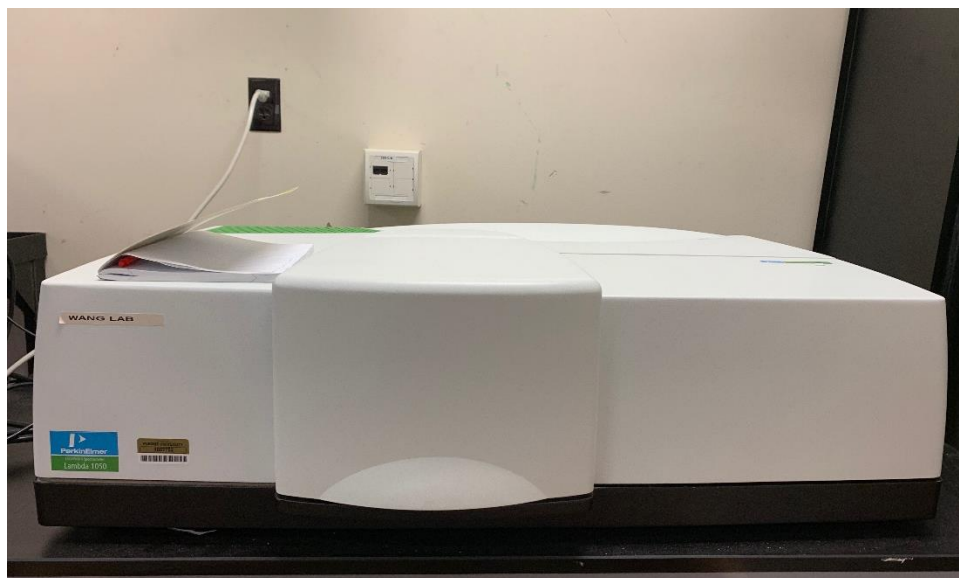


Figure 2.8 UV-Vis Spectrophotometer (PerkinElmer Lambda 1050).

For measuring transmittance spectra of thin film samples, the substrate crystal requires double polishing to ensure no scattering from the backside. The samples are mounted vertically facing the incoming beam at  $0^\circ$  incidence, and a reference substrate crystal will be mounted in parallel facing the reference beam such that data collected from the substrate will be subtracted.

## 2.6 Physical Property Measurement

The physical property measurement system (PPMS, Figure 2.9) is an extreme versatile characterization tool that is capable for electrical transport option (ETO) for collecting current voltage (I-V) curve or resistance, vibrating sample magnetometer (VSM) for collecting magnetic properties, thermal transport option, and the ferromagnetic resonance (FMR) spectroscopy. ETO and VSM modes are used more often. For example, a resistance (R) versus temperature (T) curve is one common measurement that contains many useful information such as the (super-) conductivity, magnetic field can be further applied to capture any magnetoresistance (MR) property. Additionally, ETO is capable to perform Hall measurements to explore charge carrier information, due to the definition of Hall potential, the voltage needs to be aligned perpendicularly

to the current. The standard 4-wire connection for R-T and Hall measurement is shown in Figure 2.10, a maximum of two samples (two channels) can be measured at the same time. If one desires to measure high-quality magnetic hysteresis loop, MPMS (magnetic property measurement system) is recommended because the SQUID (superconducting quantum interference device) magnetometer ensures accurate data acquisition with high sensitivity ( $\leq 10^{-8}$  emu) to temperature and magnetic field.



Figure 2.9 The PPMS system from Quantum Design.

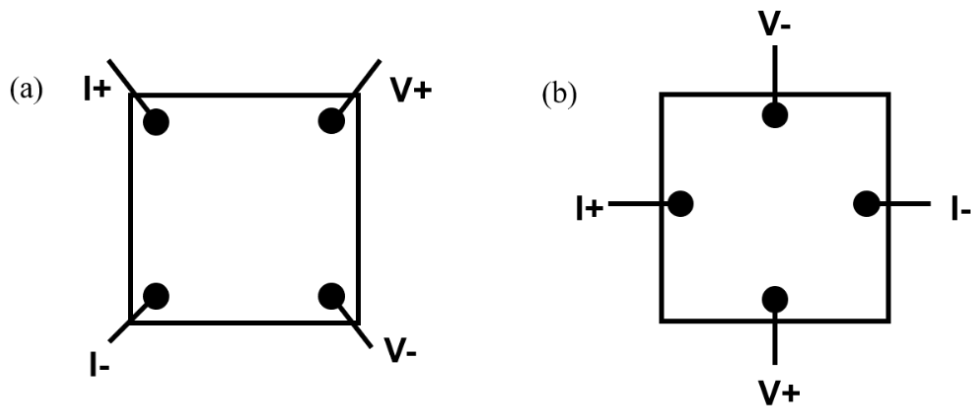


Figure 2.10 Four-wire setup for (a) typical resistance measurement, and (b) Hall measurement.

### **3. HYBRID PLASMONIC GOLD – TITANIUM NITRIDE VERTICALLY ALIGNED NANOCOMPOSITE: A NANOSCALE PLATFORM TOWARDS TUNABLE OPTICAL SENSING\***

#### **3.1 Overview**

Plasmonic nanostructures realize optical confinement at nanometer scale with structural tunabilities for desired applications. In this work, we present a hybrid plasmonic thin film platform: i.e., Au nanopillar arrays grown as vertically aligned inside a TiN matrix with controllable Au density. Compared to single phase plasmonic materials, the presented tunable hybrid nanostructure attains optical flexibility in terms of resonant peak shifting and a change on surface plasmon resonances (SPRs) at UV-Visible range, which is confirmed by numerical simulations. The tailorable hybrid platform realizes gradual tuning of the optical constants and plasma frequencies, as well as reduced losses in the near infrared regime, all with the same TiN composition. Our results on surface enhanced Raman (SERS), photoluminescence (PL) signals and chemical sensing by Fourier-transform infrared spectroscopy (FTIR) demonstrate enormous potential for tunable optical-based chemical sensing applications using these designable hybrid nanostructures.

#### **3.2 Introduction**

Plasmonic effects offered by metallic nanostructures in subwavelength scale enable strong light confinement or directional light routing that are unprecedented from their bulk counterparts.<sup>[125]</sup> Applications using such phenomena include plasmonic waveguides<sup>[126-127]</sup>, enhanced light trapping in photovoltaics<sup>[18, 128]</sup>, photocatalysis<sup>[129-130]</sup>, bio-medical sensing<sup>[131-132]</sup>, and metal-dielectrics for different metamaterial designs (e.g. hyperbolic metamaterial, negative-indexed metamaterial, etc.).<sup>[51, 102, 133-135]</sup> Specifically, taking advantage of plasmonic metallic nanostructures, localized surface plasmon resonance (LSPR) imaging and surface enhanced Raman scattering (SERS) overcome the detection limit of conventional spectroscopies<sup>[136]</sup> in biological and chemical sensing and even allow single-molecule-level detection.<sup>[137-139]</sup> Reported

---

\* This chapter is reprinted with permission from “Hybrid plasmonic Au–TiN vertically aligned nanocomposites: a nanoscale platform towards tunable optical sensing” by X. Wang, et al., *Nanoscale Adv.* **2019**, *1* (3), 1045-1054.

studies include the *in vivo* biological embryos evolution, membrane transport detections and tumor targeting using plasmonic nanoparticles.<sup>[137, 139]</sup> In addition, plasmonic nanostructures coupled to dye molecules and thin-film semiconductor layers enable enhanced light capturing or light emitting efficiency, which is promising for solar energy conversion, light-emitting devices and more applicable opportunities.<sup>[18, 140]</sup>

A key aspect in the field of plasmonic nanostructures is to manipulate light-matter interactions for optical tunability. Such tunability, achieved by tailoring the dimension, geometry and concentration of the metallic nanostructures, helps to meet crucial control requirements for photonic devices, such as resonant frequency, polarization angle or propagation directions.<sup>[141]</sup> For example, Lee *et al.* demonstrated Au and Ag nanoparticle and nanorod assemblies and tailorable plasmonic resonance frequency and bandwidth.<sup>[132]</sup> Other nanostructures including nanocubes, quasi-sphere, and pyramids, have also been explored for enhanced LSPR effects at specific optical range.<sup>[142]</sup> Considering the device applications using metallic plasmonic materials (e.g. Au, Ag, Al, Cu), additional key aspects to be addressed are the thermal and mechanical stabilities, materials compatibility and optical losses.<sup>[102, 143]</sup> To this end, new plasmonic materials such as transition metal-nitrides (i.e. TiN, TaN, et al.) have been demonstrated as low-loss plasmonic candidates with comparable optical properties to noble metals (i.e. Au and Ag), but more mechanically and thermally stable.<sup>[114, 116, 118, 144]</sup>

Indeed, the current research direction is driven to metamaterial design, coupling plasmonic nanoresonators with different components, either plasmonic or dielectric.<sup>[56, 61, 126, 145]</sup> For example, the optical losses can be compensated by dielectric gain media for low-loss plasmonics; meanwhile, enhanced plasmonic sensitivity (Fano-resonances) were reached at a specific frequency.<sup>[146]</sup> As described, hybrid plasmonic design is a straightforward approach to compensate losses from conventional noble metals. In terms of manipulating light-matter interactions, metamaterials offer novel functionalities such as hyperbolic transition<sup>[51]</sup>, epsilon near zero (ENZ) and double negative properties (DNG).<sup>[126],[143, 147-149]</sup> Currently, structures including split-ring resonators<sup>[150]</sup>, double-fishnet<sup>[134]</sup>, and periodic nanorod/nanowire assemblies<sup>[151]</sup> down to few nanometers can be fabricated by electron beam lithography (EBL)<sup>[150]</sup>, focused ion beam (FIB)<sup>[152]</sup>, and/or with the combination of self-assembling growth methods including physical vapor deposition (PVD)<sup>[56, 151]</sup> and template assisted growth<sup>[142, 153-155]</sup>.

In this work, a novel metal-nitride plasmonic material design with tailorable microstructures is presented as a tailorable hybrid material platform for tunable optical properties. The self-assembled hybrid film consists of high density, well-distributed vertically aligned Au nanopillars in the low loss titanium nitride (TiN) matrix. Both Au and TiN are plasmonic materials with plasmonic responses in neighboring wavelength regimes. Different from the previous work on Au - TaN system<sup>[144]</sup>, here, we effectively controlled the Au nanopillar density, i.e. inter-spacing of the nanopillars, and thus to tune the metasurface morphology. Such tailorable hybrid thin film is expected to change the charge carrier distributions and optical properties effectively. Compared to the nanopillars (nanowires) grown by solution-based or CVD-based methods, which typically present random pillar arrangements, this self-assembled metal-nitride hybrid material platform serves as a new route in realizing hybrid plasmonic materials with well-controlled pillar morphology and density tuning. Taking advantage of such tunable Au-TiN hybrid plasmonic material, potential applications as molecule sensing based on Fourier-transform infrared spectroscopy (FTIR) measurement, enhanced Raman scattering, and enhanced photoluminescence (PL) signal have been demonstrated.

### 3.3 Results and Discussion

To verify the overall 3D nature of the Au nanopillars in the TiN matrix, a set of transmission electron microscopy (TEM) study has been conducted on both the plan-view and cross-section TEM specimens for three different Au nanopillar densities. As shown in Figure 3.1, the Au nanopillars are growing vertically and uniformly in the TiN matrix for all cases, following the trend as marked (dashed lines) in the inset plan-views images (a-c). The Au-TiN nanocomposite grown by the one step growth method provides the advantage of growing high crystalline nanopillar assemblies with confined diameters (average diameter of 6 nm). Selected Area Electron Diffraction (SAED) patterns are displayed as inserts in Figure 3.1 (d-f), from which a cube-on-cube epitaxy is confirmed for both Au and TiN phases on MgO substrates. The two phases are well separated with sharp interfaces in between. Based on the surface energy of the phases and the substrates, Au nucleates on MgO as the Volmer-Weber (VW) island and TiN nucleates as Stranski-Krastanov (2D + 3D) mode, respectively.<sup>[68]</sup> Such two-phase growth has been reported previously<sup>[56, 144]</sup>.

A schematic illustration on the vertically aligned nanocomposite (VAN) self-assembling process is described in Figure 3.2. As evidenced from the plan-view images (a-c), the nanopillar dimension and pillar spacing interplays with each other, and the overall volume fraction of the Au nanopillars maintains a gradual increase with the increase of Au density, a detailed quantification is summarized in Figure 3.3, the number per  $\text{cm}^2$  as well as the diameter of the Au nanopillars are calculated based on low magnification plan-view TEM images with an average of 80 nanopillars being quantified.

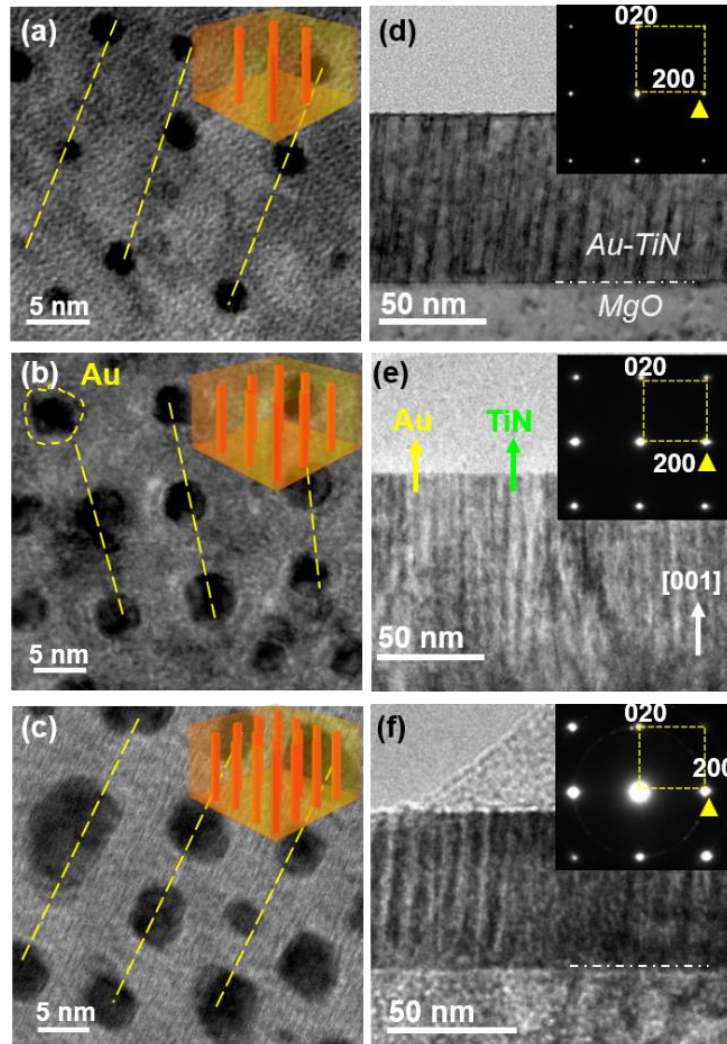


Figure 3.1 3D microstructure of Au-TiN nanocomposites grown on MgO substrates with tailored Au density. (a-c) Plan-view TEM images from top projections. (d-f) Cross-sectional TEM images and their diffraction patterns (insets) from  $\langle 100 \rangle$  zone axis.

To verify phase distribution and lattice matching of the hybrid thin film, an Au-TiN sample with a lower Au density has been selected for a detailed scanning TEM (STEM) study and the results are shown in Figure 3.4. The STEM images taken under the high-angle annular dark-field (HAADF) mode from both plan-view (3.4a) and the cross-section (3.4c) reveal a very clear contrast between the Au nanopillars and the TiN matrix, where the contrast is proportional to  $\sim Z^2$ , i.e., the Au nanopillars show a much brighter contrast than that of TiN because of the high Z number.

In addition, the Au nanopillars grow all the way to the top film surface with very sharp interface and very straight pillar structure. The average pillar diameter for the selected sample is 3 nm. More interestingly, the distribution of the nanopillars follows a certain degree of ordering in-plane (a hexagonal-close-packed-like arrangement), with an average inter-pillar spacing of 10 nm. Such arrangement of the Au nanopillars could be preferred for well-distributed pillar spacing and density, as well as to balance the in-plane-strain between the Au and TiN phases on the underlying substrate. As evidenced from Figure 3.4 (d), both atomic model (inset) and the HRSTEM image show that the Au/TiN interface transitions are relatively smooth without any obvious misfit dislocations or strain contours, which demonstrates a nearly 1:1 lattice matching between Au and TiN.

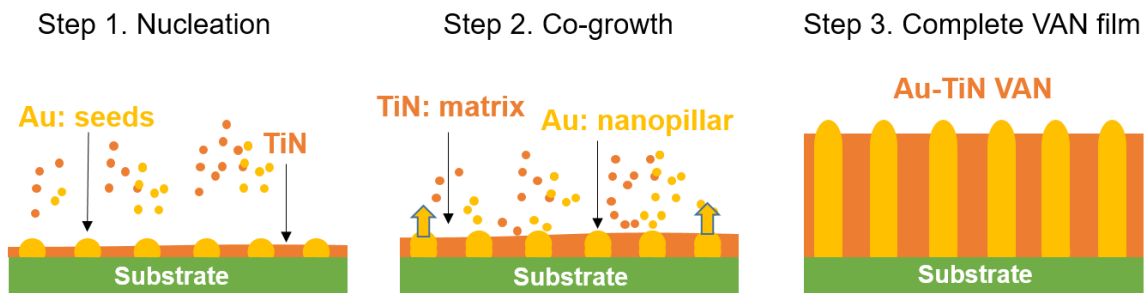


Figure 3.2 Growth mechanism of Au-TiN VAN. Step1: Au nucleation as islanded seed layer. Step 2: TiN and Au co-growth, TiN forms the matrix layer and Au nucleates on top of the seeds. Step 3: Completed VAN film, with smooth surface and protruded Au nanopillars.

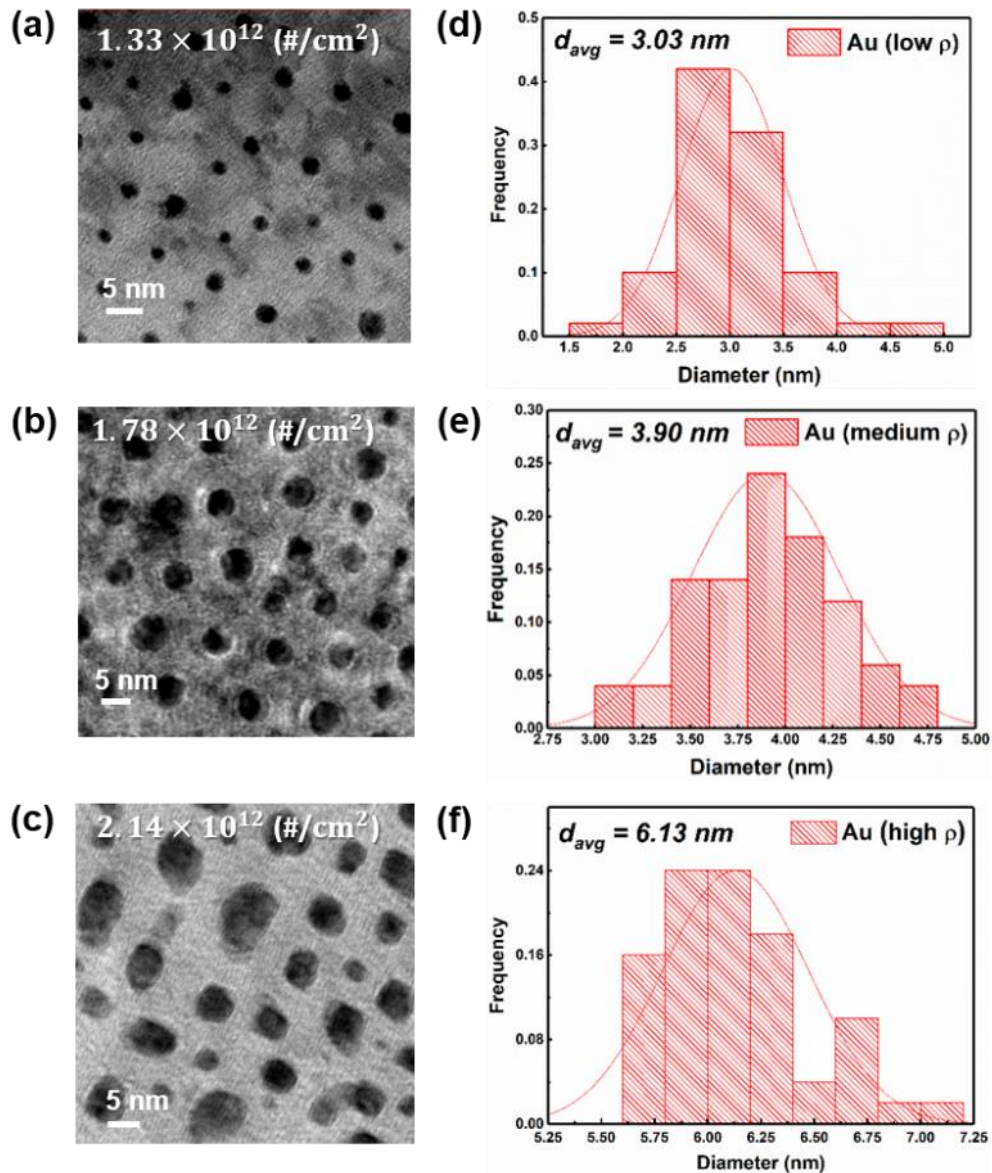


Figure 3.3 Quantification. (a-c) Plan-view TEM images and their calculated density expressed by number of nanopillars per centimeter square ( $\text{\#/cm}^2$ ). (d-f) Quantified Au dimension bar plots, which indicate nanopillar widening as Au density increases.

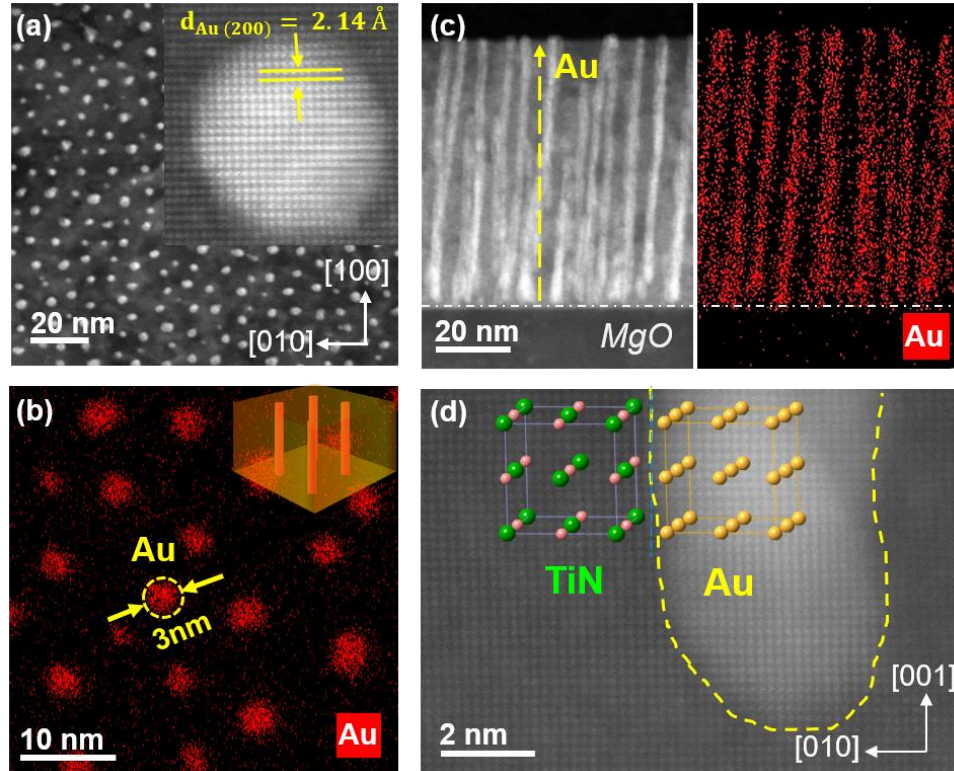


Figure 3.4 Microstructure analysis of low-density Au-TiN VAN. (a) Plan-view STEM image and high resolution of Au nanopillar at top projection. (b) EDS mapping plan-view sample. (c) Cross-sectional STEM and EDS mapping. (d) Cross-sectional HRSTEM at Au/TiN interface and the atomic model.

The overall growth orientation and film crystalline quality have been further explored by X-ray diffraction (XRD). Figure 3.5 (a) shows the  $\theta$ - $2\theta$  scans of all the films grown on (001) MgO substrates, and it is obvious that both Au and TiN phases are oriented along (00 $l$ ) with a nearly perfect lattice match ( $< 1\%$  strain). Two phenomena are observed by comparing the Au-TiN samples with various Au compositions. First, the full-width at half maximum (FWHM) value of the TiN phase gradually increases with the increase of Au density, meanwhile (002) TiN peak is maintained close to its bulk value ( $2\theta_{(002)\text{TiN}} = 42.595^\circ$ ). On the other hand, as the Au nanopillar density increases, the (002) Au peak shifts left, approaching its bulk value of  $44.363^\circ$ . These observations suggest a strong vertical strain coupling between TiN and Au for the lower Au density cases. The  $\phi$  scans (Figure 3.5b) from Au, TiN and MgO (220) planes suggest an obvious cube-on-cube relationship without any in-plane lattice rotation, which is consistent with the SAED patterns in Figure 3.1. Such epitaxial nanocomposite thin film growth is also realized on  $c$ -cut

sapphire substrates, as confirmed by the XRD results in Figure 3.5, with films dominated in (111) orientations.

To explore the tunable optical properties of these Au-TiN hybrid thin films with different Au nanopillar densities, normal incidence specular transmittance and reflectance spectra were collected in the wavelength range from 200 nm to 850 nm. An optical model was built using the *COMSOL Wave Optics* software package to retrieve the spectral responses and electric field maps for Au-TiN nanocomposite films with varied Au densities, and, to compare with the reference samples (pure TiN and pure Au films). Typical plasmonic resonances for pure TiN and Au are located at 375 nm and 500 nm, respectively. By adding Au nanopillars into the TiN matrix, the resonance peak of the nanocomposite exhibits a red shift gradually as the Au nanopillar density increases. From Figure 3.6 (a,b), the measured transmittance spectra (Figure 3.6a) are generally in a good agreement with the simulated results (Figure 3.6b), despite the facts that the peak separation is less obvious and the intensity drops due to defects in the Au-TiN nanocomposites. Depolarized reflectance spectra with  $8^\circ$  incidence are displayed in Figure 3.6 (c). Similarly, the resonance experiences a red shift and the reflectance spectrum experiences an intensity reduction (above a wavelength of  $\sim 450$  nm) as the Au nanopillar density increases, which suggests a stronger absorptance for Au-TiN hybrid nanostructure as compared to the pure TiN.

Surface scattering spectra and back scattering images of pure TiN and Au-TiN samples are coupled in Figure 3.7, which indicate the metasurface are highly smooth, and appreciable specular reflectance in the visible to infrared regime is further proved. Based on the optical measurements, the wavelength of 440 nm is selected to map the electric field (along y direction) distributions of metasurface with three different Au pillar densities (Figure 3.6d). The simulation has been performed with comparable dimensions to the real structure as seen from plan-view TEM images (the upper pane). It is noted that the increase of the Au volume fraction causes enhanced near field interactions at metasurface and the Au/TiN interfaces.

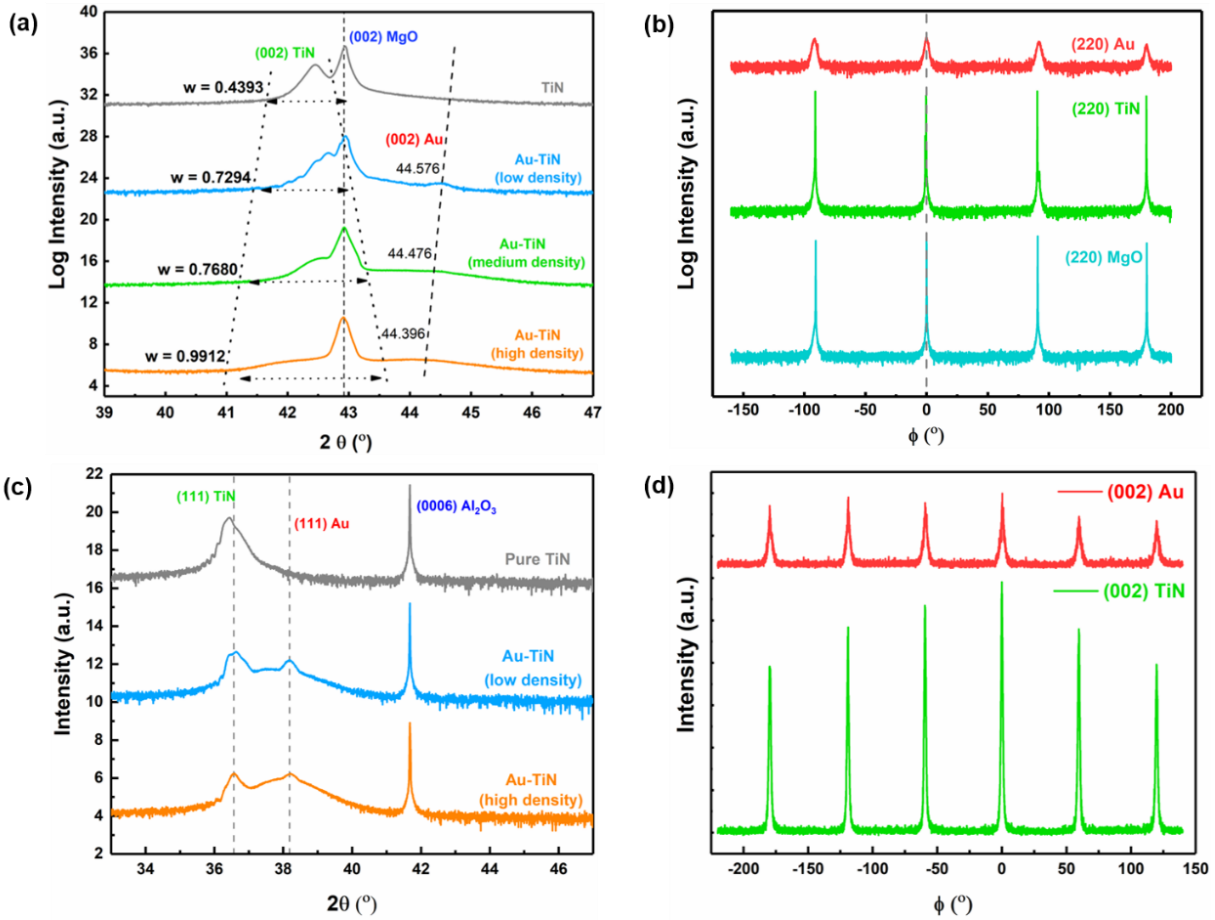


Figure 3.5 (a)  $\theta$ - $2\theta$  scans of density tuned Au-TiN nanocomposites versus a pure TiN for reference. A general widening of (002) TiN peak and continuous increase of (002) d-spacing is observed with increase of Au density. (b) Phi scan of Au-TiN on MgO substrate, indicating a four-fold symmetry without in-plane rotations. (c)  $\theta$ - $2\theta$  scans of the samples grown on (0001) sapphire substrates, the films are oriented as (111) for better lattice match. (d) Phi scan of films grown on sapphire, indicating a hexagonal (six-fold) symmetry of (111) Au and (111) TiN.

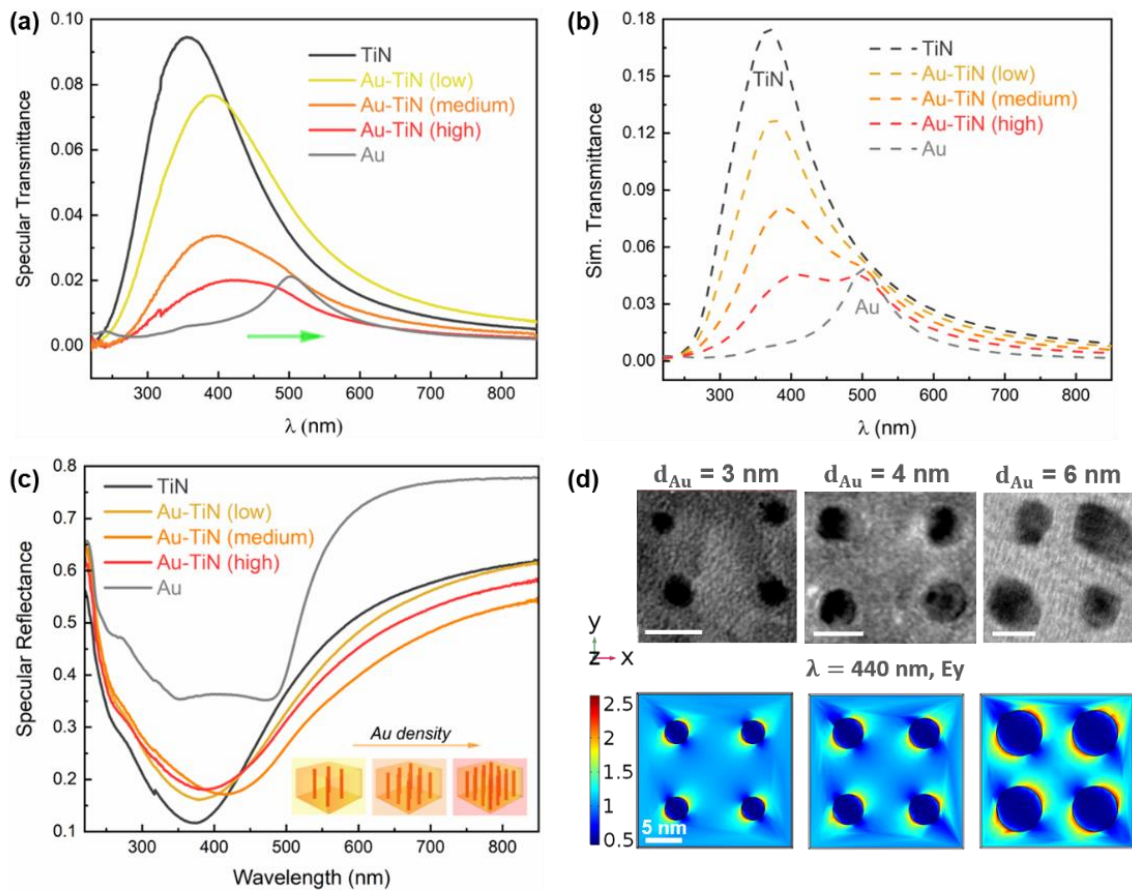


Figure 3.6 Optical spectra and numerical simulations. (a) Measurement and (b) Simulated transmittance spectra with of five samples, including a pure 80 nm Au for reference. (c) Reflectance spectra of five samples. (d) Plan-view TEM images (upper pane) and simulated electric field map at 440 nm of hybrid plasmonic metasurface (lower pane) with three different Au densities,  $d$  is the diameter of Au nanopillar. Scale bar of upper pane represents 5 nm.

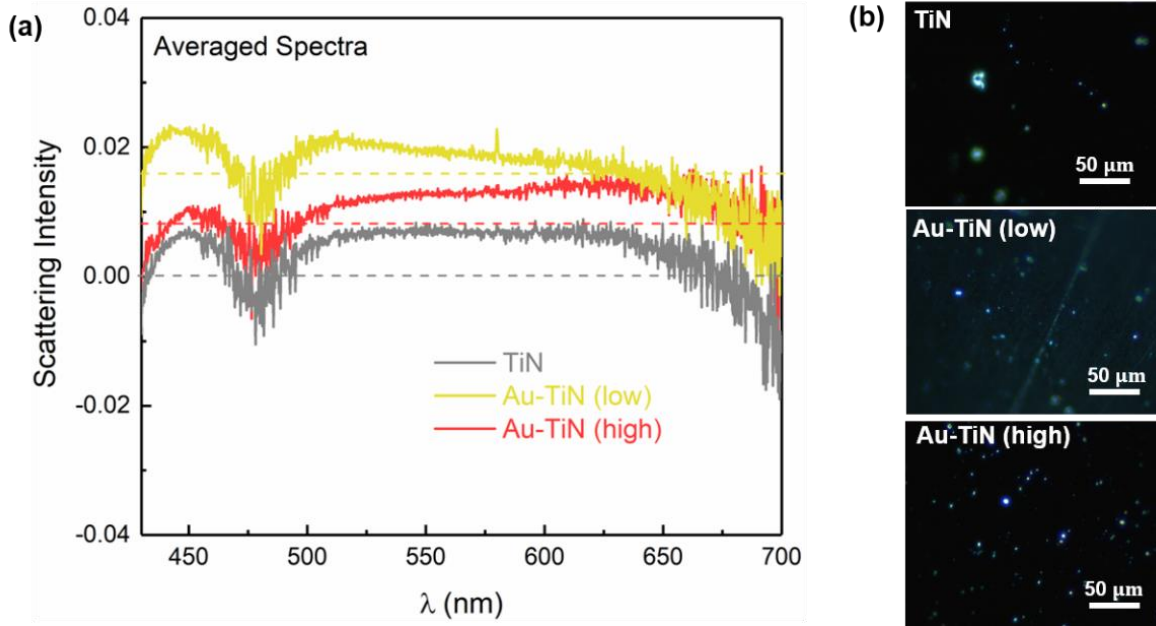


Figure 3.7 Surface scattering spectra. The scattering intensity of the three samples are too low to contribute to any reflectance signals, indicating high specular reflectance from the smooth metasurfaces. (b) Dark-field optical imaging of three thin film samples: pure TiN, low density Au-TiN and high density Au-TiN. The bright spots are attributed to micron-scale surface defects or agglomerations.

The tunable optical parameters as a function of Au nanopillar density were explored by detailed ellipsometry analysis on the films with various Au densities: 11.1 at%, 15.4 at%, 16.7 at% and 28.6 at%, which are confirmed by the EDS composition analysis (Figure 3.8), while the film thickness and nanopillar diameter (6 nm) are comparable. The psi and delta in 200 to 2500 nm range with various incident angles were collected on a 200 nm Au film, pure TiN (80 nm) and Au-TiN hybrid films (40 nm) with four different densities. A B-spline model using the commercial *CompleatEase software package* was applied to retrieve effective parameters of each film and shows a desired match with experimental results (Figure 3.9e-f). The polarized light reflectance intensities of two Au-TiN nanocomposites with high and low Au densities are shown in Figure 3.9(a-d). The resonance of the higher density Au-TiN is broadened and red shifted due to the Au addition. Next, the optical constants were retrieved from the B-Spline model. In addition, the dielectric constant of Au nanopillars from the bulk Au ( $\epsilon_{\text{bulk}}$ ) film is calculated, <sup>[156]</sup>

$$\epsilon_{\text{Au}} = \epsilon_{\text{bulk}} + \frac{i\omega_p^2(R_b - R)}{\omega(\omega\tau + i)(\omega\tau R + iR_b)} \quad R \leq R_b$$

, where  $\omega_p$  ( $13.7 \times 10^{15}$  Hz) is the plasma frequency,  $R$  ( $R=3$  nm) is diameter of Au nanopillar,  $R_b$  (35.7 nm) is mean free path and  $\tau$  ( $2.53 \times 10^{-14}$  s) is the relaxation time for free electrons in bulk Au.

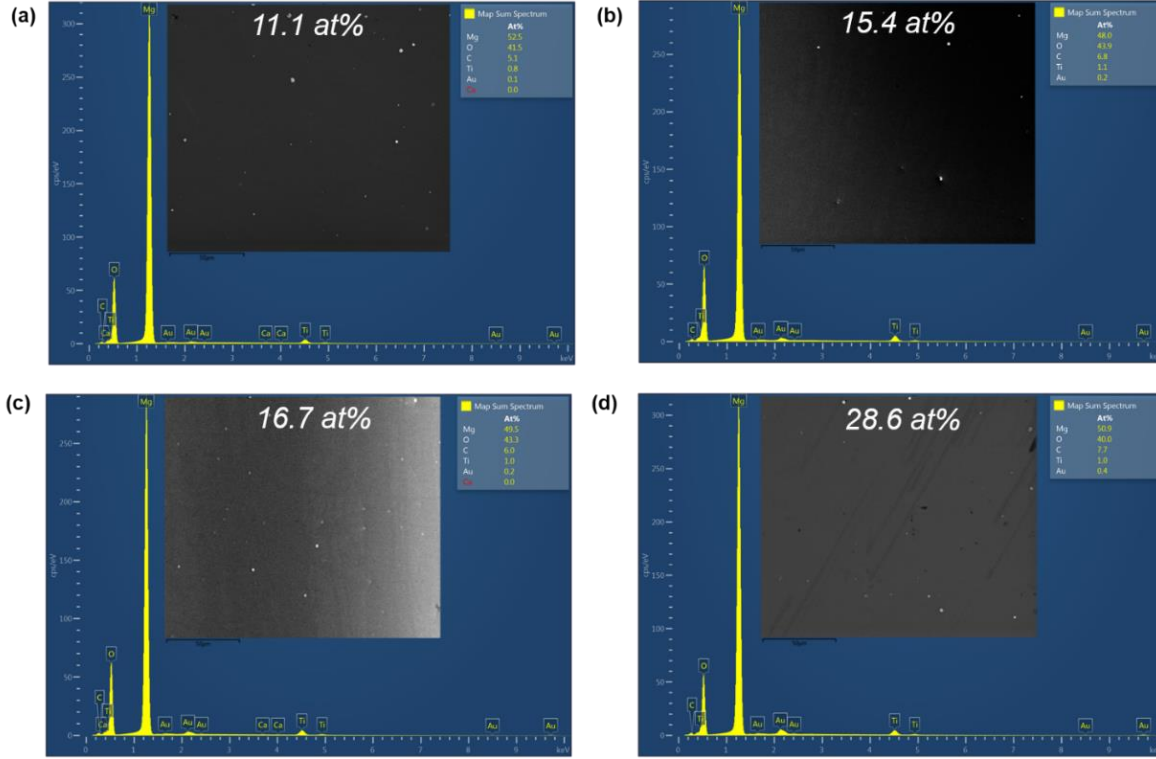


Figure 3.8 EDS mapping of critical elements from a large scale for atomic percentage quantification of Au nanopillars in the TiN matrix. Atomic percentage of elements (Mg, O, C, Ti, Au) are shown at top corner. Insets are SEM images which confirm smooth surfaces of the Au-TiN/MgO samples, with quantified Au densities: (a) 11.1 at%, (b) 15.4 at%, (c) 16.7 at% and (d) 28.6 at%. Au density calculation is carried using:  $\rho_{\text{Au at\%}} = \frac{\text{Au at\%}}{\text{Au at\%} + \text{Ti at\%}}$ .

The complex dielectric functions ( $\epsilon_1$  and  $\epsilon_2$ ) are plotted in Figure 3.10 (a-d) and the corresponding refractive index ( $n$ ) and extinction coefficient ( $k$ ) are shown in Figure 3.9 (g,h), respectively. Consider the Au-TiN hybrid films as homogeneous layer (Figure 3.10a,b), the overall dielectric constant as a function of Au density is gradually tuned towards more negative, which means higher Au density contributes to stronger plasmonic response but meanwhile maintains lower losses (smaller  $k$ ) as compared to pure Au or TiN. Such tuning is more pronounced at higher wavelength range. Interestingly, when the dielectric constants are fitted using the anisotropic model (Figure 3.10c,d), the separation between in-plane (ordinary) and out-of-plane (extra-

ordinary) responses is obvious as compared to pure TiN film (isotropic). Results indicate strong optical anisotropy in Au-TiN hybrid films. Note that the overall trend of in-plane and out-of-plane dielectric constants follow the trends of the isotropic model, i.e., the dielectric constant decreases as the Au density increases. The oscillations of extra-ordinary terms (Figure 3.10) can be correlated to vertical strain coupling effect. As a comparison, the anisotropic dielectric constants using effective medium theory (the Maxwell-Garnett (MG) method) are calculated using:

$$\epsilon_{xx, yy} = \frac{A\epsilon_{Au}\epsilon_{TiN} + (1-A)\epsilon_{TiN}[\epsilon_{TiN} + \frac{1}{2}(\epsilon_{Au} - \epsilon_{TiN})]}{A\epsilon_{TiN} + (1-A)[\epsilon_{TiN} + \frac{1}{2}(\epsilon_{Au} - \epsilon_{TiN})]}$$

$$\epsilon_{zz} = A\epsilon_{Au} + (1 - A)\epsilon_{TiN},$$

where A is the area fraction of the Au nanopillars, which is calculated according to the atomic percentage of Au quantified from SEM,  $\epsilon_{Au}$  and  $\epsilon_{TiN}$  are wavelength dependent dielectric functions of Au and TiN, respectively,  $\epsilon_{xx}$ ,  $\epsilon_{yy}$  are in-plane (ordinary) dielectric constants, while  $\epsilon_{zz}$  is the out-of-plane (extraordinary) dielectric constant. A similar trend of  $\epsilon_1$  has been observed as a function of Au density (Figure3.11).

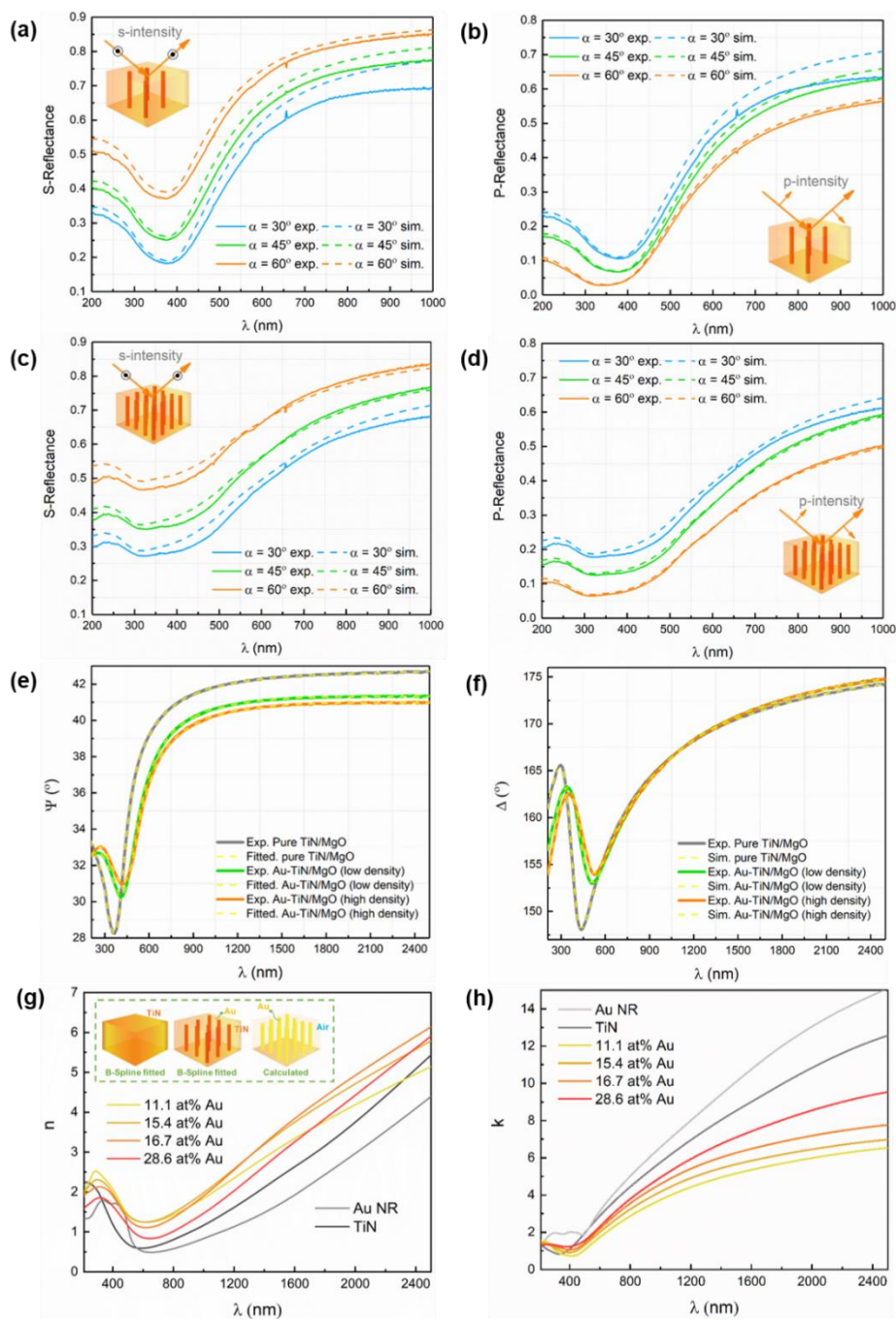


Figure 3.9 Angular dependent reflectance intensities for s- and p-polarized light excitations of (a-b) low density Au-TiN, and (c-d) high-density Au-TiN. (e)  $\Psi$  and (f)  $\Delta$  ellipsometric and fitted parameters of pure TiN and Au-TiN nanocomposites. (g)  $n$  and (h)  $k$  of Au nanorods (calculated), pure TiN film and four Au-TiN films with different Au densities. The extinction coefficient at higher wavelength range indicates lower losses of Au-TiN hybrids as compared to pure Au or TiN films.

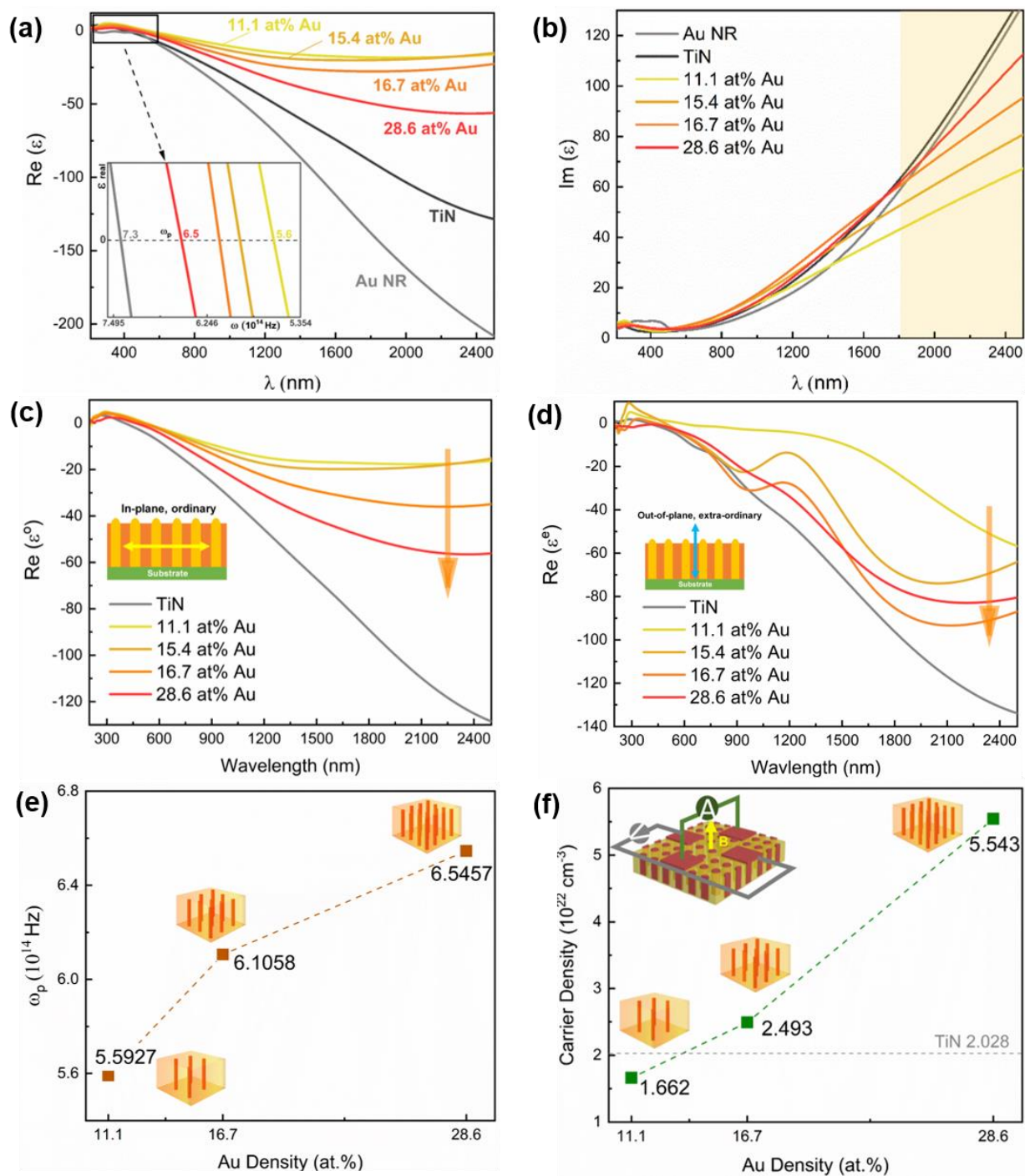


Figure 3.10 (a) Real and (b) imaginary part permittivity of the listed samples: Au ( $r = 3$  nm) nanorods (calculated), pure TiN, Au-TiN films with different Au densities (11.1 at%, 15.4 at%, 16.7 at% and 28.6 at%). (c) Ordinary (in-plane) and (d) extra-ordinary (out-of-plane) real part dielectric constants. (e) Plasma frequency as a function of three Au densities: 11.1 at%, 16.7 at% and 28.6 at% and (f) their carrier densities from Hall measurements. Pure TiN (gray dashed line) carrier density is shown as reference, and the inset is the illustration of Hall experiment setup.

Plasma frequencies retrieved from  $\epsilon_1$  are plotted as a function of Au density in Figure 3.10 (e). The shift from  $5.6 \times 10^{14}$  Hz (11.1 at% Au) to  $7.0 \times 10^{14}$  Hz (28.6 at% Au) indicates a potential increase of electron densities introduced by higher volume ratio of Au phase. Therefore, Hall measurements were performed on three Au-TiN nanocomposites with 11.1 at%, 16.7 at% and 28.6 at% Au densities, pure TiN is measured as a reference. The measurement setup with the contact geometry is shown in Figure 3.12 (d). The carrier density is calculated using the equation:

$$n_e = \frac{I \cdot B}{V_H \cdot t \cdot e} \quad (\text{cm}^{-3})$$

, where  $V_H$ ,  $I$ , and  $B$  are voltage, current and magnetic field applied, respectively, and  $t$  is film thickness. The resulted charge carrier concentration is plotted in Figure 3.10 (f). It is confirmed that increase of Au nanopillar density would increase its electron density, which induces the left shift of plasma frequency (plotted in parallel), and enhanced plasmonic resonance.

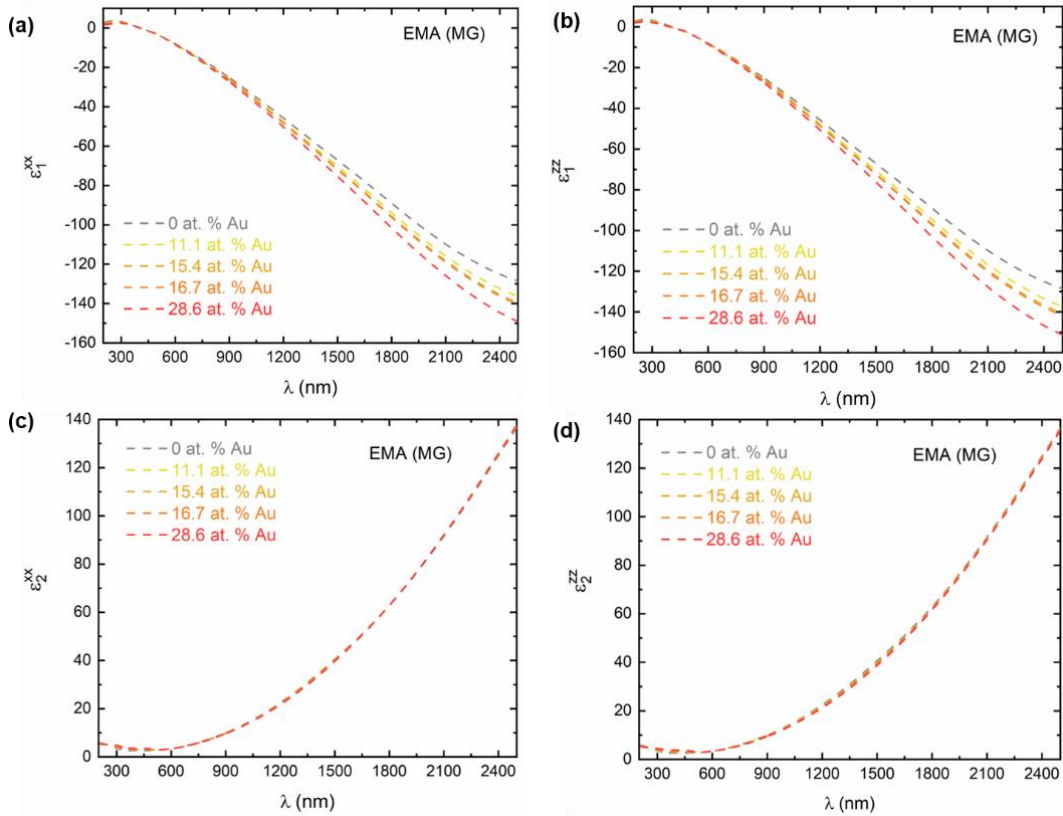


Figure 3.11 Anisotropic effective permittivity as a function of Au densities in Au-TiN hybrid thin films. (a) In plane (ordinary) real part dielectric constant, (b) out-of-plane (extra-ordinary) real part dielectric constant, (c) in plane imaginary part dielectric constant, and (d) out-of-plane imaginary part dielectric constant. Results are calculated from effective medium theory Maxwell-Garnett (MG) method.

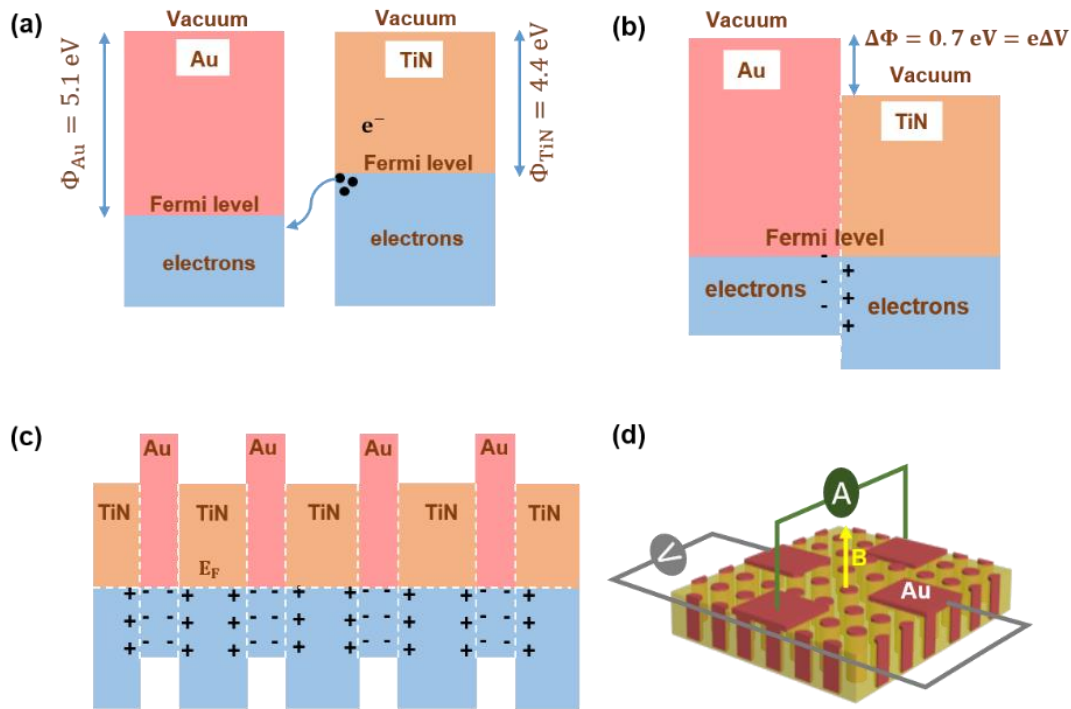


Figure 3.12 (a-c) Proposed band diagram at Au-TiN junction, and the predicted electron density profile at nanocomposite cross-section. Bulk Au and TiN have a work function of 5.1 eV and 4.4 eV, respectively. At the metallic junction (boundaries) between Au and TiN, there could be electron density variances that electrons accumulated at the Au side while holes at the TiN side. Overall, the Au-TiN nanocomposites are showing enhanced charge carrier density with increased Au nanopillar densities. (d) Experimental setup of Hall measurements.

The proposed band diagram for Au-TiN metallic junction is shown as Figure 3.12 (a-c) to illustrate the charge carrier transfer across the Au-TiN interfaces. The work functions of bulk Au and TiN are 5.1 eV and 4.4 eV, respectively. <sup>[157-158]</sup> To compensate the difference in work function and charge carrier density across the boundary, electrons move from TiN into Au when they are in contact with each other, which results in the electrons accumulated at the Au side while holes at the TiN side. Compared to the reference pure TiN sample, results demonstrate a systematic enhancement on electron density as a function of Au density. Nevertheless, other factors such as electron trapping at the nanopillar interface can also contribute to the overall enhanced charge carrier density.

Up to this point, we have demonstrated the effective dielectric tuning offered by the tailorable nanostructure. We believe that the optical tunability demonstrated in this Au-TiN hybrid system comes from multiple factors. First, the well-aligned vertical Au nanopillars in TiN matrix

platform presents very anisotropic light-matter interactions in vertical and lateral directions. This highly anisotropic hybrid system behaves differently from any of the two phases alone. Second, the strong interfacial coupling between the Au nanopillars and TiN matrix results in strong vertical strain coupling, enhanced optical anisotropy, effective charge carrier injection from Au to TiN and thus demonstrate effective tuning of optical property. Specifically, as the Au nanopillar density increases, the TiN matrix is more compressive out-of-plane; charge carrier density increases effectively, and therefore the hybrid system behaves more metallic optically. Further understanding on the interfacial charge carrier transfer mechanisms by density functional theory (DFT) calculations could be valuable for exploring the interfacial coupling between the Au nanopillars and the TiN matrix.

As Au nanoparticles (NPs) have been demonstrated as durable and effective chemical sensors,<sup>[159]</sup> a potential application of the hybrid Au-nitride metasurfaces is bio- and molecular-sensing. As a demonstration, we have explored the sensitivity of selective binding efficiency of the low and high density Au-TiN films with target analytes (-OH). Results are shown in Figure 3.13. First, the samples were washed with methanol (CH<sub>3</sub>OH) solution before the FTIR spectra being collected, the reflection dips at near 3000 cm<sup>-1</sup> and their fingerprints (1500 ~ 500 cm<sup>-1</sup>) are present and identified as the -OH stretch. The weak dip showing at ~ 3800 cm<sup>-1</sup> belongs to the free-standing -OH stretch. To prove the high potential of the Au nanopillars for sensing, the Au nanopillars were blocked by functionalizing the surface with thiol bonds in a 3-Mercaptopropionic acid (MPA) solution for 24 hours, as the Au nanopillar surface undergoes a self-assembling reaction. As expected, the -OH stretching disappeared from the FTIR spectrum, with merely background noise in the corresponding spectrum region. In the final step, the samples were treated with UV light, aiming to break the thiol bonds from the functionalized surface, and the recovery of the -OH stretching of the uncovered Au nanopillars. Within 20 mins exposure, the low density Au-TiN spectrum recovers almost to its original intensity while the high density Au sample recovers to ~ 50%. Therefore, the high potential for chemical sensing for the Au nanopillars at the hybrid plasmonic surface was demonstrated.

In addition, the reliability and effectiveness of the Au-TiN hybrid films are confirmed by comparing with the spectra from pure TiN films (Figure 3.14 a), Au colloidal nanoparticles (NPs) and nanorods (NRs) (Figure 3.14 b) samples. While TiN is not contributing to functionalization, it serves as a durable matrix to “stabilize” the well-distributed Au “nanoantenna” assemblies, such

that the bonding is more effective and stronger signals are detected from the surface of the hybrid films. It is believed that both the plasmonic effect between the closely spaced Au-Au nanopillars and the bonding efficiency between the molecule and the Au nanopillars play the role in enhancing the FTIR signal. As compared to solution based plasmonic nanostructures, our Au-TiN hybrid plasmonic surfaces are mechanically strong and thermally robust and can be reused multiple times.

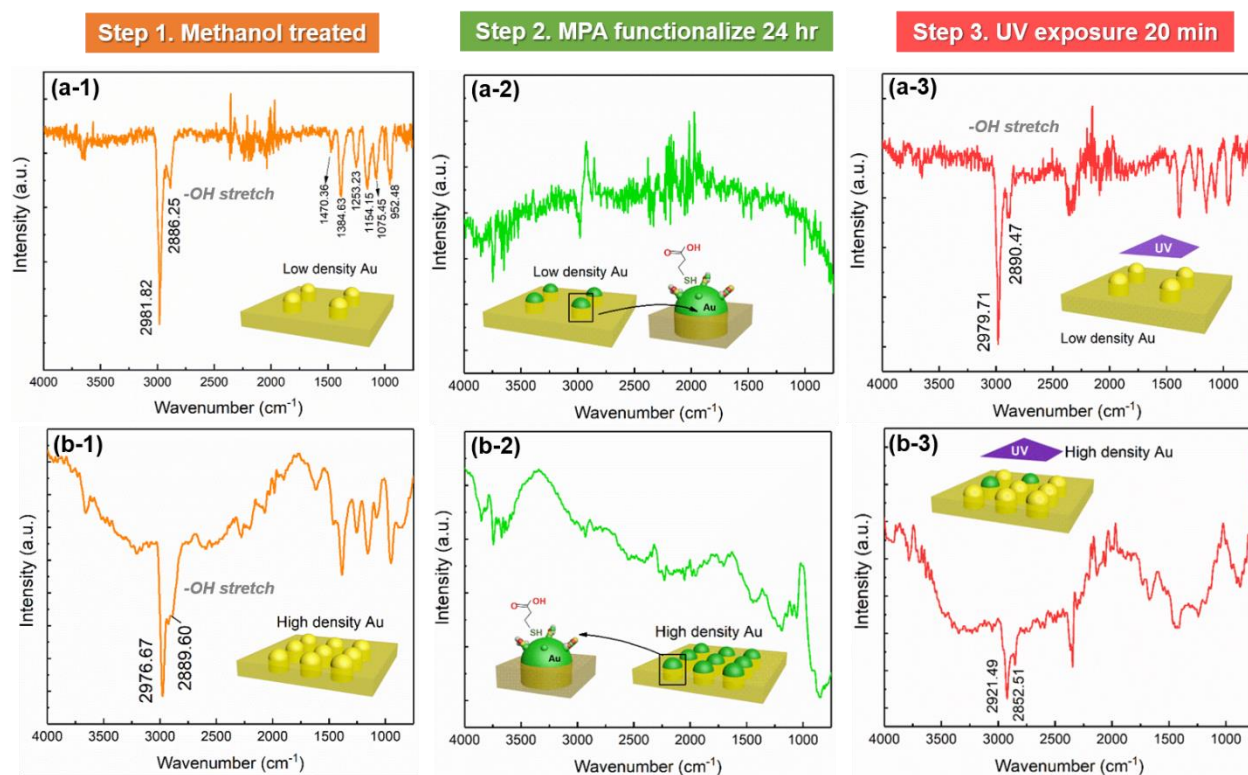


Figure 3.13 Chemical sensing demonstration. Total internal reflection spectra on set (a) low density Au-TiN film, set (b) high density Au-TiN film. Step 1: spectra after methanol treatment, signature dips located at 3000 cm<sup>-1</sup> correspond to the -OH stretch bonded with dangling Au at metasurface; step 2: spectra after 24 hr functionalization with MPA solution. The signature dips are disappeared due to the thiol bond reaction with -OH stretch; step 3: spectra of samples after 20 minutes UV exposure which serves to break the thiol bonds. The speed of this recovering process has a dependency on Au densities.

To further understand the enhanced plasmonic response of the Au-TiN hybrid metasurfaces, Raman spectra (Figure 3.15a) were collected for pure TiN, low and high density Au-TiN films. Results show that the overall Raman signals are strengthened with the increased Au densities. As stated, enhanced Raman signals in the Au-TiN hybrid systems are believed to be related to the well-controlled Au inter-pillar spacing therefore stronger near field interactions. In addition, the

first-order acoustic peaks (Table 3.1), namely transverse acoustic (TA), longitudinal acoustic (LA), transverse optical (TO) and the second-order acoustic (2A) modes maintain comparable with varied Au densities and match with reported values of TiN.<sup>[160-161]</sup> This provides a strong evidence of stable TiN stoichiometry such that the plasmonic tuning is realized by the hybrid geometry instead of a metal-semiconductor transition of TiN<sub>x</sub>.

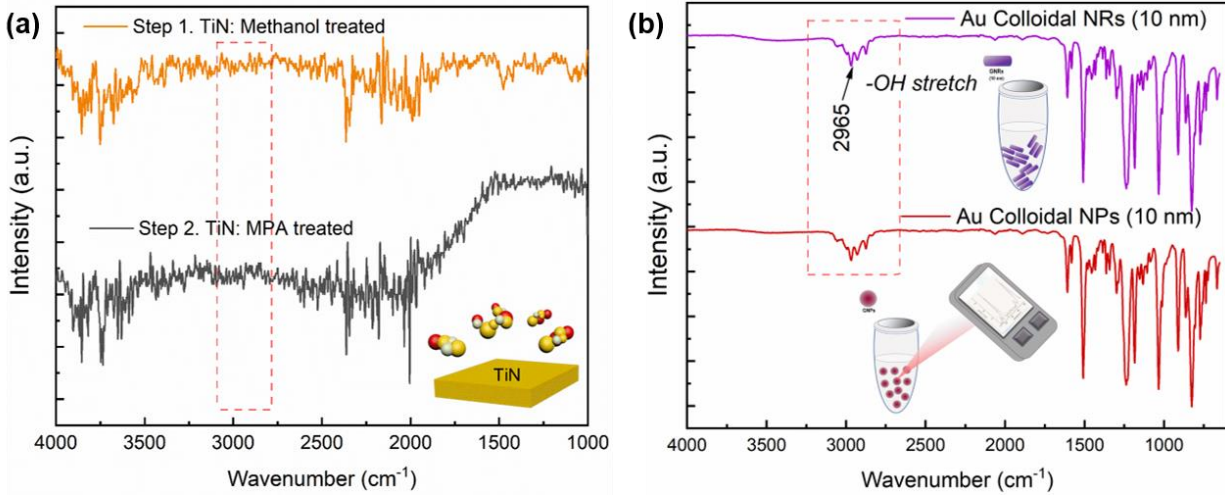


Figure 3.14 Total internal reflection FTIR spectra from reference samples. Following the similar procedure, the samples were washed with methanol before collecting the spectra. (a) Spectra of pure TiN films from the first two steps, showing no interaction with -OH stretch. (b) Spectra of Au colloidal nanoparticles (NPs) and nanorods (NRs) with diameter of 10 nm. Both shows the -OH stretching at  $\sim 2965 \text{ cm}^{-1}$ .

Table 3.1 Peak position of first-order acoustic modes from Raman measurements

Au at%	TA	LA	2A	TO
0	232.31194 ± 0.86804	311.25791 ± 0.42652	458.74409 ± 1.96543	579.29365 ± 2.74366
5	232.50029 ± 1.27455	313.12214 ± 0.58209	461.6699 ± 2.35424	576.41751 ± 2.81994
20	226.48521 ± 3.64098	311.70881 ± 2.29083	475.33719 ± 8.10779	595.83984 ± 8.59915

In addition, the ability of plasmonic Au-TiN nanostructures to modify PL from molecules is important for potential fluorescence sensing implementation.<sup>[162-164]</sup> To this end, a pure TiN and an Au-TiN sample were spin-coated with a fluorescent conjugated polymer thin film ( $\sim 10 \text{ nm}$ ), followed by PL imaging and spectroscopy. A fluorescent thin film on glass sample was also

measured as a reference. Detailed procedures are described in additional information. The PL emission spectra of the three samples upon a 365 nm laser excitation are shown in Figure 3.15 (c,d). Both plasmonic films exhibited a 10 nm blue shift as well as a sharper response (smaller FWHM) of emission peaks, as compared to glass. Meanwhile, there is an obvious fluorescence quenching attributed to LSPRs (enhanced carrier densities of the Au-TiN). This can be visualized from the PL images as shown in Figure 3.15 (b) whereby the plasmonic films result in weaker fluorescence from the conjugated polymer layer. On the other hand, comparing the two plasmonic films, there is a major PL enhancement by the Au-TiN hybrid compared to the TiN film alone, suggesting a plasmon-enhanced contribution to the fluorescence due to the presence of the Au nanopillars in TiN. <sup>[163]</sup> The exploration of plasmonic metasurfaces and their functionalities is a first-step demonstration, more explicit studies incorporating such metasurfaces for nanophotonic device are under investigation.

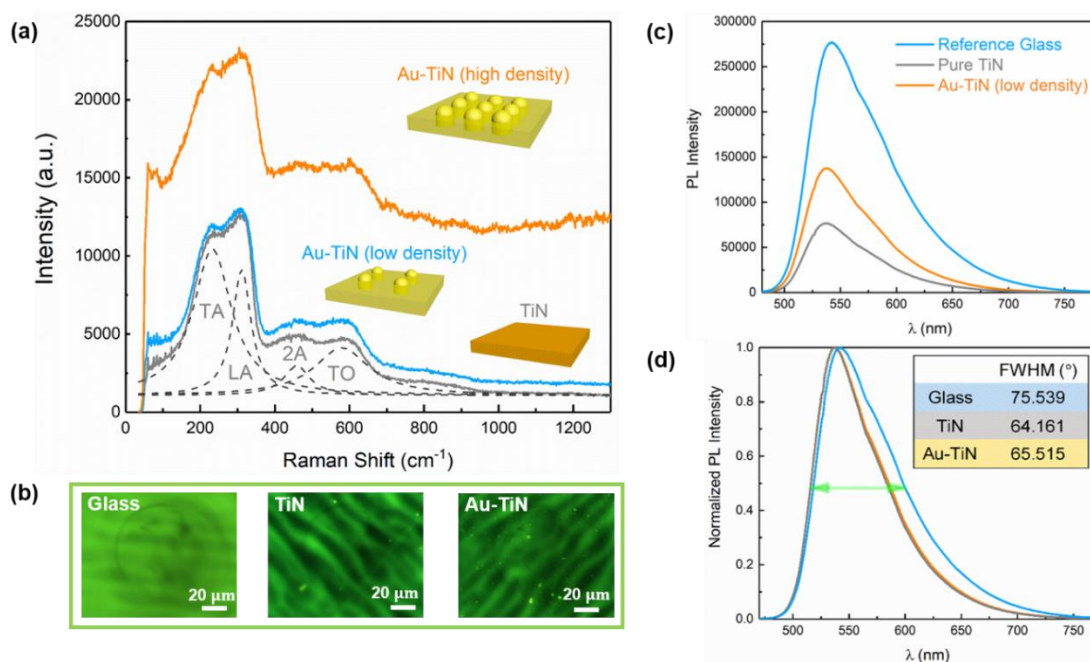


Figure 3.15 (a) Raman spectra of pure TiN, low and high density Au-TiN thin films. Enhancement on SERS signals shown as overall increase of spectrum intensity. First-order transverse acoustic (TA), longitudinal acoustic (LA), transverse optical (TO) and the second-order acoustic (2A) modes maintain comparable in Au-TiN nanocomposites and match with reported values of TiN, indicating a 1:1 ration of TiN while introducing Au phase. (b) Fluorescence (PL) images and (c,d) PL intensities and their normalized spectra excited at 365 nm for three samples: a reference glass, a pure TiN and an Au-TiN samples with spin-coated fluorescent conjugated polymer thin film (~ 10 nm).

### 3.4 Conclusion

In this work, a two-phase Au-TiN hybrid plasmonic nanostructure with tailored Au nanopillar density and tunable optical properties has been demonstrated. Both Au and TiN phases are grown epitaxially with high crystalline quality and near perfect stoichiometry with no obvious interdiffusion in between. The addition of tailorable Au phase enables optical tunability and enhanced anisotropy, including the plasmonic red shift and systematic tuning of the complex dielectric constants ( $\epsilon_1$  and  $\epsilon_2$ ) in a broad wavelength range from 210 nm to 2500 nm. Also, the plasmon frequency is effectively tuned as the Au density varies, which correlates to its internal carrier density variation of the metallic nanostructures. As compared to colloidal Au NPs or NRs, our demonstration on the high chemical sensitivity and plasmon enhanced properties of the nanocomposite structures based on the FTIR, Raman and PL measurements suggest the fascinating potentials of Au-TiN hybrid thin film as robust and reusable functional SERS substrates for sensing and nanophotonic devices.

### 3.5 Additional Information

Gold nanoparticles were prepared by the citrate reduction method, using gold chloride trihydrate ( $\text{HAuCl}_4 \cdot 3\text{H}_2\text{O}$ ,  $\geq 99.9\%$ ), and trisodium citrate dihydrate (USP testing specifications) at a molar ratio of 1:3.5; Au NRs were purchased from Nanopartz. The samples were submerged in 50 mM 3-Mercaptopropionic acid (Sigma Aldrich) ethanolic solution for 24 hours at room temperature; after incubation, samples were washed with ethanol and DI water to remove any unreacted MPA. The successful Au-MPA self-assembling was demonstrated by irradiating the sample at a specific wavelength of 365 nm via a UV lamp UVGL-25, in order to break specifically the Au-thiol bonds formed. The functional group present before and after self-assembly were confirmed via ATR-FTIR spectroscopy using a Spectrum 100 FTIR Spectrometer (Perkin Elmer, Waltham, MA).

Fluorescent thin films were coated on TiN and Au-TiN surface before PL measurements. A fluorescent conjugated polymer poly (9,9-dioctylfluorene-*alt*-benzothiadiazole) (F8BT) was dissolved in chloroform to a concentration of 4.2 mg/mL (6.3 mg of F8BT was dissolved in 1.5 mL of chloroform). The solution was heated in a water bath at 45 °C and simultaneously stirred at 5000 rpm for 15 min and then sonicated for 15 min. Finally, 50  $\mu\text{L}$  of the F8BT solution was

dynamically spin coated onto the samples at a spin speed of 5000 rpm for 60 seconds. The same spin coating conditions were also used to coat a cleaned glass substrate with F8BT. Prior to spin coating, the glass substrate was cleaned in an ultrasonic bath containing detergent (0.5 wt%; Sparkleen, Fischer Scientific) for 10 min., and, subsequently, in a 50:50 solution of hydrochloric acid and ethanol for 10 min. The substrate was triple rinsed in ultrapure water (Mili-Q) after each bath cleaning step. The bright-field/dark-field imaging was performed on an inverted microscope (Axio Vert.A1, Carl Zeiss Microscopy, LLC.) coupled to an imaging spectrometer (Shamrock SR303i-A, Andor Technology Ltd.). Photoluminescence imaging and spectroscopy were carried out using an excitation source (X-Cite® 120Q, Excelitas Technologies Corp.) combined with a 365 nm excitation filter and a 397 nm long pass filter.

## 4. SELF-ASSEMBLED SILVER – TITANIUM NITRIDE HYBRID PLASMONIC METAMATERIAL: TAILORABLE TILTED NANOPILLAR AND OPTICAL PROPERTIES<sup>†</sup>

### 4.1 Overview

Key challenges limiting the adoption of metallic plasmonic nanostructures for practical devices include structural stability and the ease of large-scale fabrication. Overcoming these issues may require novel metamaterial fabrication with potentials for improved durability under extreme conditions. To this end, we report a self-assembled growth of a hybrid plasmonic metamaterial in thin-film form, with epitaxial Ag nanopillars embedded in TiN, a mechanically strong and chemically inert matrix. Our key achievement lies in a successful control of tilt angle of the Ag nanopillars (from 0° to 50°), which is attributed to the interplay between the growth kinetics and thermodynamics during the deposition. Such an anisotropic nature offered by the tilted nanopillars is crucial to achieving broadband, asymmetric optical selectivity. Optical spectra coupled with numerical simulations demonstrate strong plasmonic resonance, as well as angular selectivity in a broad UV-visible to near-infrared regime. The nanostructured metamaterial in this work, which consists of highly conductive metallic nanopillars in a durable nitride matrix have potential to serve as a novel hybrid material platform for highly tailorable nanoscale metamaterial designs, suitable for high temperature optical applications.

### 4.2 Introduction

Metamaterials as plasmonic nano-resonators with novel functionalities are attractive for various device applications including nano-photonics circuits, bio-medical sensing, plasmon-enhanced photocatalysis and photovoltaics.<sup>[18, 129, 131, 135, 151-152, 165-172]</sup> Through tailoring material or/and geometrical parameters of such nanostructured building blocks, light-matter interactions can be manipulated for selective responses. From geometrical perspective, nanopillar or nanowire become favorable candidates owing to their three-dimensional tunability and optical anisotropy, which functions as “nanoantennas” for highly sensitive energy harvesting, photodetection, or light

---

<sup>†</sup> This chapter is reprinted with permission from “Self-Assembled Ag–TiN Hybrid Plasmonic Metamaterial: Tailorable Tilted Nanopillar and Optical Properties” by X. Wang, et al., *Adv. Opt. Mater.* **2018**, 7 (3), 1801180.

selectivity in terms of angular, frequency, or polarization.<sup>[141, 173-175]</sup> From the material perspective, metal-based plasmonic and optical nanostructures (gold (Au), silver (Ag), aluminum (Al) and copper (Cu)) have drawn a great deal of attention because of their strong surface-enhanced Raman scattering (SERS) and surface plasmon modes (SPs) which range from visible to near-infrared (Vis-NIR)<sup>[132, 142, 170, 176-177]</sup> Variable patterned nano-resonators (e.g. nanoprisms, nanorods, nanohole arrays or single nanoparticles) has been demonstrated for improved resolution and signal-to-noise ratios for localized surface plasmon resonance (LSPR) spectroscopy.<sup>[15, 138, 178-181]</sup>

In parallel, challenges remain in the plasmonic metamaterials, namely long-term durability and ease of fabrication. On one hand, metals such as Ag, Al and Cu experience poor thermal stability and fast chemical reactions upon thermal fluctuations. Furthermore, potential inter-diffusion at metal-matrix (i.e. oxides, semiconductor) interface deteriorates device sensitivity at high temperatures.<sup>[148, 179, 182]</sup> One effective approach is the design of hybrid plasmonic nanostructures such that the unstable phase can be embedded or covered with a durable material. Examples such as Ag/Au core-shell nanoparticles, Ag/AgS<sub>2</sub> nanoprisms or Ag/graphene fishnet hybrids have been designed to enhance the overall stability and signal-to-noise ratios of SERS signals.<sup>[148, 179, 183-185]</sup> On the other hand, existing metamaterial fabrication techniques such as e-beam lithography (EBL) or focused ion-beam (FIB) techniques are time consuming for nanoscale geometries. Beam damage and limited patterning scale are also concerns to the fabrication of high quality and large-scale photonic devices. Alternative methods such as anodized alumina template and seeded growth are capable of producing epitaxial nanopillars/nanoparticles, but have limitations in material and morphology selections.<sup>[56, 151, 186-187]</sup> Recent demonstrations on the two-phase nanocomposite growth using physical vapor deposition techniques open up more possibilities in fabricating high quality, large scale metamaterials.<sup>[59]</sup>

In this work, we propose a novel nanoscale metamaterial system that composes of tilted Ag nanopillars in a titanium nitride (TiN) matrix, grown as hybrid thin film form. The three-dimensional Ag-TiN framework is illustrated in Figure 4.1. Here, we highlight the structural tunability in terms of pillar tilting angle, which can be tailored by precise growth control. Different from oblique angle deposition which produces mostly single-phase tilted nanorods,<sup>[152, 188-189]</sup> our method achieves a two-phase self-assembly with high epitaxial quality and high density nanopillar assemblies approaching deep subwavelength scale (<10 nm), which is very challenging for the current fabrication techniques. Such tilted geometry presents enormous opportunities in achieving

optical anisotropy and angular selectivity. In addition, compare to patterned metallic nanostructure or metasurfaces,<sup>[152, 182, 187]</sup> our robust TiN serves as a barrier against diffusion and surface chemical reaction for Ag, and provides overall mechanical integrity. Detailed studies of the physical properties have been performed, which include specular reflectance and dielectric measurements from ultra-violet (UV) to infrared (IR) region, thermal and mechanical tests, along with a complete microstructural analysis to correlate the optical responses with the tiled Ag nanopillar geometries.

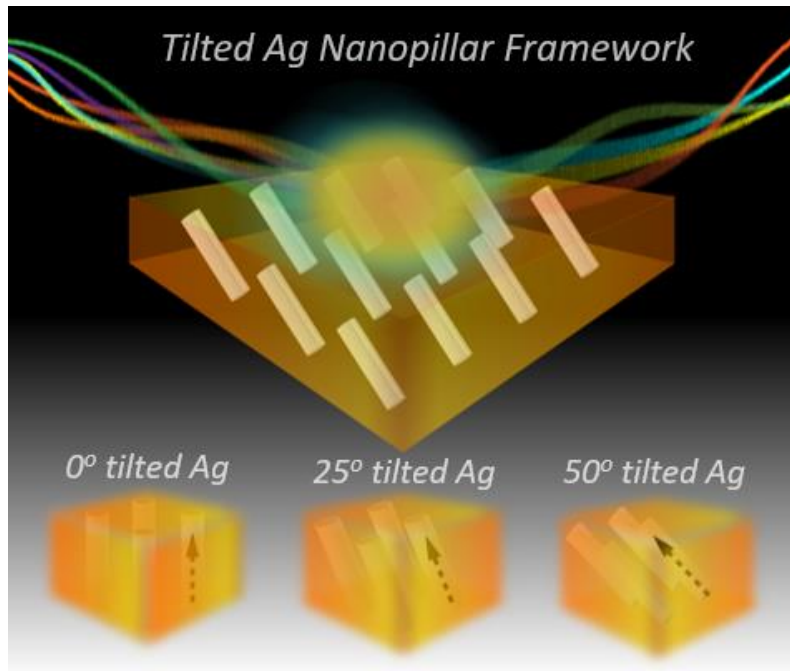


Figure 4.1 Schematic illustration of Ag-nitride (TiN) hybrid plasmonic metamaterial thin film. Ag nanopillars with subwavelength scale are tailored in terms of their tilting angles (lower pane). The hybrid plasmonic configuration brings new functionalities such as optical anisotropy and angular selectivity.

### 4.3 Results and Discussion

A set of Ag-TiN hybrid thin films were deposited following the structure designs as illustrated in Figure 4.1, where the embedded Ag nanopillars are tilted (I)  $0^\circ$ , (II)  $25^\circ$  and (III)  $50^\circ$ , respectively. Such tilting is achieved by a precision growth control technique discussed below. To confirm the tilting pillars and the overall film morphology, plan-view TEM images are presented in Figure 4.2 (a-c) for all three samples. Upon increasing the tilt angle from  $0^\circ$  to  $50^\circ$ , the top projections of Ag nanopillar assemblies change from round to elongated shapes. With comparable

Ag density controlled for all samples, the metasurface affected by Ag tilting geometries could effectively change the surface plasmonic resonances (SPRs), to be discussed in later sections. The corresponding cross-sectional STEM images of different tilting configurations are shown in Figure 4.2 (d-f), in which distinct Ag nanopillars are clearly identified with a uniform distribution and tilt angle for each case. Selected Area Electron Diffraction (SAED) patterns taken from the  $\langle 100 \rangle$  zone axis (inset images) confirms high-quality epitaxy, as well as a cube-on-cube matching of (002) atomic planes of Ag and TiN on magnesium oxide (MgO) substrates.

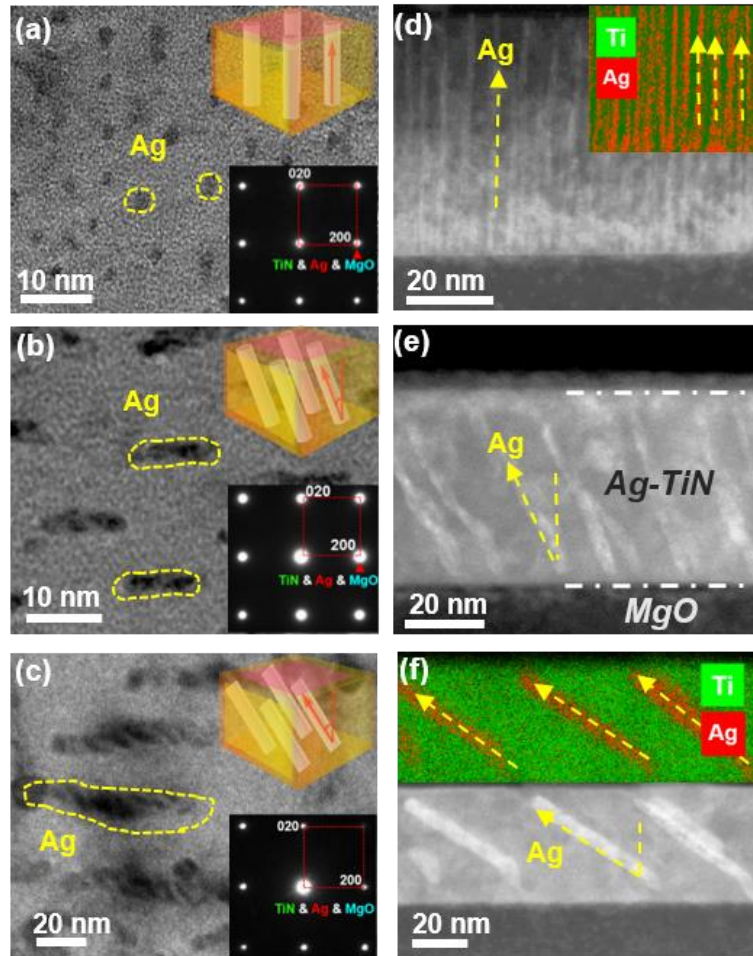


Figure 4.2 Three-dimensional morphology of epitaxial Ag-TiN hybrid thin films with different nanopillar tilting geometries. (a-c) Plan-view TEM images of  $0^\circ$  tilted,  $25^\circ$  tilted and  $50^\circ$  tilted Ag. (d-f) Cross-sectional STEM images corresponding to each geometry. Insets are SAED patterns taken at  $\langle 100 \rangle$  zone axis, as well as EDS mapping of two extreme tilting angles. Ag: red, Ti: green.

Energy-dispersive X-ray spectroscopy (EDS) mappings of Ti (green) and Ag (red) are shown as insets in Figure 4.2 (d,f), which clearly confirm the growth of Ag nanopillars in a TiN matrix with very clean interfaces and without obvious intermixing. Based on the (S)TEM results, detailed quantifications including nanopillar dimensions and tilting angles are being correlated to three deposition rates. Results indicate that lower deposition rate increases the tilting angle and broadens the nanopillar dimension slightly, meanwhile the nanopillar lengths remain comparable even though the overall film thickness is reduced.

In parallel, X-ray diffraction (XRD) was collected to confirm the film crystallinity from a large area. The  $\theta$ - $2\theta$  scans of three hybrid films and a pure TiN film are shown in Figure 4.3. The growth orientation is identified as  $(002)_{\text{Ag}} \parallel (002)_{\text{TiN}} \parallel (002)_{\text{MgO}}$  for the Ag-TiN hybrid films. Peak positions are identified as:  $2\theta_{\text{TiN}(002)} = 42.60^\circ$ ,  $2\theta_{\text{Ag}(002)} = 44.283^\circ$ ,  $2\theta_{\text{MgO}(002)} = 42.916^\circ$ , which match well with all the peak positions of the bulk counterparts. Close lattice matching between MgO ( $a_{\text{MgO}} = 0.421$  nm) substrate and TiN ( $a_{\text{TiN}} = 0.424$  nm) provides a desired epitaxial template for the growth of Ag nanopillars, evidenced by the dominated Ag (00 $l$ ) peaks without any other orientations. Compare to pure TiN, the two phase heteroepitaxial Ag-TiN results in a slightly broadened (002) TiN peak, which could be related to the vertical coupling at Ag/TiN interface or minor variations on TiN stoichiometry at the interfaces. Overall, the films maintain high quality and very smooth surface as seen from the satellite peaks of (002) TiN. A phi ( $\phi$ ) scan of Ag-TiN hybrid film (Figure 4.3b) demonstrates a four-fold symmetry of the film, and excellent in-plane alignment, with cube-on-cube matching for all the phases. Successful tilted growth of Ag-TiN hybrid film is also achieved on *c*-cut sapphire substrate, with the growth orientation as  $(111)_{\text{Ag}} \parallel (111)_{\text{TiN}} \parallel (0001)_{\text{sapphire}}$  based on XRD (Figure 4.3c). The corresponding STEM images (Figure 4.3d) demonstrate well-ordered nanopillar assembly achieved on sapphire as compared to films grown on MgO substrate.

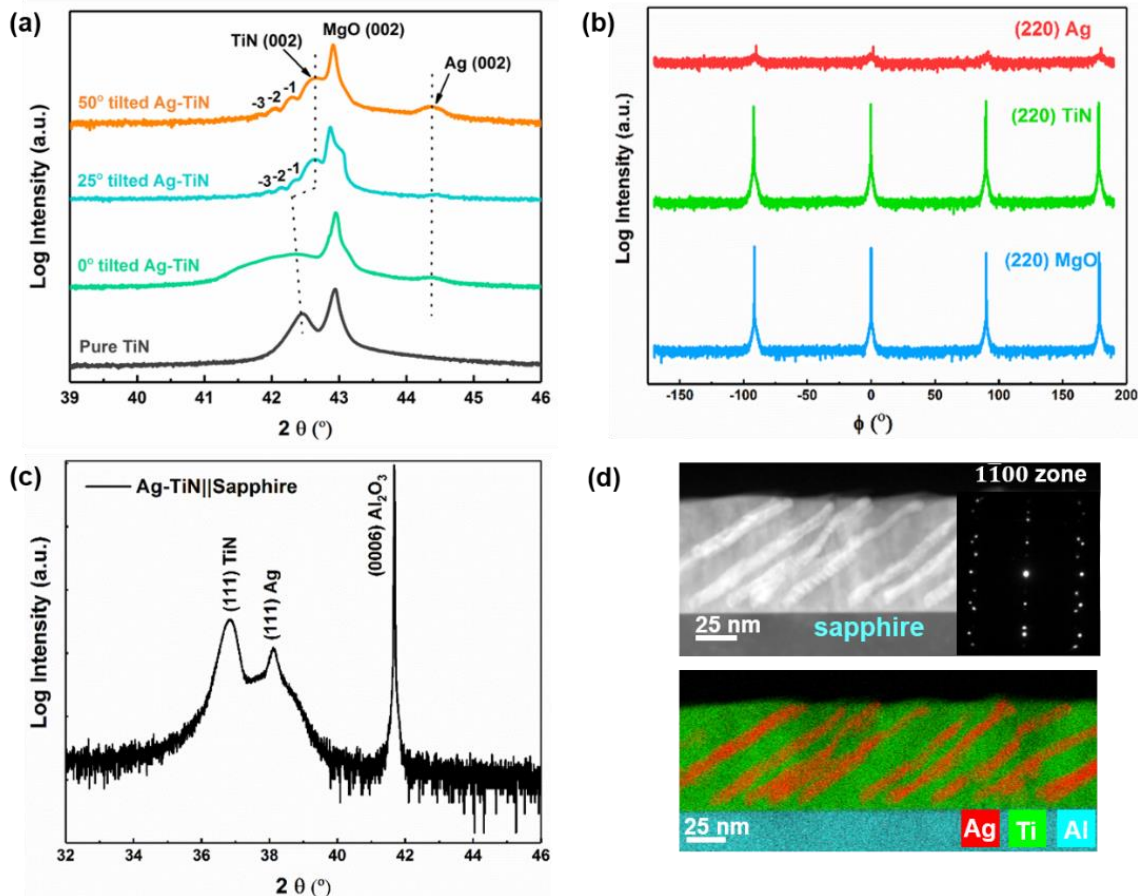


Figure 4.3 (a) XRD  $\theta$ - $2\theta$  scan of pure TiN and three Ag-TiN hybrid films grown on MgO substrate. Ag nanopillar is grown as (001). Satellite peaks of TiN indicate high film quality. (b) XRD phi scan at (220) plane. The four-fold geometry demonstrates desired in-plane matching of Ag, TiN and MgO substrate as (00 $l$ ). (c) XRD  $\theta$ - $2\theta$  scan of Ag-TiN grown on c-cut sapphire substrate. (d) EDS mapping taken from  $\langle 1\bar{1}00 \rangle$  zone axis reveals tilted Ag nanopillars, which proves a repeatable tilting geometry by controlling the deposition rate. Note that films grown on sapphire is orientated as (111) with lowest surface energy, therefore, the tilting geometry would be stable under different growth rates.

Both (S)TEM and XRD results confirm the preferred growth orientation of (002) Ag nanopillars. To explore the growth mechanism for the tilted nanopillars, high resolution STEM was performed on the 50° tilted Ag-TiN/MgO hybrid film from three dimensions, as illustrated in Figure 4.4 (top center). Cross-sectional STEM images taken from the  $\langle 100 \rangle$  zone axis are shown in Figure 4.4 (a-b). The Ag nanopillars growth experiences two steps: the initial nucleation marked in the yellow box (Figure 4.4a) and the subsequent tilted growth.

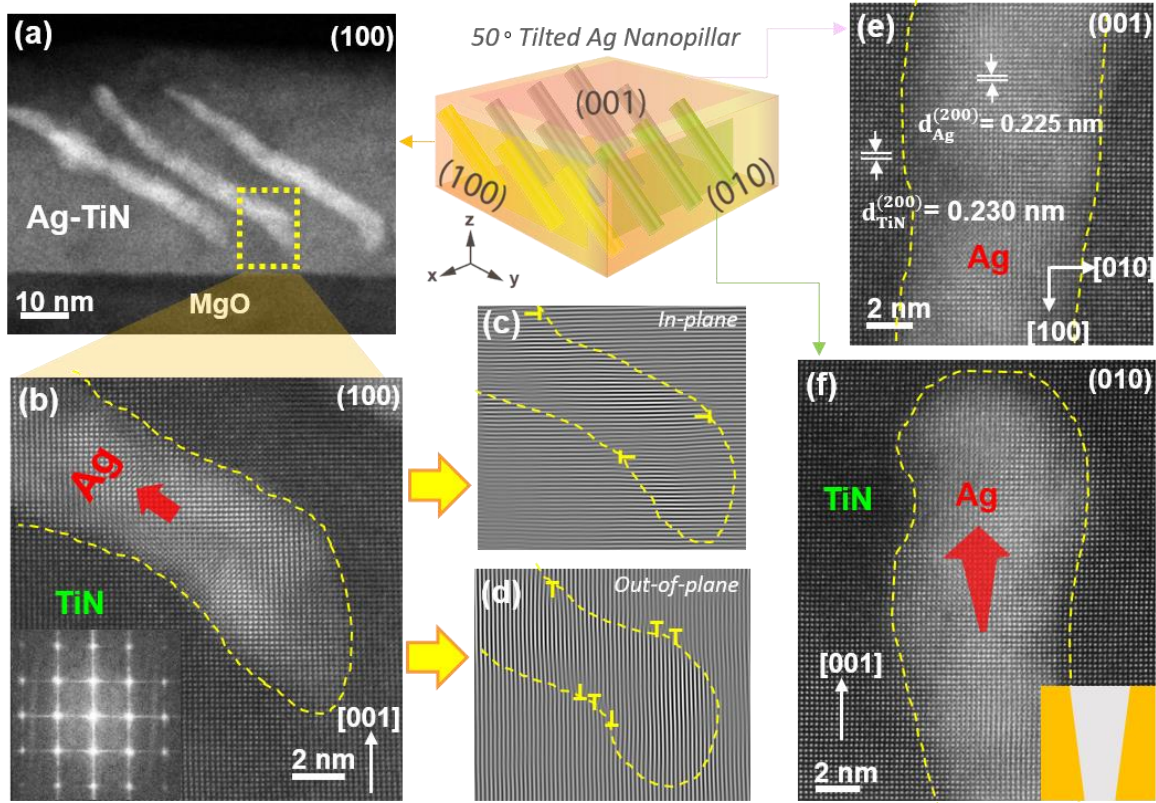


Figure 4.4 3D STEM images of 50° Ag-TiN hybrid thin film. Schematic illustration is shown at top center showing three faces (100), (010) and (001). (a) Cross-sectional STEM and its (b) high magnification image taken at  $\langle 100 \rangle$  zone axis, (100) face. (c-d) IFFT filtered image both in-plane and out-of-plane with edge dislocations marked at Ag/TiN interface. (e) HRSTEM image of plan-view ((001) face) nanopillar. (f) Cross-sectional HRSTEM image taken from  $\langle 010 \rangle$  zone axis, showing projection of one tilted nanopillar from [010] direction.

For the first few atomic layers, Ag adatoms stack vertically on top of each other. After the initial nucleation, the Ag adatoms continuously shift to the left while maintaining the (002) atomic stacking along the  $c$ -axis, resulting in the tilted nanopillar morphology. Inversed Fourier Transformed images (IFFT) (Figure 4.4c-d) of Ag/TiN phase boundary indicate strained interface with few edge dislocations along in-plane and out-of-plane directions, which is also proven by the atomic resolution Ag/TiN from the top projection (Figure 4.4e). When viewed from the orthogonal  $\langle 010 \rangle$  zone axis (Figure 4.4f), the nanopillars appear to be mostly vertically aligned. Minor contrast variations across the length of the Ag nanopillar indicate the “vertical pillar” is tilted inward, which is in the projection of [010] as illustrated. Therefore, the self-assembled 50° Ag nanopillar assembly is demonstrated from a three-dimensional perspective.

The underlying mechanism of this self-assembled tilting geometry is attributed to the competition between growth kinetics and thermodynamics. On one hand, high kinetic energy of PLD method allows fast thin-film deposition and facilitates the Ag nanopillars to grow vertically along the primary growth direction. With a nearly-perfect lattice matching between TiN and MgO, Ag prefers to grow as epitaxial (00 $l$ ). Such pillar-in-matrix nanostructures are realized by the difference in surface energies, i.e., Ag has higher surface energy and thus nucleates in the Volmer-Weber (VW) island growth mode, and TiN nucleates as Stranski-Krastanov (2D + 3D) mode, both on oxides.<sup>[68]</sup> Under a high growth rate (upper pane of Figure 4.5), the Ag and TiN adatoms grow and nucleate effectively as vertical columns with limited time for adatoms diffusion on the substrate surface, leading to vertically aligned nanopillars. Thus, Ag nucleus appears fine and densely packed as observed from Figure 4.2 (a).

On the other hand, when the growth rate reduces (lower pane of Figure 4.5), the adatoms diffusion along the lateral direction is enabled by a longer resting time, searching for a thermodynamically favorable state of growth; thus, larger nuclei and lateral tilting of the pillars become possible. Note that the growth of the hybrid Ag-TiN film is intentionally started from TiN to minimize strains at initial growth stage, which is the reason why a very thin layer of TiN is formed at the interface. The thickness of this layer is affected by growth rate as well, that under low rate this TiN layer tends to grow thicker before the Ag adatoms diffuse and agglomerate until stable nucleus is formed. After the nucleation process, the TiN growth is suppressed by tilted growth of Ag, leading to a thinner film as compared to the fast deposition rate. Comparing the surface energies of different Ag crystallographic planes, (111) is the lowest among (100), (110) and (111).<sup>[190]</sup> This low-energy plane has the tendency to be exposed to minimize surface energy for low growth rates, which in turn results in tilted growth that remains stacked in the [001] orientation. While the overall kinetic energy is largely determined by the laser photons, the degree of tilting is primarily controlled by fine tuning of deposition rate parameters. Compared with 0° and 25° tilting geometry shown in Figure 4.2, the 50° tilting reaches to a relative thermodynamic stable state. Note that the inhomogeneity in the hybrid materials (i.e. nanopillar diameter, nucleus density) is inevitable when tailoring the tilting angle parameters. In this study, the optical property is mainly focused on the angular dependent (anisotropic) light-matter interactions such that the dimension effect can be minimized.

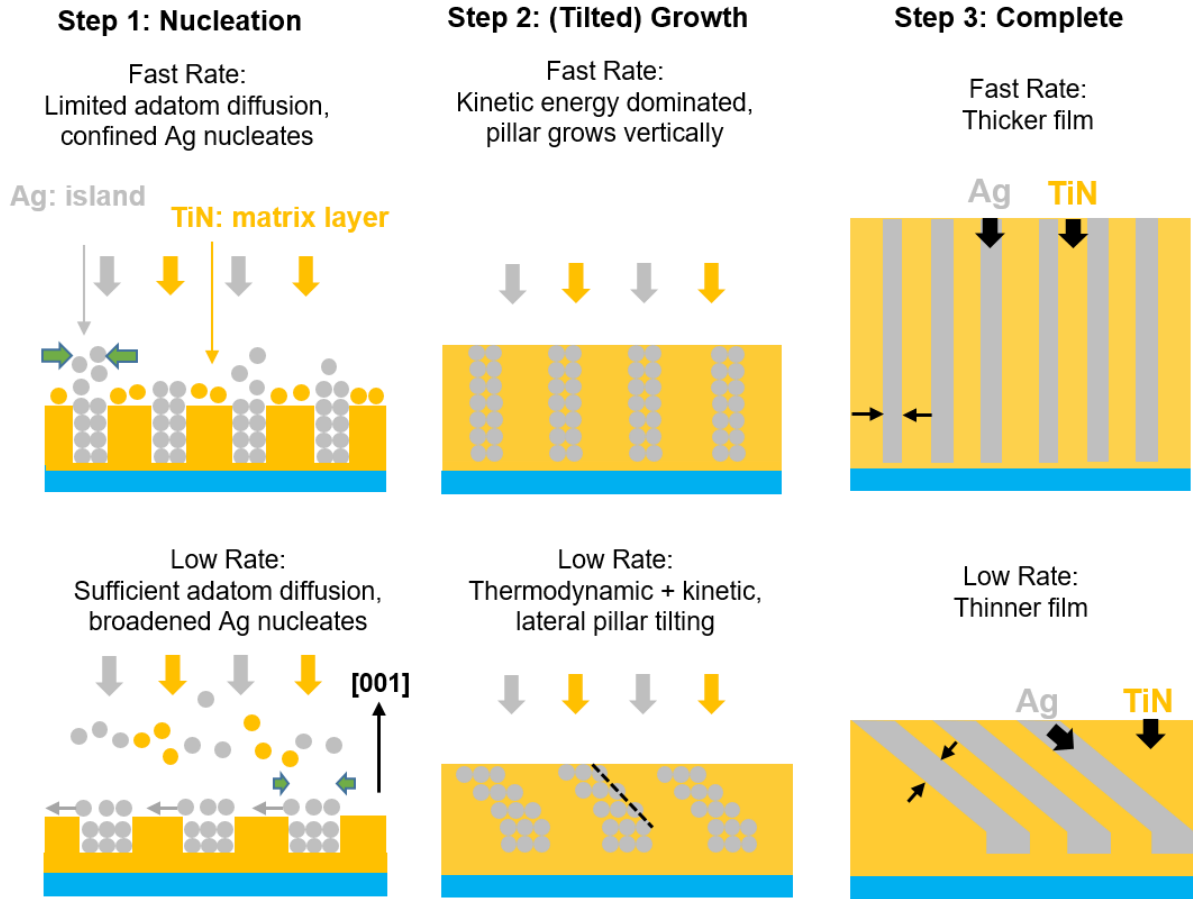


Figure 4.5 Growth mechanism of Ag-TiN hybrid thin films on MgO substrate. Tilting of Ag nanopillar is controlled by tuning the deposition rate. Upper pane: fast rate deposition. Adatoms diffusion is limited, Ag nucleates are small. High kinetic energy dominates the growth, Ag growth is suppressed (green arrow), leading to straight thin nanopillars. Lower pane: Low deposition rate. More adatoms diffusion (longer resting time) and broadened the Ag dimension (green arrow indicates smaller suppression), exposure of low-energy facets and tilted nanopillar growth. Tilted nanopillar growth is more thermodynamically favorable.

Optical measurements on Ag-TiN hybrid thin films demonstrate a variable spectrum response by tailoring the Ag nanopillar geometry. Optical reflectance and transmittance spectra of pure TiN, 0° tilted and 50° tilted Ag-TiN thin films samples were collected under a normal incident depolarized light. The absorbance spectrum is retrieved from reflectance as  $A(\lambda) = 1 - R(\lambda)$ , since transmittance is negligible, and a Lorentz function is applied to split the peaks. The results are shown in Figure 4.6. Pure TiN film (85 nm) (grey curve) exhibits plasmonic behavior, with an absorbance peak located at 374 nm. For Ag-TiN hybrid structures (blue and orange curves), two separate peaks are observed. To correlate the peak positions of the two phases, *COMSOL*

*Multiphysics Wave Optics Module* was applied to simulate optical spectra and the corresponding electric field map. Parameters such as film thickness, pillar dimension as well as the inter-pillar distance are comparable to (S)TEM results. In order to identify peak positions, pure Ag and TiN spectra are simulated individually, from which it is confirmed that the left ( $\sim 350$  nm) and right ( $\sim 374$  nm) resonance peak (Figure 4.6a) belongs to Ag and TiN phase, respectively. A careful comparison on peak positions reveals a red shift (40 nm) of TiN resonance, which is related to a minor change in TiN stoichiometry or defects states at Ag/TiN interface. Variations of Ag resonance peaks position (330 nm  $\sim$  350 nm) is owing to the change of nanopillar aspect ratio, while intensity variation is caused by light propagation direction with respect to nanopillar tilting direction. It can be explained by stronger electron oscillations at the resonant frequency when the incident light propagates into the vertically aligned nanopillar, or LSPR at the Ag/TiN interfaces. Compare to pure TiN, Ag-TiN hybrid film presents a broadened absorptance (Figure 4.6a), such increase of linewidths lies in the superposition of two-phase plasmonic resonances, which implies enhanced electron oscillation and stronger near-field coupling upon electromagnetic field excitation, or it could be contributed by the variations in material composition, interfacial strains and degree of ordering of nanopillars between simulation and experiments. A general enhancement of the baseline intensity results from scattering at interfaces or defects.

Next, the field enhancement maps are retrieved close to the resonant frequencies of two phases and displayed in Figure 4.6 (b). At 350 nm, electrical field of y-polarization ( $E_y$ ) is dominated by Ag nanopillars, while the TiN excitation is maximized at 420 nm. Additionally, the  $0^\circ$  tilted Ag nanopillar reveals more centrosymmetric electric field distribution, while it becomes more anisotropic when the nanopillar is tilted. Such field distribution inside tilted geometries indicates potential angular selectivity when the light is propagating along different directions. The non-centrosymmetric or anisotropic nature of this nanostructure is further proved by the second harmonic generation (SHG) (Figure 4.6c). The polar plot indicates a transition from two-fold rotational symmetry at p-out ( $0^\circ$ ) into a four-fold symmetry at s-out ( $90^\circ$ ) with decreased SHG intensity. Such non-centrosymmetry is inherently contributed by the lattice strain, since both TiN and the tilted Ag undergo lattice distortion during thin film growth, which breaks the centrosymmetry from their bulk counterparts. <sup>[191]</sup>

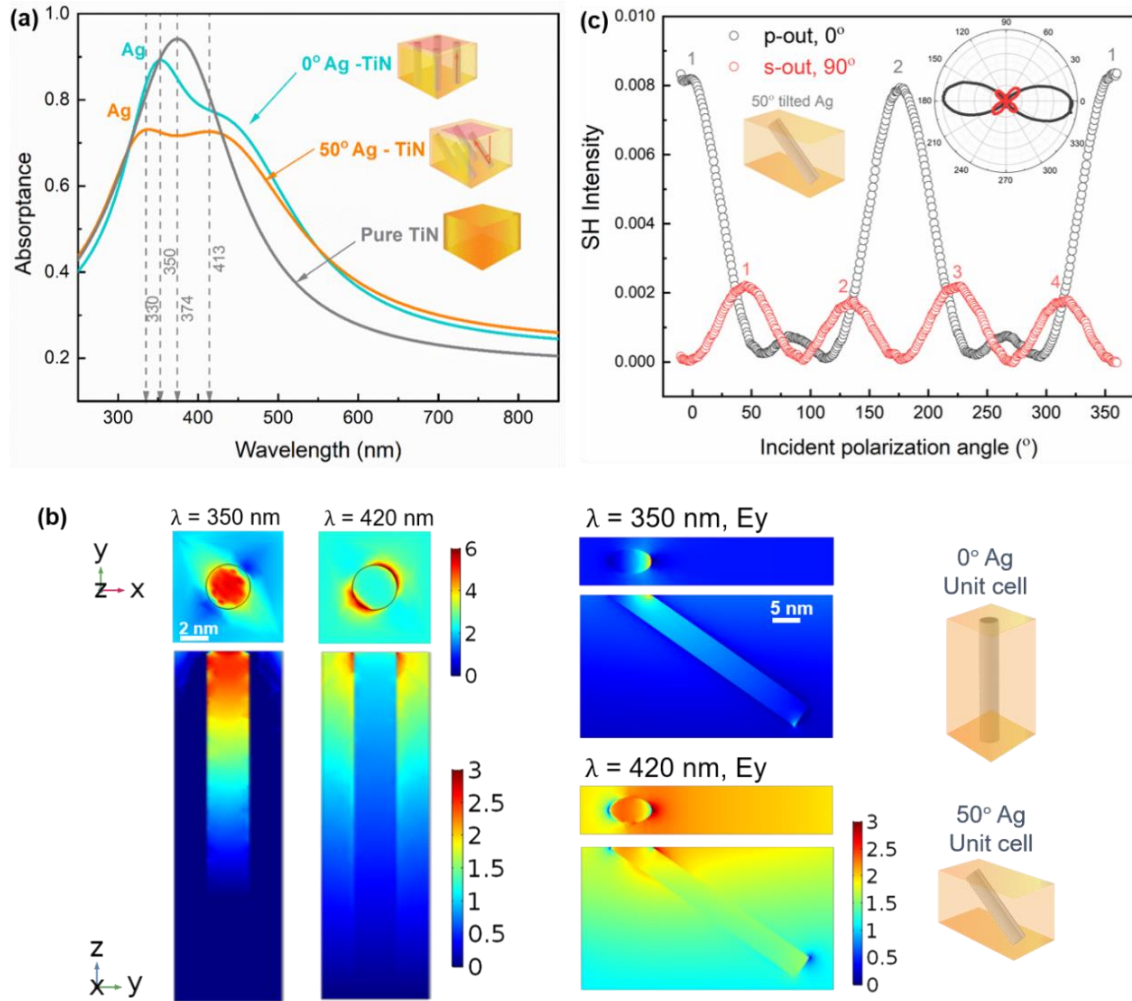


Figure 4.6 (a) Absorbance spectra of pure TiN,  $0^\circ$  tilted Ag-TiN and  $50^\circ$  tilted Ag-TiN hybrid thin films. Two peaks observed at  $330\text{ nm} \sim 350\text{ nm}$  and  $374\text{ nm}$  correspond to Ag SPR and TiN signals. (b) 2D electric field ( $E_y$ ) distribution on  $0^\circ$  tilted Ag-TiN and  $50^\circ$  tilted Ag-TiN hybrid films close to resonant frequencies ( $350\text{ nm}$  and  $420\text{ nm}$ ). (c) SHG of  $50^\circ$  tilted Ag-TiN hybrid film, collected from p- and s- output polarizations, inset is the polar plot of SH intensity.

To demonstrate potential angular selectivity (anisotropy) over a wide spectral range, detailed ellipsometry and Fourier Transform Infrared (FTIR) spectroscopy measurements have been performed. Non-polarized angular reflectance at  $210\text{ nm} \sim 2500\text{ nm}$  range of  $0^\circ$  Ag-TiN and  $50^\circ$  tilted Ag-TiN thin films with thickness of  $45\text{ nm}$ , are retrieved from ellipsometry data and summarized in Figure 4.7. Since the tilt of Ag nanopillars breaks the symmetry along the normal incidence, it is important to differentiate incident beams with respect to the direction of nanopillars. For the sake of convenience, we use the following convention: (1) When the light propagates along tilted nanopillars (or  $[010]$  direction), as shown in Figure 4.7 (a), the incident angles are positive

( $30^\circ \sim 70^\circ$ ); (2) when light propagates in the opposite direction ( $[0\bar{1}0]$  direction), as shown in Figure 4.7 (b), the incident angles are negative ( $-30^\circ \sim -70^\circ$ ). For positive angles of incidence, the overall reflectance drops with increased incident angles due to the enhanced localized plasmonic resonance along the nanopillar interface, reaching a more pronounced dip ( $\sim 10\%$ ) at 400 nm. For negative angles of incidence, however, the reflection is stronger throughout the spectrum range, while the dropped reflectance at higher angles ( $\alpha \leq -60^\circ$ ) could be caused by internal reflection as light propagates inside the film.

The above explanation is supported by the simulated Ey maps (Figure 4.7e), where obvious interface resonance is observed at positive angle excitations (along nanopillar), while enhanced reflectance from Ag nanopillar and metasurface is observed at negative angle excitations. As a comparison, the reflectance from two propagating directions show similar trend in  $0^\circ$  Ag-TiN film (Figure 4.7c-d) with centrosymmetric distribution of electric field, it is certified that the Ag-TiN hybrid film exhibits strong optical anisotropy that is sensitive to the direction of incoming light.

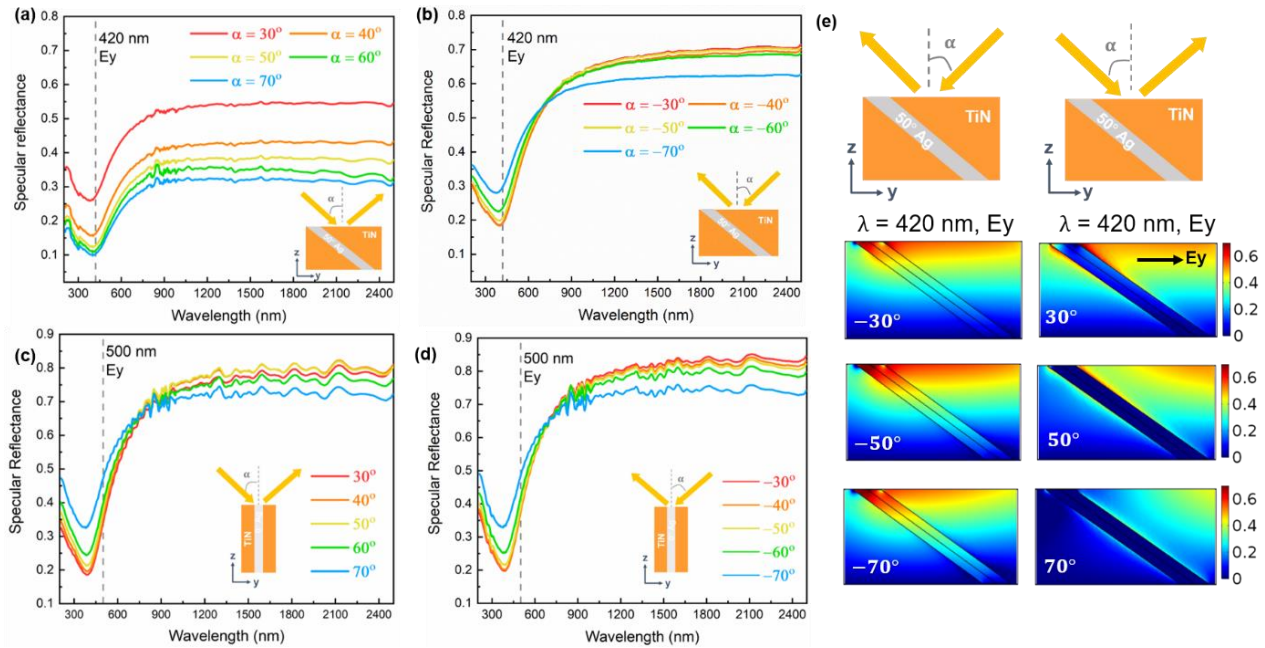


Figure 4.7 Angular dependent specular reflectance. Two sets of data with  $180^\circ$  apart were measured for each sample, as illustrated in the inset images. (a,b) Specular reflectance from  $50^\circ$  Ag-TiN film. (c,d) Specular reflectance from  $0^\circ$  Ag-TiN film. (e) Electrical field maps at 420 nm of the  $50^\circ$  Ag-TiN film.

In addition, the effective refractive index and permittivity of the 50° tilted Ag-TiN and a pure TiN are fitted using a B-Spline model, shown in Figure 4.8. The slight decrease in the extinction coefficient indicates lower losses in this wavelength range for the Ag-TiN hybrid sample. Besides, the hybrid films show a pronounced dielectric tuning towards the infrared regime, as well as a plasma frequency shift, supported by the temperature dependent resistivity (R-T) via the electrical transport property measurement (Figure 4.9).

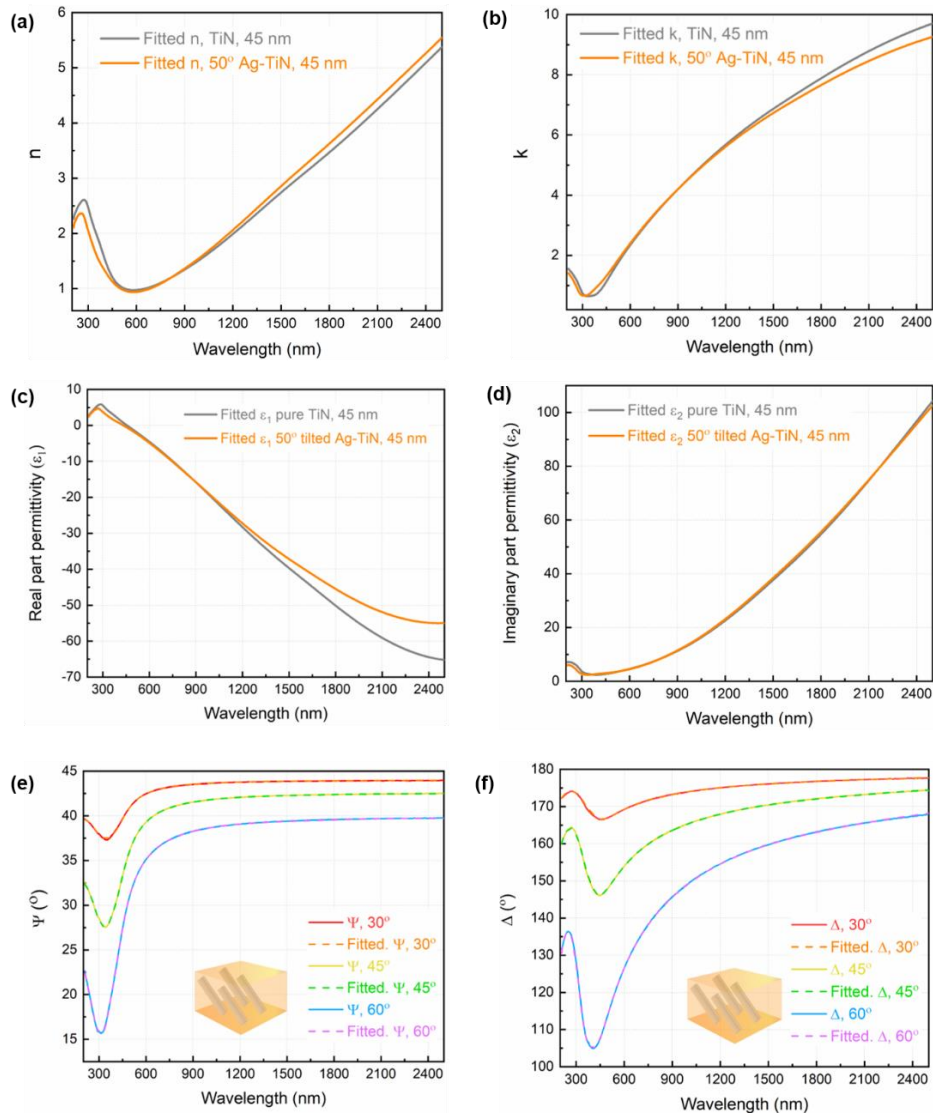


Figure 4.8 (a) Fitted  $n$  and (b)  $k$  of pure TiN and 50° tilted Ag-TiN hybrid film. (c-d) Fitted effective permittivity. (e)  $\Psi$  and (f)  $\Delta$  spectra of 50° tilted Ag-TiN hybrid film and fitted spectra from optical model. Results demonstrate a dielectric tuning of the hybrid film which is more pronounced in the near infrared region. The model is built using B-Spline function of film and MgO on substrate, with MSE of 1.529.

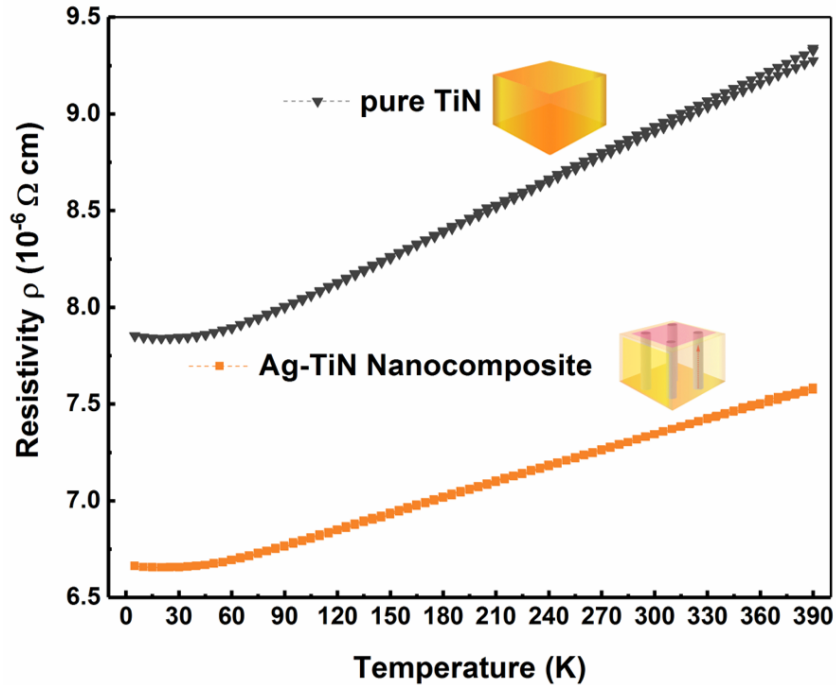


Figure 4.9 Electrical transport properties of pure TiN and 0° tilted Ag-TiN hybrid film. Both films show metallic behavior with increased electron concentrations at elevated temperatures. With addition of Ag phase, the hybrid Ag-TiN film exhibits enhanced conductivity.

In the longer wavelength regime (2  $\mu\text{m}$  to 10  $\mu\text{m}$ ), specular reflectance of the 50° Ag-TiN film was measured by FTIR. Here, the propagation directions of light follow the convention of the sign of angles as described above, where incident angles are set to be  $\alpha = 30^\circ \sim 70^\circ$  and  $\alpha = -30^\circ \sim -70^\circ$  with respect to the pillar geometry. To visualize the angular dependent reflectance, spectra along y-z plane are plotted together with polar plots of reflectance at four arbitrary wavelengths ( $\lambda = 2, 3, 5, 8 \mu\text{m}$ ), as shown in Figure 4.10 (c). It is noted that the asymmetry of the polar plot becomes more pronounced towards short-wavelength IR. The reflectance reaches its maximum around  $\alpha = -30^\circ$  throughout the spectrum (red arrows). Such trend is observed at the visible range as well (Figure 4.10b). Combining the illustration, the angular selectivity or anisotropic behavior of the hybrid film is dominated by tilted nanopillar especially at lower incident angles and shorter wavelengths (2  $\mu\text{m} \sim 5 \mu\text{m}$ ). It is noted that the angular selectivity in this work is modest, but much higher selectivity is expected with improved periodicity and ordering of the nanopillars which are currently under investigation. Highly angular-selective hybrid films are expected to find promising applications as functional nanoantennas, sensors, and related applications.

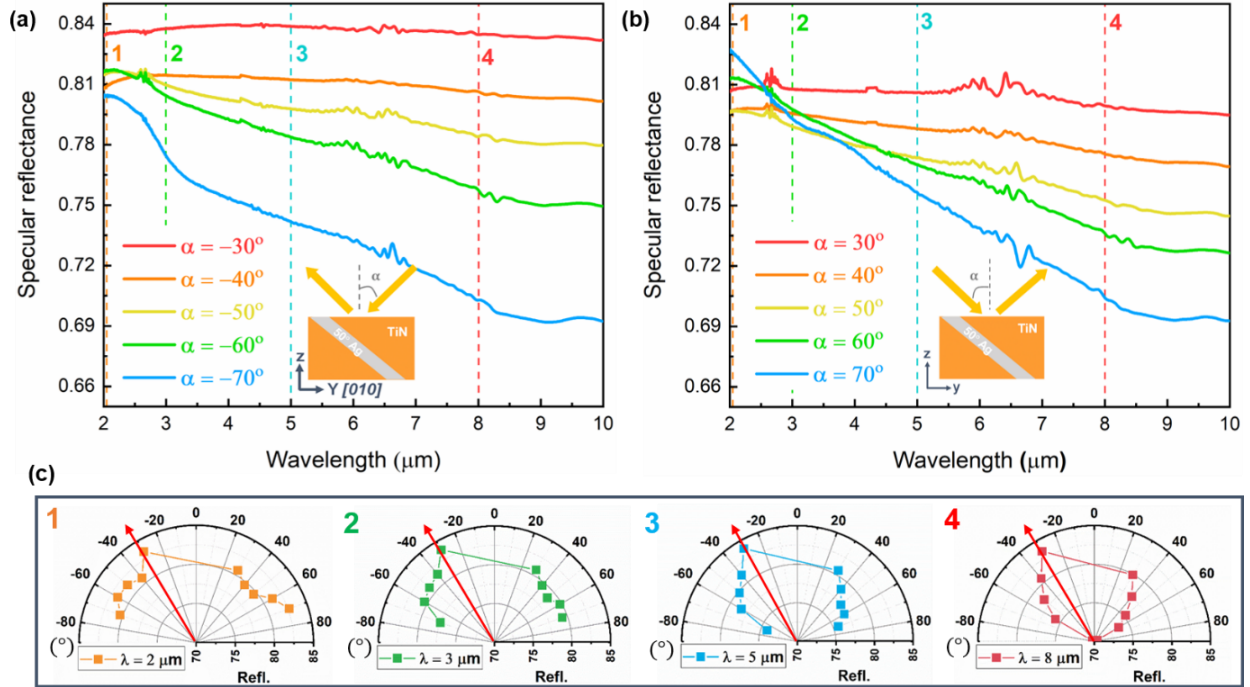


Figure 4.10 Room temperature specular reflectance of 50° tilted Ag-TiN hybrid film. FTIR reflectance spectra grouped by incident light propagating (a) along nanopillar tilting direction ([010]) and (b) backside of nanopillar ([0 $\bar{1}$ 0]), inset images show incident light direction from the cross-sectional view of unit cell. (c) Polar plot showing reflectance intensities versus incident angles at four wavelengths: 2  $\mu\text{m}$  (orange), 3  $\mu\text{m}$  (green), 5  $\mu\text{m}$  (blue) and 8  $\mu\text{m}$  (red).

Metamaterial stability is critical for device applications. Here, a highly stable hybrid nanostructure is achieved by applying TiN as the matrix to encapsulate Ag nanopillars. To test the thermal stability, an as-deposited Ag-TiN sample (grown on MgO) was annealed at 500 °C for one hour under vacuum, followed by ex-situ optical and XRD measurements as shown in Figure 4.11 (a-b). Neither peak-shifting nor peak-broadening has been observed, which indicates excellent phase stability after heat treatment. Furthermore, thermal emissivity measurements provide more evidence of high-temperature stability at the infrared range. The measurement was performed in a high-vacuum chamber coupled with an FTIR spectrometer<sup>[192]</sup>. Three spectra collected at the sample (50° Ag-TiN grown on sapphire) temperatures of 432 °C, 471 °C and 519 °C are shown in Figure 4.11 (c). Results demonstrate very stable emissivity within the temperature range, while the spectrum differs from that of the room-temperature one caused by the incident angles (within  $\pm 32^\circ$ ). The nanopillars maintain their sharpness at sub-micron sized interfaces without any interdiffusion or damage after the high-temperature measurements, as indicated in cross-sectional STEM images shown in Figure 4.11 (d).

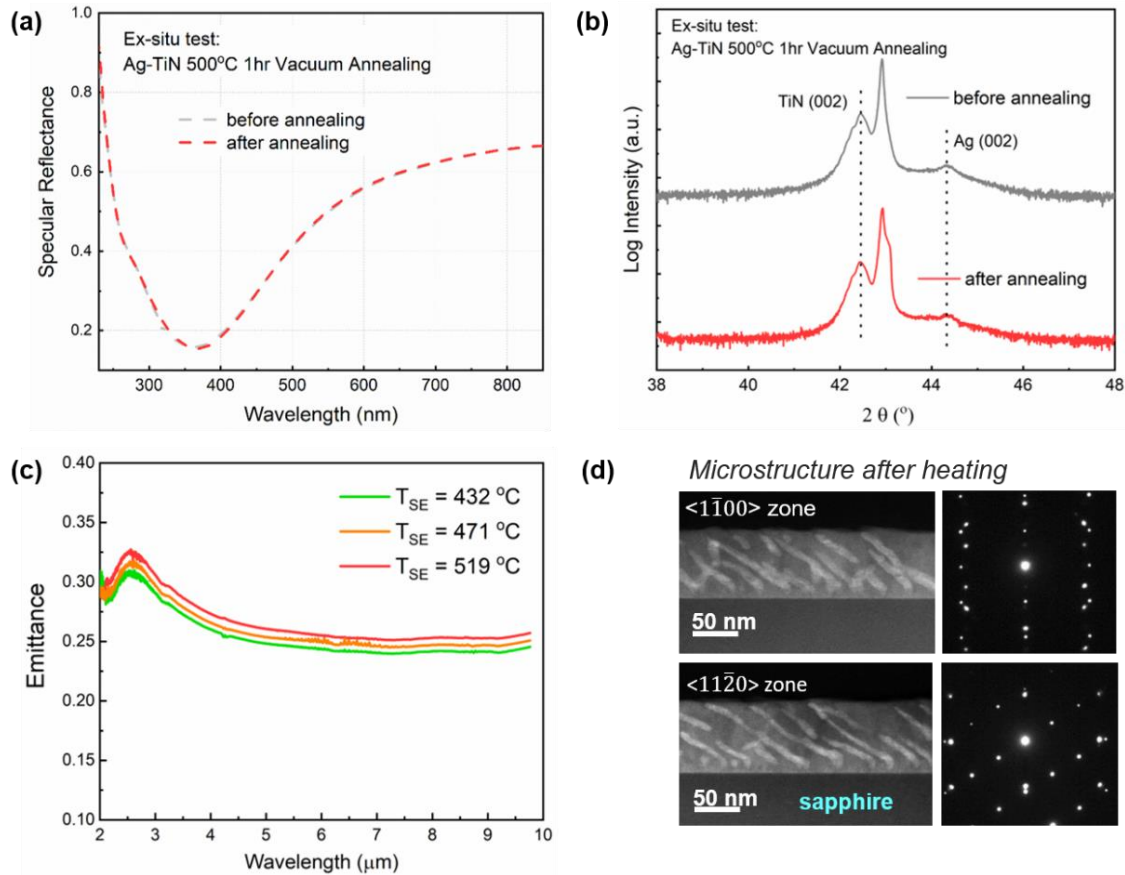


Figure 4.11 Thermal stability tests. (a) Reflectance spectra and (b) XRD  $\theta$ - $2\theta$  scans of Ag-TiN before and after 500 °C 1 hr vacuum annealing. (c) Emissivity spectra measured on a 50° Ag-TiN/sapphire hybrid at sample temperatures of 432 °C, 471 °C and 519 °C. Spectra variations from room-temperature FTIR reflectance spectra may be caused by measurement angle mismatch or temperature effect. (d) Cross-sectional STEM images and diffraction patterns taken from two zones of sapphire substrate,  $\langle 1\bar{1}00 \rangle$  and  $\langle 11\bar{2}0 \rangle$ . The Ag/TiN interface remains clean without interdiffusion and the diffraction patterns remain sharp.

To test the mechanical stability, a set of nanoindentation experiments was performed on thick TiN (1  $\mu\text{m}$ ) and Ag-TiN (600 nm) hybrid films grown on MgO. TiN is known as a refractory coating material with superior hardness ( $H_{\text{TiN}} = 23 - 25 \text{ GPa}$ ) compares to relatively soft noble metals ( $H_{\text{Au}} = 188 \sim 216 \text{ MPa}$ ,  $H_{\text{Ag}} = 250 \text{ MPa}$ ). Figure 4.12 displays the typical loading-unloading plots on indent distance ( $h_c$ ) versus hardness ( $H$ ) and Elastic Modulus ( $E_r$ ). Surprisingly, the averaged  $H$  and  $E_r$  values for Ag-TiN hybrid film ( $H = 32 \text{ GPa}$ ,  $E_r = 337 \text{ GPa}$ ) are comparable to pure TiN film ( $H = 34 \text{ GPa}$ ,  $E_r = 335 \text{ GPa}$ ) without obvious softening induced by the Ag nanopillars. As a comparison to metallic nanostructures or metasurfaces,<sup>[148, 165, 177]</sup> our hybrid thin film metamaterial is durable to thermal vibration, chemical reaction or mechanical

deformation, which plays an important role in maintaining device performance in terms of signal-to-noise ratio or specular sensitivity. More interestingly, this metal-nitride hybrid platform provides enormous opportunities for realizing other nanoscale metal plasmonic structures in which thermal stability and long-term durability could be enhanced significantly.

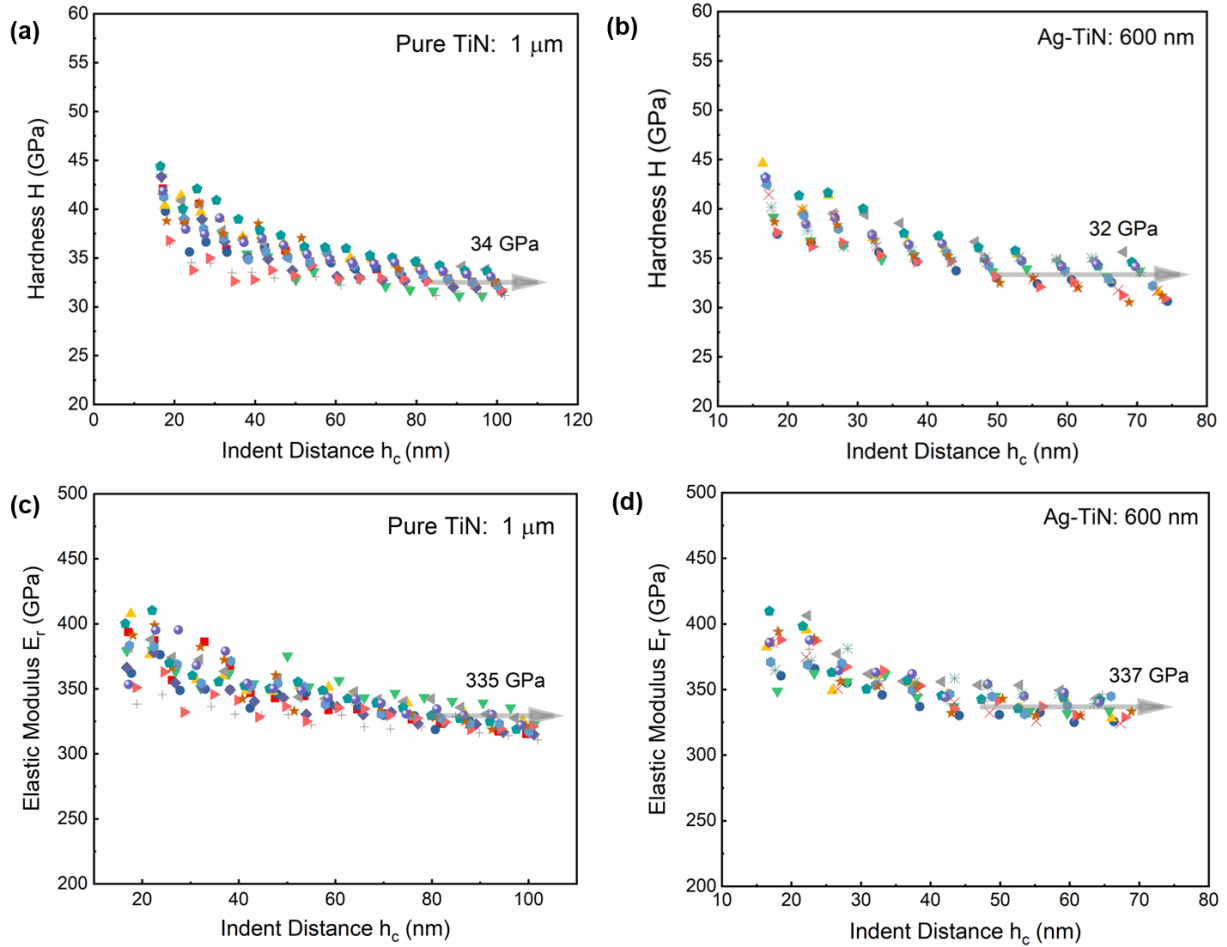


Figure 4.12 Nano-indentation plots on thick TiN and Ag-TiN hybrid films on MgO. Results are retrieved from a set of loading-unloading cycles with dependence of indentation distance. The indent depth is controlled within 12% of film thickness to avoid substrate effect. Hardness data sets of (a) pure TiN bulk film and (b) Ag-TiN hybrid film. Elastic modulus of (c) pure TiN and (d) Ag-TiN hybrid film.

#### 4.4 Conclusion

In this work, self-assembled Ag-TiN nanoscale hybrid plasmonic thin films are demonstrated with tailorable Ag nanopillar tilting geometries and anisotropic optical properties. Distinguished nanopillars with high epitaxial quality are confirmed by XRD and (S)TEM studies.

Tilting of Ag nanopillars is effectively controlled by film growth rate (or adatom flux), i.e., decreased deposition rate facilitates in-plane adatoms diffusion and leads to thermodynamically favored tilted nanopillar growth. The Ag-TiN hybrid material shows strong absorption in the visible regime, with contributions from both Ag and TiN SPRs phases and can be tuned by varying the tilting geometry. Tilted Ag nanopillars offer advantages such as enhanced electromagnetic (EM) interactions at nanopillar interfaces, strong anisotropic interactions with light and tunable dielectric constants, and obvious asymmetric angular selectivity based on the broadband reflectance data in the UV to mid-infrared regime. Combined with high thermal stability and enhanced mechanical integrity, such plasmonic metal-nitride hybrid nanostructures with structural and optical tunability present a promising and unique platform for novel nanoscale metamaterial design incorporating tailored angular and spectral selectivity, along with superior long-term durability.

#### 4.5 Additional Information

Second harmonic generations (SHGs) were measured on an amplified Ti : sapphire laser system at room temperature with central wavelength of 780 nm, laser impinging power of 10 mW and pulse duration of  $\sim 70$  fs. The polarization of the incident light was controlled by a half-wave plate and the SHG signal in the reflection from the sample with an angle of incidence at  $45^\circ$  was measured while with output polarization is fixed at either  $0^\circ$  (p-out) or  $90^\circ$  (s-out).

Specular reflectance ( $2\ \mu\text{m} \sim 10\ \mu\text{m}$ ) at various angles of incidence were measured using Thermo Fisher Nexus 670 Fourier Transform Infrared (FTIR) spectrometer and a specular reflectance accessory (VeeMax II, PIKE Technologies, Inc.). The reference for specular reflectance measurement is a 200 nm Au evaporated on glass slide with Ti adhesion layer. High-temperature emissivity is measured by a high vacuum chamber coupled with an FTIR spectrometer with a liquid nitrogen cooled mercury cadmium telluride (MCT) detector and an XT-KBr beam splitter (Thermo Fisher Nexus 670). Details of high-temperature emissivity measurement can be found elsewhere.<sup>[192]</sup>

Nano-indentation experiment was performed on a Bruker Hysitron TI Premier instrument. A set of loading-unloading cycles were applied with changes on indent distance, which is controlled within 12% of film thickness to avoid substrate effect.

*COMSOL Multiphysics Wave Optics Module* with frequency domain is applied for optical simulation. Optical constant for Ag is taken from Rakic,<sup>[193]</sup> while refractive index for TiN is retrieved from ellipsometry measurements. The simulated geometry is based on the cross-sectional STEM images, including the film thickness, Ag tilting angles, nanopillar dimension and the inter-pillar distance. The unit cell of hybrid film is set as one pillar in matrix with periodic boundaries, resulting in a perfect ordering of pillar-in-matrix geometry. A plane wave source with depolarized light of the electric field was applied. Angular dependent reflectivity (R%) is simulated with changes of incident angle ( $\alpha$ ) from 30° to 60°.

## 5. ALUMINUM NITRIDE-BASED HYBRID THIN FILMS WITH SELF-ASSEMBLED PLASMONIC GOLD AND SILVER NANOCOMPOSITES<sup>‡</sup>

### 5.1 Overview

Aluminum nitride (AlN)-based two-phase nanocomposite thin films with plasmonic Au and Ag nanoinclusions have been demonstrated using a one-step thin film growth method. Such AlN-based nanocomposites, while maintaining their wide bandgap semiconductor behavior, present tunable optical properties such as bandgap, plasmonic resonance, and complex dielectric function. Depending on growth atmosphere, the metallic nanoinclusions self-organized into different geometries, such as nano-dendrites, nano-disks, and nanoparticles, providing enhanced optical anisotropy in-plane and out-of-plane. The infrared transmission measurements demonstrate the signature peaks of AlN as well as a broad transmission window attributed to the plasmonic nanoinclusions. This unique AlN-metal hybrid thin film platform provides a route to modulate the optical response of wide bandgap III-V nitride semiconductors towards infrared sensing or all optical based integrated circuits.

### 5.2 Introduction

Plasmonic nanostructure is known by its outstanding properties in manipulating light-matter interactions, owing to the surface plasmon polaritons (SPPs) and localized surface plasmon resonance (LSPRs). The famous example of Lycurgus cup<sup>[19]</sup> with Au nanoparticle color centers is known for centuries, opens the route for artificial (meta)material designs in combining metallic nanostructures in different material media for multi-functionalities. With a pronounced difference in electromagnetic parameters, metal-dielectric combination at nanoscale is of great interest. It induces SPR that have various applications, including photovoltaic and photocatalytic devices<sup>[194]</sup>, bio-medical sensing<sup>[131]</sup>, integrated nanophotonic circuits<sup>[127]</sup>, etc. From materials science perspective, the metal-dielectric metamaterial can be termed nanocomposite, namely two- or

---

<sup>‡</sup> This chapter is reprinted with permission from “AlN-based hybrid thin films with self-assembled plasmonic Au and Ag nanoinclusions” by X. Wang, et al., *Appl. Phys. Lett.* **2019**, *114* (2), 5.

multi-phase materials that are physically or/and chemically fabricated into a whole unit. Limited success has been made in the areas of metal-oxide hybrid thin film systems.<sup>[195-196]</sup>

Wide bandgap semiconductors, especially the III-V nitride family including GaN, AlN, and their alloys, have been widely explored for optoelectronic devices such as solid state lasers, solid state lighting, and photovoltaics, as well as high power electronics.<sup>[197-199]</sup> On the other hand, research directions on exploring new materials towards future all optical based integrated circuits excite the community in searching for various materials with a wide range of optical tunabilities. An effective approach is to combine the plasmonic nanostructure designs with the nitride based dielectric materials to achieve such tunability. Very recently an initial demonstration of the epitaxial growth of vertically aligned nanocomposite of metal-transition metal nitrides, such as Au-TaN or Ag-TiN<sup>[144, 200]</sup> has suggested the possibilities of integrating such dissimilar materials together in a hybrid material form. However, such integration focused on two plasmonic systems with limited tunabilities of dielectric function. It is expected that incorporating metallic nanoinclusions into dielectric III-V nitride systems could present a large range of optical tunabilities, especially the complex dielectric functions in a wide optical range. However, such demonstration is very challenging and has not yet been realized, largely due to the complexity in different growth conditions of metal and the III-V nitrides as well as their lattice compatibility, as plasmonic metals are mostly in FCC structures while III-V nitrides are Wurtzite (hexagonal close packed).

In this work, we demonstrate the possibility of incorporating plasmonic Au and Ag nanoinclusions in III-V nitrides with various geometries. As a model system, we selected AlN as the matrix material for this demonstration. AlN presents a wide bandgap of  $\sim 6$  eV and has been widely incorporated in III-V-based optoelectronic devices as effective buffer for GaN growth, and alloy components for bandgap tuning.<sup>[124, 201-202]</sup> AlN has also shown piezoelectric properties for MEMS<sup>[203]</sup>, microwave (GHz) filters,<sup>[204], [205]</sup> as well as other optical capabilities<sup>[206-207]</sup>. These unique properties make AlN an ideal candidate for optoelectronic based applications as compared to most oxides. By careful control of the growth conditions, the Au and Ag nanoinclusions in AlN present various geometries and offer pronounced tunabilities in bandgap, optical absorption, dielectric function and anisotropy, as well as plasmon resonance at the mid-infrared range. Furthermore, such hybrid systems can also be integrated on Si substrates for the FTIR measurements demonstrated in this work.

### 5.3 Results and Discussion

To identify the growth orientation and crystalline quality of metal-AlN hybrid thin films, the as-grown AlN/sapphire, Au-AlN/sapphire and Ag-AlN/sapphire thin film samples were characterized using XRD. The  $\theta$ - $2\theta$  scans from  $32 \sim 45^\circ$  were collected and displayed separately in Figure 5.1. Pure AlN (5.1a) grown on c-cut sapphire exhibits a strong (0002) *h*-AlN peak at  $35.735^\circ$ , which is close to other literature reports.<sup>[208]</sup> On the other hand, multiple peaks have been observed in the nanocomposite samples (5.1b, c), where (111) Au at  $38.220^\circ$ , (111) Ag at  $38.117^\circ$  and a weak (002) Ag at  $44.334^\circ$  are identified. Such strong and sharp metal peaks indicate good crystallinity as well as clear phase separation of the metallic phase. Meanwhile, the (0002) AlN growth is suppressed as seen from a broader (0002) AlN peak and an additional peak at  $40.41^\circ$  in the Au-AlN nanocomposite film. The (0002) AlN position remains almost identical in three samples ( $\sim 35.7^\circ$ ), which indicates the interfacial strain between AlN and sapphire substrate is unaffected by introducing secondary phase, and the (0002) AlN is expected to dominate the initial thin film growth.

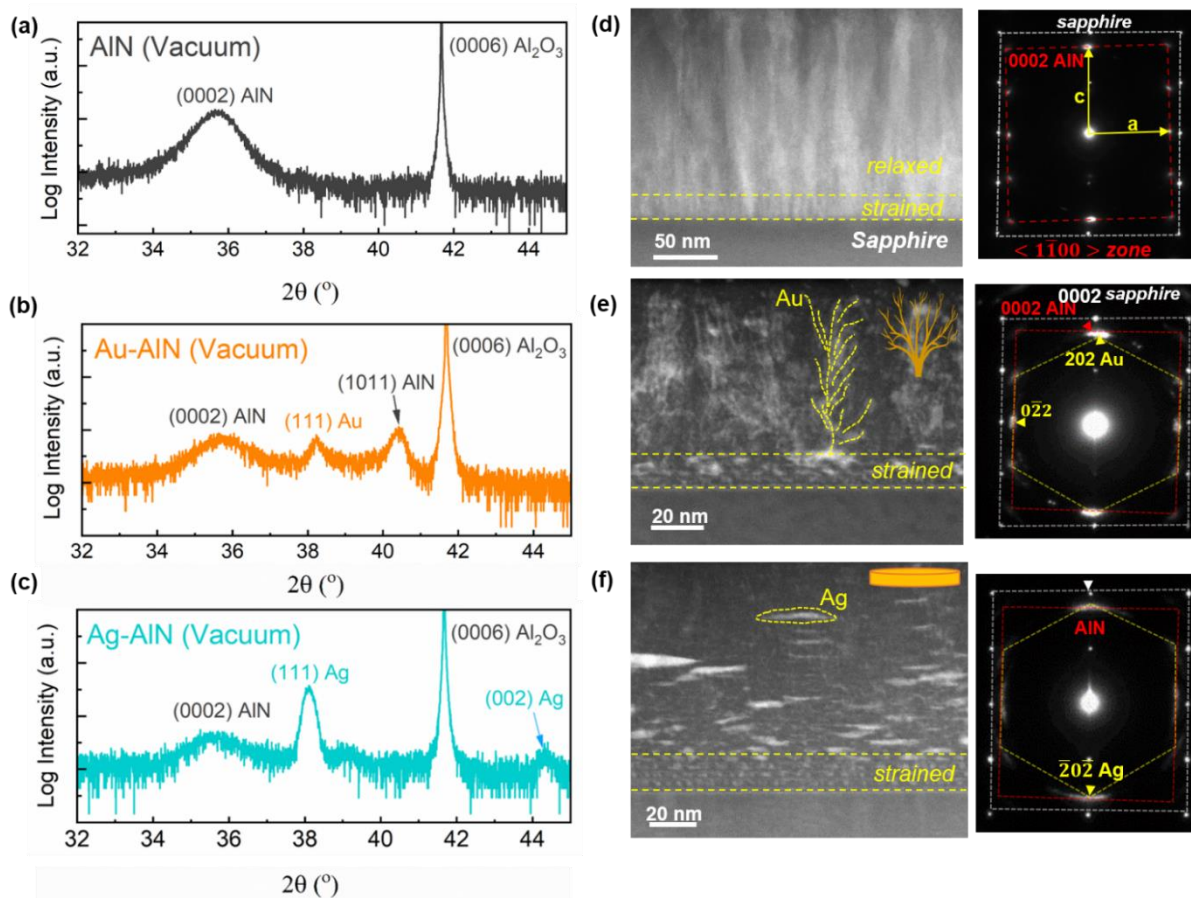


Figure 5.1 XRD  $\theta$ - $2\theta$  scans of vacuum grown films: (a) AlN (b) Au-AlN and (c) Ag-AlN on c-cut sapphire substrate. HAADF-STEM images (left) and corresponding SAED patterns of (d) AlN on sapphire, (e) Au-AlN on sapphire and (f) Ag-AlN on sapphire. Samples were viewed from  $\langle 1\bar{1}00 \rangle$  zone axis.

The microstructures were further explored using Scanning Transmission Electron Microscopy (STEM), the STEM images are coupled with selected area diffraction patterns (SAEDs) from the  $\langle 1\bar{1}00 \rangle$  zone axis. Pure AlN film, in Figure 5.1 (d), shows a columnar growth as typically seen in AlN with a sharp film-substrate interface. As expected, Au-AlN (Figure 5.1e) and Ag-AlN (Figure 5.1f) are self-assembled into two phases. Clear diffraction patterns (DPs) indicate the high epitaxial quality of the films. Interestingly, their morphologies are vastly different. With the same metal density, the Au nano-inclusions are dendritic-like nanostructure (as illustrated in Figure 5.1e) which is very fine and dispersed; While Ag adatoms agglomerated into “nano-disks” with sharp boundaries. Careful comparisons of the STEM images indicate that at the initial ( $\sim 15$  nm) growth stage, both Au and Ag appear as very fine particles with well-ordered arrangement

within AlN. These particles are grown as seeds to direct the self-assembling process and phase separation in the later growth stage. Refer to the XRD results, there is about 14.25% interfacial strain between (0002) AlN ( $2\theta = 35.735^\circ$ ) and (0006) sapphire ( $2\theta = 41.672^\circ$ ), which means the initial AlN layer could be highly strained. Therefore, it is possible that the well-ordered Au (Ag) nanoinclusions serve to compensate the large strain between AlN and sapphire substrate in the initial growth stage. Once the films reach their critical thickness, a self-organized growth of the metallic phases, either as dendritic-like or disk-like nanostructures, start in the second stage. In the second stage, the morphologies are largely resulted from the different surface energies between the metal and AlN and the growth kinetics. The surface morphology of the two nanocomposites were further examined using scanning electron microscopy (SEM). As seen from Figure 5.2, the Au and Ag are agglomerated with uniform distribution on the top surface, which could be important for potential applications such as light harvesting or enhanced Raman sensing. Beside the films grown in vacuum, we explored the nanocomposite growth in the backpressure of N<sub>2</sub> (50 mtorr) for both Au-AlN and Ag-AlN on sapphire. The TEM and EDS results are displayed in Figure 5.3. Under N<sub>2</sub> atmosphere, both Au and Ag self-organize into much more confined nanoparticles (NPs). These results suggest the growth morphologies are largely controlled by the growth kinetics during the deposition.

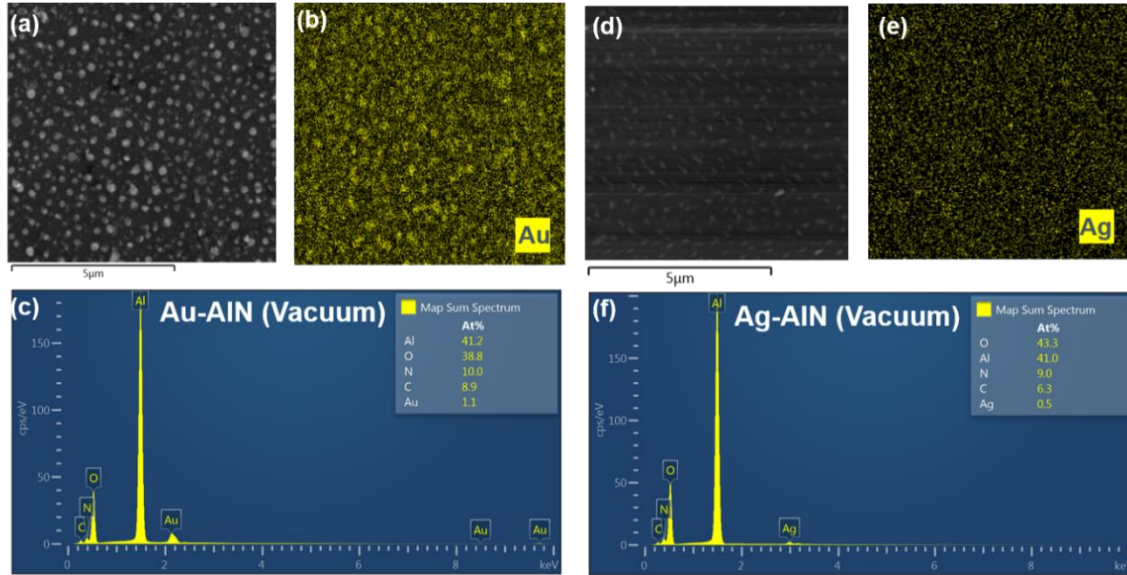


Figure 5.2 (a) SEM of Au-AIN (Vac) sample viewing from top, showing the saturation of Au particles at top surface. (b) EDX mapping of Au. (c) EDX spectrum of critical elements, including Al, O, N, and Au. (d) SEM of Ag-AIN (Vac) sample viewing from top, showing similarly the Ag saturation. (e) EDX mapping of Ag. (f) EDX spectrum of critical elements: O, Al, N, Ag. The quantified Au (Ag) atomic fraction is approximately 8.35 at% (4.65 at% for Ag), note that substrate ( $\text{Al}_2\text{O}_3$ ) signals could contribute to errors.

Self-organized Au and Ag nanoinclusions acting as plasmonic resonators inside AlN are expected to tune the overall physical properties. A set of optical transmittance (T%) and reflectance (R%) measurements from 200 nm ~ 1500 nm was performed on all five samples: AlN, Au-AIN (Vacuum), Ag-AIN (Vacuum), Au-AIN ( $\text{N}_2$ ) and Ag-AIN ( $\text{N}_2$ ). Compared to pure AlN (Figure 5.4a), the attenuated transmittance (~ 30%) intensities of the nanocomposite films are contributed to the strong absorption at resonance frequency and enhanced reflectance intensities (~ 35%) of the metallic phases. Specifically, plasmonic resonance is estimated from the absorbance spectra ( $A = 1 - R - T$ ) (Figure 5.4c), with Au at 352 nm and Ag at 445 nm, the variations of the resonance are mainly affected by the nanoinclusion morphology, and are overall in consistent with other reported values<sup>[209]</sup>. According to the T% spectra (Figure 5.4 a), *Tauc* plot was applied to retrieve the bandgaps of three samples, and  $(\alpha h\nu)^2$  as a function of photon energy is plotted in Figure 5.4 (b). From the *Tauc* plot, bandgap tuning is effectively achieved through adding the metallic nanoinclusions. The bandgap of AlN thin film is 5.36 ~ 5.48 eV, while Au-AIN and Ag-AIN are both reduced to 4.63 ~ 4.72 eV and 4.76 ~ 4.85 eV, respectively. Such optical tuning is possibly related to the change of charge carrier density in the systems because of the metallic nanoinclusions.

Electrical transport measurements were conducted on the samples in a temperature range from 3K to 390 K. Figure 5.4 (d) shows the resistivity versus temperature (3 K ~ 390 K) plot. Both Au-AlN and Ag-AlN films show obvious semiconductor behavior but with much enhanced conductivity (AlN, not shown here, is out of range in the transport measurement). The optical properties of the nanocomposites grown in N<sub>2</sub> are shown in Figure 5.7 (a), where more ordered nanoparticles exhibit pronounced plasmonic resonance, namely, the 440 nm of Ag NPs and 540 nm of Au NPs that are consistent with reported studies.<sup>[209]</sup> Note that variations of T% of films grown in different environment are owing to the geometry and dimension of nano-inclusions. For example, the dendritic Au as compared to Au NPs are rather dispersed, such that the plasmonic resonance is blue shifted and the overall extinction is higher.

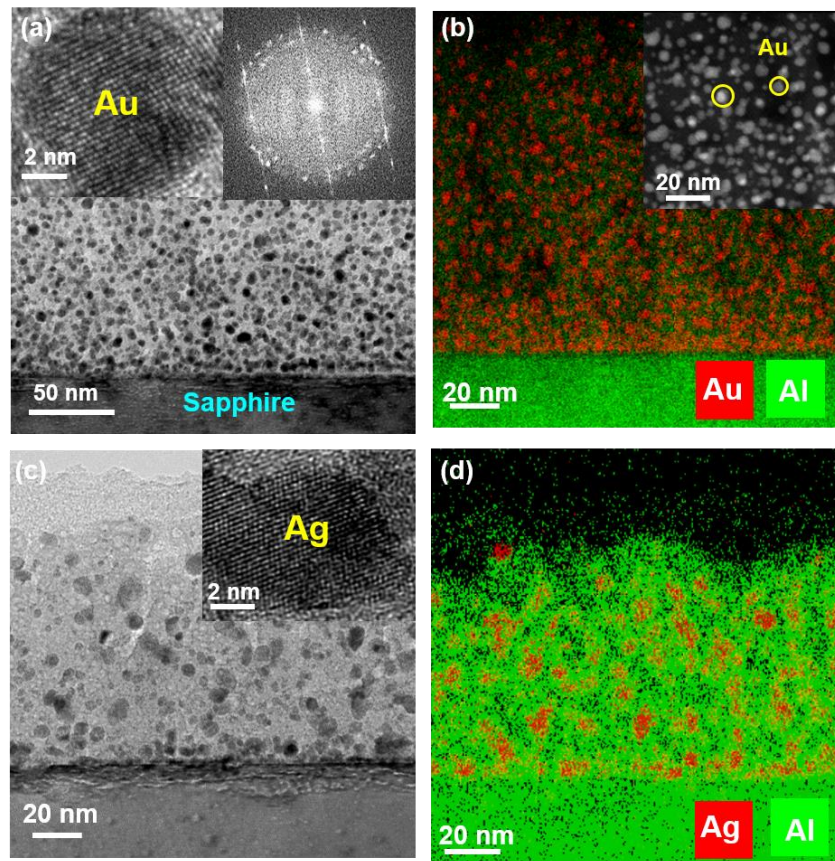


Figure 5.3 (a) TEM image of Au-AlN nanocomposite grown in 50 mtorr N<sub>2</sub>, insets are high resolution image of Au nanoparticle, and selected area electron diffraction (SAED) patterns of the film. (b) EDX mapping of Au-AlN (N<sub>2</sub>) sample, inset is corresponding STEM image with Au NPs marked out in yellow circles. Elements including Au and Al are mapped in red and green, respectively. (c) TEM image of Ag-AlN (N<sub>2</sub>) sample, inset is HRTEM image of Ag nanoparticle. (d) EDX mapping of Ag-AlN (N<sub>2</sub>).

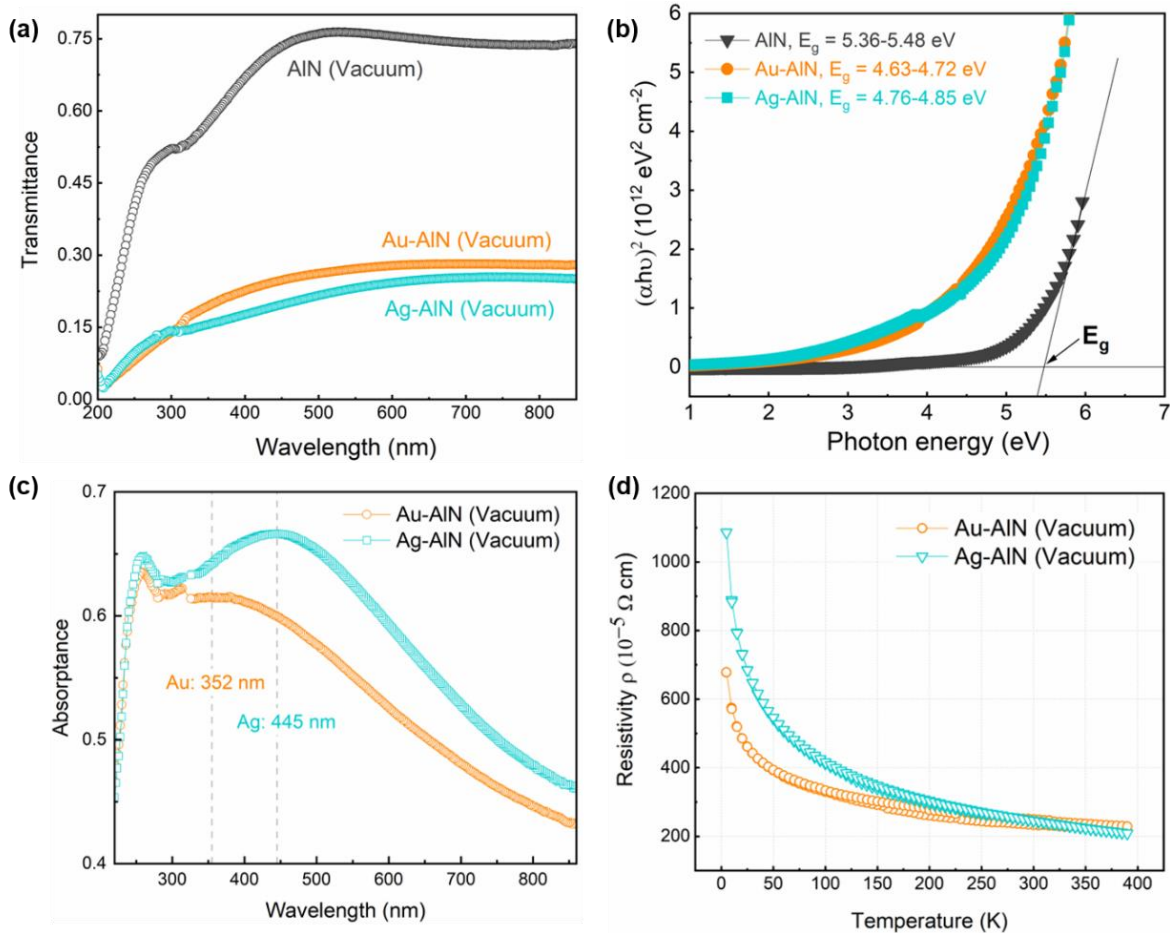


Figure 5.4 (a) Transmittance spectra of pure AlN, Au-AlN and Ag-AlN films grown in vacuum condition. (b) Tauc plot of the bandgap. (c) Absorbance spectra of the two nanocomposites, calculated from  $A = 1 - R - T$ . (d) Resistivity versus temperature curves of Au-AlN and Ag-AlN films, note that pure AlN resistivity is out of range.

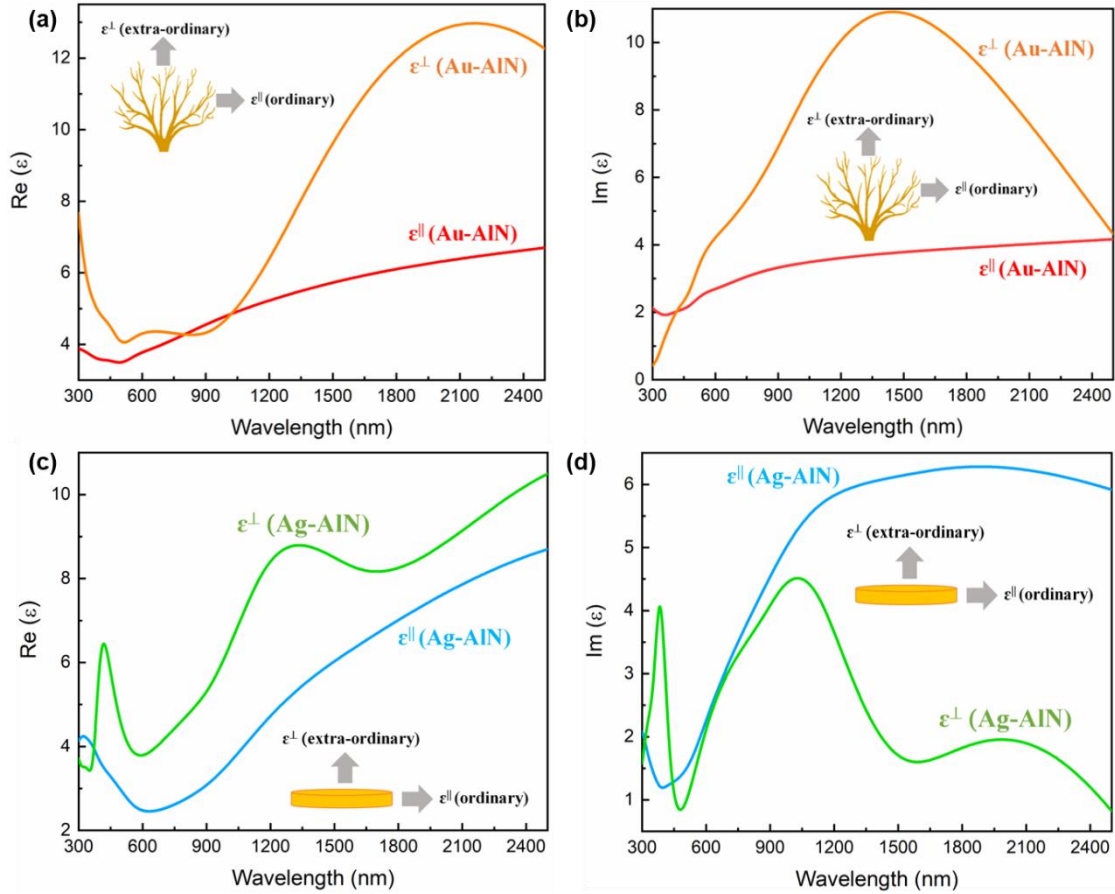


Figure 5.5 Optical parameters of  $\epsilon_1$  of Au-AIN and Ag-AIN films grown in vacuum. (a) Anisotropic  $\epsilon_1$  of Au-AIN, and (b) corresponding  $\epsilon_2$  values. (c) Anisotropic  $\epsilon_1$  of Ag-AIN, and (d) corresponding  $\epsilon_2$  values, inset images illustrate in-plane ( $\parallel$ ) and out-of-plane ( $\perp$ ) direction with respect to the Au and Ag geometries.

Ellipsometry parameters ( $\Psi, \Delta$ ) in a broad spectral range (210 nm ~ 2500 nm) were collected to retrieve effective optical parameters. The addition of secondary phase breaks the overall symmetry of the hybrid films, the fitting models were treated as anisotropic models such that the in-plane (ordinary) and out-of-plane (extra-ordinary) parameters can be specified (Figure 5.5). Comparing the anisotropic dielectric constants in the two films with Au and Ag nano-inclusions, we observe a significant difference between the ordinary ( $\parallel$ ) and extraordinary ( $\perp$ ) values. Specifically, the nano-dendritic Au-AIN one with out-of-plane Au nano-inclusions induces more optical oscillations in the perpendicular direction, represented by much larger  $\epsilon_{1\perp}$  value (Figure 5.5a,b). On the other hand, Ag-AIN with Ag nano-disks exhibits stronger metallic property in-plane as seen from its lower  $\epsilon_{1\parallel}$  and larger  $\epsilon_{2\parallel}$  values (Figure 5.5c,d). The isotropic optical parameters of pure AIN and nanocomposite films are displayed in Figure 5.6. Again, with

plasmonic metallic nanoinclusions, the films are still semiconducting ( $\epsilon_1 > 0$ ) in the measured spectrum range, but with much broader range of dielectric tuning as a function of the wavelength (Figure 5.6b). The decreased real part of the dielectric constants ( $\epsilon_1$ ) at lower wavelength range (300 nm ~ 1200 nm) is mainly affected by the metallic nanoinclusions while the films behave more dielectric at near infrared regime (NIR). Detailed ellipsometric parameters and fitted optical constants of Au-AIN ( $N_2$ ) and Ag-AIN ( $N_2$ ) are shown in Figure 5.7.

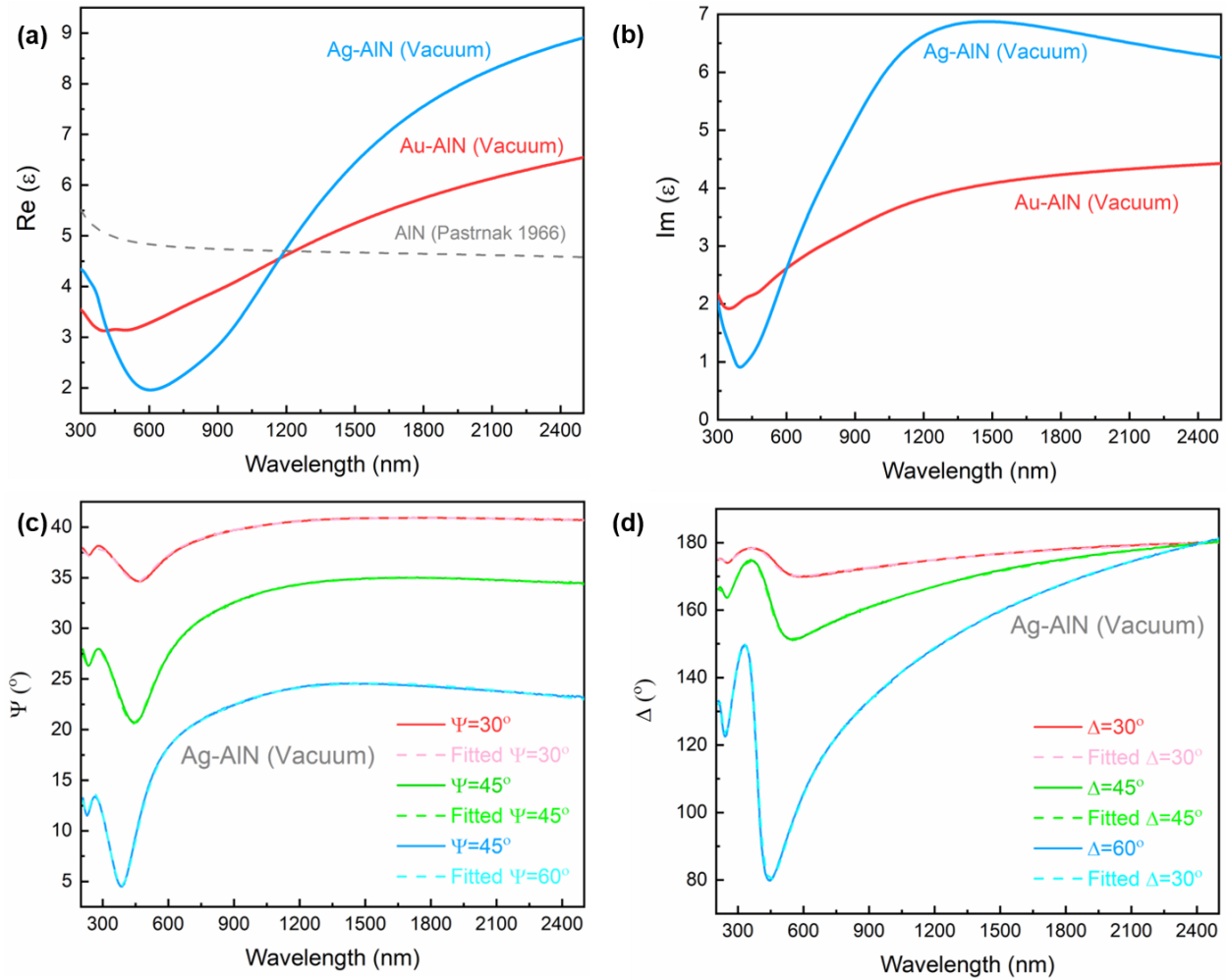


Figure 5.6 Ellipsometry fitted (a) real part dielectric constant and (b) imaginary part of Ag-AIN (Vac) and Au-AIN (Vac) films. (c, d) Raw and fitted ellipsometric parameters ( $\Psi, \Delta$ ) of the vacuum grown Ag-AIN (Vac) to show the accuracy of data fitting.

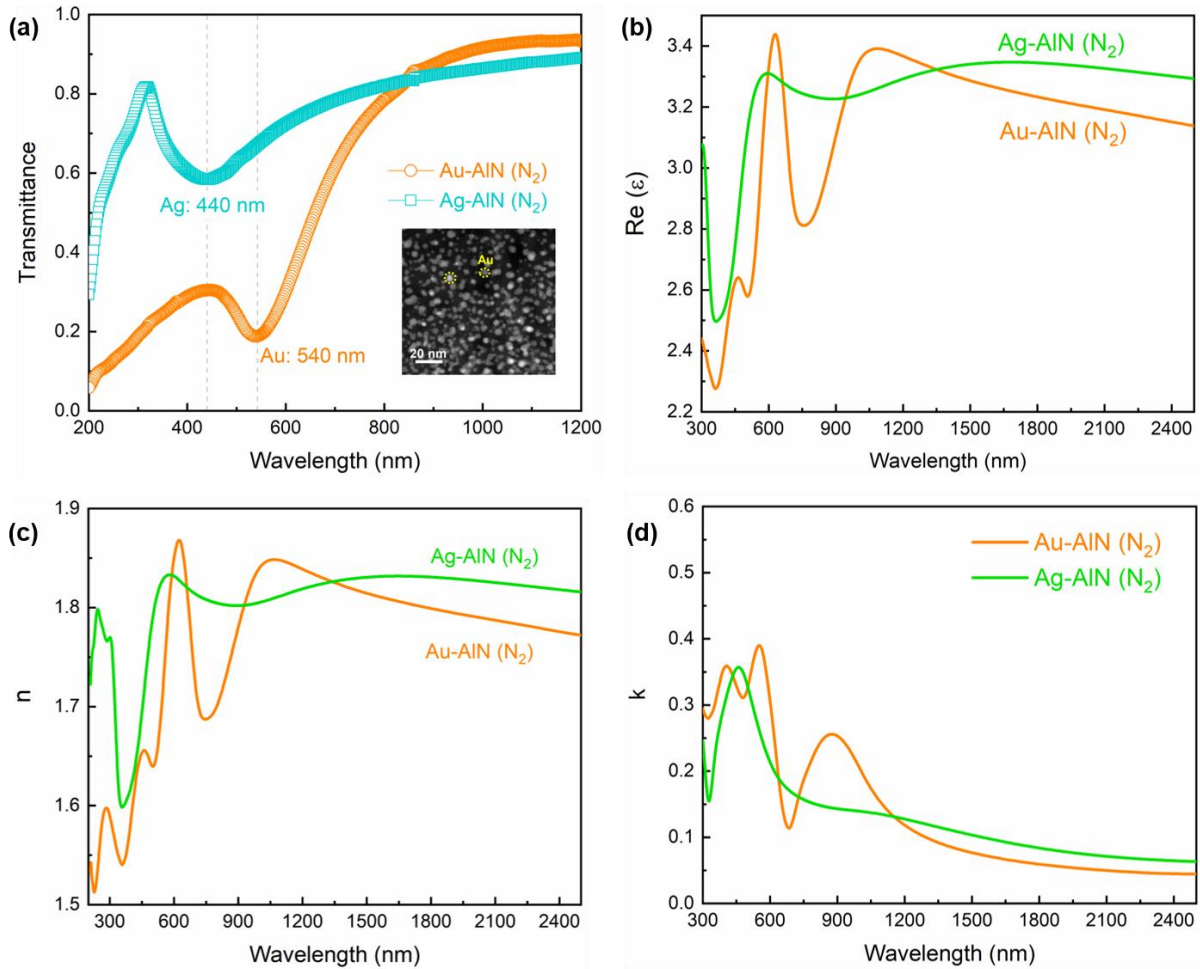


Figure 5.7 Optical properties of Ag-AIN and Au-AIN films grown in  $N_2$ . (a) Transmittance spectra with inset STEM image showing the Au nanoparticles being embedded in nanocrystalline AIN matrix. (b-d) Fitted dielectric constant, effective refractive index of Ag-AIN ( $N_2$ ) and Au-AIN ( $N_2$ ) films.

Infrared (IR) properties of metal-AIN hybrid films (vacuum grown) were further investigated using FTIR. The measurement was conducted using a transmission setup with a built-in polarizer (s-pol and p-pol). Here, the two edges of the thin film samples were polished to wedge angles ( $45^\circ$ ) to allow multiple bounces in the film, such that light-matter interactions would be strong for enhanced signal. As illustrated in Figure 5.8 (insets), the number of bounces inside film is calculated using:

$$N = l \div t$$

where  $l$  is the width of polished sample, and  $t$  is film thickness. For more accurate comparison, we controlled the number of bounces of all the measured samples ( $N \sim 6$ ), and the resulted spectra in Figure 5.8 are calculated from:

$$T = \frac{T_{sample}^{p-pol}}{T_{background}^{p-pol}} \div \frac{T_{sample}^{s-pol}}{T_{background}^{s-pol}}$$

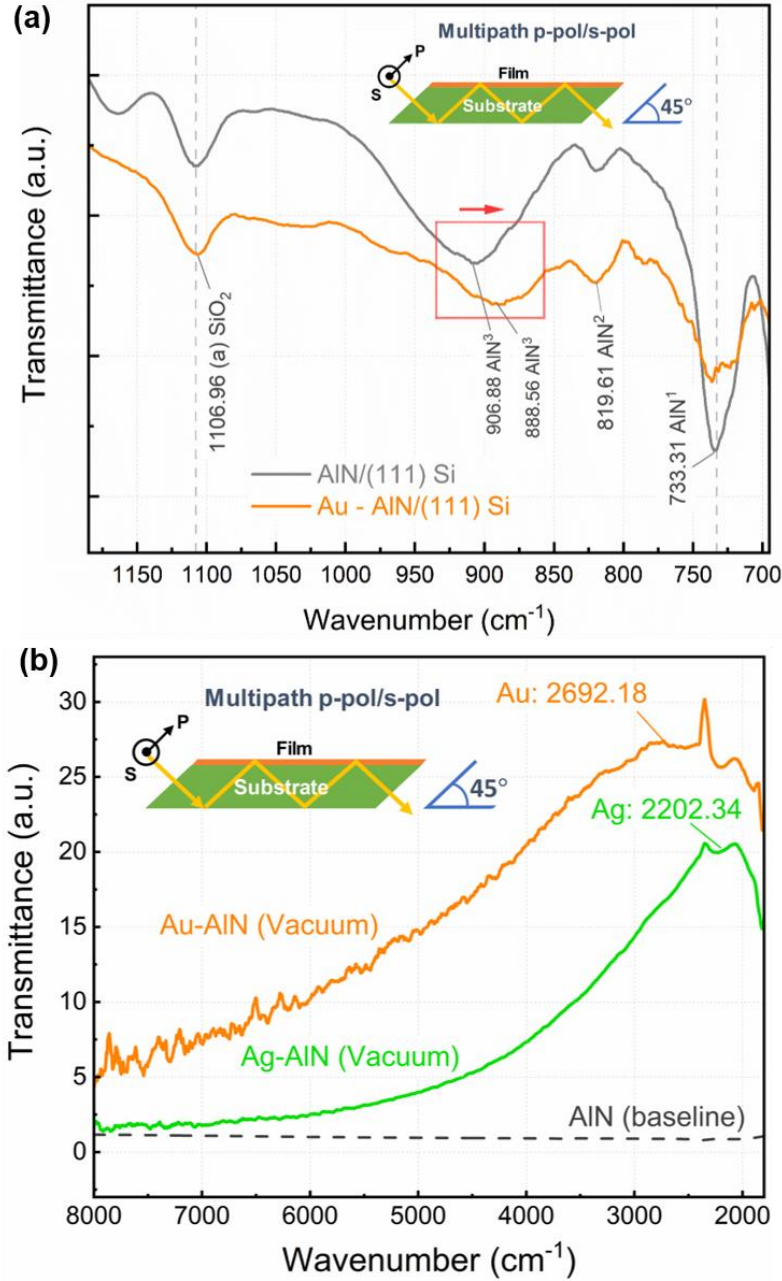


Figure 5.8 (a) Mid-IR transmittance spectra of AlN/Si and Au-AlN/Si samples grown in vacuum, inset is the illustration of optical path through the sample. (b) Transmittance spectra in the near-IR range of Au-AlN/sapphire and Ag-AlN/sapphire, AlN spectrum is applied as baseline. Note that the transmittance is taken from ratio of p-pol intensity/s-pol intensity.

The mid-IR spectra were collected for films grown on (111) Si substrates due to the wide transparency range of Si ( $1.2 \mu\text{m} \sim 15 \mu\text{m}$ ). Transmittance spectra of AlN/Si and Au-AlN/Si samples are shown in Figure 5.8 (a). The strong dip at  $\sim 733.31 \text{ cm}^{-1}$  is assigned to  $E_1$  (TO) mode of AlN (active phonon mode), and a wider dip at  $906.88 \text{ cm}^{-1}$  (AlN/Si) and  $888.56 \text{ cm}^{-1}$  (Au-AlN/Si) corresponds to the  $A_1$  (LO) mode of AlN, namely the longitudinal optic phonons.<sup>[210]</sup> Note that a minor shift ( $\sim 18 \text{ cm}^{-1}$ ) is related to the Au addition. A weak dip at  $\sim 819.61 \text{ cm}^{-1}$  corresponding to  $E_1$  (LO) mode is caused by cubic-AlN phase, and another defect at  $\sim 1106 \text{ cm}^{-1}$  belongs to a very thin amorphous  $\text{SiO}_2$  layer on (111) Si substrate. Next, the spectra at near IR were collected of films grown on c-cut sapphire. In this regime, we are more interested to observe any signatures from the plasmonic counterparts. Therefore, the pure AlN spectrum is applied as background for the Au-AlN and Ag-AlN nanocomposite films. Figure 5.8 (b) shows the spectra after baseline correction, where a pronounced transmission window is observed, with peak positions at  $2692.18 \text{ cm}^{-1}$  for Au, and  $2202.34 \text{ cm}^{-1}$  for Ag. The sharper resonance of Ag is possibly due to a more confined geometry (nano-disks) as compared to relatively dispersed Au nanostructures. This infrared transmission window is correlated with accumulative scattering effect and/or the higher order surface plasmon polaritons (SPP) modes from the dispersed Au (Ag) nano-inclusions.<sup>[211]</sup> Such unique properties demonstrate tuneable IR resonance, and can be further explored for potential sensing applications.

## 5.4 Conclusion

In this work, a two-phase plasmonic metamaterial system of metal-AlN with plasmonic Au and Ag nano-inclusions have been demonstrated. Different nanoscale morphologies including dendritic-like Au and disk-like Ag have been formed under high vacuum growth, while under  $\text{N}_2$ , uniform nanoparticles are self-organized in AlN. Based on the hybrid film geometries, optical spectra, coupled with electrical transport (R-T) measurements, demonstrate effective bandgap tuning, a change of electronic states, as well as enhanced absorption attributed to plasmonic color-centers. The two-phase nanocomposites exhibit obvious optical anisotropy in terms of effective dielectric constants, while maintaining their semiconductor nature. We further tested the IR transmission property and identified the (LO), (TO) AlN signature peaks (dips) in both pure AlN and Au-AlN films. In addition, plasmonic inclusions enable a broad transmission window in the mid IR range of the nanocomposites. This initial demonstration of plasmonic nano-inclusions in

III-V nitrides presents a unique platform for designing metal-semiconductor metamaterials for optoelectronics and all optical-based integrated circuits on sapphire or Si substrates.

### **5.5 Additional Information**

Fourier transform infrared spectroscopy (FTIR) spectra were measured (using a Nicolet 8700 FT-IR Spectrometer, Fisher Scientific) at room temperature, with an input polarizer fixed at either  $0^\circ$  (p-pol) or  $90^\circ$  (s-pol). High sensitivity mercury cadmium telluride (MCT) detector and Indium Antimonide (InSb) detector were used for mid-IR and near-IR range, respectively. The FTIR samples were prepared by mechanical polishing with sample mounted on a  $45^\circ$  sample holder for wedge angle.

## 6. THREE-DIMENSIONAL TRILAYER HYBRID METAMATERIALS WITH TUNABLE GOLD NANOSTRUCTURES AND OPTICAL PROPERTIES<sup>§</sup>

### 6.1 Overview

Engineering plasmonic nanostructures from three dimensions is very attractive towards controllable and tunable nanophotonic components and devices. Here, complex trilayer Au-based heterostructures composed of a dielectric spacer sandwiched by two hybrid Au-TiN nanoplasmonic claddings, are offering a broad range of structural and property tunability. As the spacer changes from a pure insulating BaTiO<sub>3</sub> to a semi-conductive Au-BaTiO<sub>3</sub>, the dimension of the vertically aligned Au nanorod arrays are tailored. Such variation on the dimension of the Au nanostructures is attributed to the surface energy and strain evolved in the spacer layer. Optical properties and the change of surface plasmon resonances are demonstrated by the transmittance and specular reflectance. Numerical simulations suggest a gap plasmon induced field enhancement, where the field distribution is strongly affected by the tailored Au nanorods as either separated or channeled. The retrieved uniaxial dielectric tensors suggest a tunable hyperbolic property which is affected by the difference in spacer geometries. The complex 3D hybrid plasmonic heterostructures present potential design opportunities in tunable metamaterials towards light harvesting, sensing and nanophotonic devices.

### 6.2 Introduction

Artificially patterned plasmonic morphologies present enormous opportunities in controlling light-matter interactions and tunable optical properties beyond natural materials.<sup>[51, 133, 135, 145]</sup> Such nanostructures as metamaterials can be implemented for next-generation nanophotonic devices yielding effective light trapping, electro-optical modulators and ultrafast switching,<sup>[18, 26, 125, 172, 212-215]</sup> taking advantages of fundamental localized surface plasmon resonance (LSPR) and the surface enhanced Raman scattering (SERS) effects. While with significant progress being demonstrated in the field, there are still challenges that have hindered their practical applications.<sup>[135]</sup> These include building the metasurface into three-dimensions, or

---

<sup>§</sup> This chapter is reprinted with permission from “Three-dimensional hybrid heterostructure with tunable Au nanorods and optical properties” by X. Wang, et al., under review.

incorporating multiple material components with reduced losses. The ultimate solutions rely on developing better fabrication methods and a wise choice of materials.

Hyperbolic metamaterial (HMM) is defined as extreme anisotropic media by hybridizing metals and dielectrics in nanoscale.<sup>[47, 51, 216]</sup> Two representative geometries, wire HMM and multilayer HMM have been demonstrated, offering a wide choice of material combinations and geometrical tunabilities.<sup>[31, 49-50]</sup> Specifically, metallic phase itself covers a wide range of resonance frequencies from ultraviolet to near-infrared.<sup>[94, 217-218]</sup> However, the availability of dielectric component depends on specific geometry and fabrication methods. Wire HMMs produced by anodized alumina template provide an easy approach to achieve hybridized media with ordered vertical nanowire arrays in dielectric Al<sub>2</sub>O<sub>3</sub>. On the other hand, multilayer HMM is easier to grow. Dielectrics such as nitrides, carbides and fluorides can be achieved.<sup>[216]</sup> Adding structural complexity provided by lithography and patterning brings additional functionalities and novel phenomena including enhanced anisotropy, negative refraction, stronger nonlinearity and spontaneous emission. For example, e-beam or ion-beam patterning on top of the multilayer HMM creates a unique “fishnet” nanostructure, which has been demonstrated as negative refraction metamaterial (NIM) achievable in multiple material systems.<sup>[48, 52]</sup> Another approach is to modify the structure by replacing metals with low-loss plasmonic candidates such as graphene, doped oxides or transition metal nitrides.<sup>[59, 104, 114]</sup>

Different from the abovementioned top-down approaches, bottom-up deposition techniques provide alternative approaches in realizing epitaxial heterostructures, with extra benefits such as large-scale surface coverage, flexible control of layer thickness, and easy-access to on-chip integration.<sup>[64]</sup> For example, pulsed laser deposition (PLD) has been used to grow oxide-metal vertically aligned nanocomposite (VAN) films with metallic plasmonic nanorods/nanopillars embedded in a matrix phase.<sup>[56, 58, 219]</sup> Such platform provides unique design flexibilities including the layer thickness, the aspect ratio, tilting angles, packing density of nanorods, as well as a broad range of material candidates (i.e. metal, oxides, nitrides).<sup>[58, 61-62, 81]</sup> Recent demonstrations have shown its early success in building complex geometries in 3D.<sup>[220]</sup>

Coupling the multilayer HMM and the VAN geometries, in this study, trilayer hybrid heterostructures with 3D complex geometrical designs and tailorable optical properties are proposed. As illustrated in Figure 6.1, the trilayer structures are composed of a hybrid Au-TiN VAN as thin metallic claddings, and a dielectric spacer in two forms, i.e., pure BTO (BaTiO<sub>3</sub>) (left

panel) or hybrid Au-BTO VAN (right panel). Previous works have demonstrated the low-loss plasmonic properties of Au-TiN VAN as a robust hybrid platform beyond pure Au, and the tunable Au dimension by controlling deposition parameters.<sup>[62, 221]</sup> Here, BTO is selected as the dielectric oxide because of its structural compatibility and unique functionalities, such as: 1) desirable insulating property to enable a gap plasmon induced field enhancement,<sup>[136, 222-224]</sup> 2) stable stoichiometry to accommodate the growth with nitride-metal under reduced O<sub>2</sub> pressure, 3) close lattice match with Au and can be co-grown as VAN structure.<sup>[216, 221]</sup> By adjusting the 20-nm dielectric spacer from pure BTO to the hybrid Au-BTO VAN, tailorable Au nanorod dimensions are expected and the growth mechanisms in both cases are compared and discussed. Thorough optical property characterizations including plasmonic, complex dielectric function and optical anisotropy are measured and compared for both cases to evaluate the effectiveness of the 3D metamaterial designs.

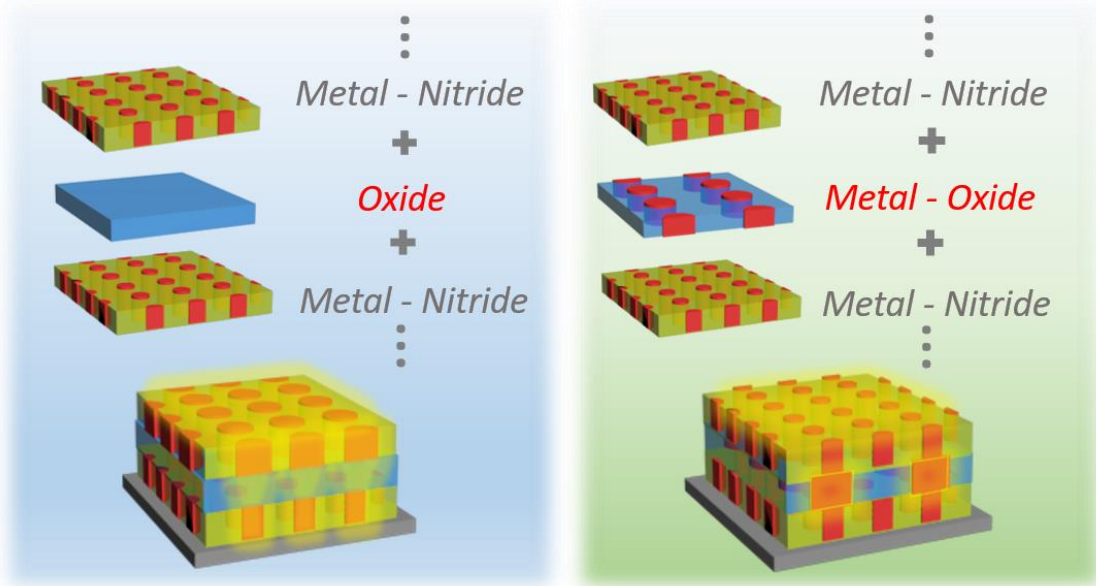


Figure 6.1 Illustrations of the trilayer film composed of metal-nitride nanocomposite claddings with a pure oxide spacer (left) and a metal-oxide nanocomposite spacer (right). Color represents different material, red: Au, yellow: TiN, blue: BaTiO<sub>3</sub>, grey: MgO.

### 6.3 Results and Discussion

Two sets of trilayer films were deposited for investigation, including (1) Au-TiN/BTO/Au-TiN and (2) Au-TiN/Au-BTO/Au-TiN on single-crystalline MgO. X-ray diffraction (XRD)  $\theta$ - $2\theta$

scans collected from a large surface area are shown in Figure 6.2 (a-1,b-1), where the films all exhibit high epitaxial quality. The Au (002) and BTO (002) peaks are well coupled and not discernible at  $44.70^\circ$ , their bulk lattice parameters indicate a merely 1.012% out-of-plane strain. However, the interface between TiN (002) and BTO (002) is highly strained with a lattice mismatch of 5.077%. Phi ( $\phi$ ) scan at (220) plane (Figure 6.3) suggests a four-fold symmetry of the trilayer stack without in-plane rotations.

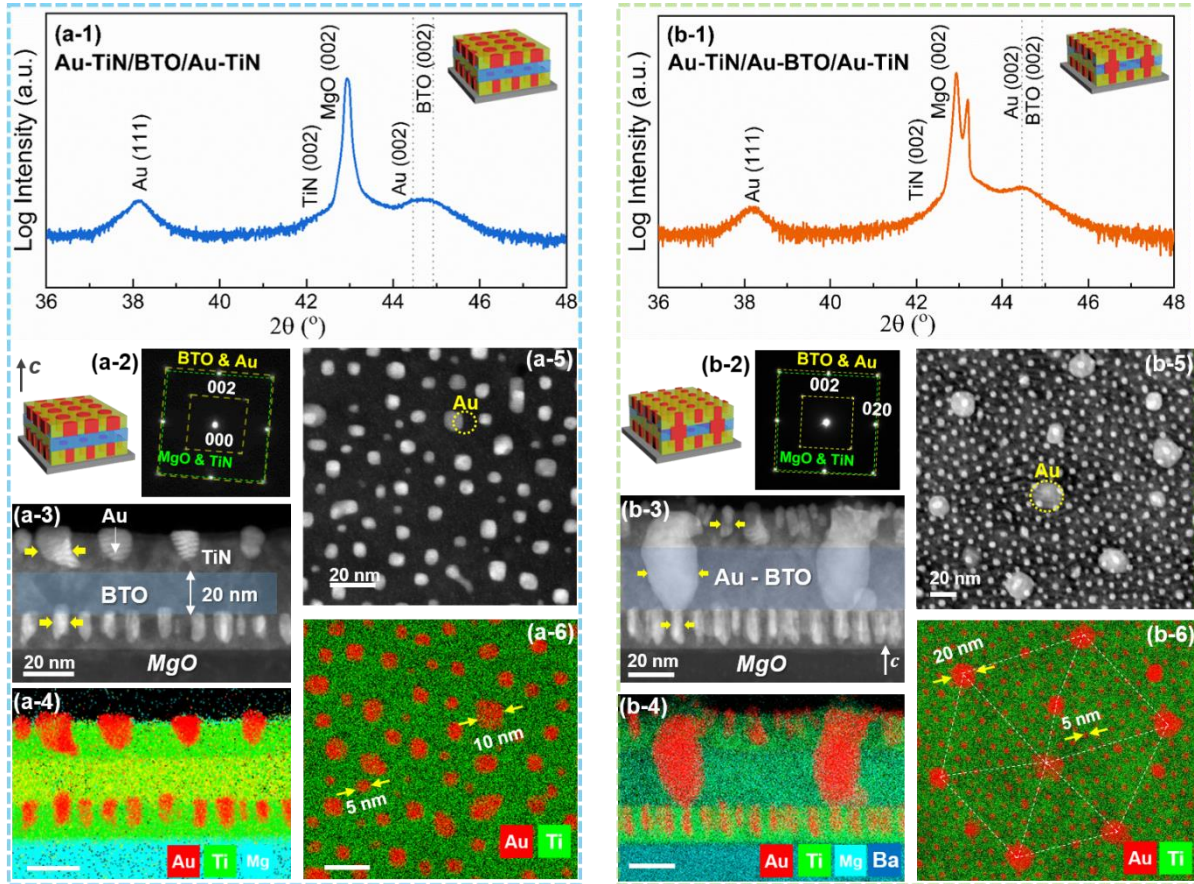


Figure 6.2 Left: Au-TiN/BTO/Au-TiN film grown on MgO. (a-1) XRD  $\theta$ - $2\theta$  scan. (a-2) SAED patterns at  $\langle 001 \rangle$  zone axis, (a-3) cross-sectional STEM micrograph and (a-4) corresponding EDX mapping, Au: red, Ti: green, Mg: cyan. Plan-view (a-5) STEM and (a-6) EDX mapping of Au and Ti. Right: Au-TiN/Au-BTO/Au-TiN film grown on MgO. (b-1) XRD  $\theta$ - $2\theta$  scan. (b-2) SAED patterns at  $\langle 001 \rangle$  zone axis. (b-3) Cross-sectional STEM micrograph and (b-4) EDX mapping. Plan-view (b-5) STEM image and (b-6) EDX mapping of Au and Ti.

The scanning transmission electron microscopy (STEM) micrographs revealing the 3D morphology of the samples are displayed in the bottom pane of Figure 6.2. Trilayer film composed of Au-TiN cladding with pure BTO spacer and Au-BTO spacer grown on MgO crystals are

displayed in the left and right panel, respectively. For the Au-TiN/BTO/Au-TiN stack, selected area electron diffraction (SAED) patterns from  $\langle 001 \rangle$  zone axis in Figure 6.2 (a-2) indicate high epitaxial quality of a cubic structure with four-fold symmetry. The cross-sectional STEM micrograph and energy-dispersive X-ray spectroscopy (EDX) mapping are displayed in Figure 6.2 (a-3,4), respectively. Distinct boundaries at Au/TiN, TiN/BTO and TiN/MgO interface are identified, with vertically aligned Au nanopillar arrays well-distributed in the TiN matrix. Interestingly, the dimension of Au nanopillar is much wider in the bottom cladding than that in the top cladding layer, as marked by the yellow arrows in Figure 6.2 (a-3). Such widening effect was further explored by gradually stacking the film into five layers, as shown in Figure 6.4. From previous demonstrations,<sup>[62]</sup> the diameter of Au nanopillar was mostly limited to a maximum of 8 nm in a single-layer Au-TiN film. Here, the diameter has been successfully tailored to 20 nm when a dielectric spacer is introduced in between the Au-TiN cladding layers. The plan-view STEM micrograph coupled with EDX mapping are shown in Figure 6.2 (a-5,6). As marked by the yellow arrows, two sets of Au nanopillar arrays with diameter of 5 nm (bottom cladding) and 10 nm (top cladding) are observed, respectively.

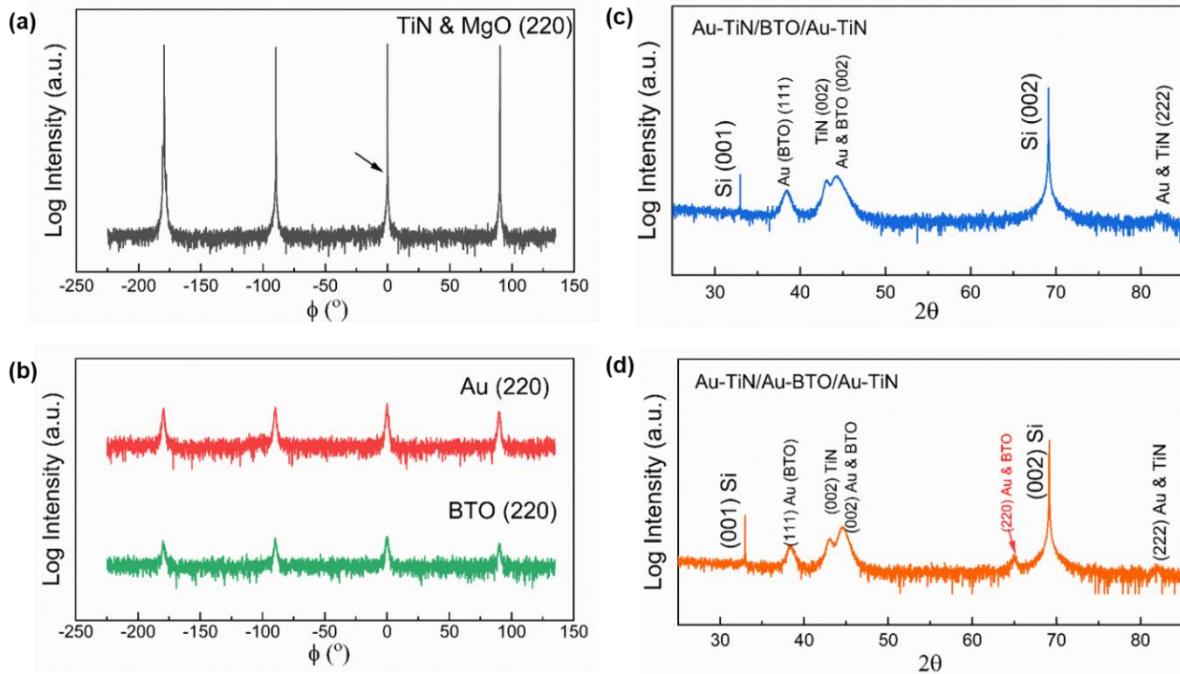


Figure 6.3 (a,b) XRD  $\phi$  scan at (220) plane of Au-TiN/BTO/Au-TiN film grown on MgO substrate. XRD  $\theta$ - $2\theta$  scan of (c) Au-TiN/thick BTO/Au-TiN film grown on Si substrate, and (d) Au-TiN/thick Au-BTO/Au-TiN film grown on Si substrate.

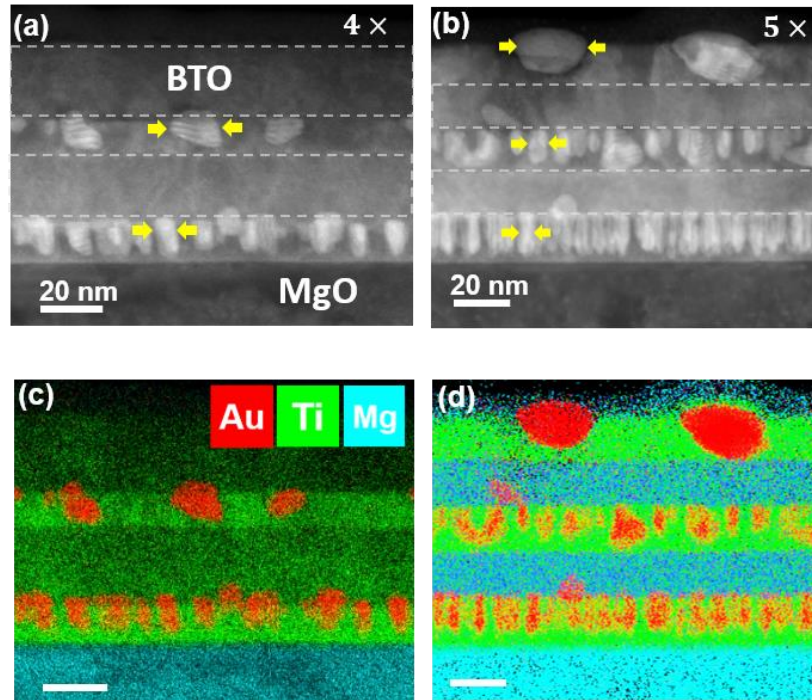


Figure 6.4 Cross-sectional STEM micrographs of (a) four-layer stack and (b) five-layer stack. (c,d) Corresponding cross-sectional EDX mapping. The Au nanopillar array in the hybrid Au-TiN cladding shows a gradual increase from 5 nm (1st layer) to approximately 20 nm (5<sup>th</sup> layer), as marked by the yellow arrows.

On the right panel, the Au-TiN/Au-BTO/Au-TiN trilayer also exhibits high epitaxial quality as seen from the sharp SAED patterns in Figure 6.2 (b-2). The Au nanopillar in BTO matrix owns an average diameter of 20 nm (yellow arrows), which is much wider than Au grown in TiN matrix. However, the diameter at top cladding remains unaffected and maintained consistently at 5 nm as confirmed by the cross-sectional STEM micrograph and EDX mapping in Figure 6.2 (b-3,4). The corresponding plan-view images shown in Figure 6.2 (b-5,6) also confirm the existence of the two sets of Au nanopillars, i.e., one set of 5 nm ones being uniformly distributed in the claddings, and another set of 20 nm ones with a hexagonal-like periodicity (marked by dashed lines).

To understand the mechanism of the tunable Au dimension, the plan-view images of the Au-TiN/Au-BTO/Au-TiN trilayer were further explored. According to Figure 6.5 (a,b), each large Au nanopillar in the spacer layer was found to be adjacent to an average of four smaller ones in the claddings. It is attributed to that Au adatoms at the top layer nucleate preferably close to

themselves with lower surface energy and better adatom nucleation. Figure 6.5 (c) shows the high-resolution STEM micrograph specifically at the Au/BTO boundary. Atomic sharp stacking of Au {002} is visualized, matching well with the surrounding BTO matrix. Such a desired matching condition is confirmed by the Fast Fourier Transform (FFT) processed images in Figure 6.5 (d,e), showing the atomic stacking along [100] and [010] respectively. Except a half-plane  $\frac{1}{2}d_{(100)}$  shifting (shaded red box), the interface between Au and BTO is nearly coherent without obvious misfit dislocations. An atomic model (Figure 6.5f) is generated based on the area marked by the yellow box Figure 6.5(c).

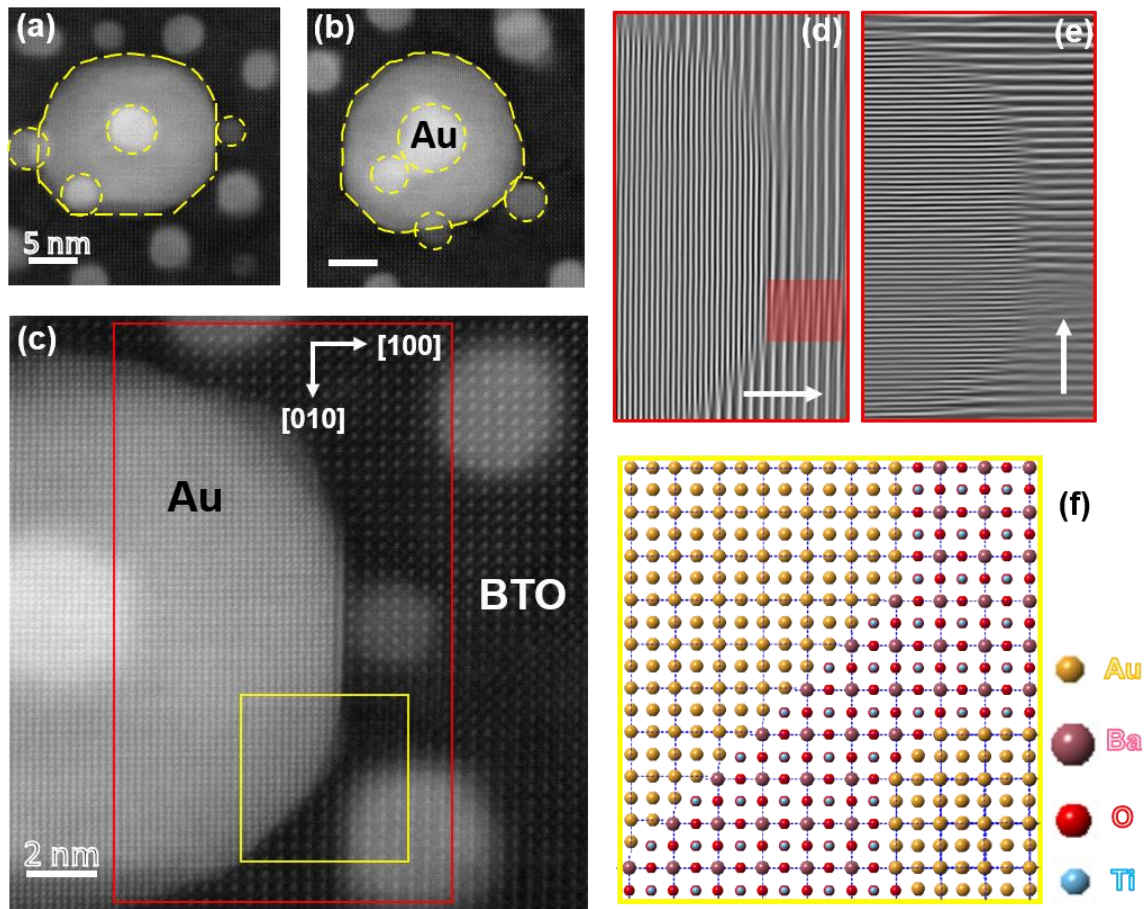


Figure 6.5 Plan-view high resolution microstructure of trilayer with Au-BTO spacer. (a,b) STEM micrographs at Au interface. Scale bar represents 5 nm. (c) High-resolution plan-view STEM image. IFFT filtered images along (d) [100] and (e) [010] directions. (f) Atomic model built at Au/BTO interface corresponding to the yellow box of (c).

Overall, the two different spacers result in the geometrical variation of the trilayer nanostructures, which can be attributed to the different surface energy and strain energy of the two different spacers. Figure S3 presents the EDX mapping and 2D schematics for the two cases with either the pure BTO spacer or the Au-BTO spacer. For the pure BTO spacer case, it is noted that the Au nanorod dimension from the first to the third layer is nearly doubled (i.e.  $d$ ,  $2d$ , approximately). The tailored Au dimensions can be attributed to the inherit variations of surface energies and lattice mismatch strain between the first Au-TiN layer nucleate on MgO and the second Au-TiN layer nucleate on BTO. For the Au-BTO spacer, the Au nanorod in the spacer layer is about 4 times of the Au nanorod in the Au-TiN layers. Besides a desired lattice matching, this broadening effect is attributed to the lower surface energy of BTO phase presents a 2D growth mode that limits the Au nucleation sites and allow the agglomeration. It is interesting to note that when Au-TiN nucleate on top of Au-BTO, the size of Au is comparable to the first cladding layer. This is because both Au and TiN favor to rest on Au (more metallic) instead of BTO due to the minimization of surface energy, which results in a competitive growth that narrows down the nucleus size. In addition, the different interface energy and strain energy also play a role in affecting the overall morphology of the Au nanorods. The Au nanorods in TiN matrix are very straight while the Au in BTO are more faceted and curved.

Taking advantage of the tailored Au nanorod arrays, the as-deposited trilayer films were expected to show tunable plasmonic properties. Numerical simulations based on *COMSOL Wave Optics Module* were performed to predict the optical performance. Figure 6.7 displays the unpolarized optical spectra ( $0^\circ$  incidence) and the electric field distribution for Au-TiN/BTO/Au-TiN (Figure 6.7a) and Au-TiN/Au-BTO/Au-TiN (Figure 6.7b) trilayer, respectively. The accuracy of the simulation was confirmed by comparing with the measured transmittance (T) spectra shown in Figure 6.7(c,d). Three wavelengths (400 nm, 600 nm and 800 nm) were selected to retrieve the 2D electric field maps, where each set of maps is displayed at same intensity scale (a-1 and b-1). As a comparison, both films exhibit the strongest field intensity at 600 nm dominated by the excitation of the LSPR mode of Au nanorods at Au/BTO interface. However, the overall field intensity is much higher at the Au-BTO/Au-BTO/Au-TiN trilayer, where the field enhancement becomes highly confined at the vertical boundary of Au in the 20 nm dielectric spacer due to the strong LSP mode at the Au/BTO interface.<sup>[225]</sup> It is also inferred that the strong surface plasmon mode of Au-TiN claddings allows an intense field enhancement at the spacer layer, such field

excitation provides valuable insights to the study of spontaneous emission and sensing applications.<sup>[226]</sup>

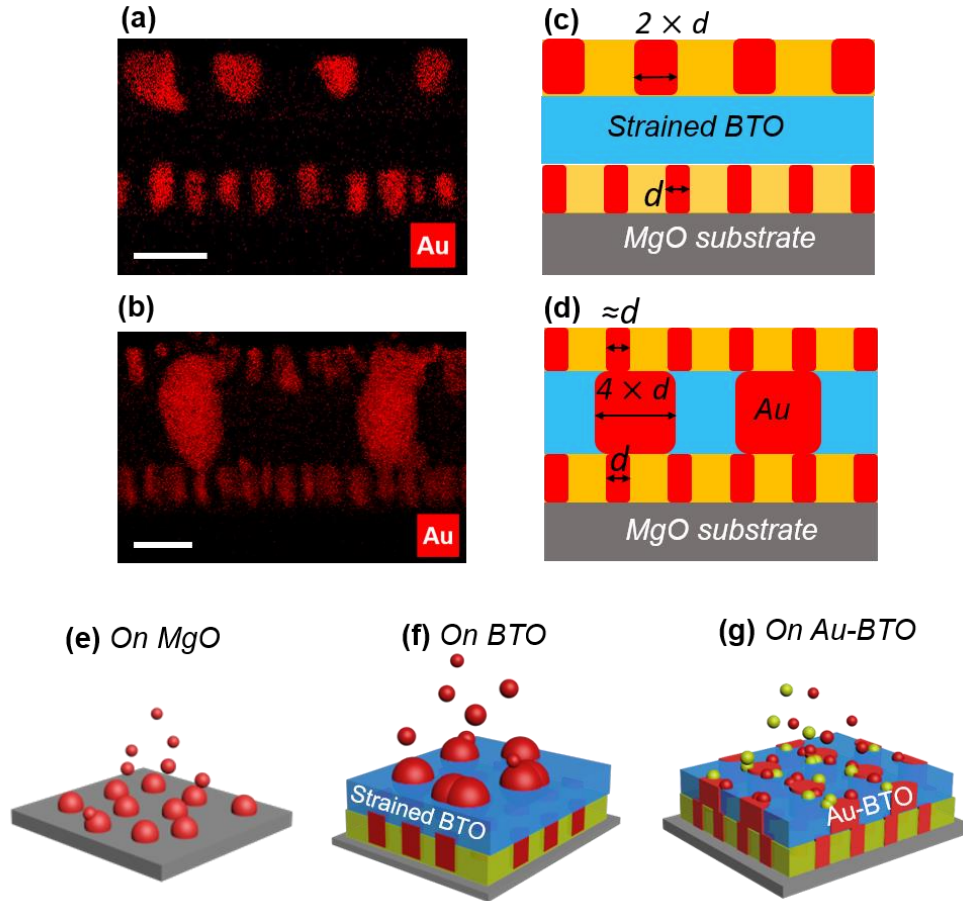


Figure 6.6 (a,b) EDX mapping of Au,  $d$  is the diameter of nanopillars,  $d = 5$  nm. (c,d) 2D illustrations of the two trilayer films. 3D illustration of the Au nucleation on (e) MgO substrate, on (f) strained BTO layer and on (g) strained Au-BTO layer. Colors represent different adatoms. TiN: yellow, Au: red, BTO: blue, MgO: grey.

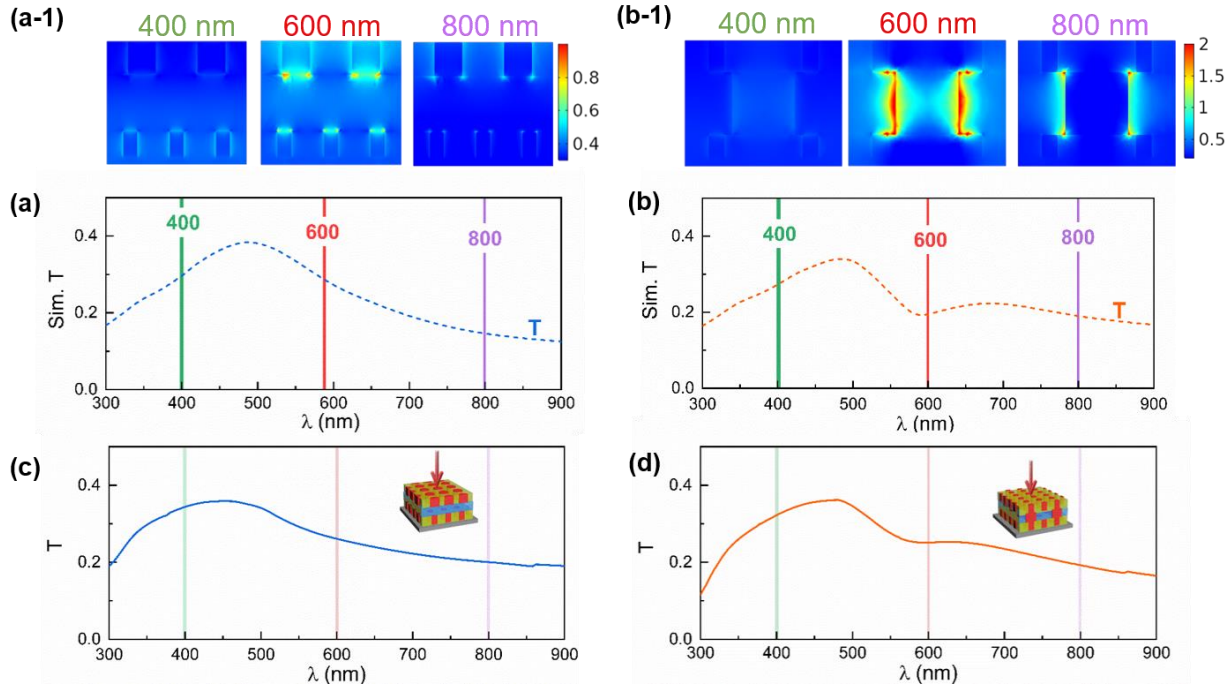


Figure 6.7 Simulated transmittance spectrum of Au-TiN/BTO/Au-TiN film. (a-1) 2D electric-field maps at 400 nm, 600 nm and 800 nm. (b) Simulated transmittance spectrum of Au-TiN/Au-BTO/Au-TiN film and (b-1) corresponding 2D E-field maps. (c,d) Measured transmittance spectrum of two trilayer films.

Next, polarized light reflectance ( $R$ ) at incident angles ranging from  $55^\circ$  to  $75^\circ$  were collected. Figure 6.8 displays two sets of measurements (solid lines) coupled with corresponding fitted spectra (dashed lines) retrieved from a uniaxial model. Original ellipsometry measured and fitted amplitude  $\Psi$  and phase difference  $\Delta$  values are displayed in Figure S6.9. Retrieving dielectric function of single-layer VAN such as Au-BTO has been previously reported using effective medium theory,<sup>[56, 227]</sup> here, in order to compare the overall optical properties of the complex heterostructures, the optical model is simplified where the trilayer stack is treated as one homogeneous layer. Accordingly, any 2<sup>nd</sup> or 3<sup>rd</sup> order oscillations from the embedded interfaces are neglected accordingly. From Figure 6.8, the model exhibits a reasonable match in general, the small variances observed at s-polarized reflectance are potentially caused by internal reflections or scattering. The overall reflectance intensity and the trend are comparable between two different trilayer samples. The dip at around 490 nm represent the strong surface plasmon resonance (SPR) caused by the plasmonic TiN surface, while small variations or oscillations as marked by the red

arrows close to 600 nm correspond to the LSPs of Au nanorods with different geometry. These features are comparable to those observed in transmittance spectra as shown in Figure 6.7. The overall reflectance intensity of s-polarization (Figure 6.8b,e) is higher than that of the p-polarization (c,f), owing to a more significant in-plane light interaction. The p-polarization shows a change of reflectance at high angles (75°) which is potentially driven by a hyperbolic nature of the trilayer with alternative metallic and dielectric components.<sup>[228]</sup>

Further, the dielectric constants in ordinary ( $\epsilon^{xx} = \epsilon^{yy} = \epsilon^o$ ) and extra-ordinary ( $\epsilon^{zz} = \epsilon^{e0}$ ) directions are retrieved and shown in Figure 6.9. While both films exhibit similar losses from their imaginary part ( $\epsilon_2$ ), the separation between the two orthogonal tensors of real part ( $\epsilon_1$ ) indicates strong optical anisotropy in both trilayer films, where the in-plane behaves more metallic ( $\epsilon_1^o < 0$ ) and out-of-plane behaves more dielectric ( $\epsilon_1^{e0} > 0$ ). As marked by grey arrows in Figure 6.9(a,b), the ordinary terms of real part ( $\epsilon_1^{xx,yy}$ ) exhibit a change of epsilon near zero (ENZ) point from 670 nm for Au-TiN/BTO/Au-TiN film to 787 nm for Au-TiN/Au-BTO/Au-TiN film, potentially owing to the variances of charge carrier concentration and the electric field distribution. Such tuning of ENZ property can be utilized potentially for direct SPP excitation towards enhanced plasmonic sensing, magneto-optical coupling, optical switching, etc.<sup>[229-231]</sup> As a result, hyperbolic dispersion of type II ( $\epsilon_1^o < 0$ ,  $\epsilon_1^{e0} > 0$ ) is generated in both trilayer films, their  $k$ -space hyperboloid topologies at selected wavelength (1  $\mu\text{m}$ ) are different as indicated by the inset images in Figure 6.9 (a,c). Previous studies of Au-BTO VANs have demonstrated a type I hyperbolic property with strong dispersion variations at vertical interface. Here, the planar interface is playing a dominant role such that the overall trend of hyperbolic property follows common metal-insulator-metal (MIM) hyperbolic metamaterials.<sup>[228]</sup>

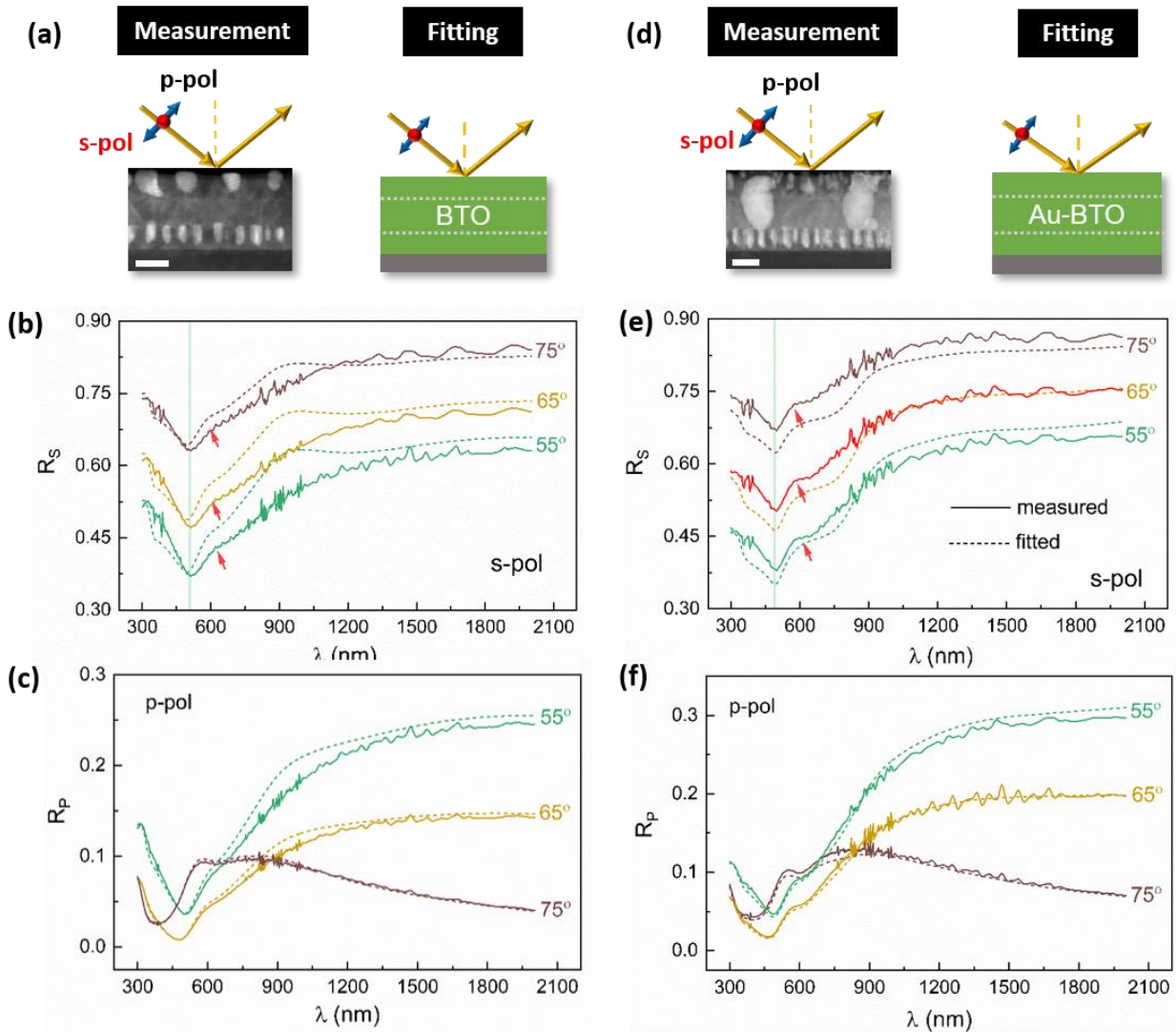


Figure 6.8 (a,d) Schematic illustrations on the real samples and models applied for data fitting of two trilayer films. (b) S-polarized and (c) p-polarized angular dependent reflectance, measured (solid lines) and fitted spectra (dashed lines) for trilayer film with BTO spacer. (e) S-polarized and (f) p-polarized angular dependent reflectance, measured (solid lines) and fitted spectra (dashed lines) for the trilayer film with Au-BTO spacer.

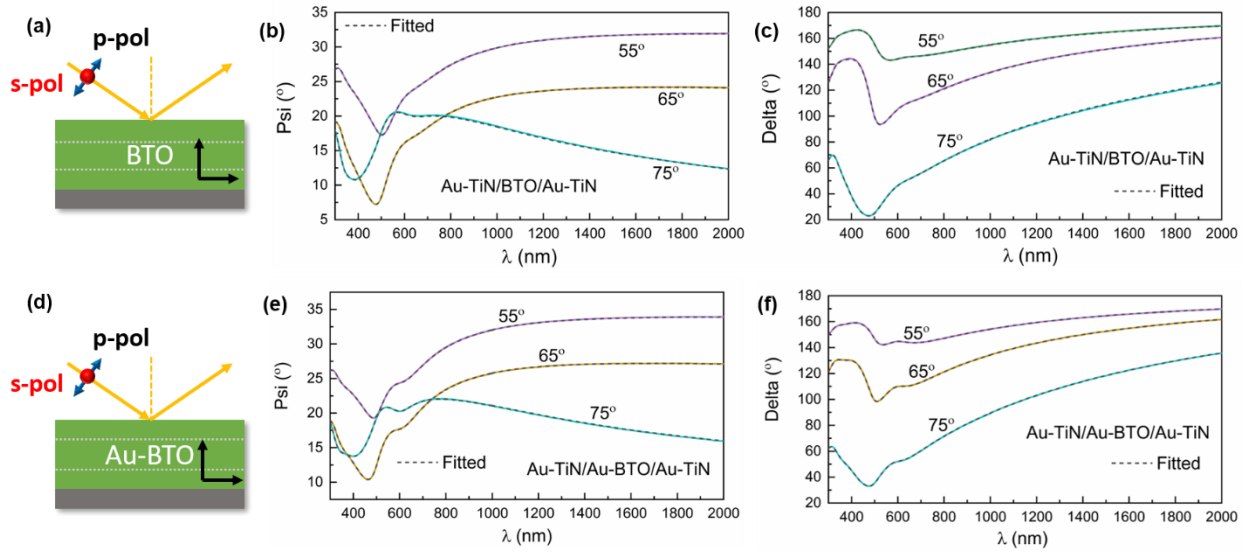


Figure 6.9 (a) Model of Au-TiN/BTO/Au-TiN trilayer. Measured and fitted (b) Psi and (c) Delta spectra at three incident angles from  $55^\circ$  to  $75^\circ$ . (a) Model of Au-TiN/Au-BTO/Au-TiN trilayer. Measured and fitted (dashed lines) (e) Psi and (f) Delta spectra collected at three incident angles from  $55^\circ$  to  $75^\circ$ . The model shows desired matching with measurement, the mean square error (MSE) is below 3.

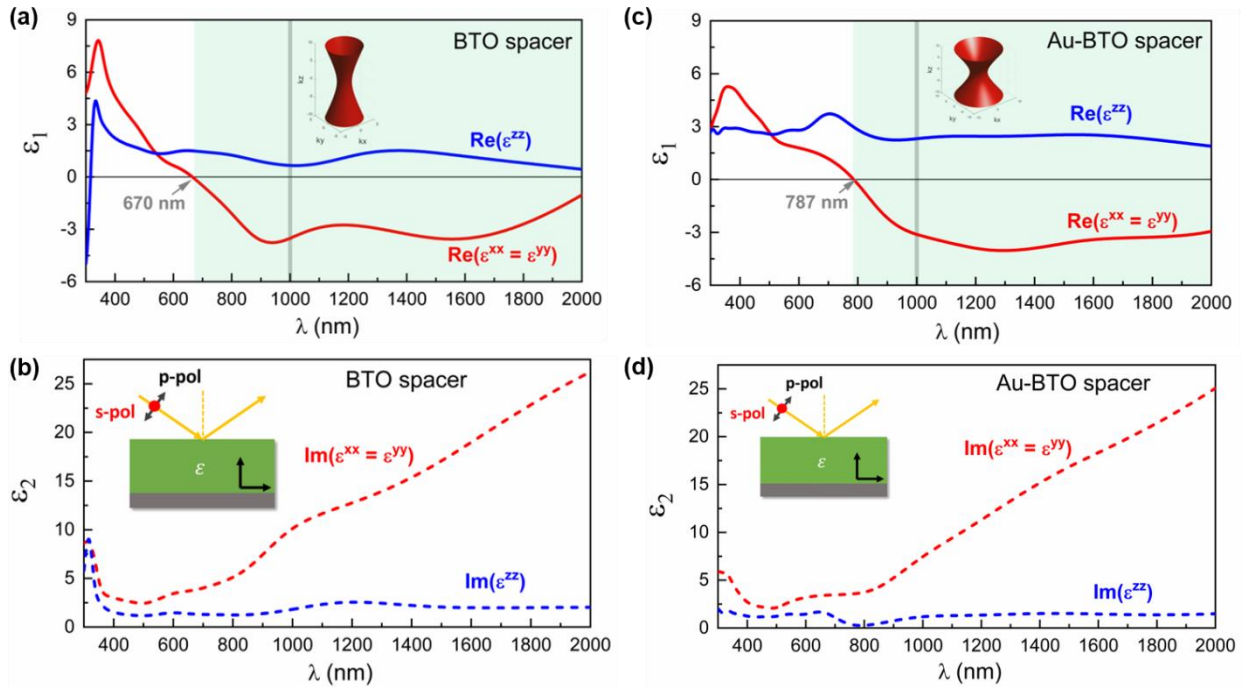


Figure 6.10 (a) Real-part and (b) imaginary-part dielectric functions of Au-TiN/BTO/Au-TiN trilayer, (c) real-part and (d) imaginary-part dielectric constant of Au-TiN/Au-BTO/Au-TiN film.

Aside from the geometrical tuning, the thin film technique offers additional benefits including flexibility of interlayer thickness and the on-chip fabrication and integration. As a demonstration, trilayer films with thick spacer layers (60 nm) were successfully deposited on (001) Si substrates with epitaxial film quality and very similar Au nanorod geometries (Figure S6.11) as those on MgO substrates. Corresponding optical properties of these thicker trilayers are shown in Figure S6.12. Potential applications using these 3D hybrid metamaterials for Si-based photonic devices are worth to explore in future studies.<sup>[50, 232-233]</sup> Here, the hybrid Au-TiN as cladding is unique in terms of its highly durable plasmonic property and geometrical tunability as reported by related studies.<sup>[62, 102, 234-235]</sup>

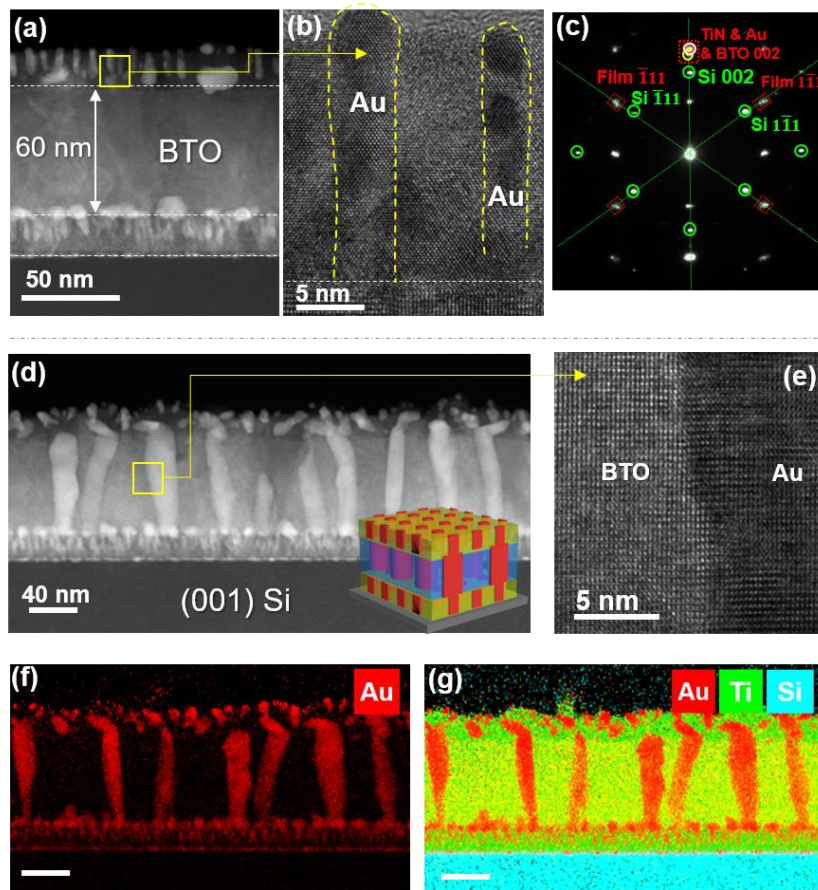


Figure 6.11 (a) Cross-sectional STEM micrograph of Au-TiN/BTO/Au-TiN film grown on Si (001), (b) HRTEM image of the top cladding. (c) SAED patterns corresponding to a large sample area. (d) Cross-sectional STEM micrograph and (e) HRTEM image at BTO/Au interface. (f,g) EDX mapping.

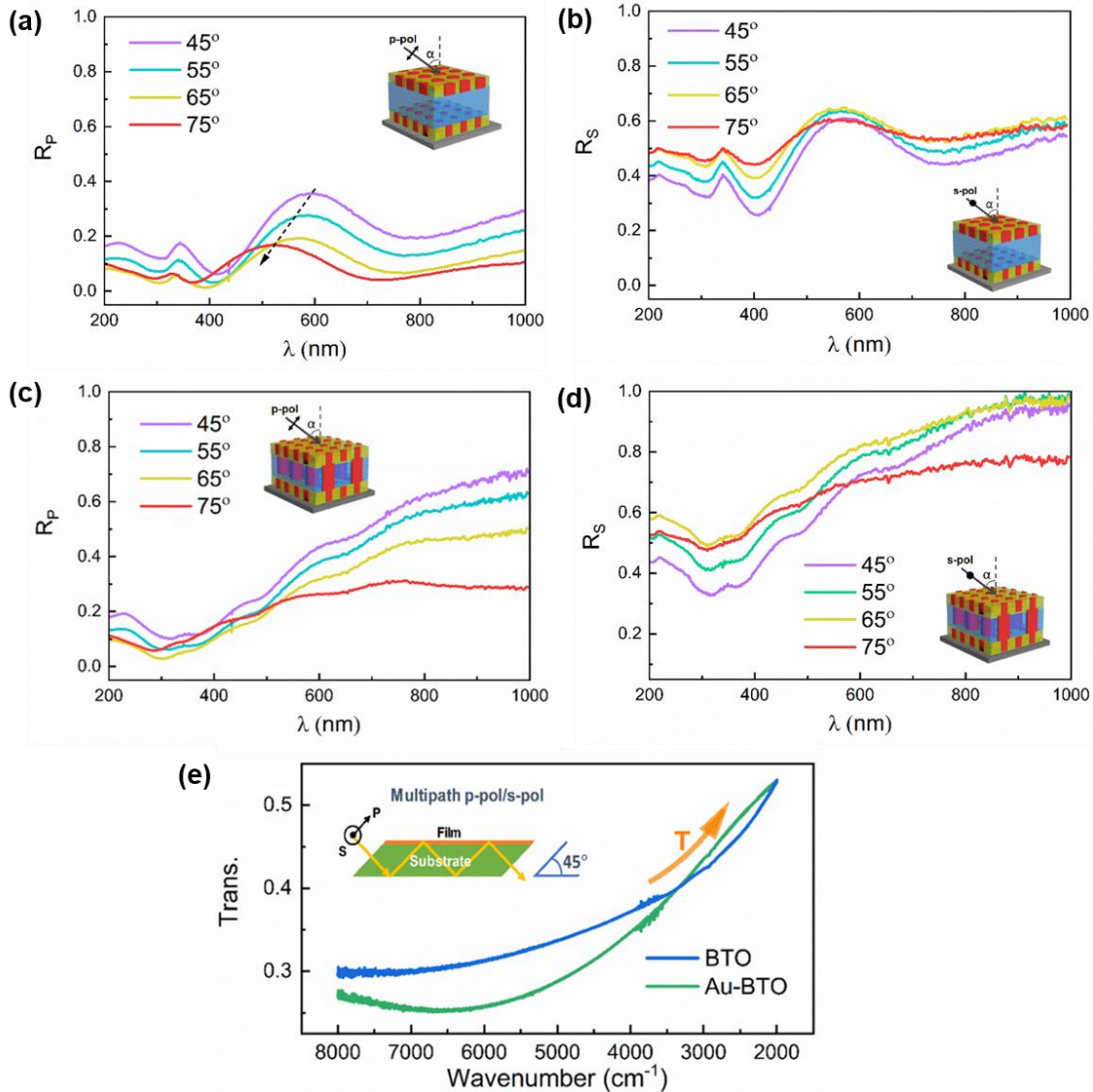


Figure 6.12 (a,b) P- and s-polarized reflectance spectra of Au-TiN/thick BTO/Au-TiN film measured at four ( $45^\circ$  to  $75^\circ$  with  $10^\circ$  interval) incident angles. (c,d) P- and s-polarized reflectance of the Au-TiN/thick Au-BTO/Au-TiN film. (e) Multipath depolarized IR transmittance comparing trilayers with thick spacers. The depolarized transmission intensity was derived from their polarized counterparts with incident beam propagating at  $45^\circ$  and bouncing multiple times inside the film.

More effective tuning can be realized by specifying spacer layer thickness or impedance, incorporating different VAN material platforms or coupling additional functional layers towards three-dimensional metamaterials.<sup>[61, 236]</sup> Potential applications such as direct excitation of the SPP mode within the nanoscale thin film platform could be of great importance towards building effective nanosensors which surpass the size and detection limit.<sup>[237-238]</sup>

## 6.4 Conclusion

Unique self-assembled 3D trilayer heterostructures composed of hybrid Au-TiN claddings and tunable dielectric spacer layers (i.e., pure BTO or Au-BTO) are demonstrated in this study. The complex 3D stacking geometry offers high freedom of tunability, where the variation of the Au nanorod diameter (5 nm to 20 nm) is attributed to the effect of surface energy and lattice strain introduced by the different spacers. Both SPP mode (TiN) and LSPR affected by (Au nanorods) contribute to the plasmonic resonance at 400 nm to 600 nm. Variations of field distributions are correlated to the Au nanorods with change of dimensions and interface. When the Au nanorods are channeled through the spacer, an intense field enhancement is observed at the boundaries between Au and BTO. The dielectric function of the trilayer as a whole unit exhibits a type II hyperbolic property with a tunable in-plane ENZ affected by the designable geometry. The 3D trilayer heterostructure design in the presented work demonstrates an effective approach to tailor the geometry of the nanoscale building blocks via surface energy and strain control which can be adopted in designing complex metamaterial systems for more effective plasmonic sensing devices.

## 7. SUMMARY AND OUTLOOK

### 7.1 Summary

To conclude the key highlights and achievements in this thesis, the metal-nitride nanocomposites have been explored starting from Au-TiN and Ag-TiN VAN systems, where the hybrid plasmonic phases have been successfully integrated on MgO, sapphire and Si substrates. Microstructure characterizations prove the high epitaxial quality, smooth surface coverage, and no intermixing or interdiffusions of the constituent materials. Interestingly, the nanostructured metal phase can be tailored by controlling growth parameters. Specifically, the capability of geometrical tuning has been demonstrated such as the volume fraction, as well as tuning the tilting angle of Ag nanopillars from  $0^\circ$  to  $50^\circ$ . These tunable two-phase designs play multiplex roles towards enhanced functionalities. On the one hand, coupling two plasmonic components realize a tuning of charge carrier density and optical anisotropy as compared to single-phase metallic films. Embedding metal inside TiN enhances the overall material durability and opens-up possibilities in coupling other unstable metals with TiN. These hybrid plasmonic thin films with nanopillars protruded on top can serve as SERS substrates for sensing applications. For example, successful demonstration using Au-TiN for chemical bonding detection has been achieved. On the other hand, the tunable features of the nanocomposite films offer additional control of optical properties, in Chapter 4, tilting of Ag nanopillar realizes a three-dimensional anisotropy as well as angular selectivity that covers visible to infrared regime. These properties are beneficial if being applied to high-temperature absorbers or nanoantenna devices.

The last two chapters explore coupling between dissimilar materials beyond metallic in order to extend dielectric properties beyond metallic. To achieve that, wide-bandgap III-V AlN is selected and being coupled with plasmonic metals. Both Au and Ag are grown as inhomogeneous nanoinclusions due to the drastic structural variation and lattice mismatch. But the hybrid nanocomposite films exhibit textured growth without intermixing. Moreover, such coupling results in interesting property tuning including a change of bandgap and carrier concentration, and optical anisotropy as resolved by dissimilar uniaxial dielectric tensors. This work offers some interesting design opportunities for tunable semiconductor thin films realized by two-phase coupling scheme alternative to doping, the structure can be improved to achieve precise control of geometry and

functionality. Finally, a complex stacking of trilayer is demonstrated using Au-TiN VAN as the cladding since its growth is more desired to compensate additional coupling with dissimilar materials. Specifically, BTO and Au-BTO VAN are integrated as the spacer layers in between Au-TiN VAN claddings, to resolve the structural tunability with and without Au interconnection. Interestingly, the Au nanostructure can be tailored effectively owing the strain and surface energy of the spacer, and as a result, a tunable plasmonic resonance and electric field enhancement have been achieved. Coupling Au-TiN with BTO or Au-BTO can be treated as a complex hyperbolic metamaterial combining both wire and multilayer configurations. Additionally, it offers benefits to tune the nanostructure as well as the hyperbolic transitions and degree of anisotropy effectively.

## 7.2 Outlook

Several key prospects in terms of improving the structure and performance along the path of investigating two-phase nanocomposite structures are proposed. First, one major challenge remaining in heterostructure growth is the ordering of the nanopillars. It has become a crucial factor for developing nanocomposites towards metamaterial applications, since periodic patterning is the prerequisite for predicting controllable light-matter interactions or manipulation over wavefront. The advantage of the metal-oxide or metal-nitride nanocomposites lies in deep-subwavelength scaled features over the entire centimeter range sample area, which is very challenging to achieve in current lithographic patterning methods. Bottom-up thin film deposition method is relatively easy to achieve. However, it relies on complex growth mechanisms and the controlling factors involving kinetics and thermodynamics are rather sophisticated. Some progress has been made in enhancing the ordering of the VAN nanostructures, including strain control from three dimensions. For example, specific crystal lattices and symmetries are selected to incorporate strain at both substrate/film and matrix/pillar interfaces (Figure 7.1), which affect the nucleation process and ordered growth.<sup>[59, 90]</sup> In earlier discussions on the Au-TaN/MgO system, the 3.68% compressive strain at TaN/MgO interface couples with 3.55% tensile strain at Au/MgO interface, generating an overall strain compensation by distributing Au nanopillars in TaN matrix in an ordered fashion. Such concept can be utilized for coupling more functional two-phase systems. Another method is substrate templating, via thermally treating the substrate by annealing and formation of predefined terraces in order to modify the surface energies, such that the film adatoms will have some preferences for nucleation.<sup>[239]</sup> However, this method could not be applied to a

wide range of substrate materials. As mentioned in Chapter 1, additional processing such as lithographic patterning can be combined to pattern the nucleation sites artificially, the trenches can be considered as defect sites where adatoms are preferably nucleate on top. With a careful growth process, an ordered growth can be achieved although the whole processing time is expected to increase.

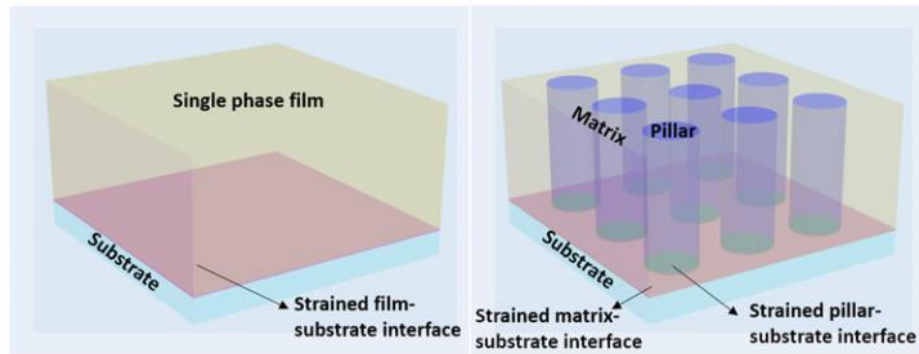


Figure 7.1 Schematic of three-dimensional strain coupling of VAN.<sup>[90]</sup>

Another future direction is to bridge the gap between nanostructures and functionalities which requires intensive experimental effort. Understanding self-assembly of the PLD technique is fundamentally important, within all possible geometries of two-phase assemblies (i.e., nanoparticle-in-matrix, nanopillar-in-matrix, multilayer or superlattice), how can one predict exact output geometry through all possible controlling parameters, and how to tune the structure effectively by knowing which specific parameter to change are insightful questions to answer. As most of the functionalities (i.e., magnetic, optical, electrical) will be affected by even tiny changes the nanostructures, understanding the link or relation between structure and performance is crucial. In addition, some of the properties, such as coupling effects between electrical and magnetic, optical and magnetic are still underexplored but are rising their importance in many applications such as neuromorphic computing, spintronic devices, ultrafast switching, etc. These research directions offer a plethora of new coupling configurations, and a wide range of material candidates can be possibly grown using the PLD technique. As proposed, it is possible to apply entirely ceramic candidates to grow VAN with hyperbolic dispersion, such that instability or ohmic losses brought by the metallic counterparts can be avoided. Moreover, multi-phase self-assembly of nanocomposite thin films can be possibly realized beyond two-phase coupling, thus more functionalities can be achieved via a single designable geometry.

Lastly, implementing hybrid thin film platform into practical applications and device integrations is always the goal of the nanocomposite designs. Previous demonstration in utilizing TiN-Au to detect chemical bonds have proved the promising prospects towards bio-chemical sensing applications. Moreover, these solid-state thin films are durable for multi-testing and reusable upon chemical treatment, they are highly resistant to or thermal or laser treatment that are of great advantageous as compared to the solution-based candidates. In addition, as some of the hybrid plasmonic films can be grown on Si substrates, future explorations towards Si integration of nanophotonic chips could be critical for future integrated photonics and electronics.

## REFERENCES

- [1] A. Sommerfeld, Ueber die Fortpflanzung elektrodynamischer Wellen längs eines Drahtes. *Annalen der Physik* **1899**, 303, 233.
- [2] R. W. Wood, On a Remarkable Case of Uneven Distribution of Light in a Diffraction Grating Spectrum. *Proceedings of the Physical Society of London* **1902**, 18, 269.
- [3] G. Mie, Beiträge zur Optik trüber Medien, speziell kolloidaler Metallösungen. *Annalen der Physik* **1908**, 330, 377.
- [4] U. Fano, The Theory of Anomalous Diffraction Gratings and of Quasi-Stationary Waves on Metallic Surfaces (Sommerfeld's Waves). *J. Opt. Soc. Am.* **1941**, 31, 213.
- [5] E. Kretschmann, H. Raether, Notizen: Radiative Decay of Non Radiative Surface Plasmons Excited by Light. In *Zeitschrift für Naturforschung A*, 1968; Vol. 23, p 2135.
- [6] S. I. Bozhevolnyi, J. B. Khurgin, The case for quantum plasmonics. *Nat. Photonics* **2017**, 11, 398.
- [7] M. S. Tame, K. R. McEnery, Ş. K. Özdemir, J. Lee, S. A. Maier, M. S. Kim, Quantum plasmonics. *Nature Physics* **2013**, 9, 329.
- [8] Z. Jacob, V. M. Shalaev, Plasmonics Goes Quantum. *Science* **2011**, 334, 463.
- [9] J. Park, H. Kim, B. Lee, High order plasmonic Bragg reflection in the metal-insulator-metal waveguide Bragg grating. *Optics Express* **2008**, 16, 413.
- [10] S. A. Maier, Plasmonics: fundamentals and applications. Springer Science & Business Media, **2007**.
- [11] B. Wiley, Y. G. Sun, Y. N. Xia, Synthesis of silver nanostructures with controlled shapes and properties. *Accounts Chem. Res.* **2007**, 40, 1067.
- [12] X. M. Qian, X. H. Peng, D. O. Ansari, Q. Yin-Goen, G. Z. Chen, D. M. Shin, L. Yang, A. N. Young, M. D. Wang, S. M. Nie, In vivo tumor targeting and spectroscopic detection with surface-enhanced Raman nanoparticle tags. *Nat. Biotechnol.* **2008**, 26, 83.
- [13] M. Rycenga, C. M. Cobley, J. Zeng, W. Li, C. H. Moran, Q. Zhang, D. Qin, Y. Xia, Controlling the Synthesis and Assembly of Silver Nanostructures for Plasmonic Applications. *Chemical Reviews* **2011**, 111, 3669.
- [14] P. Zilio, M. Malerba, A. Toma, R. P. Zaccaria, A. Jacassi, F. D. Angelis, Hybridization in Three Dimensions: A Novel Route toward Plasmonic Metamolecules. *Nano Letters* **2015**, 15, 5200.

- [15] X. M. Qian, S. M. Nie, Single-molecule and single-nanoparticle SERS: from fundamental mechanisms to biomedical applications. *Chemical Society Reviews* **2008**, *37*, 912.
- [16] A. J. Haes, C. L. Haynes, R. P. Van Duyne, Nanosphere Lithography: Self-Assembled Photonic and Magnetic Materials. *MRS Proceedings* **2011**, *636*, D4.8.1.
- [17] H. R. Stuart, D. G. Hall, Absorption enhancement in silicon-on-insulator waveguides using metal island films. *Appl. Phys. Lett.* **1996**, *69*, 2327.
- [18] H. A. Atwater, A. Polman, Plasmonics for improved photovoltaic devices. *Nat. Mater.* **2010**, *9*, 205.
- [19] D. J. Barber, I. C. Freestone, AN INVESTIGATION OF THE ORIGIN OF THE COLOR OF THE LYCURGUS CUP BY ANALYTICAL TRANSMISSION ELECTRON-MICROSCOPY. *Archaeometry* **1990**, *32*, 33.
- [20] V. G. Veselago, The Electrodynamics of Substances with Simultaneously Negative Values of  $\epsilon$  and  $\mu$ . *Soviet Physics Uspekhi* **1968**, *10*, 509.
- [21] J. B. Pendry, Negative Refraction Makes a Perfect Lens. *Physical Review Letters* **2000**, *85*, 3966.
- [22] D. R. Smith, W. J. Padilla, D. C. Vier, S. C. Nemat-Nasser, S. Schultz, Composite Medium with Simultaneously Negative Permeability and Permittivity. *Physical Review Letters* **2000**, *84*, 4184.
- [23] G. H. B. Thompson, Unusual Waveguide Characteristics associated with the Apparent Negative Permeability obtainable in Ferrites. *Nature* **1955**, *175*, 1135.
- [24] M. A. Mohammad, M. Muhammad, S. K. Dew, M. Stepanova, Springer, **2012**.
- [25] G. Rius Suñé, Electron beam lithography for nanofabrication. Universitat Autònoma de Barcelona, **2008**.
- [26] N. F. Yu, P. Genevet, M. A. Kats, F. Aieta, J. P. Tetienne, F. Capasso, Z. Gaburro, Light Propagation with Phase Discontinuities: Generalized Laws of Reflection and Refraction. *Science* **2011**, *334*, 333.
- [27] G. Dolling, M. Wegener, C. M. Soukoulis, S. Linden, Negative-index metamaterial at 780 nm wavelength. *Opt. Lett.* **2007**, *32*, 53.
- [28] M. Decker, N. Feth, C. M. Soukoulis, S. Linden, M. Wegener, Retarded long-range interaction in split-ring-resonator square arrays. *Physical Review B* **2011**, *84*, 7.
- [29] H. Xu, D.-H. Qin, Z. Yang, H.-L. Li, Fabrication and characterization of highly ordered zirconia nanowire arrays by sol-gel template method. **2003**, *80*, 524.

- [30] H. Masuda, K. Fukuda, ORDERED METAL NANO HOLE ARRAYS MADE BY A 2-STEP REPLICATION OF HONEYCOMB STRUCTURES OF ANODIC ALUMINA. *Science* **1995**, 268, 1466.
- [31] J. Yao, Z. W. Liu, Y. M. Liu, Y. Wang, C. Sun, G. Bartal, A. M. Stacy, X. Zhang, Optical negative refraction in bulk metamaterials of nanowires. *Science* **2008**, 321, 930.
- [32] W. Dickson, G. A. Wurtz, P. Evans, D. O'Connor, R. Atkinson, R. Pollard, A. V. Zayats, Dielectric-loaded plasmonic nanoantenna arrays: A metamaterial with tuneable optical properties. **2007**, 76.
- [33] J. Gao, X. Wu, Q. Li, S. Du, F. Huang, L. Liang, H. Zhang, F. Zhuge, H. Cao, Y. Song, Template-Free Growth of Well-Ordered Silver Nano Forest/Ceramic Metamaterial Films with Tunable Optical Responses. *Adv Mater* **2017**, 29.
- [34] J. Gao, X. Wu, Q. Li, S. Du, F. Huang, L. Liang, H. Zhang, F. Zhuge, H. Cao, Y. Song, Template-Free Growth of Well-Ordered Silver Nano Forest/Ceramic Metamaterial Films with Tunable Optical Responses. *Adv. Mater.* **2017**, 29, 1605324.
- [35] W. Zhou, T. W. Odom, Tunable subradiant lattice plasmons by out-of-plane dipolar interactions. *Nature Nanotechnology* **2011**, 6, 423.
- [36] G. Vecchi, V. Giannini, J. Gómez Rivas, Shaping the Fluorescent Emission by Lattice Resonances in Plasmonic Crystals of Nanoantennas. **2009**, 102.
- [37] M. Decker, M. W. Klein, M. Wegener, S. Linden, Circular dichroism of planar chiral magnetic metamaterials. *Opt. Lett.* **2007**, 32, 856.
- [38] M. C. Gwinner, E. Koroknay, L. Fu, P. Patoka, W. Kandulski, M. Giersig, H. Giessen, Periodic Large-Area Metallic Split-Ring Resonator Metamaterial Fabrication Based on Shadow Nanosphere Lithography. **2009**, 5, 400.
- [39] A. E. Nikolaenko, F. De Angelis, S. A. Boden, N. Papasimakis, P. Ashburn, E. Di Fabrizio, N. I. Zheludev, Carbon Nanotubes in a Photonic Metamaterial. *Physical Review Letters* **2010**, 104.
- [40] W. Wu, E. Kim, E. Ponizovskaya, Y. Liu, Z. Yu, N. Fang, Y. R. Shen, A. M. Bratkovsky, W. Tong, C. Sun, X. Zhang, S. Y. Wang, R. S. Williams, Optical metamaterials at near and mid-IR range fabricated by nanoimprint lithography. *Applied Physics A* **2007**, 87, 143.
- [41] A. Nemati, Q. Wang, M. Hong, J. Teng, Tunable and reconfigurable metasurfaces and metadevices. *Opto-Electronic Advances* **2018**, 1, 180009.
- [42] H.-T. Chen, A. J. Taylor, N. Yu, A review of metasurfaces: physics and applications. *Reports on Progress in Physics* **2016**, 79, 076401.

- [43] S. Y. Chang, X. X. Guo, X. J. Ni, *Annual Reviews*, **2018**, 48.
- [44] N. Meinzer, W. L. Barnes, I. R. Hooper, Plasmonic meta-atoms and metasurfaces. *Nat. Photonics* **2014**, 8, 889.
- [45] F. Ding, A. Pors, S. I. Bozhevolnyi, Gradient metasurfaces: a review of fundamentals and applications. *Reports on Progress in Physics* **2018**, 81, 44.
- [46] L. Huang, X. Chen, H. Mühlenbernd, H. Zhang, S. Chen, B. Bai, Q. Tan, G. Jin, K.-W. Cheah, C.-W. Qiu, J. Li, T. Zentgraf, S. Zhang, Three-dimensional optical holography using a plasmonic metasurface. *Nature Communications* **2013**, 4, 2808.
- [47] C. L. Cortes, W. Newman, S. Molesky, Z. Jacob, Quantum nanophotonics using hyperbolic metamaterials. *J. Opt.* **2012**, 14, 15.
- [48] C. García-Meca, J. Hurtado, J. Martí, A. Martínez, W. Dickson, A. V. Zayats, Low-Loss Multilayered Metamaterial Exhibiting a Negative Index of Refraction at Visible Wavelengths. *Phys. Rev. Lett.* **2011**, 106, 067402.
- [49] D. Lu, J. J. Kan, E. E. Fullerton, Z. Liu, Enhancing spontaneous emission rates of molecules using nanopatterned multilayer hyperbolic metamaterials. *Nat. Nanotechnol.* **2014**, 9, 48.
- [50] C. R. Simovski, P. A. Belov, A. V. Atrashchenko, Y. S. Kivshar, Wire Metamaterials: Physics and Applications. *Adv. Mater.* **2012**, 24, 4229.
- [51] A. Poddubny, I. Iorsh, P. Belov, Y. Kivshar, Hyperbolic metamaterials. *Nat. Photonics* **2013**, 7, 948.
- [52] J. Valentine, S. Zhang, T. Zentgraf, E. Ulin-Avila, D. A. Genov, G. Bartal, X. Zhang, Three-dimensional optical metamaterial with a negative refractive index. *Nature* **2008**, 455, 376.
- [53] H. Zheng, J. Wang, S. E. Lofland, Z. Ma, L. Mohaddes-Ardabili, T. Zhao, L. Salamanca-Riba, S. R. Shinde, S. B. Ogale, F. Bai, D. Viehland, Y. Jia, D. G. Schlom, M. Wuttig, A. Roytburd, R. Ramesh, Multiferroic BaTiO<sub>3</sub>-CoFe<sub>2</sub>O<sub>4</sub> Nanostructures. *Science* **2004**, 303, 661.
- [54] S. Misra, L. Li, J. Jian, J. Huang, X. Wang, D. Zemlyanov, J.-W. Jang, F. H. Ribeiro, H. Wang, Tailorable Au Nanoparticles Embedded in Epitaxial TiO<sub>2</sub> Thin Films for Tunable Optical Properties. *ACS Applied Materials & Interfaces* **2018**, 10, 32895.
- [55] J. Jian, X. Wang, S. Misra, X. Sun, Z. Qi, X. Gao, J. Sun, A. Donohue, D. G. Lin, V. Pol, J. Youngblood, H. Wang, L. Li, J. Huang, H. Wang, Broad Range Tuning of Phase Transition Property in VO<sub>2</sub> Through Metal-Ceramic Nanocomposite Design. *Adv. Funct. Mater.* **2019**, 29, 1903690.

- [56] L. Li, L. Sun, J. S. Gomez-Diaz, N. L. Hogan, P. Lu, F. Khatkhatay, W. Zhang, J. Jian, J. Huang, Q. Su, M. Fan, C. Jacob, J. Li, X. Zhang, Q. Jia, M. Sheldon, A. Alu, X. Li, H. Wang, Self-Assembled Epitaxial Au-Oxide Vertically Aligned Nanocomposites for Nanoscale Metamaterials. *Nano Lett* **2016**, *16*, 3936.
- [57] J. Huang, L. Li, P. Lu, Z. Qi, X. Sun, X. Zhang, H. Wang, Self-assembled Co-BaZrO<sub>3</sub> nanocomposite thin films with ultra-fine vertically aligned Co nanopillars. *Nanoscale* **2017**, *9*, 7970.
- [58] R. L. Paldi, X. Sun, X. Wang, X. Zhang, H. Wang, Strain-Driven In-plane Ordering in Vertically Aligned ZnO–Au Nanocomposites with Highly Correlated Metamaterial Properties. *ACS Omega* **2020**, *5*, 2234.
- [59] J. Huang, X. Wang, N. L. Hogan, S. Wu, P. Lu, Z. Fan, Y. Dai, B. Zeng, R. Starko-Bowes, J. Jian, H. Wang, L. Li, R. P. Prasankumar, D. Yarotski, M. Sheldon, H. T. Chen, Z. Jacob, X. Zhang, H. Wang, Nanoscale Artificial Plasmonic Lattice in Self-Assembled Vertically Aligned Nitride-Metal Hybrid Metamaterials. *Adv. Sci.* **2018**, *5*, 1800416.
- [60] W. Zhang, R. Ramesh, J. L. MacManus-Driscoll, H. Wang, Multifunctional, self-assembled oxide nanocomposite thin films and devices. *MRS Bull.* **2015**, *40*, 736.
- [61] X. Wang, J. Jian, Z. Zhou, C. Fan, Y. Dai, L. Li, J. Huang, J. Sun, A. Donohue, P. Bermel, X. Zhang, H. T. Chen, H. Wang, Self-Assembled Ag–TiN Hybrid Plasmonic Metamaterial: Tailorable Tilted Nanopillar and Optical Properties. *Adv. Opt. Mater.* **2018**, *7*, 1801180.
- [62] X. Wang, J. Jian, S. Diaz-Amaya, C. E. Kumah, P. Lu, J. Huang, D. G. Lim, V. G. Pol, J. P. Youngblood, A. Boltasseva, L. A. Stanciu, D. M. O'Carroll, X. Zhang, H. Wang, Hybrid plasmonic Au–TiN vertically aligned nanocomposites: a nanoscale platform towards tunable optical sensing. *Nanoscale Advances* **2019**, *1*, 1045.
- [63] A. P. Chen, Z. X. Bi, C. F. Tsai, J. Lee, Q. Su, X. H. Zhang, Q. X. Jia, J. L. MacManus-Driscoll, H. Y. Wang, Tunable Low-Field Magnetoresistance in (La<sub>0.7</sub>Sr<sub>0.3</sub>MnO<sub>3</sub>)<sub>(0.5)</sub>:(ZnO)<sub>(0.5)</sub> Self-Assembled Vertically Aligned Nanocomposite Thin Films. *Adv. Funct. Mater.* **2011**, *21*, 2423.
- [64] A. Chen, Q. Su, H. Han, E. Enriquez, Q. Jia, Metal Oxide Nanocomposites: A Perspective from Strain, Defect, and Interface. *Adv Mater* **2019**, *31*, e1803241.
- [65] W. Zhang, A. Chen, Z. Bi, Q. Jia, J. L. MacManus-Driscoll, H. Wang, Interfacial coupling in heteroepitaxial vertically aligned nanocomposite thin films: From lateral to vertical control. *Current Opinion in Solid State and Materials Science* **2014**, *18*, 6.
- [66] J. L. MacManus-Driscoll, Self-Assembled Heteroepitaxial Oxide Nanocomposite Thin Film Structures: Designing Interface-Induced Functionality in Electronic Materials. *Adv. Funct. Mater.* **2010**, *20*, 2035.

- [67] W. R. Grove, VII. On the electro-chemical polarity of gases. *Philosophical Transactions of the Royal Society of London* **1852**, 142, 87.
- [68] M. Ohring, *Materials Science of Thin Films*. **2001**.
- [69] J. L. MacManus-Driscoll, P. Zerrer, H. Wang, H. Yang, J. Yoon, A. Fouchet, R. Yu, M. G. Blamire, Q. Jia, Strain control and spontaneous phase ordering in vertical nanocomposite heteroepitaxial thin films. *Nat. Mater.* **2008**, 7, 314.
- [70] A. Chen, W. Zhang, F. Khatkhatay, Q. Su, C.-F. Tsai, L. Chen, Q. X. Jia, J. L. MacManus-Driscoll, H. Wang, Magnetotransport properties of quasi-one-dimensionally channeled vertically aligned heteroepitaxial nanomazes. *Appl. Phys. Lett.* **2013**, 102, 093114.
- [71] A. Chen, Z. Bi, C.-F. Tsai, J. Lee, Q. Su, X. Zhang, Q. Jia, J. L. MacManus-Driscoll, H. Wang, Tunable Low-Field Magnetoresistance in  $(\text{La}_{0.7}\text{Sr}_{0.3}\text{MnO}_3)_{0.5}:(\text{ZnO})_{0.5}$  Self-Assembled Vertically Aligned Nanocomposite Thin Films. *Adv. Funct. Mater.* **2011**, 21, 2423.
- [72] L. Mohaddes-Ardabili, H. Zheng, S. B. Ogale, B. Hannoyer, W. Tian, J. Wang, S. E. Lofland, S. R. Shinde, T. Zhao, Y. Jia, L. Salamanca-Riba, D. G. Schlom, M. Wuttig, R. Ramesh, Self-assembled single-crystal ferromagnetic iron nanowires formed by decomposition. *Nat. Mater.* **2004**, 3, 533.
- [73] J. L. MacManus-Driscoll, S. R. Foltyn, Q. X. Jia, H. Wang, A. Serquis, L. Civale, B. Maiorov, M. E. Hawley, M. P. Maley, D. E. Peterson, Strongly enhanced current densities in superconducting coated conductors of  $\text{YBa}_2\text{Cu}_3\text{O}_{7-x} + \text{BaZrO}_3$ . *Nat. Mater.* **2004**, 3, 439.
- [74] L. Mohaddes-Ardabili, H. Zheng, S. B. Ogale, B. Hannoyer, W. Tian, J. Wang, S. E. Lofland, S. R. Shinde, T. Zhao, Y. Jia, L. Salamanca-Riba, D. G. Schlom, M. Wuttig, R. Ramesh, Self-assembled single-crystal ferromagnetic iron nanowires formed by decomposition. *Nat. Mater.* **2004**, 3, 533.
- [75] A. Chen, J.-M. Hu, P. Lu, T. Yang, W. Zhang, L. Li, T. Ahmed, E. Enriquez, M. Weigand, Q. Su, H. Wang, J.-X. Zhu, J. L. MacManus-Driscoll, L.-Q. Chen, D. Yarotski, Q. Jia, Role of scaffold network in controlling strain and functionalities of nanocomposite films. *Sci. Adv.* **2016**, 2, e1600245.
- [76] A. P. Chen, W. R. Zhang, F. Khatkhatay, Q. Su, C. F. Tsai, L. Chen, Q. X. Jia, J. L. MacManus-Driscoll, H. Wang, Magnetotransport properties of quasi-one-dimensionally channeled vertically aligned heteroepitaxial nanomazes. *Appl. Phys. Lett.* **2013**, 102, 4.
- [77] W. Si, S. J. Han, X. Shi, S. N. Ehrlich, J. Jaroszynski, A. Goyal, Q. Li, High current superconductivity in  $\text{FeSe}_{0.5}\text{Te}_{0.5}$ -coated conductors at 30 tesla. *Nature Communications* **2013**, 4, 1347.

- [78] R. X. Liang, P. Dosanjh, D. A. Bonn, D. J. Baar, J. F. Carolan, W. N. Hardy, GROWTH AND PROPERTIES OF SUPERCONDUCTING YBCO SINGLE-CRYSTALS. *Physica C* **1992**, *195*, 51.
- [79] E. D. Palik, Handbook of optical constants of solids. Academic press, **1998**, 3.
- [80] D. Zhang, S. Misra, L. Li, X. Wang, J. Jian, P. Lu, X. Gao, X. Sun, Z. Qi, M. Kalaswad, X. Zhang, H. Wang, Tunable Optical Properties in Self-Assembled Oxide-Metal Hybrid Thin Films via Au-Phase Geometry Control: From Nanopillars to Nanodisks. *Adv. Opt. Mater.* *n/a*, 1901359.
- [81] M. Kalaswad, D. Zhang, X. Gao, L. L. Contreras, H. Wang, X. Wang, H. Wang, Integration of Hybrid Plasmonic Au–BaTiO<sub>3</sub> Metamaterial on Silicon Substrates. *ACS Applied Materials & Interfaces* **2019**, *11*, 45199.
- [82] G. Armelles, A. Cebollada, A. García-Martín, M. U. González, Magnetoplasmonics: Combining Magnetic and Plasmonic Functionalities. *Adv. Opt. Mater.* **2013**, *1*, 10.
- [83] J. B. González-Díaz, A. García-Martín, G. Armelles, D. Navas, M. Vázquez, K. Nielsch, R. B. Wehrspohn, U. Gösele, Enhanced Magneto-Optics and Size Effects in Ferromagnetic Nanowire Arrays. *Adv. Mater.* **2007**, *19*, 2643.
- [84] J. Huang, Z. Qi, L. Li, H. Wang, S. Xue, B. Zhang, X. Zhang, H. Wang, Self-assembled vertically aligned Ni nanopillars in CeO<sub>2</sub> with anisotropic magnetic and transport properties for energy applications. *Nanoscale* **2018**, *10*, 17182.
- [85] B. Zhang, J. Huang, J. Jian, B. X. Rutherford, L. Li, S. Misra, X. Sun, H. Wang, Tuning magnetic anisotropy in Co–BaZrO<sub>3</sub> vertically aligned nanocomposites for memory device integration. *Nanoscale Adv.* **2019**, *1*, 4450.
- [86] M. H. Huang, Y. Wu, H. Feick, N. Tran, E. Weber, P. Yang, Catalytic Growth of Zinc Oxide Nanowires by Vapor Transport. *Adv. Mater.* **2001**, *13*, 113.
- [87] K. Ueno, S. Juodkazis, M. Mino, V. Mizeikis, H. Misawa, Spectral sensitivity of uniform arrays of gold nanorods to dielectric environment. *J. Phys. Chem. C* **2007**, *111*, 4180.
- [88] B. Luk'yanchuk, N. I. Zheludev, S. A. Maier, N. J. Halas, P. Nordlander, H. Giessen, C. T. Chong, The Fano resonance in plasmonic nanostructures and metamaterials. *Nat. Mater.* **2010**, *9*, 707.
- [89] T. Koschny, P. Markos, E. N. Economou, D. R. Smith, D. C. Vier, C. M. Soukoulis, Impact of inherent periodic structure on effective medium description of left-handed and related metamaterials. *Physical Review B* **2005**, *71*, 22.

- [90] J. Huang, J. L. MacManus-Driscoll, H. Wang, New epitaxy paradigm in epitaxial self-assembled oxide vertically aligned nanocomposite thin films. *Journal of Materials Research* **2017**, *32*, 4054.
- [91] N. M. Aimon, H. K. Choi, X. Y. Sun, D. H. Kim, C. A. Ross, Templated Self-Assembly of Functional Oxide Nanocomposites. *Adv. Mater.* **2014**, *26*, 3063.
- [92] Y. Zhu, K. Mimura, M. Isshiki, Oxidation Mechanism of Copper at 623-1073 K. *MATERIALS TRANSACTIONS* **2002**, *43*, 2173.
- [93] M. Walkowicz, P. Osuch, B. Smyrak, T. Knych, E. Rudnik, Ł. Cieniek, A. Róžańska, A. Chmielarczyk, D. Romaniszyn, M. Bulanda, Impact of oxidation of copper and its alloys in laboratory-simulated conditions on their antimicrobial efficiency. *Corrosion Science* **2018**, *140*, 321.
- [94] M. W. Knight, N. S. King, L. Liu, H. O. Everitt, P. Nordlander, N. J. Halas, Aluminum for plasmonics. *ACS nano* **2014**, *8*, 834.
- [95] A. Jakab, C. Rosman, Y. Khalavka, J. Becker, A. Trügler, U. Hohenester, C. Sönnichsen, Highly Sensitive Plasmonic Silver Nanorods. *ACS Nano* **2011**, *5*, 6880.
- [96] X.-M. Li, M.-H. Bi, L. Cui, Y.-Z. Zhou, X.-W. Du, S.-Z. Qiao, J. Yang, 3D Aluminum Hybrid Plasmonic Nanostructures with Large Areas of Dense Hot Spots and Long-Term Stability. *Adv. Funct. Mater.* **2017**, *27*, 1605703.
- [97] M. Losurdo, I. Bergmair, B. Dastmalchi, T.-H. Kim, M. M. Giangregorio, W. Jiao, G. V. Bianco, A. S. Brown, K. Hingerl, G. Bruno, Graphene as an Electron Shuttle for Silver Deoxidation: Removing a Key Barrier to Plasmonics and Metamaterials for SERS in the Visible. *Adv. Funct. Mater.* **2014**, *24*, 1864.
- [98] C. Xue, X. Chen, S. J. Hurst, C. A. Mirkin, Self-Assembled Monolayer Mediated Silica Coating of Silver Triangular Nanoprisms. *Adv. Mater.* **2007**, *19*, 4071.
- [99] M. M. Shahjamali, Y. Zhou, N. Zараee, C. Xue, J. Wu, N. Large, C. M. McGuirk, F. Boey, V. Dravid, Z. Cui, G. C. Schatz, C. A. Mirkin, Ag–Ag<sub>2</sub>S Hybrid Nanoprisms: Structural versus Plasmonic Evolution. *ACS Nano* **2016**, *10*, 5362.
- [100] H. Liu, T. Liu, L. Zhang, L. Han, C. Gao, Y. Yin, Etching-Free Epitaxial Growth of Gold on Silver Nanostructures for High Chemical Stability and Plasmonic Activity. *Adv. Funct. Mater.* **2015**, *25*, 5435.
- [101] J. B. Khurgin, A. Boltasseva, Reflecting upon the losses in plasmonics and metamaterials. *MRS Bull.* **2012**, *37*, 768.
- [102] A. Boltasseva, H. A. Atwater, Low-Loss Plasmonic Metamaterials. *Science* **2011**, *331*, 290.

- [103] J. B. Khurgin, Replacing noble metals with alternative materials in plasmonics and metamaterials: how good an idea? *Philosophical Transactions of the Royal Society A: Mathematical, Physical and Engineering Sciences* **2017**, 375, 20160068.
- [104] H. Lin, B. C. P. Sturmberg, K.-T. Lin, Y. Yang, X. Zheng, T. K. Chong, C. M. de Sterke, B. Jia, A 90-nm-thick graphene metamaterial for strong and extremely broadband absorption of unpolarized light. *Nat. Photonics* **2019**, 13, 270.
- [105] V. G. Kravets, R. Jalil, Y. J. Kim, D. Ansell, D. E. Aznakayeva, B. Thackray, L. Britnell, B. D. Belle, F. Withers, I. P. Radko, Z. Han, S. I. Bozhevolnyi, K. S. Novoselov, A. K. Geim, A. N. Grigorenko, Graphene-protected copper and silver plasmonics. *Scientific Reports* **2014**, 4, 5517.
- [106] I. Milosev, H. H. Strehblow, B. Navinsek, Comparison of TiN, ZrN and CrN hard nitride coatings: Electrochemical and thermal oxidation. *Thin Solid Films* **1997**, 303, 246.
- [107] S. Veprek, S. Reiprich, A concept for the design of novel superhard coatings. *Thin Solid Films* **1995**, 268, 64.
- [108] A. S. Garcia, J. A. Diniz, J. W. Swart, L. P. B. Lima, M. V. Puydinger Dos Santos.
- [109] N. K. Ponon, D. J. Appleby, E. Arac, P. King, S. Ganti, K. S. Kwa, A. O'Neill, Effect of deposition conditions and post deposition anneal on reactively sputtered titanium nitride thin films. *Thin Solid Films* **2015**, 578, 31.
- [110] K. Inumaru, T. Ohara, S. Yamanaka, Pulsed laser deposition of epitaxial titanium nitride on MgO (001) monitored by RHEED oscillation. *Applied surface science* **2000**, 158, 375.
- [111] H. Wang, A. Tiwari, A. Kvit, X. Zhang, J. Narayan, Epitaxial growth of TaN thin films on Si(100) and Si(111) using a TiN buffer layer. **2002**, 80, 2323.
- [112] P. Tiwari, X. D. Wu, S. R. Foltyn, Q. X. Jia, I. H. Campbell, P. A. Arendt, R. E. Muenchausen, D. E. Peterson, T. E. Mitchell, J. Narayan, Synthesis of epitaxial Pt on (100)Si using TiN buffer layer by pulsed laser deposition. **1994**, 65, 2693.
- [113] P. Prieto, J. F. Marco, J. E. Prieto, S. Ruiz-Gomez, L. Perez, R. P. Del Real, M. Vázquez, J. De La Figuera, Epitaxial integration of CoFe<sub>2</sub>O<sub>4</sub> thin films on Si (001) surfaces using TiN buffer layers. *Applied Surface Science* **2018**, 436, 1067.
- [114] G. V. Naik, V. M. Shalaev, A. Boltasseva, Alternative Plasmonic Materials: Beyond Gold and Silver. *Adv. Mater.* **2013**, 25, 3264.
- [115] G. V. Naik, J. L. Schroeder, X. Ni, A. V. Kildishev, T. D. Sands, A. Boltasseva, Titanium nitride as a plasmonic material for visible and near-infrared wavelengths. *Opt. Mater. Express* **2012**, 2, 478.

- [116] W. Li, U. Guler, N. Kinsey, G. V. Naik, A. Boltasseva, J. G. Guan, V. M. Shalaev, A. V. Kildishev, Refractory Plasmonics with Titanium Nitride: Broadband Metamaterial Absorber. *Adv. Mater.* **2014**, *26*, 7959.
- [117] N. Kinsey, A. A. Syed, D. Courtwright, C. Devault, C. E. Bonner, V. I. Gavrilenko, V. M. Shalaev, D. J. Hagan, E. W. Van Stryland, A. Boltasseva, Effective third-order nonlinearities in metallic refractory titanium nitride thin films. **2015**, *5*, 2395.
- [118] L. L. Gui, S. Bagheri, N. Strohsfeldt, M. Hentschel, C. M. Zgrabik, B. Metzger, H. Linnenbank, E. L. Hu, H. Giessen, Nonlinear Refractory Plasmonics with Titanium Nitride Nanoantennas. *Nano Letters* **2016**, *16*, 5708.
- [119] J. M. Reed, M. R. Ferdinandus, N. Kinsey, C. DeVault, U. Guler, V. M. Shalaev, A. Boltasseva, A. Urbas *CLEO: QELS Fundamental Science*, **2016**, FTu1A. 6.
- [120] H. A. Atwater, The promise of plasmonics. *Scientific American* **2007**, *296*, 56.
- [121] J. Narayan, P. Tiwari, X. Chen, J. Singh, R. Chowdhury, T. Zheleva, EPITAXIAL-GROWTH OF TIN FILMS ON (100) SILICON SUBSTRATES BY LASER PHYSICAL VAPOR-DEPOSITION. *Appl. Phys. Lett.* **1992**, *61*, 1290.
- [122] A. Moatti, J. Narayan, High-quality TiN/AlN thin film heterostructures on c-sapphire. *Acta Materialia* **2018**, *145*, 134.
- [123] F. Santerre, M. A. El Khakani, M. Chaker, J. P. Dodelet, Properties of TiC thin films grown by pulsed laser deposition. *Applied Surface Science* **1999**, *148*, 24.
- [124] R. F. Davis, III-V nitrides for electronic and optoelectronic applications. *Proceedings of the IEEE* **1991**, *79*, 702.
- [125] J. A. Schuller, E. S. Barnard, W. S. Cai, Y. C. Jun, J. S. White, M. L. Brongersma, Plasmonics for extreme light concentration and manipulation. *Nat. Mater.* **2010**, *9*, 193.
- [126] R. F. Oulton, V. J. Sorger, D. A. Genov, D. F. P. Pile, X. Zhang, A hybrid plasmonic waveguide for subwavelength confinement and long-range propagation. *Nat. Photonics* **2008**, *2*, 496.
- [127] Y. R. Fang, M. T. Sun, Nanoplasmonic waveguides: towards applications in integrated nanophotonic circuits. *Light-Sci. Appl.* **2015**, *4*, 11.
- [128] V. E. Ferry, L. A. Sweatlock, D. Pacifici, H. A. Atwater, Plasmonic Nanostructure Design for Efficient Light Coupling into Solar Cells. *Nano Letters* **2008**, *8*, 4391.
- [129] S. Linic, P. Christopher, D. B. Ingram, Plasmonic-metal nanostructures for efficient conversion of solar to chemical energy. *Nat. Mater.* **2011**, *10*, 911.

- [130] Y. Kim, J. G. Smith, P. K. Jain, Harvesting multiple electron-hole pairs generated through plasmonic excitation of Au nanoparticles. *Nat. Chem.* **2018**, *10*, 763.
- [131] J. N. Anker, W. P. Hall, O. Lyandres, N. C. Shah, J. Zhao, R. P. Van Duyne, Biosensing with plasmonic nanosensors. *Nat. Mater.* **2008**, *7*, 442.
- [132] K. S. Lee, M. A. El-Sayed, Gold and silver nanoparticles in sensing and imaging: Sensitivity of plasmon response to size, shape, and metal composition. *J. Phys. Chem. B* **2006**, *110*, 19220.
- [133] V. M. Shalaev, Optical negative-index metamaterials. *Nat. Photonics* **2007**, *1*, 41.
- [134] J. Valentine, S. Zhang, T. Zentgraf, E. Ulin-Avila, D. A. Genov, G. Bartal, X. Zhang, Three-dimensional optical metamaterial with a negative refractive index. *Nature* **2008**, *455*, 376.
- [135] C. M. Soukoulis, M. Wegener, Past achievements and future challenges in the development of three-dimensional photonic metamaterials. *Nat. Photonics* **2011**, *5*, 523.
- [136] J. J. Mock, R. T. Hill, A. Degiron, S. Zauscher, A. Chilkoti, D. R. Smith, Distance-dependent plasmon resonant coupling between a gold nanoparticle and gold film. *Nano Letters* **2008**, *8*, 2245.
- [137] X. H. N. Xu, W. J. Brownlow, S. V. Kyriacou, Q. Wan, J. J. Viola, Real-time probing of membrane transport in living microbial cells using single nanoparticle optics and living cell imaging. *Biochemistry* **2004**, *43*, 10400.
- [138] A. D. McFarland, R. P. Van Duyne, Single silver nanoparticles as real-time optical sensors with zeptomole sensitivity. *Nano Letters* **2003**, *3*, 1057.
- [139] K. J. Lee, P. D. Nallathamby, L. M. Browning, C. J. Osgood, X. H. N. Xu, In vivo imaging of transport and biocompatibility of single silver nanoparticles in early development of zebrafish embryos. *Acs Nano* **2007**, *1*, 133.
- [140] N. J. B. David J. Garfield, Samia M. Hamed, Nicole A. , Cheryl A. Tajon, Bining Tian, Brian Shevitski, Edward S. Barnard, Yung Doug Suh, Shaul Aloni, Jeffrey B. Neaton, Emory M. Chan, Bruce E. Cohen, P. James Schuck, Enrichment of molecular antenna triplets amplifies upconverting nanoparticle emission. *Nat. Photonics* **2018**.
- [141] Y. C. Shen, D. X. Ye, I. Celanovic, S. G. Johnson, J. D. Joannopoulos, M. Soljacic, Optical Broadband Angular Selectivity. *Science* **2014**, *343*, 1499.
- [142] M. Rycenga, C. M. Cobley, J. Zeng, W. Y. Li, C. H. Moran, Q. Zhang, D. Qin, Y. N. Xia, Controlling the Synthesis and Assembly of Silver Nanostructures for Plasmonic Applications. *Chemical Reviews* **2011**, *111*, 3669.

- [143] J. B. Khurgin, How to deal with the loss in plasmonics and metamaterials. *Nature Nanotechnology* **2015**, *10*, 2.
- [144] J. J. Huang, X. J. Wang, N. L. Hogan, S. X. Wu, P. Lu, Z. Fan, Y. M. Dai, B. B. Zeng, R. Starko-Bowes, J. Jian, H. Wang, L. G. Li, R. P. Prasankumar, D. Yarotski, M. Sheldon, H. T. Chen, Z. Jacob, X. H. Zhang, H. Y. Wang, Nanoscale Artificial Plasmonic Lattice in Self-Assembled Vertically Aligned Nitride-Metal Hybrid Metamaterials. *Adv. Sci.* **2018**, *5*, 9.
- [145] S. Jahani, Z. Jacob, All-dielectric metamaterials. *Nat. Nanotechnol.* **2016**, *11*, 23.
- [146] Z. K. Zhou, X. N. Peng, Z. J. Yang, Z. S. Zhang, M. Li, X. R. Su, Q. Zhang, X. Y. Shan, Q. Q. Wang, Z. Y. Zhang, Tuning Gold Nanorod-Nanoparticle Hybrids into Plasmonic Fano Resonance for Dramatically Enhanced Light Emission and Transmission. *Nano Letters* **2011**, *11*, 49.
- [147] Y. C. Jun, J. Reno, T. Ribaudou, E. Shaner, J. J. Greffet, S. Vassant, F. Marquier, M. Sinclair, I. Brener, Epsilon-Near-Zero Strong Coupling in Metamaterial-Semiconductor Hybrid Structures. *Nano Letters* **2013**, *13*, 5391.
- [148] X. M. Li, M. H. Bi, L. Cui, Y. Z. Zhou, X. W. Du, S. Z. Qiao, J. Yang, 3D Aluminum Hybrid Plasmonic Nanostructures with Large Areas of Dense Hot Spots and Long-Term Stability. *Adv. Funct. Mater.* **2017**, *27*, 9.
- [149] R. G. Freeman, M. B. Hommer, K. C. Grabar, M. A. Jackson, M. J. Natan, Ag-clad Au nanoparticles: Novel aggregation, optical, and surface-enhanced Raman scattering properties. *J. Phys. Chem.* **1996**, *100*, 718.
- [150] N. Liu, H. C. Guo, L. W. Fu, S. Kaiser, H. Schweizer, H. Giessen, Three-dimensional photonic metamaterials at optical frequencies. *Nat. Mater.* **2008**, *7*, 31.
- [151] J. H. Gao, X. Z. Wu, Q. W. Li, S. Y. Du, F. Huang, L. Y. Liang, H. L. Zhang, F. Zhuge, H. T. Cao, Y. L. Song, Template-Free Growth of Well-Ordered Silver Nano Forest/Ceramic Metamaterial Films with Tunable Optical Responses. *Adv. Mater.* **2017**, *29*, 8.
- [152] P. Zilio, M. Malerba, A. Toma, R. P. Zaccaria, A. Jacassi, F. De Angelis, Hybridization in Three Dimensions: A Novel Route toward Plasmonic Metamolecules. *Nano Letters* **2015**, *15*, 5200.
- [153] Y. Yang, J. L. Shi, G. Kawamura, M. Nogami, Preparation of Au-Ag, Ag-Au core-shell bimetallic nanoparticles for surface-enhanced Raman scattering. *Scr. Mater.* **2008**, *58*, 862.
- [154] E. K. Payne, K. L. Shuford, S. Park, G. C. Schatz, C. A. Mirkin, Multipole plasmon resonances in gold nanorods. *J. Phys. Chem. B* **2006**, *110*, 2150.

- [155] X. J. Wu, J. Z. Chen, C. L. Tan, Y. H. Zhu, Y. Han, H. Zhang, Controlled growth of high-density CdS and CdSe nanorod arrays on selective facets of two-dimensional semiconductor nanoplates. *Nat. Chem.* **2016**, 8, 470.
- [156] R. J. Pollard, A. Murphy, W. R. Hendren, P. R. Evans, R. Atkinson, G. A. Wurtz, A. V. Zayats, V. A. Podolskiy, Optical Nonlocalities and Additional Waves in Epsilon-Near-Zero Metamaterials. *Phys. Rev. Lett.* **2009**, 102, 4.
- [157] G. J. H. D. W. H. H. Sachtler, A. A. Holscher, The work function of gold. *Surf. Sci.* **1966**, 5, 221.
- [158] S. A. Vitale, J. Kedzierski, P. Healey, P. W. Wyatt, C. L. Keast, Work-Function-Tuned TiN Metal Gate FDSOI Transistors for Subthreshold Operation. *IEEE Trans. Electron Devices* **2011**, 58, 419.
- [159] K. Saha, S. S. Agasti, C. Kim, X. N. Li, V. M. Rotello, Gold Nanoparticles in Chemical and Biological Sensing. *Chemical Reviews* **2012**, 112, 2739.
- [160] M. Stoehr, C. S. Shin, I. Petrov, J. E. Greene, Raman scattering from TiN<sub>x</sub> (0.67 ≤ x ≤ 1.00) single crystals grown on MgO(001). *Journal of Applied Physics* **2011**, 110, 4.
- [161] Y. H. Cheng, B. K. Tay, S. P. Lau, H. Kupfer, F. Richter, Substrate bias dependence of Raman spectra for TiN films deposited by filtered cathodic vacuum arc. *Journal of Applied Physics* **2002**, 92, 1845.
- [162] D. Huang, C. P. Byers, L. Y. Wang, A. L. Hoggard, B. Hoenee, S. Dominguez-Medina, S. S. Chen, W. S. Chang, C. F. Landes, S. Link, Photoluminescence of a Plasmonic Molecule. *Acs Nano* **2015**, 9, 7072.
- [163] T. V. Shahbazyan, Theory of Plasmon-Enhanced Metal Photoluminescence. *Nano Letters* **2013**, 13, 194.
- [164] U. S. Raikar, V. B. Tangod, B. M. Mastiholi, V. J. Fulari, Fluorescence quenching using plasmonic gold nanoparticles. *Opt. Commun.* **2011**, 284, 4761.
- [165] P. K. Jain, S. Eustis, M. A. El-Sayed, Plasmon coupling in nanorod assemblies: Optical absorption, discrete dipole approximation simulation, and exciton-coupling model. *J. Phys. Chem. B* **2006**, 110, 18243.
- [166] R. B. Jiang, B. X. Li, C. H. Fang, J. F. Wang, Metal/Semiconductor Hybrid Nanostructures for Plasmon-Enhanced Applications. *Adv. Mater.* **2014**, 26, 5274.
- [167] Z. W. Liu, W. B. Hou, P. Pavaskar, M. Aykol, S. B. Cronin, Plasmon Resonant Enhancement of Photocatalytic Water Splitting Under Visible Illumination. *Nano Letters* **2011**, 11, 1111.

- [168] N. J. Halas, S. Lal, W. S. Chang, S. Link, P. Nordlander, Plasmons in Strongly Coupled Metallic Nanostructures. *Chemical Reviews* **2011**, *111*, 3913.
- [169] L. Y. Lu, Z. Q. Luo, T. Xu, L. P. Yu, Cooperative Plasmonic Effect of Ag and Au Nanoparticles on Enhancing Performance of Polymer Solar Cells. *Nano Letters* **2013**, *13*, 59.
- [170] K. Aydin, V. E. Ferry, R. M. Briggs, H. A. Atwater, Broadband polarization-independent resonant light absorption using ultrathin plasmonic super absorbers. *Nature Communications* **2011**, *2*, 7.
- [171] W. Lewandowski, M. Fruhnert, J. Mieczkowski, C. Rockstuhl, E. Gorecka, Dynamically self-assembled silver nanoparticles as a thermally tunable metamaterial. *Nature Communications* **2015**, *6*, 9.
- [172] N. Engheta, Circuits with light at nanoscales: Optical nanocircuits inspired by metamaterials. *Science* **2007**, *317*, 1698.
- [173] Y. C. Shen, C. W. Hsu, Y. X. Yeng, J. D. Joannopoulos, M. Soljacic, Broadband angular selectivity of light at the nanoscale: Progress, applications, and outlook. *Appl. Phys. Rev.* **2016**, *3*, 13.
- [174] T. Shegai, S. Chen, V. D. Miljkovic, G. Zengin, P. Johansson, M. Kall, A bimetallic nanoantenna for directional colour routing. *Nature Communications* **2011**, *2*, 6.
- [175] J. Lin, J. P. B. Mueller, Q. Wang, G. H. Yuan, N. Antoniou, X. C. Yuan, F. Capasso, Polarization-Controlled Tunable Directional Coupling of Surface Plasmon Polaritons. *Science* **2013**, *340*, 331.
- [176] H. R. Stuart, D. G. Hall, Island size effects in nanoparticle-enhanced photodetectors. *Appl. Phys. Lett.* **1998**, *73*, 3815.
- [177] A. Jakab, C. Rosman, Y. Khalavka, J. Becker, A. Trugler, U. Hohenester, C. Sonnichsen, Highly Sensitive Plasmonic Silver Nanorods. *Acs Nano* **2011**, *5*, 6880.
- [178] A. B. Dahlin, J. O. Tegenfeldt, F. Hook, Improving the instrumental resolution of sensors based on localized surface plasmon resonance. *Analytical Chemistry* **2006**, *78*, 4416.
- [179] C. Xue, X. Chen, S. J. Hurst, C. A. Mirkin, Self-assembled monolayer mediated silica coating of silver triangular nanoprisms. *Adv. Mater.* **2007**, *19*, 4071.
- [180] E. M. Hicks, X. Y. Zhang, S. L. Zou, O. Lyandres, K. G. Spears, G. C. Schatz, R. P. Van Duyne, Plasmonic properties of film over nanowell surfaces fabricated by nanosphere lithography. *J. Phys. Chem. B* **2005**, *109*, 22351.
- [181] N. F. Yu, F. Capasso, Flat optics with designer metasurfaces. *Nat. Mater.* **2014**, *13*, 139.

- [182] M. W. Knight, N. S. King, L. F. Liu, H. O. Everitt, P. Nordlander, N. J. Halas, Aluminum for Plasmonics. *Acs Nano* **2014**, *8*, 834.
- [183] H. P. Liu, T. Z. Liu, L. Zhang, L. Han, C. B. Gao, Y. D. Yin, Etching-Free Epitaxial Growth of Gold on Silver Nanostructures for High Chemical Stability and Plasmonic Activity. *Adv. Funct. Mater.* **2015**, *25*, 5435.
- [184] M. Losurdo, I. Bergmair, B. Dastmalchi, T. H. Kim, M. M. Giangregroio, W. Y. Jiao, G. V. Bianco, A. S. Brown, K. Hingerl, G. Bruno, Graphene as an Electron Shuttle for Silver Deoxidation: Removing a Key Barrier to Plasmonics and Metamaterials for SERS in the Visible. *Adv. Funct. Mater.* **2014**, *24*, 1864.
- [185] M. M. Shahjamali, Y. Zhou, N. Zaraee, C. Xue, J. S. Wu, N. Large, C. M. McGuirk, F. Boey, V. Dravid, Z. F. Cui, G. C. Schatz, C. A. Mirkin, Ag-Ag<sub>2</sub>S Hybrid Nanoprisms: Structural versus Plasmonic Evolution. *Acs Nano* **2016**, *10*, 5362.
- [186] W. T. Lu, S. Sridhar, Superlens imaging theory for anisotropic nanostructured metamaterials with broadband all-angle negative refraction. *Physical Review B* **2008**, *77*, 4.
- [187] M. S. Rill, C. Plet, M. Thiel, I. Staude, G. Von Freymann, S. Linden, M. Wegener, Photonic metamaterials by direct laser writing and silver chemical vapour deposition. *Nat. Mater.* **2008**, *7*, 543.
- [188] Y. J. Liu, H. Y. Chu, Y. P. Zhao, Silver Nanorod Array Substrates Fabricated by Oblique Angle Deposition: Morphological, Optical, and SERS Characterizations. *J. Phys. Chem. C* **2010**, *114*, 8176.
- [189] D. X. Ye, Y. P. Zhao, G. R. Yang, Y. G. Zhao, G. C. Wang, T. M. Lu, Manipulating the column tilt angles of nanocolumnar films by glancing-angle deposition. *Nanotechnology* **2002**, *13*, 615.
- [190] L. Vitos, A. V. Ruban, H. L. Skriver, J. Kollar, The surface energy of metals. *Surf. Sci.* **1998**, *411*, 186.
- [191] F. Che, S. Grabtchak, W. M. Whelan, S. A. Ponomarenko, M. Cad, Relative SHG measurements of metal thin films: Gold, silver, aluminum, cobalt, chromium, germanium, nickel, antimony, titanium, titanium nitride, tungsten, zinc, silicon and indium tin oxide. *Results Phys.* **2017**, *7*, 593.
- [192] H. Tian, Z. G. Zhou, T. R. Liu, C. Karina, U. Guler, V. ShalaeV, P. Bermel, High temperature efficient, stable Si wafer-based selective solar absorbers. *Appl. Phys. Lett.* **2017**, *110*, 5.
- [193] A. D. Rakic, A. B. Djuricic, J. M. Elazar, M. L. Majewski, Optical properties of metallic films for vertical-cavity optoelectronic devices. *Appl. Optics* **1998**, *37*, 5271.

- [194] C. Clavero, Plasmon-induced hot-electron generation at nanoparticle/metal-oxide interfaces for photovoltaic and photocatalytic devices. *Nat. Photonics* **2014**, 8, 95.
- [195] S. Misra, L. Li, J. Jian, J. Huang, X. Wang, D. Zemlyanov, J.-W. Jang, F. H. Ribeiro, H. Wang, Tailorable Au Nanoparticles Embedded in Epitaxial TiO<sub>2</sub> Thin Films for Tunable Optical Properties. *ACS Applied Materials & Interfaces* **2018**.
- [196] J. Huang, T. Jin, S. Misra, H. Wang, Z. Qi, Y. Dai, X. Sun, L. Li, J. Okkema, H.-T. Chen, P.-T. Lin, X. Zhang, H. Wang, Tailorable Optical Response of Au–LiNbO<sub>3</sub> Hybrid Metamaterial Thin Films for Optical Waveguide Applications. *Adv. Opt. Mater.* **0**, 1800510.
- [197] C. Edmunds, L. Tang, M. Cervantes, M. Shirazi-Hd, J. Shao, A. Grier, A. Valavanis, J. D. Cooper, D. Li, G. Gardner, D. N. Zakharov, Z. Ikonic, D. Indjin, P. Harrison, M. J. Manfra, O. Malis, Comparative study of intersubband absorption in AlGa<sub>N</sub>/Ga<sub>N</sub> and AlIn<sub>N</sub>/Ga<sub>N</sub> superlattices: Impact of material inhomogeneities. *Physical Review B* **2013**, 88, 10.
- [198] F. A. Ponce, D. P. Bour, Nitride-based semiconductors for blue and green light-emitting devices. *Nature* **1997**, 386, 351.
- [199] Y. Taniyasu, M. Kasu, T. Makimoto, An aluminium nitride light-emitting diode with a wavelength of 210 nanometres. *Nature* **2006**, 441, 325.
- [200] J. J. X. Wang, Z. Zhou, C. Fan, Y. Dai, L. Li, J. Huang, J. Sun, A. Donohue, P. Bermel, X. Zhang, H.-T. Chen and H. Wang, Self-Assembled Ag-TiN Hybrid Plasmonic Metamaterial: Tailorable Tilted Nanopillar and Optical Properties. *Adv. Opt. Mater.* **2018**.
- [201] B. Padavala, C. D. Frye, X. J. Wang, Z. H. Ding, R. F. Chen, M. Dudley, B. Raghothamachar, P. Lu, B. N. Flanders, J. H. Edgar, Epitaxy of Boron Phosphide on Aluminum Nitride(0001)/Sapphire Substrate. *Crystal Growth & Design* **2016**, 16, 981.
- [202] S. Zhao, A. T. Connie, M. H. T. Dastjerdi, X. H. Kong, Q. Wang, M. Djavid, S. Sadaf, X. D. Liu, I. Shih, H. Guo, Z. Mi, Aluminum nitride nanowire light emitting diodes: Breaking the fundamental bottleneck of deep ultraviolet light sources. *Scientific Reports* **2015**, 5, 5.
- [203] K. Tonisch, V. Cimalla, C. Foerster, H. Romanus, O. Ambacher, D. Dontsov, Piezoelectric properties of polycrystalline AlN thin films for MEMS application. *Sens. Actuator A-Phys.* **2006**, 132, 658.
- [204] H. Okano, N. Tanaka, Y. Takahashi, T. Tanaka, K. Shibata, S. Nakano, PREPARATION OF ALUMINUM NITRIDE THIN-FILMS BY REACTIVE SPUTTERING AND THEIR APPLICATIONS TO GHZ-BAND SURFACE-ACOUSTIC-WAVE DEVICES. *Appl. Phys. Lett.* **1994**, 64, 166.
- [205] M. A. Dubois, P. Muralt, Properties of aluminum nitride thin films for piezoelectric transducers and microwave filter applications. *Appl. Phys. Lett.* **1999**, 74, 3032.

- [206] T. Prokofyeva, M. Seon, J. Vanbuskirk, M. Holtz, S. A. Nikishin, N. N. Faleev, H. Temkin, S. Zollner, Vibrational properties of AlN grown on (111)-oriented silicon. *Physical Review B* **2001**, *63*, 7.
- [207] C. Edmunds, J. Shao, M. Shirazi-Hd, M. J. Manfra, O. Malis, Terahertz intersubband absorption in non-polar m-plane AlGa<sub>N</sub>/Ga<sub>N</sub> quantum wells. *Appl. Phys. Lett.* **2014**, *105*, 4.
- [208] K. Jagannadham, A. K. Sharma, Q. Wei, R. Kalyanraman, J. Narayan, Structural characteristics of AlN films deposited by pulsed laser deposition and reactive magnetron sputtering: A comparative study. *J. Vac. Sci. Technol. A-Vac. Surf. Films* **1998**, *16*, 2804.
- [209] K. L. Kelly, E. Coronado, L. L. Zhao, G. C. Schatz, The optical properties of metal nanoparticles: The influence of size, shape, and dielectric environment. *J. Phys. Chem. B* **2003**, *107*, 668.
- [210] J. Ibanez, S. Hernandez, E. Alarcon-Llado, R. Cusco, L. Artus, S. V. Novikov, C. T. Foxon, E. Calleja, Far-infrared transmission in Ga<sub>N</sub>, AlN, and AlGa<sub>N</sub> thin films grown by molecular beam epitaxy. *Journal of Applied Physics* **2008**, *104*, 7.
- [211] Y. C. Chen, Y. T. Chang, H. H. Chen, F. T. Chuang, C. H. Cheng, S. C. Lee, Enhanced Transmission of Higher Order Plasmon Modes With Random Au Nanoparticles in Periodic Hole Arrays. *IEEE Photonics Technol. Lett.* **2013**, *25*, 47.
- [212] N. I. Zheludev, Y. S. Kivshar, From metamaterials to metadevices. *Nat. Mater.* **2012**, *11*, 917.
- [213] I. Staude, J. Schilling, Metamaterial-inspired silicon nanophotonics. *Nat. Photonics* **2017**, *11*, 274.
- [214] J. B. Pendry, D. Schurig, D. R. Smith, Controlling electromagnetic fields. *Science* **2006**, *312*, 1780.
- [215] K. Trofymchuk, A. Reisch, P. Didier, F. Fras, P. Gilliot, Y. Mely, A. S. Klymchenko, Giant light-harvesting nanoantenna for single-molecule detection in ambient light. *Nat. Photonics* **2017**, *11*, 657.
- [216] L. Ferrari, C. H. Wu, D. Lepage, X. Zhang, Z. W. Liu, Hyperbolic metamaterials and their applications. *Prog. Quantum Electron.* **2015**, *40*, 1.
- [217] J. M. McMahon, G. C. Schatz, S. K. Gray, Plasmonics in the ultraviolet with the poor metals Al, Ga, In, Sn, Tl, Pb, and Bi. *Physical Chemistry Chemical Physics* **2013**, *15*, 5415.
- [218] S. Liu, G. Chen, P. N. Prasad, M. T. Swihart, Synthesis of Monodisperse Au, Ag, and Au–Ag Alloy Nanoparticles with Tunable Size and Surface Plasmon Resonance Frequency. *Chemistry of Materials* **2011**, *23*, 4098.

- [219] J. Huang, X. Wang, X. L. Phuah, P. Lu, Z. Qi, H. Wang, Plasmonic Cu nanostructures in ZnO as hyperbolic metamaterial thin films. *Materials Today Nano* **2019**, *8*, 100052.
- [220] A. Chen, Z. Harrell, P. Lu, E. Enriquez, L. Li, B. Zhang, P. Dowden, C. Chen, H. Wang, J. L. MacManus-Driscoll, Q. Jia, Strain Enhanced Functionality in a Bottom-Up Approach Enabled 3D Super-Nanocomposites. *Adv. Funct. Mater.* **2019**, *29*, 1900442.
- [221] L. G. Li, L. Y. Sun, J. S. Gomez-Diaz, N. L. Hogan, P. Lu, F. Khatkhatay, W. R. Zhang, J. Jian, J. J. Huang, Q. Su, M. Fan, C. Jacob, J. Li, X. H. Zhang, Q. X. Jia, M. Sheldon, A. Alu, X. Q. Li, H. Y. Wang, Self-Assembled Epitaxial Au-Oxide Vertically Aligned Nanocomposites for Nanoscale Metamaterials. *Nano Lett.* **2016**, *16*, 3936.
- [222] C. Ciraci, R. T. Hill, J. J. Mock, Y. Urzhumov, A. I. Fernández-Domínguez, S. A. Maier, J. B. Pendry, A. Chilkoti, D. R. Smith, Probing the Ultimate Limits of Plasmonic Enhancement. *Science* **2012**, *337*, 1072.
- [223] Y. Kurokawa, H. T. Miyazaki, Metal-insulator-metal plasmon nanocavities: Analysis of optical properties. *Physical Review B* **2007**, *75*, 13.
- [224] K. J. Choi, M. Biegalski, Y. L. Li, A. Sharan, J. Schubert, R. Uecker, P. Reiche, Y. B. Chen, X. Q. Pan, V. Gopalan, L. Q. Chen, D. G. Schlom, C. B. Eom, Enhancement of ferroelectricity in strained BaTiO<sub>3</sub> thin films. *Science* **2004**, *306*, 1005.
- [225] P. J. Schuck, D. P. Fromm, A. Sundaramurthy, G. S. Kino, W. E. Moerner, Improving the mismatch between light and nanoscale objects with gold bowtie nanoantennas. *Phys. Rev. Lett.* **2005**, *94*, 4.
- [226] J. J. Baumberg, J. Aizpurua, M. H. Mikkelsen, D. R. Smith, Extreme nanophotonics from ultrathin metallic gaps. *Nat. Mater.* **2019**, *18*, 668.
- [227] L. V. Alekseyev, E. E. Narimanov, T. Tumkur, H. Li, Y. A. Barnakov, M. A. Noginov, Uniaxial epsilon-near-zero metamaterial for angular filtering and polarization control. *Appl. Phys. Lett.* **2010**, *97*, 131107.
- [228] P. Shekhar, J. Atkinson, Z. Jacob, Hyperbolic metamaterials: fundamentals and applications. *Nano Convergence* **2014**, *1*, 14.
- [229] D. Traviss, R. Bruck, B. Mills, M. Abb, O. L. Muskens, Ultrafast plasmonics using transparent conductive oxide hybrids in the epsilon-near-zero regime. *Appl. Phys. Lett.* **2013**, *102*, 121112.
- [230] J. A. Girón-Sedas, F. Reyes Gómez, P. Albella, J. R. Mejía-Salazar, O. N. Oliveira, Giant enhancement of the transverse magneto-optical Kerr effect through the coupling of  $\epsilon$ -near-zero and surface plasmon polariton modes. *Phys. Rev. B* **2017**, *96*.

- [231] E. Moncada-Villa, O. N. Oliveira, J. R. Mejía-Salazar,  $\epsilon$ -Near-Zero Materials for Highly Miniaturizable Magnetoplasmonic Sensing Devices. *The Journal of Physical Chemistry C* **2019**, *123*, 3790.
- [232] L. Chen, X. Li, G. P. Wang, W. Li, S. H. Chen, L. Xiao, D. S. Gao, A Silicon-Based 3-D Hybrid Long-Range Plasmonic Waveguide for Nanophotonic Integration. *J. Lightwave Technol.* **2012**, *30*, 163.
- [233] J. A. Dionne, L. A. Sweatlock, M. T. Sheldon, A. P. Alivisatos, H. A. Atwater, Silicon-Based Plasmonics for On-Chip Photonics. *IEEE J. Sel. Top. Quantum Electron.* **2010**, *16*, 295.
- [234] G. V. Naik, J. Kim, A. Boltasseva, Oxides and nitrides as alternative plasmonic materials in the optical range Invited. *Opt. Mater. Express* **2011**, *1*, 1090.
- [235] X. Wang, X. Ma, E. Shi, P. Lu, L. Dou, X. Zhang, H. Wang, Large-Scale Plasmonic Hybrid Framework with Built-In Nanohole Array as Multifunctional Optical Sensing Platforms. *Small* **2020**, e1906459.
- [236] X. J. Wang, T. Nguyen, Y. Cao, J. Jian, O. Malis, H. Y. Wang, AlN-based hybrid thin films with self-assembled plasmonic Au and Ag nano-inclusions. *Appl. Phys. Lett.* **2019**, *114*, 5.
- [237] J. R. Mejía-Salazar, O. N. Oliveira, Plasmonic Biosensing. *Chemical Reviews* **2018**, *118*, 10617.
- [238] K. V. Sreekanth, Y. Alapan, M. Elkabbash, E. Ilker, M. Hinczewski, U. A. Gurkan, A. De Luca, G. Strangi, Extreme sensitivity biosensing platform based on hyperbolic metamaterials. *Nat. Mater.* **2016**, *15*, 621.
- [239] M. Fan, B. Zhang, H. Wang, J. Jian, X. Sun, J. Huang, L. Li, X. Zhang, H. Wang, Self-Organized Epitaxial Vertically Aligned Nanocomposites with Long-Range Ordering Enabled by Substrate Nanotemplating. *Adv. Mater.* **2017**, *29*, 1606861.